Improving Hydrologic Prediction via Data Assimilation, Data Fusion and High-Resolution Modeling

by

Arezoo Rafieei Nasab

Presented to the Faculty of the Graduate School of

The University of Texas at Arlington in Partial Fulfillment

of the Requirements

for the Degree of

DOCTOR OF PHILOSOPHY

THE UNIVERSITY OF TEXAS AT ARLINGTON

December 2014

Acknowledgements

It is difficult to overstate my gratitude to my advisor, Dr. Dong-Jun Seo. Without his active supervision and constant support, this journey wouldn't have been possible.

Also, I would like to thank all other people who have helped throughout my Ph.D. program by providing invaluable technical and scientific guidance. I wish to thank Dr. Zhegtao Cui and Mr. Brian Cosgrove for their endless help from National Weather Service. I would like to thank Mr. Robert Corby and Mr. Paul McKee from West Gulf River Forecast Center for their support. I also thank Dr. Brian Nelson from National Climatic Data Center. Dr. Haksu Lee has been a great support during my program and I am thankful for all the help.

This thesis would not have been possible without the love and support of my family. My deepest gratitude to my parents and my husband for teaching me the importance of learning and all their sacrifices for me.

November 21, 2014

Abstract

Improving Hydrologic Prediction via Data Assimilation, Data Fusion and High-Resolution Modeling

Arezoo Rafieei Nasab, PhD

The University of Texas at Arlington, 2014

Supervising Professor: Dong-Jun Seo

With population growth, urbanization and climate change, accurate and skillful monitoring and prediction of water resources and water-related hazards are becoming increasingly important to maintaining and improving the quality of life for human beings and well-being of the ecosystem in which people live. Because most hydrologic systems are driven by atmospheric processes that are chaotic, hydrologic processes operate at many different scales, and the above systems are almost always under-observed, there are numerous sources of error in hydrologic prediction. This study aims to advance the understanding of these uncertainty sources and reduce the uncertainties to the greatest possible extent. Toward that end, we comparatively evaluate two data assimilation (DA) techniques ensemble Kalman filter (EnKF) and maximum likelihood ensemble filter (MLEF) to reduce the uncertainty in initial conditions of soil moisture. Results show MLEF is a strongly favorable technique for assimilating streamflow data for updating soil moisture.

In most places, precipitation is by far the most important forcing in hydrologic prediction. Because radars do not measure precipitation directly, radar QPEs are subject to various sources of error. In this study, the three Next Generation Radar (NEXRAD)-based QPE products, the Digital Hybrid Scan Reflectivity (DHR), Multisensor Precipitation Estimator (MPE) and Next Generation Multisensor QPE (Q2), and the radar QPE from the Collaborative Adaptive Sensing of the Atmosphere (CASA) radar are comparatively evaluated for high-resolution hydrologic modeling

in the Dallas-Fort Worth Metroplex (DFW) area. Also, since they generally carry complementary information, one may expect to improve accuracy by fusing multiple QPEs. This study develops and comparatively evaluates four different techniques for producing high-resolution QPE by fusing multiple radar-based QPEs. Two experiments were carried out for evaluation; in one, the MPE and Q2 products were fused and, in the other, the MPE and CASA products were fused. Result show that the Simple Estimation (SE) is an effective, robust and computationally inexpensive data fusion algorithm for QPE.

The other main goal of this study is to provide accurate spatial information of streamflow and soil moisture via distributed hydrologic modeling. Toward that end, we evaluated the NWS's Hydrology Laboratory Research Distributed Hydrologic Model (HL-RDHM) over the Trinity River Basin for several headwater basins. We also develop a prototype high resolution flash flood prediction system for Cities of Fort Worth, Arlington and Grand Prairie, a highly urbanized area. Ideally, the higher the resolution of distributed modeling and the precipitation input is, the more desirable the model output is as it provides better spatiotemporal specificity. There are, however, practical limits to the resolution of modeling. To test and ascertain the limits of high-resolution polarimetric QPE and distributed hydrologic modeling for advanced flash flood forecasting in large urban area, we performed sensitivity analysis to spatiotemporal resolution. The results indicate little consistent pattern in dependence on spatial resolution while there is a clear pattern for sensitivity to temporal resolution. More research is needed, however, to draw firmer conclusions and to assess dependence on catchment scale.

Table of Contents

Acknowledgements iii

Abstract iv

Table of Contents vi

List of Illustrations x

List of Tables xviii

Chapter 1 Introduction and overview 1

Chapter 2 Comparative evaluation of maximum likelihood ensemble filter and ensemble Kalman filter for real-time assimilation of streamflow data 6

2.1. Introduction 7

2.2. Formulation of the assimilation problem 10

2.3. Application of DA techniques 13

2.3.1. Ensemble Kalman filter (EnKF) 15

2.3.2. Maximum likelihood ensemble filter (MLEF) 17

2.3.3. Initialization 19

2.4. Error and uncertainty modeling 19

2.4.1. Error in model dynamics 20

2.4.2. Observational errors 21

2.4.3. Error in model runoff 22

2.5. Evaluation experiments 24

2.6. Results 28

2.6.1. Sensitivity to error variances of streamflow and runoff observations 28

2.6.2. Homoscedastic vs. heteroscedastic error modeling 30

2.6.3. Comparative results of MLEF and EnKF 31

2.7. Conclusions 41

Chapter 3 Comparative evaluation of radar-based quantitative precipitation estimates (QPE) 45
3.1. Introduction to hydrologic application of weather radar 45
3.2. Quantitative precipitation estimation (QPE) 48
3.2.1. NEXRAD Digital Hybrid Scan Reflectivity (DHR) 49
3.2.2. Multisensor Precipitation Estimator (MPE) 50
3.2.3. Q2 QPE 51
3.2.4. Collaborative Adaptive Sensing of Atmosphere (CASA) 52
3.3. Study area, data acquisition and preparation 54
3.3.1. Rain gauge observation 55
3.3.2. DHR 55
3.3.3. MPE 57
3.3.4. Q2 QPE 58
3.3.5. CASA QPE 59
3.4. Methodology 60
3.4.1. Error statistics 60
3.4.2. QPE merging 61
3.5. Results 63
3.5.1. Native spatial resolution and 1 hour temporal resolution 63
3.5.2. Full HRAP spatial resolution and 1 hour temporal resolution 69
3.5.3. Native spatial resolution and 15 minute temporal resolution 72
3.6. Conclusion 75
Chapter 4 Improving high-resolution precipitation analysis via fusion of multiple radar-based precipitation products 78
4.1. Introduction 79

4.2. Approach 81
4.3. Methodology 84
4.3.1. Direct Estimation (DE) 84
4.3.2. Bias Correction (BC) 86
4.3.3. Reduced-Dimension Bias Correction (RBC) 87
4.3.4. Simple Estimation (SE) 88
4.4. Study area and data acquisition 89
4.5. Estimation of statistical parameters 92
4.6. Evaluation 97
4.7. Results 99
4.8. Conclusion 107
Chapter 5 Evaluation of the NWS distributed hydrologic model over the Trinity River Basin in Texas 109
5.1. Introduction 110
5.2. Model description 112
5.2.1. Distributed model 112
5.2.2. Lumped model 116
5.2.3. Model performance measures 116
5.3. Study area and data used 118
5.4. Results 119
5.5. Conclusion 126
Chapter 6 High resolution distributed model and scale sensitivity 127
6.1. Introduction 127
6.2. Study area and data acquisition 129
6.3. Hydrologic model 133

6.4. Derivation of rating curves 134
6.5. Calibration and initialization 137
6.6. Scale sensitivity 142
6.5.1. Sensitivity analysis to spatial resolution 143
6.5.2. Sensitivity to temporal resolution 149
6.7. Conclusion and future research recommendations 155
Chapter 7 Conclusion and future research recommendations 158
7.1. Comparative evaluation of maximum likelihood ensemble filter and ensemble Kalman filter 158
7.2. Comparative evaluation of radar-based quantitative precipitation estimates (QPE) 159
7.3. Improving high-resolution precipitation analysis via fusion of multiple radar-based precipitation products 160
7.4. Evaluation of the NWS distributed hydrologic model over the Trinity River Basin in Texas 161
7.5. High resolution distributed model and scale sensitivity 162
Appendix A Derivation of high-resolution permanent impervious area (PCTIM) 165
Appendix B Derivation of high-resolution kinematic-wave channel routing parameters 169
Appendix C Derivation of rating curves 177
References 180
Biographical Information 198

List of Illustrations

Figure 2-1 Schematic of the DA cycles based on the fixed-lag smoother formulation. 12

Figure 2-2 Standard deviation of the error in streamflow simulation as a function of the observed streamflow. 23

Figure 2-3 The study basin of MTPT2 in Texas in the service area of the West Gulf River Forecast Center (WGRFC). 26

Figure 2-4 Sensitivity of the performance of MLEF on the variance of the streamflow observation error as measured by RMSE of streamflow prediction. The black, red, and green lines represent the base model simulation, the control simulation by MLEF and the ensemble mean of perturbed simulations with MLEF, respectively. 29

Figure 2-5 Effect of heteroscedastic modeling of observation errors in streamflow, MAP and runoff on RMSE of streamflow prediction with MLEF. The variables C_P and C_Q denote the multiplicative coefficients for MAP and streamflow observations (see Eqs. (2-18) and (2-19)). The abbreviations HETERO and HOMO denote heteroscedastic and homoscedastic modeling of observation errors, respectively. 31

Figure 2-6 Performance of streamflow prediction with MLEF and EnKF at varying levels of the error assumed for the model dynamics. 33

Figure 2-7 Sensitivity of DA performance on the ensemble size (S). 34

Figure 2-8 Sensitivity of DA performance on the number of streamflow observations assimilated at a given assimilation cycle (N_f). 35

Figure 2-9 (Top) Time series of the base (purple), MLEF control (green) and EnKF ensemble mean (red) simulations for the last ten of the 20 events whose peak flow exceeds 100 (m3/sec); one of the 10 events is also blown up at log scale; (Middle) Time series of the difference between the simulated and observed flow; (Bottom) the periods of best performance among the MLEF (green), EnKF (red) and base (purple) model simulations in terms of the absolute error. 38

Figure 2-10 Example ensemble DA results for rising (upper panel) and falling limbs (lower panel). The left panel shows the observed and simulated hydrographs within the forecast time window of 72 hours. The right panel shows the simulated soil moisture states, observed and DA-adjusted MAP and MAPE, and unadjusted and adjusted TCI over the assimilation window (to the left of the orange vertical line) and the prediction window (to the right of the orange line). The vertical orange line denotes the prediction time of May 13, 20Z, 2004 (upper panel) and May 14, 20Z, 2004 (lower panel). 39

Figure 2-11 An example (prediction time Mar 18, 20Z, 1997) of significantly different performance between MLEF and EnKF. 40

Figure 3-1 location and coverage of 8-radar (CASA) in the DFW Urban Testbed 53

Figure 3-2 Study domain encompassing Cities of Fort Worth, Arlington and Grand Prairie and rain gauge locations 54

Figure 3-3 DHR reflectivity field of KFWS radar (Mar 10, 05:24Z, 2013) 56

Figure 3-4 Derived DHR QPE, mapped into HRAP coordinate system, aggregated into hourly rainfall (Mar 10, 05Z, 2013) 57

Figure 3-5 Left: Hourly MPE over WGRFC domain, the rectangle whithin the texas boundary represents the study area, Right: Hourly MPE over DFW domain (Mar 10, 05Z, 2013) 57

Figure 3-6 Mapped and aggregated 5 min Q2 into hourly Q2 QPE (Mar 10, 05Z, 2013)..... 58

Figure 3-7 Aggregated 1 min CASA into hourly CASA QPE (Mar 10, 05Z, 2013)..... 59

Figure 3-8 Scatter Plot of DHR, MPE, Q2 and CASA QPE versus gauge rainfall for all the rain gauges in the Grand Prairie at their native spatial resolution and 1 hour temporal resolution. 64

Figure 3-9 Weights assigned to CASA, Q2, DHR and MPE in the merging process. Threshold is the conditioning value. Sample size for each case is given in parenthesis. 66

Figure 3-10 Multiplicative bias for CASA, Q2, DHR, MPE and the merged product at their native spatial resolution and hourly temporal resolution. Threshold is the conditioning value. Sample size for each case is given in parenthesis. 67
Figure 3-11 RMSE values for CASA, Q2, DHR, MPE and the merged product at their native spatial resolution and hourly temporal resolution. Threshold is the conditioning value. Sample size for each case is given in parenthesis. 67
Figure 3-12 Correlation coefiicient for CASA, Q2, DHR, MPE and the merged product at their native spatial resolution and hourly temporal resolution. Threshold is the conditioning value. Sample size for each case is given in parenthesis. 68
Figure 3-13 MSE decomposition for CASA, Q2, DHR, MPE and the merged product at their native spatial resolution and hourly temporal resolution. The upper panel shows the bias in mean, the middle panel shows the bias in standard deviation and the bottom panel illustrates the strength of covariation. 69
Figure 3-14 Scatter plot of DHR, MPE, Q2 and CASA QPE versus gauge rainfall at ~4 km and 1 hour. 71
Figure 3-15 Scatter plot of DHR, Q2 and CASA QPE versus gauge rainfall at their native spatial resolution and 15 minute temporal resolution. 72
Figure 3-16 Weights assigned to CASA, Q2, and DHR in the merging process. Threshold is the conditioning value. Sample size for each case is given in parenthesis. 73
Figure 3-17 Multiplicative bias for CASA, Q2, DHR, and the merged product at their native spatial resolution and 15 min temporal resolution. Threshold is the conditioning value. Sample size for each case is given in parenthesis. 74
Figure 3-18 RMSE for CASA, Q2, DHR, and the merged product at their native spatial resolution and 15 min temporal resolution. Threshold is the conditioning value. Sample size for each case is given in parenthesis. 74

Figure 3-19 Correlation coefficient bias for CASA, Q2, DHR, and the merged product at their native spatial resolution and 15 min temporal resolution. Threshold is the conditioning value. Sample size for each case is given in parenthesis. 75
Figure 4-1 The data flow for MPE, Q2, and fusion of the two QPEs. 82
Figure 4-2 High Water Warning System (HWWS) network operated by the City of Grand Prairie with the HRAP pixels overlaid. 91
Figure 4-3 Relative departure of the 15-min precipitation at the five rain gauges of 6000, 6080, 6090, 6100 and 6300 from their spatial mean for the period of record. 91
Figure 4-4 a) Lagged (0, 15, 30 and 45 min) spatial correlograms of the observation errors in Q2 QPE. B) Lagged spatial correlograms of the gauge precipitation. c) Lagged cross correlograms between the gauge precipitation and the Q2 estimates. 95
Figure 4-5 the eigenvalue spectra (expressed as cumulative eigenvalues) of the inverse of the modified error covariance matrix, Λ^{-1}, in DE for hypothetical choices of α=0, 1 and 10. 96
Figure 4-6 Weights given to the 64 15-min 1-km Q2 estimates and the 1-hr 4-km MPE estimate for estimation of the 32nd of the 64 state variables 97
Figure 4-7 a) through d) show the percent reduction in root mean square error (RMSE) in estimation of 15-min point precipitation by the four procedures, DE, BC, RBC and SE, over the Q2 estimates (in white) and over the MPE estimates disaggregated to the 15-min 1-km scale using the Q2 estimates (in gray). E) through h) show the percent reduction in RMSE of hourly precipitation estimates by the four procedures over the Q2 estimates aggregated to 1-hr and 4-km scale (in white) and the MPE estimate (in gray). 101
Figure 4-8 Scatter and quantile-quantile plots of the SE-fused 15-min 1-km precipitation vs. the verifying observation. 103
Figure 4-9 Scatter and quantile-quantile plots of 1-hr 4-km precipitation estimates by aggregated Q2 (top), MPE (middle) and fusion (bottom) vs. the verifying 1-hr point precipitation. 104

Figure 4-10 The precipitation accumulation maps by Q2, MPE, DE and SE, respectively, for a 8-hr event in May 08, 2014, over DFW. 105
Figure 4-11 Scatter and quantile-quantile plots of the 15-min CASA (left) and SE-fused (right) precipitation vs. the verifying 15-min point precipitation. 106
Figure 5-1 Schematic of SAC-SMA model 113
Figure 5-2 A priori parameter example obtained from NWS for a) UZTWM, b) UZFWM, c) LZFSM, and d) LZFPM. 115
Figure 5-3 A priori specific discharge 115
Figure 5-4 Left: WGRFC domain, Right: Trinity River Forecast Group 118
Figure 5-5 % Bias, RMSE, Correlation Coefficient and Nash-Sutcliffe efficiency indices of HL-RDHM and SAC-UHG (AB_OPT) for 10 headwater basins in Trinity River basin 120
Figure 5-6 Left: BRPT2 unit hydrograph derived via AB_OPT, Right: Simulated streamflow from SAC-UHG versus observed streamflow 121
Figure 5-7 Left: JAKT2 unit hydrograph derived via AB_OPT, Right: Simulated streamflow from SAC-UHG versus observed streamflow 122
Figure 5-8 Streamflow simulation from HL-RDHM and streamflow observation time series for some significant events (peak flow above 98 percentile) 122
Figure 5-9 Left: MDST2 unit hydrograph derived via AB_OPT, Middle: Simulated streamflow from SAC-UHG versus observed streamflow, Right: Simulated streamflow from HL-RDHM versus observed flow. 124
Figure 5-10 Time series of simulated streamflow (HL-RDHM) versus observed streamflow of some significant events (with peak flow above 99 percentile) 124
Figure 5-11 Left: RYET2 unit hydrograph derived from AB_OPT, Middle: Simulated flow resulted from SAC-UHG versus observed flow, Right: Simulated flow resulted from HL-RDHM versus observed flow 125

Figure 5-12 Time series of simulated versus observed streamflow of some significant events (peak flow above 99 percentile) for SAC-UHG (upper panel) and HL-RDHM (lower panel). Arrow shows the one significant event simulation in both SAC-UHG and HL-RDHM 125
Figure 6-1 Relative error in streamflow simulation at the catchment outlet as a function of the scale of subbasin delineation and the magnitude of error in precipitation input (from Smith et al. 2004b). 129
Figure 6-2 a) Radar umbrellas of XUTA b) Study domain and selected basins for the scale sensitivity (Area of each basin is given in the figure in bold (km^2)) 131
Figure 6-3 Cross-correlation between 15-min precipitation and streamflow time series indicating time-to-peaks of approximately 1.75, 3.25 and 3.25 hours for Catchments 6033, 6013 and 6133, respectively..... 132
Figure 6-4 PCTIM at 1/16 HRAP resolution over the three study catchments. 132
Figure 6-5 Left: Shifted observed stage versus simulated flow forced by MPE (1/8 HRAP & 15 min) at log-log scale, The lower dashed green line is corresponding to the stage that there is a change in the cross section and the upper dash green line is the road height. Right: Shifted observed stage versus simulated flow forced by MPE (1/8 HRAP & 15 min). Red dots are the empirical fitted rating curve. Black line is rating curve derived from Kean and Smith method. . 136
Figure 6-6 a) RMSE value b) Difference between the simulated and observed volume c) Simulated peak flow versus observed peak flow for individual events d) Timing error as a function of observed peak flow, e) Probability of detection f) False alarm rate for the best five combination of multiplicative factor for Q0 (specific discharge) and QM (exponent) for 6033 (best case, Q0=1.1, QM=1.5)..... 139
Figure 6-7 a) RMSE value b) Difference between the simulated and observed volume c) Simulated peak flow versus observed peak flow for individual events d) Timing error as a function of observed peak flow, e) Probability of detection f) False alarm rate for the best five combination of

multiplicative factor for Q0 (specific discharge) and QM (exponent) for 6103 (best case, Q0=1, QM=1.1)..... 140
Figure 6-8 a) RMSE value b) Difference between the simulated and observed volume c) Simulated peak flow versus observed peak flow for individual events d) Timing error as a function of observed peak flow, e) Probability of detection f) False alarm rate for the best five combination of multiplicative factor for Q0 (specific discharge) and QM (exponent) for 6133 (best case, Q0=1.1, QM=1.1)..... 141
Figure 6-9 a) (simulated peak flow – observed peak flow) as a function of the observed peak flow, b) (simulated time-to-peak – observed time-to-peak) as a function of the observed peak flow, and c) (simulated flow volume – observed flow volume) as a function of the observed flow volume for significant events at different spatial resolutions for Catchment 6033..... 144
Figure 6-10 a) (simulated peak flow – observed peak flow) as a function of the observed peak flow, b) (simulated time-to-peak – observed time-to-peak) as a function of the observed peak flow, and c) (simulated flow volume – observed flow volume) as a function of the observed flow volume for significant events at different spatial resolutions for Catchment 6103 145
Figure 6-11 a) (simulated peak flow – observed peak flow) as a function of the observed peak flow, b) (simulated time-to-peak – observed time-to-peak) as a function of the observed peak flow, and c) (simulated flow volume – observed flow volume) as a function of the observed flow volume for significant events at different spatial resolutions for Catchment 6133 146
Figure 6-12 Cross correlation between simulated and observed flow as function of spatial resolutions. They are based on the combined time series of all three catchments. 148
Figure 6-13 Cross correlation between observed and simulated flows forced by CASA QPE (in red) and by MPE precipitation (in black) as a function of spatial resolution for all 3 catchments (left) and for Catchment 6033 only (right). 148

Figure 6-14 Smoothed power spectra of observed (in black) and simulated (in color) streamflow at all spatial resolutions forced by the CASA QPE (Left) and the MPE (Right)..... 149
Figure 6-15 Percentage increase in RMSE at 1, 5, 15, 30 and 60 minute temporal resolutions... 150
Figure 6-16 a) (simulated peak flow – observed peak flow) as a function of the observed peak flow, b) (simulated time-to-peak – observed time-to-peak) as a function of the observed peak flow, and c) (simulated flow volume – observed flow volume) as a function of the observed flow volume for significant events at different temporal resolutions for Catchment 6033..... 151
Figure 6-17 a) (simulated peak flow – observed peak flow) as a function of the observed peak flow, b) (simulated time-to-peak – observed time-to-peak) as a function of the observed peak flow, and c) (simulated flow volume – observed flow volume) as a function of the observed flow volume for significant events at different temporal resolutions for Catchment 6103..... 152
Figure 6-18 a) (simulated peak flow – observed peak flow) as a function of the observed peak flow, b) (simulated time-to-peak – observed time-to-peak) as a function of the observed peak flow, and c) (simulated flow volume – observed flow volume) as a function of the observed flow volume for significant events at different temporal resolutions for Catchment 6133..... 153
Figure 6-19 Autocorrelations of observed (in black) and simulated (in color) streamflow at different temporal resolutions..... 154
Figure 6-20 Smoothed power spectra of observed (in black) and simulated (in color) streamflow at all temporal resolutions (left) and at resolutions of 1-, 5- and 15-min only (right). 155

List of Tables

Table 2-1 Description of terms used in the equations (2-1) and (2-2). 14

Table 2-2 Summary of the parameter settings used in the three experiments 25

Table 3-1 Availability of radar-based QPEs and rain gauge data for the study and their spatiotemporal resolution. 55

Table 5-1 SAC-SMA parameters, the units, description and the allowable range 114

Table 5-2 Area, time to peak, adjustment factors for precipitation and PE 119

Table 6-1 Selected multiplicative factors for precipitation, specific discharge and exponent. 142

Table 6-2 RMSE values for different spatial resolutions 143

Table 6-3 RMSE values for different temporal resolutions 150

Chapter 1

Introduction and overview

The main sources of errors in hydrologic predictions may be categorized into three categories, the input uncertainty, the parametric uncertainty and the uncertainty in the initial conditions. One of the main goals of this dissertation is to enhance the understanding of these uncertainties and reduce them to the greatest possible extent. Data assimilation as an appealing technique for reducing uncertainty in initial conditions is discussed in Chapter 1. Precipitation is very often the most important forcing in hydrologic predictions. Improving its accuracy will improve the quality of hydrologic prediction by reducing uncertainties in the observed boundary conditions. Toward that end, we carried out in Chapter 2 comparative evaluation of different Quantitative Precipitation Estimates (QPEs). Utilizing the multiple sources of QPE available in DFW, we applied several fusion techniques to improve the quality and accuracy of the precipitation forcing in Chapter 3.

The widespread availability of radar-based precipitation estimates at high spatial resolution led to transformation from lumped hydrologic modeling toward distributed hydrologic modeling. One of the main foci of this study is to provide accurate spatiotemporally-detailed information about important hydrologic variables such as streamflow and soil moisture. Toward that end, we evaluated the NWS's Hydrology Laboratory Research Distributed Hydrologic Model (HL-RDHM) over the Trinity River Basin for several headwater basins in Chapter 4. One of the largest benefits from high-resolution distributed modeling may be realized in large urban areas. One of the main outcomes of this dissertation is the development of a prototype flash flood prediction system for the Cities of Fort Worth, Arlington and Grand Prairie as a highly urbanized area. Ideally, the higher the resolution of distributed modeling and the precipitation input is, the more desirable the model output is as it provides better spatiotemporal specificity. There are,

however, practical limits to the resolution of modeling. In this work, we test and ascertain the limits of high-resolution polarimetric QPE and distributed hydrologic modeling for advanced flash flood forecasting in large urban areas and identify the scale at which the relative error may be at minimum given the quality of radar QPE. A brief description of each chapter as well as the objectives and new contributions is given below:

Uncertainties in the initial conditions (IC) of soil moisture and observed boundary conditions (BC) of precipitation and potential evaporation (PE) introduce considerable errors in hydrologic predictions. In recent years, data assimilation (DA) has been gaining great attention to reduce these uncertainties. Soil moisture is seldom observed at the catchment scale. To infer soil moisture states, one may instead assimilate streamflow observations. The relationship between streamflow and soil moisture, however, is highly nonlinear for which popular data assimilation (DA) techniques in oceanography and weather forecasting such as ensemble Kalman filter (EnKF) may not work well. Maximum likelihood ensemble filter (MLEF), a more recently developed technique, does not assume linear observation equation. In this dissertation, EnKF and MLEF are comparatively evaluated for updating the soil moisture states of the Sacramento soil moisture accounting model (SAC) by assimilating observations of streamflow, mean areal precipitation (MAP) and mean areal potential evapotranspiration (MAPE). The study is a first of its kind in the hydrologic literature and advances understanding of the strengths and limitations of the DA techniques for problems involving nonlinear processes and nonlinear observation equations. Based on this study, an algorithm has been developed and implemented for assimilation of water quality and streamflow observations in support of real-time water quality forecasting at the Water Quality Control Center of the National Institute of Environmental Research in the Republic of Korea.

In most places, precipitation is by far the most important forcing in hydrologic prediction. Accurate quantitative precipitation estimation (QPE) can provide valuable lead time in hydrologic prediction owing to the time lag in streamflow response to precipitation input. Due to large

variability of precipitation in space and time, however, QPE remains a large challenge. Today, weather radars are routinely used for QPE. In some areas, there may be multiple sources of QPE including rain gauges, radars and satellites. Because radars do not measure precipitation directly, radar QPEs are subject to various sources of error. In this study, the three Next Generation Radar (NEXRAD)-based QPE products, the Digital Hybrid Scan Reflectivity (DHR), Multisensor Precipitation Estimator (MPE) and Next Generation Multisensor QPE (Q2), and the radar QPE from the Collaborative Adaptive Sensing of the Atmosphere (CASA) radar are comparatively evaluated for high-resolution hydrologic modeling in the Dallas-Fort Worth Metroplex (DFW) area. This study advances understanding of the error characteristics and properties of the above QPE products for their effective use in hydrologic applications. Based on this study, the CASA and MPE products are being used for the ongoing development and implementation of the prototype flash flood prediction system for areas of Fort Worth, Arlington and Grand Prairie in DFW, which is expected to save lives and properties via improved emergency management.

In many areas, there exist multiple sources of radar-based QPE. In DFW, for example, the MPE, Q2 and CASA products are available. Because they generally carry complementary information, one may expect to improve accuracy by fusing multiple QPEs. While multisensor merging of satellite, radar and/or rain gauge data for improved QPE is widely investigated, fusion of multiple gridded QPEs of different spatiotemporal resolutions for high-resolution QPE is relatively new. This study develops and comparatively evaluates four different techniques for producing high-resolution QPE by fusing multiple radar-based QPEs. Two experiments were carried out for evaluation; in one, the MPE and Q2 products were fused and, in the other, the MPE and CASA products were fused. This study advances identification and understanding of the factors that are important in fusion of radar QPE products and development of effective, robust and computationally inexpensive data fusion algorithms for QPE. Such an algorithm, Simple Estimation (SE), has been developed from this study which may be expected to improve QPE very

inexpensively at all resolutions of the ingredient QPEs. This study advances understanding of precipitation fusion and the relationships among different fusion procedures, and evaluation of multiple radar QPEs in the DFW area.

Availability of radar QPE has revolutionized hydrologic modeling in recent years from lumped approaches to distributed approaches. In the latter, the catchments are subdivided into subcatchments of the scale of the modeler's choice to utilize not only high-resolution radar QPE but also a wide variety of physiographic information readily available via Geographic Information Systems (GIS). While distributed modeling does utilize a wealth of additional information, the highly nonlinear nature of the rainfall-runoff processes meant that the errors in the high-resolution observed and fixed boundary conditions, such as, e.g., precipitation and soil properties, respectively, can easily be amplified and propagated through the model(s), resulting in a deterioration, rather than an improvement, in the quality of model simulations compared to lumped models. The negative impact of such nonlinear error growth can be larger for high-resolution hydrologic modeling. This study comparatively assesses streamflow simulation over the Trinity River Basin in TX between operational lumped and distributed models. The lumped models used are the SAC and unit hydrograph. The distributed models used are the gridded version of SAC and kinematic-wave routing as implemented in the NWS's Hydrology Laboratory Research Distributed Hydrologic Model (HLRDHM). This study advances understanding of the capabilities and limitations of distributed hydrologic modeling over a large area, and identification and inference of sources of error in such modeling. The potential benefits from distributed modeling are very large; when successfully applied at high resolution, it enables monitoring and prediction of a large part of the terrestrial water cycle at any location in the model domain, including precipitation, evapotranspiration, soil moisture, infiltration, runoff and streamflow.

One of the largest benefits from high-resolution distributed modeling may be realized in large urban areas where population density is high and increasing, urbanization changes

physiography and hence the hydrologic and hydraulic conditions, and the impact of climate change may be larger in that even a small storm can produce deadly flash flooding. With the ongoing deployment of the CASA weather radar systems, the DFW area offers a unique testbed for very high-resolution hydrologic modeling driven by very high-resolution QPE. This study builds on the advances in understanding and modeling and analysis capabilities from the studies above to develop a high-resolution flash flood prediction system for the Cities for Fort Worth, Arlington and Grand Prairie. Due to the nonlinear growth of error, however, there is a limit to the resolution of modeling given the accuracy and resolution of the QPE, the errors in the hydrologic model structures, parameters and states, and other unknown/unknowable anthropogenic and natural sources of error. This study advances understanding of the dependence of the quality of streamflow simulation on the resolution of QPE and modeling of soil moisture and routing, and tests the limits of advanced precipitation sensing and hydrologic modeling for flash flooding prediction in the real world. The result of this study is currently being implemented in the prototype flash flood prediction system for emergency managers in DFW in preparation for the spring storm season of 2015.

Admittedly, the research carried out in this dissertation addresses only a few challenges in hydrologic prediction. Undoubtedly, much additional work is needed to fully address them. It is hoped that the additional knowledge gained and the tools developed will serve as building blocks and lead to an evolving system for monitoring and prediction of water resources and water-related hazards, particularly in large urban areas, that integrates advanced sensing, data fusion, data assimilation and high-resolution modeling to provide accurate, and time- and location-specific information that improves the quality of life and sustainability.

Chapter 2

Comparative evaluation of maximum likelihood ensemble filter and ensemble Kalman filter for real-time assimilation of streamflow data

Various data assimilation (DA) methods have been used and are being explored for use in operational streamflow forecasting. For ensemble forecasting, ensemble Kalman filter (EnKF) is an appealing candidate for familiarity and relative simplicity. EnKF, however, is optimal in the second-order sense, only if the observation equation is linear. As such, without an iterative approach, EnKF may not be appropriate for assimilating streamflow data for updating soil moisture states due to the strong nonlinear relationships between the two. Maximum likelihood ensemble filter (MLEF), on the other hand, is not subject to the above limitation. Being an ensemble extension of variational assimilation (VAR), MLEF also offers a strong connection with the traditional single-valued forecast process through the control, or the maximum likelihood, solution. In this work, we apply MLEF and EnKF as a fixed lag smoother to the Sacramento (SAC) soil moisture accounting model and unit hydrograph (UH) for assimilation of streamflow, mean areal precipitation (MAP) and potential evaporation (MAPE) data for updating soil moisture states. For comparative evaluation, three experiments were carried out. Comparison between homoscedastic versus heteroscedastic modeling of selected statistical parameters for DA indicates that heteroscedastic modeling does not improve over homoscedastic modeling, and that homoscedastic error modeling with sensitivity analysis may suffice for application of MLEF for soil moisture updating using streamflow data. Comparative evaluation with respect to the model errors associated with soil moisture dynamics, the ensemble size and the number of streamflow observations assimilated per cycle showed that, in general, MLEF outperformed EnKF under varying conditions of observation and model errors, and ensemble size, and that MLEF performed well with an ensemble size as small as 5 while EnKF required a much larger ensemble size to

perform closely to MLEF. Also, MLEF was not very sensitive to the uncertainty parameters and performed reasonably well over relatively wide ranges of parameter settings, an attribute desirable for operational applications where accurate estimation of such parameters is often difficult.

2.1. Introduction

Uncertainties in the initial conditions (IC) of soil moisture and observed boundary conditions (BC) of precipitation and potential evaporation (PE) introduce considerable errors in hydrologic forecasts. In recent years, data assimilation (DA) has been gaining great attention to reduce these uncertainties (Brocca et al., 2010; Clark et al., 2008; De Lannoy et al., 2007; Liu et al., 2011; Liu and Gupta, 2007; Reichle et al., 2002; Seo et al., 2003). DA makes inference on the model states by bringing together all available observations from often disparate sources, quantifying the uncertainties in the model and observation errors, and updating the state variables by optimally combining model predictions with observations. In addition to DA in the single-valued sense, ensemble DA is also necessary to allow state updating in operational ensemble forecasting systems (Seo et al. 2006; Demargne et al. 2014; Cloke and Pappenberger 2009; Schaake et al. 2007a, 2007b; Shellekens et al. 2011; Thielen et al. 2008; Werner et al. 2005, 2009).

In hydrologic forecasting, one would ideally like to assimilate soil moisture observations to update the model ICs of soil moisture, in which case the observation equation would be linear. In reality, however, soil moisture states are seldom observed in-situ and, even if such measurements are available, they are generally not representative of the conditions at the scale where the hydrologic models operate. Streamflow observations, on the other hand, are much more widely available and reflect the catchment-wide conditions, albeit only in some spatiotemporally integrated sense. For the use of streamflow data for updating of soil moisture states, the

observation equation involved is generally highly nonlinear, which poses an additional challenge in DA.

Various DA techniques such as Kalman filtering (Kalman 1960), variational assimilation (VAR, Jazwinski 1970, Li and Navon 2001, Seo et al. 2003, 2009), particle filtering (Weerts and Serafy, 2006), etc., have their own merits and demerits (Liu and Gupta, 2007; Liu et al. 2013). Extensions of Kalman filter have been developed to deal with nonlinear systems. Extended Kalman filter (EKF), e.g., involves linearizing the model dynamics using the first-order Taylor series approximation (Maybeck 1979). To overcome the limitations of EKF, a Monte Carlo-based Kalman filter, or EnKF, was proposed by Evensen (1994). The novelty of EnKF is in its ability to deal with nonlinear model dynamics naturally without linearizing model equations (Moradkhani et al. 2005). Unlike VAR, EnKF does not assume temporally constant model error covariance or requires a separate adjoint model. For the above reasons and algorithmic simplicity, EnKF has gained great popularity in various applications recently (Evensen 2003, Chen et al. 2011, Xie and Zheng 2010).

Variations of EnKF and different types of ensemble filter have also been developed. Anderson (2001) proposed an ensemble-based filter called ensemble adjustment Kalman filter (EAKF) in which both the mean and covariance of updated ensembles are preserved. He concluded that EAKF is superior to EnKF especially for small ensemble sizes. Another variant of EnKF was introduced by Whitaker and Hamill (2002) called ensemble square root filter (ESRF) in which the perturbation of observation is avoided. Sakov and Oke (2008) presented a linear approximation of ESRF with comparable performance. Bocquet (2011) proposed a deterministic variant of EnKF named finite-size ensemble transform Kalman filter (ETKF-N) which is less sensitive to sampling errors. Van Leeuwen and Evensen (1996) introduced ensemble smoother (ES), and Evensen and van Leeuwen (2000) developed ensemble Kalman smoother (EnKS). Cohn et al. (1994) used a fixed-lag smoother to incorporate all available observation at current time as

well as a fixed amount of time past each analysis time. In this work, we use a fixed-lag smoother formulation of EnKF.

Unlike VAR, however, EnKF and its variants assume linear observation equation. As such, if the observation equation is nonlinear as in assimilating streamflow data for updating soil moisture states, EnKF may not be expected to perform well. To address the above limitation in EnKF, Zupanski (2005) developed maximum likelihood ensemble filer (MLEF) which combines the strength of EnKF and VAR. MLEF may be considered as an ensemble extension of VAR in which, once the VAR solution-like maximum likelihood or control solution is obtained, ensemble members are generated by perturbing the control states and propagating them forward as in EnKF. The purpose of this work is to compare EnKF with MLEF for assimilation of streamflow data in soil moisture updating.

In MLEF, the analysis solution is obtained as a model state that maximizes the posterior conditional probability distribution. The maximum likelihood solution, in the single-valued sense, is superior to ensemble mean if the normality assumption is not met. In operational forecasting, provision of such a "most likely" solution, in addition to the ensemble members, is very important to the human forecasters as the former provides a reference solution for the existing manual DA process, referred to as run-time modifications (MOD) in NWS (Seo et al. 2009). The maximum likelihood state is estimated via iterative minimization, thus making the MLEF approach closely related to iterated Kalman filter (Jazwinski 1970; Cohn 1997; Zupanski 2005). As with other ensemble data assimilation algorithms, MLEF produces an estimate of the uncertainty in the analysis solution (e.g., analysis error covariance). Unlike VAR, however, MLEF does not require an adjoint code and solves a reduced-rank problem in ensemble subspace with superior preconditioning (Zupanski 2005).

MLEF has been used in various studies such as carbon transport (Lokupitiya et al. 2008; Zupanski et al. 2007b), aerosol retrieval (Carrio et al. 2008), wind power forecasting (Zupanski et

al. 2010) and targeting additional observations for forecasting of tropical cyclones (Kim et al. 2010). To the best of the authors' knowledge, however, MLEF has never been used in hydrologic applications or objectively compared with EnKF for streamflow assimilation until this paper. Additional significant new contributions of this paper include systematic sensitivity analysis of DA performance with respect to the ensemble size, the number of streamflow observations assimilated per cycle and the magnitude of model and observational errors, and comparative evaluation of performance of DA under homoscedastic and heteroscedastic modeling of observation errors.

It is noted here that the evaluation carried out in this work is in the single-valued sense only. That is, we only consider the DA techniques as minimization tools for single-valued analysis. By "single-valued", we mean analysis or prediction expressed by a single representative value, such as the maximum likelihood solution in MLEF or the ensemble mean in EnKF, rather than by multiple values such as an ensemble. The term single-valued forecast was introduced recently in the hydrologic literature (Schaake et al. 2007a, 2007b, Wu et al. 2011, Regonda et al. 2013, Demargne et al. 2014) to distinguish from deterministic forecast. This chapter is organized as follow. Section 2.2 describes the formulation of the assimilation problem. Section 2.3 describes the EnKF and MLEF methodologies. Error modeling is described in Section 2.4. Section 2.5 describes the study basins, data used and experiment design. We present the results in Section 2.6. Section 2.7 provides conclusion and future research recommendations.

2.2. Formulation of the assimilation problem

Assume a headwater basin with a stream gauge at the outlet with hourly observations of streamflow, mean areal precipitation (MAP) and mean areal potential evaporation (MAPE) available in real time. Assume also that lumped rainfall-runoff and routing models operate for

continuous simulation and prediction of streamflow at the catchment outlet. The rainfall-runoff and routing models used in this work are the Sacramento soil moisture accounting model (SAC) (Burnash et al. 1973) and unit hydrograph (UH) (Chow et al. 1988), respectively. The SAC model has six state variables which are updated by DA: the upper zone tension water content (UZTWC), the upper zone free water content (UZFWC), the lower zone tension water content (LZTWC), the lower zone supplemental free water content (LZFSC), the lower zone primary free water content (LZFPC) and tension water content in the additional impervious area (ADIMC) (Burnash et al. 1973).

Our problem is then to assimilate the observations of MAP, MAPE and streamflow for real-time updating of the soil moisture states of the rainfall-runoff model. To account for the time lag between the generation of runoff and its arrival at the catchment outlet, we formulate the DA problem as fixed-lag smoothing (Schweppe 1973, Li and Navon 2001) following Seo et al. (2003, 2009) and Lee et al. (2011, 2012). The size of the fixed lag, or the assimilation window, should be comparable to the response time of the basin. The experience thus far indicates that the size of the window should be about the length of the unit hydrograph, or the basin response time of fast runoff (Seo et al. 2003, 2009; Lee et al. 2011). Figure 2-1 depicts the sequential assimilation process using the fixed-lag smoother.

Estimates of MAP, in particular those based on radar estimates of precipitation (Seo et al. 2010), and MAPE are subject to systematic biases. To correct them as part of the DA process, we introduce multiplicative adjustment factors for MAP and MAPE and adjust, or update, them over the assimilation window along with the initial model soil moisture states at the beginning of the assimilation window (Lee et al. 2011). Note that adjusting multiplicative biases for MAP and MAPE in this way amounts to adjusting the model soil moisture states within the assimilation window, which results in updating the soil moisture states at the end of the assimilation window, or at the prediction time.

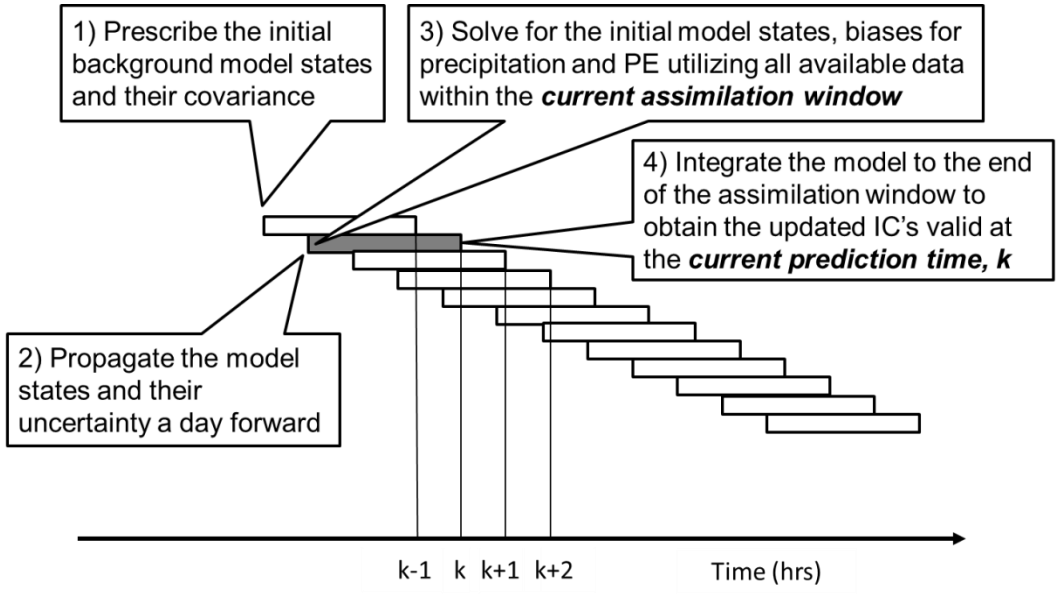

Figure 2-1 Schematic of the DA cycles based on the fixed-lag smoother formulation.

We also introduced the additive error in the total channel inflow (TCI), which combines the surface and groundwater runoffs from the SAC (Seo et al. 2009). The motivation for the additive error in model runoff is to account for possible model structural and/or parametric errors that may not be captured by the random errors assumed in the soil moisture dynamics. The above problem may be cast as the following weakly-constrained nonlinear minimization:

$$
\begin{aligned}
\text{Minimize}\quad J_K = {} & \frac{1}{2}\left[X_B - X_{S,K-L}\right]^T P_f^{-1}\left[X_B - X_{S,K-L}\right] \\
& + \frac{1}{2}\left[Z_Q - H_Q\left(X_{S,K-L}, X_P, X_E, X_{Rs}, W\right)\right]^T R_Q^{-1}\left[Z_Q - H_Q\left(X_{S,K-L}, X_P, X_E, X_{Rs}, W\right)\right] \\
& + \frac{1}{2}\left[Z_P - H_P X_P\right]^T R_P^{-1}\left[Z_P - H_P X_P\right] \\
& + \frac{1}{2}\left[Z_E - H_E X_E\right]^T R_E^{-1}\left[Z_E - H_E X_E\right] \\
& + \frac{1}{2} X_{Rs}^T R_{Rs}^{-1} X_{Rs} + \frac{1}{2} W^T Q_W^{-1} W
\end{aligned}
\qquad (2\text{-}1)
$$

$$\text{Subject to} \quad X_{S,k} = M\left(X_{S,k-1}, X_{P,k}, X_{E,k}\right) + W_{k-1} \quad k = K - L + 1, \ldots, K, \qquad (2\text{-}2)$$

$$X_{S,j}^{min} \leq X_{S,j,k} \leq X_{S,j}^{max}, \quad j = 1, \ldots, N; k = K - L, \ldots, K$$

In Eq. (2-1), J_K denotes the objective function at the current hour K, L denotes the length of the assimilation window in hours, and k indexes the time step in hours, Z, X, H, R, P_f, W and Q_w denote the observation vector consisting of all observations valid within the assimilation window, the control vector consisting of all control variables (i.e. the variables to be updated), the observation equation which relates the control variables with the observations, the observation error covariance matrix, the forecast error covariance matrix, the random error in the model dynamics within the assimilation window and the covariance matrix of the above random error, respectively; the subscripts Q, P, E, B and Rs signify streamflow, precipitation, potential evaporation (PE), the background (i.e., a priori or before-DA) model state, and model runoff, respectively, and the superscript T denotes the matrix transpose. The detailed explanation of the variables appearing in Eq.(2-1) is given in Table 2-1. In Eq.(2-2), M denotes the soil moisture accounting model, W_{k-1} denotes the model error vector valid at time step k-1, $X_{S,j}^{min}$ and $X_{S,j}^{max}$ denote the lower and upper bounds of the j-th SAC state variable, $X_{S,j}$, and N denotes the number of the SAC states. Other variables are explained in Table 2-1. To specify the a priori, or background, estimates for the control vector, we assume no biases for MAP (i.e. $X_{P,k}$= 1) and MAPE (i.e. $X_{E,k}$ = 1), no model error in runoff (i.e. $X_{Rs,k}$ = 0), and X_B=$X_{S,K-L}$. In the following section, we describe how EnKF and MLEF are applied to solve the above assimilation problem.

2.3. Application of DA techniques

Let X_k denote the vector of model states at time step k and assume that the model dynamics over a single time step is described by Eq ((2-3):

Table 2-1 Description of terms used in the equations (2-1) and (2-2).

General Term	General Description	Specific Term	Specific Description
X	The control vector	$X_{S,K-L}$	The six SAC states valid at hour K-L $X_S=[X_{S,i,K-L}, X_{S,i,K-L+1}, \ldots, X_{S,i,K}]^T$, j=1, …, 6
		X_P	Control vector of time-varying biases in the precipitation. $X_P=[X_{P,K-L}, X_{P,K-L+1}, \ldots, X_{P,K}]^T$
		X_E	Control vector of time-varying biases in potential evaporation. $X_E=[X_{E,K-L}, X_{E,K-L+1}, \ldots, X_{E,K}]^T$
		X_{Rs}	The additive error in the total channel inflow (TCI), which combines the surface and groundwater runoffs from the SAC (Seo et al. 2009). $X_{Rs}=[X_{Rs,K-L}, X_{Rs,K-L+1}, \ldots, X_{Rs,K}]^T$
		X_B	Model-generated (i.e. without-DA) SAC states at the beginning of the assimilation window. $X_B= X_{S,K-L}$
Z	Observation vectors	Z_Q	Hourly streamflow observations to be assimilated in the current cycle.
		Z_P	Hourly MAP observations within the assimilation window.
		Z_E	Hourly MAPE observations within the assimilation window.
H	Structure function that relates the control variables with the observed variables	$H_Q( )$	The SAC and UH routing models.
		H_P	Equal to Z_P.
		H_E	Equal to Z_E.
R	Observation error covariance matrix	R_Q	Observation error covariance matrix of streamflow.
		R_P	Observation error covariance matrix of MAP.
		R_E	Observation error covariance matrix of MAPE.
		R_{Rs}	Error covariance matrix of model runoff.

$$X_k = M(X_{k-1}) + W_{k-1} \quad (2\text{-}3)$$

where $M(\,)$ denotes the dynamical model, W_{k-1}denotes the temporally-uncorrelated model error at time $k-1$ with zero mean and covariance of $Q_{w,k-1}$, and X_{k-1} and W_{k-1} are assumed to be independent. The observation equation is written in generality as:

$$Z_k = G(X_k) + V_k \quad (2\text{-}4)$$

where Z_k denotes the vector of the observations at time step k, G( ) denotes the model-simulated observation, V_k denotes the vector of temporally-uncorrelated observation errors with mean zero and covariance of R_k, and X_k and V_k are assumed to be independent. In G( ), the model-simulated streamflow is from SAC-UH while the model-simulated MAP and MAPE are simply the observed MAP and estimated MAPE multiplied by their respective adjustment factors.

2.3.1. Ensemble Kalman filter (EnKF)

EnKF (Evensen 1994) is based on a Monte Carlo application of Kalman filter (Kalman 1960). In our formulation, to arrive at a linear observation equation from nonlinear mapping of soil moisture to streamflow, we augment the state vector with the observation vector as follows (Lorentzen and Nævdal 2011):

$$Y_k = \begin{bmatrix} X_k \\ G(X_k) \end{bmatrix} \quad (2\text{-}5)$$

where X_k denotes the original state vector, Y_k denotes the augmented state vector and $G(X_k)$ comprise the model-simulated streamflow, MAP, and MAPE. Owing to the augmentation, the observation equation may be expressed as $Z_k = HY_k$ where H denotes the linear observation operator in which the diagonal elements corresponding to the state variables and the observations are given by zero and unity, respectively, with all other elements being zeros. The ensemble of the augmented state vector is given by:

$$Y_k = \begin{bmatrix} X_k^1 & X_k^2 & \cdots & X_k^S \\ G(X_k^1) & G(X_k^2) & \cdots & G(X_k^S) \end{bmatrix} \tag{2-6}$$

where S denoted the ensemble size. The model dynamics equation for the jth ensemble member is given by:

$$X_{f,k}^j = M\left(X_{a,k-1}^j\right) + W_{k-1}^j \tag{2-7}$$

where M( ) denotes the dynamical model, W_{k-1}^j denotes the random model error at time $k-1$ corresponding to the j^{th} ensemble member, $X_{a,k-1}^j$ denotes the updated state variable corresponding to the j^{th} ensemble member at time step $k-1$and $X_{f,k}^j$ denotes the forecasted state variable at time step k. In the analysis step, each ensemble member is updated via the Kalman gain equation:

$$Y_{a,k}^j = Y_{f,k}^j + K_k\left(Z_{o,k} - HY_{f,k}^j\right) \tag{2-8}$$

where $Y_{f,k}^j$ denotes the augmented state vector at time step k, $Y_{a,k}^j$ denotes the updated augmented state vector, H denotes the linear observation operator, K_k denotes the Kalman gain matrix at time step k, and $Z_{o,k}$ denotes the vector of normally-distributed observations with mean equal to the actual observations and variance equal to the observation error covariance, i.e., $Z_{o,k} \sim N(Z_k, R)$, where R is a diagonal matrix. We note here that, after the realizations of $Z_{o,k}$ are drawn, they are shifted and scaled to preserve the prescribed mean and variance (Lorentzen and Nævdal 2011). The above operation reduces the sampling error. The Kalman gain is given by:

$$K_k = P_{f,k}H^T\left(HP_{f,k}H^T + R_k\right)^{-1} \tag{2-9}$$

The forecast error covariance is approximated by:

$$P_{f,k} = \frac{1}{S-1}\left(Y_{f,k} - \overline{Y_{f,k}}\right)\left(Y_{f,k} - \overline{Y_{f,k}}\right)^T \tag{2-10}$$

where S denotes the ensemble size and $\overline{Y_{f,k}}$ denotes the mean of $Y_{f,k}$. In the above, it is important to note that, even though the observation equation is made linear in appearance via state

augmentation, the analysis solution is in general still not optimal because it assumes that streamflow responds to soil moisture linearly near the solution. Accordingly, the analysis solution of Eq. (2-8), which is a linear projection, may not be close to the true optimal solution. To locate the optimal solution, iterations are generally necessary using, e.g., iterative Kalman filter (Lorentzen and Nævdal 2011). In this work, we assess the quality of the above solution against the MLEF solution.

2.3.2. Maximum likelihood ensemble filter (MLEF)

In this subsection, we describe the key elements of MLEF. For details, the reader is referred to Zupanski (2005). As in EnKF, the state variables evolve according to Eq. (3-1). The analysis step for MLEF, however, is quite different from that of EnKF as shown below. Evaluation of the forecast error covariance in MLEF may be more easily understood by introducing the second-order moment equation of Eq. (2-1) following the first-order Taylor series approximation as in EKF:

$$P_{f,k} = \widetilde{M}_{k-1,k} P_{a,k-1} \widetilde{M}^{T}_{k-1,k} + R_{W,k-1} \tag{2-11}$$

where $P_{f,k}$ denotes the covariance matrix of the forecast model states at time step k, $\widetilde{M}_{k-1,k}$ denotes the Jacobian of the model with respect to the state variables evolving from time step k-1 to time step k, $P_{a,k-1}$ denotes the analysis (i.e. updated) covariance matrix of the model states at time step k-1, and $R_{W,k-1}$ denotes the model error covariance matrix at time step k-1. In the original formulation of MLEF (Zupanski 2005), model errors were ignored. In this work, we consider them as described in Section 2.4. For now, however, we assume no dynamical model errors for simplicity without loss of generality. The square root of the analysis error covariance matrix may be evaluated numerically as follows:

$$P^{1/2}_{a,k-1} = (p_1 p_2 \dots p_S) \tag{2-12}$$

where

$$p_i = (p_{1,i} p_{2,i} \cdot \cdot \cdot p_{N,i})^T \tag{2-13}$$

In the above, S denotes the ensemble size and N denotes the dimensionality of the state vector. Denoting the square root matrix of the forecast error covariance as $P_f^{1/2} = (b_1 b_2 \ldots b_S)$, we have the following finite difference approximation for b_i:

$$b_i = M(X_{k-1} + p_i) - M(X_{k-1}) \sim \widetilde{M}_{k-1,k} p_i \tag{2-14}$$

where X_{k-1} denotes the control (i.e. maximum likelihood) analysis from the previous time step, $M(X_{k-1} + p_i)$ denotes the nonlinear ensemble one-step prediction and $M(X_{k-1})$ denotes the nonlinear control one-step prediction representing the most likely dynamical state derived from the maximum likelihood approach. For efficient minimization of Eqs. (2-1) and (2-2) in ensemble subspace, Hessian preconditioning is performed via the following change of variable (Zupanski 2005):

$$X - X_b = P_f^{1/2} (I + C)^{-T/2} \zeta \tag{2-15}$$

where ζ denotes the control vector in ensemble subspace. The i-th column of the square root matrix of the NxN symmetric matrix C, referred to as the information matrix, is approximated as follows (Zupanski 2005):

$$(R^{-1/2} \widetilde{G} P_f^{1/2})_i = R^{-1/2} \widetilde{G} b_i \approx R^{-1/2} G(X + b_i) - R^{-1/2} G(X) \tag{2-16}$$

where $\widetilde{G}$ denotes the Jacobian of the nonlinear observation equation, G( ). Following preconditioning using Eq.(2-15), the constrained nonlinear minimization problem of Eqs. (2-1) and (2-2) may be solved iteratively in the ensemble subspace via gradient-based minimization. An important aspect of MLEF is that the gradient (see Zupanski 2005 for the expression) is evaluated via the finite-difference approximation in Eq. (2-16). As such, unlike VAR, MLEF does not require adjoint code. Once the minimum is found, the analysis error covariance may be calculated as the inverse Hessian matrix at minimum, X_{opt}, which amounts to evaluating the information matrix **C** as follows using X_{opt}:

$$P_a^{1/2} = P_f^{1/2}[I + C(X_{opt})]^{-T/2} \quad (2\text{-}17)$$

The columns of the matrix $P_a^{1/2}$ are then used as the initial perturbations for the next assimilation cycle.

2.3.3. Initialization

In the very first step of MLEF and EnKF, it is necessary to perturb the control and state variables, respectively, to generate the ensemble ICs. In this work, we used a lognormal distribution with mean of zero and variance of a fraction of the soil water bucket size for the SAC soil moisture states. For the multiplicative biases for MAP and MAPE, a lognormal distribution with mean of zero and standard deviation of a 0.07 in the normal space is used, which correspond to mean of unity and standard deviation of 0.07 in the lognormal space. For the additive error to TCI, the ICs are perturbed based on a normal distribution with mean zero and standard deviation of 0.07 (mm/hr). The above standard deviations may be too small or too large depending on whether the initial assimilation window covers a storm or an inter-storm period. Given that each evaluation period is preceded by many assimilation cycles (see Section 2.5), thereby allowing the covariance of the model states to evolve dynamically, we did not attempt to refine the initialization strategy. Indeed, limited sensitivity analysis suggests that the choice of the starting values of the above parameters has rather modest impact on the overall performance of EnKF and MLEF. If the number of preceding assimilation cycles is small, however, it is possible that the impact may be larger.

2.4. Error and uncertainty modeling

The DA problem formulated above requires specification of a number of uncertainty parameters. In this section, we describe how they are modeled and specified.

2.4.1. Error in model dynamics

In EnKF, to account for the uncertainty in the SAC soil moisture dynamics, we introduce a random error, W_{k-1}, in Eq. (2-1). It is assumed that the model errors among the six SAC states are independent of one another. The standard deviation of the model error for each state is assumed to be a fraction, ranging from 0 to 0.1, of the soil water depth corresponding to the particular SAC soil moisture state. The random realizations of the model errors are then added to the propagated state variables (Lorentzen and Nævdal 2011). In MLEF, the model errors are accounted for by inflating the square root matrix of the forecast error covariance, b_i (see Eq. (2-14)). It is important to note that, in this approach, the effect of model errors in Eq. (2-14) should reflect only the increased uncertainty due to the residual model errors, i.e., the difference between the perturbed dynamics and the control dynamics due solely to the model errors. If, e.g., the direction and magnitude of the model error are identical between the perturbation run and the control run, the residual model error would be zero. As such, one may expect the residual model error to be added to b_i in MLEF to be significantly smaller than the model error W_{k-1}^{j} in EnKF. Whereas in EnKF the standard deviation of the model error for each state variable is modeled as a fraction of the soil water content, that of the residual model error in MLEF is modeled as a fraction of the soil water bucket size as specified by the SAC parameters. The above modeling assumes that the residual model error in a perturbation run relative to the control run is proportional to the size of the soil water bucket whereas the model error itself is proportional to the amount of soil water in the bucket. Additional research is needed to ascertain the above postulation and to improve error modeling. The multiplicative biases in MAP, MAPE and the additive bias in TCI are modeled as time-invariant and hence no dynamical model errors are assumed (i.e. $X_{P,k} = X_{P,k-1}$). This does not mean, however, that the above biases do not change in time; they vary from assimilation cycle to another depending on the magnitude of the measurement error covariance relative to that of other terms (see Eq. (2-1)).

2.4.2. Observational errors

Observational errors are generally heteroscedastic and correlated temporally (Lee et al. 2011). Due to lack of truth, however, observation errors are difficult to model in practice. Heteroscedasticity, i.e., dependence of the variance of a random variable on the magnitude of its realization, is important in hydrologic DA because streamflow and precipitation generally exhibit strong heteroscedasticity. In this work, we assume that all observational errors are temporally uncorrelated and consider both homoscedastic and heteroscedastic models. For homoscedastic modeling, we used a range of values for each error variance and examine the performance of DA. Such an approach allows assessment of the sensitivity of DA to the error variance when its quantification is difficult due to the independence assumption.

Heteroscedastic modeling was considered for streamflow, MAP and the error in runoff. For MAPE, we used homoscedastic modeling only, given its limited variability. The errors in streamflow observations originate from the errors in water level measurement and rating curves (Clark et al. 2008). Due to the concave relationship between streamflow and stage, the errors at high water levels translate into larger errors in discharge (Sorooshian and Dracup 1980). Also, there is larger uncertainty at high water levels, due to the larger uncertainty in the rating curves (Clark et al. 2008).

For heteroscedastic formulation of observation error variances for streamflow and MAP, we used the following formulations (Sorooshian and Dracup 1980; Carpenter and Georgakakos 2004; Weerts and Serafy 2006; Clark et al. 2008; Rakovec et al. 2012):

$$\sigma_Q = C_Q Z_Q + C_{Qo} \ (\mathrm{m3/sec}) \tag{2-18}$$

$$\sigma_P = C_P Z_P + C_{Po} \ (\mathrm{mm/hr}) \tag{2-19}$$

Where Z_Q and Z_P denote the streamflow and MAP observations, respectively, σ_Q and σ_P denote the observation error standard deviations for streamflow and MAP, respectively, C_Q and C_P denote the multiplicative coefficients for the streamflow and MAP observation error standard

deviation, respectively, and C_{Qo} and C_{Po} denote the additive coefficients for the streamflow and MAP observation error standard deviation, respectively. The additive coefficients are introduced to keep the variance positive when the observation is zero. The coefficients in Eqs.(2-18) and (2-19) should be carefully chosen. Inaccurate heteroscedastic modeling may deteriorate, rather than improve, the performance compared to homoscedastic modeling. Ideally, the parameters should be estimated based on statistical analysis using the truth. Due to lack of such data, however, the above coefficients are estimated from sensitivity analysis- (see Section 2.6) over the ranges reported in the literature (Carpenter and Georgakakos, 2004; Weerts and Serafy 2006; Clark et al. 2008; Rakovec et al. 2012). Based on the above analysis, we chose 0.15 and 0.25 for C_P, and 0.03 and 0.3 for C_Q.

2.4.3. Error in model runoff

The error assumed in the soil moisture dynamics of the model may not account for biases due to structural and/or parametric errors that may exist in other parts of the soil moisture accounting and routing models. To account for such errors, we employed an additive error to TCI, or X_{Rs} (see Eq.(2-1)), as a control variable. This error may be modeled as time-varying or uniform within the assimilation window and is assumed to have an a priori mean of zero. Because runoff is not directly observed, variance of X_{Rs} cannot be estimated empirically. In this work, it is inferred from the observed and simulated streamflow via the following steps. Assuming that UH is perfect, we introduce the random additive error to runoff in the UH operation as shown below:

$$Z_Q(t) = \int_0^t \{I(\tau) + w(\tau)\}\, u(t-\tau)d\tau \tag{2-20}$$

where I( ) denotes the model-simulated runoff, TCI, Z_Q( ) denotes the observed streamflow, w( ) denotes the model runoff error and u( ) denotes the UH. Assuming stationarity of w( ) within the UH duration, we have for error variance of simulated streamflow:

$$\sigma_{eq}^2 = \sigma_{Rs}^2 \int_0^t \int_0^t u(t-\tau)\, u(t-s) ds d\tau \quad (2\text{-}21)$$

where σ_{eq}^2 denotes the error variance of simulated streamflow and σ_{Rs}^2 denotes the runoff error variance. In reality, UH is not perfect. As such, σ_{Rs}^2 estimated in this way is likely to be an overestimate as phase or timing errors in UH would be incorrectly attributed to σ_{Rs}^2. Isolating timing errors (Liu et al. 2011), however, was beyond the scope of this work and we parameterize the error variance, σ_{eq}^2, as a function of the observed streamflow to account for heteroscedasticity. The resulting σ_{Rs} (mm/hr) for the study basin, MTPT2 (see below), is given by (see also Figure 2-2):

$$\sigma_{Rs} = \left(\frac{\sqrt{Z_Q + 135.5} - 11.6}{0.07} \right) \ /103.84 \ \ (\mathrm{mm/hr}) \quad (2\text{-}22)$$

where Z_Q denotes the observed flow in m^3/s.

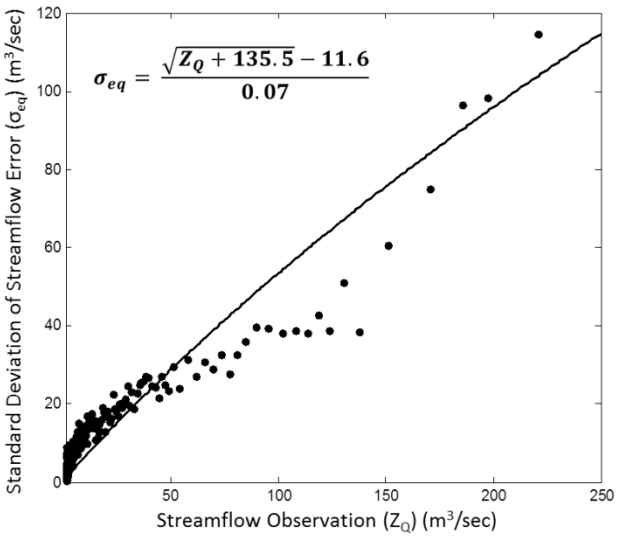

Figure 2-2 Standard deviation of the error in streamflow simulation as a function of the observed streamflow.

2.5. Evaluation experiments

A series of sensitivity analysis, referred to as Experiment 1, was first carried out to determine the optimal values for the observation error variance for streamflow and variance of the additive error to TCI. By sensitivity analysis, we mean analysis of how the performance of DA may be affected by the settings of the uncertainty parameters. The rationale for setting the uncertainty parameters in this way, rather than via explicit optimization, is that, for the DA procedure to be operationally viable, it has to perform reasonably well even with suboptimal parameter settings which may be easily estimated. For the above, we assumed variances for observation errors in MAP and MAPE to be 10 mm and 1 $(mm/hr)^2$, respectively (Seo et al. 2003). We then compared heteroscedastic vs. homoscedastic models of observational errors for streamflow and MAP, and of dynamic model error while keeping all other conditions the same; this is referred to as Experiment 2.

For comparative evaluation, we carried out twin sensitivity experiments for EnKF and MLEF under varying conditions of the dynamic model error, the ensemble size and the number of streamflow observations assimilated in each cycle while the other parameters are kept at the values obtained from the above sensitivity analyses; this is referred to as Experiment 3. Table 2-2 summarizes the parameter settings used in these experiments.

Table 2-2 Summary of the parameter settings used in the three experiments

Experiment	Observational error variance			Additive error to TCI $(mm/hr)^2$	Soil moisture dynamical model error	Ensemble Size	No. of Streamflow data used per cycle
	MAP $(mm/hr)^2$	MAPE $(mm/hr)^2$	Streamflow $(m^3/s)^2$				
1. AS[a] to streamflow error variance	10	1	1, 10, 50, 100	1	0.03	30	1
AS to additive error variance to TCI	10	1	10	0.01, 0.1, 1, 10	0.03	30	1
2. Homoscedastic vs. Heteroscedastic error modeling	10	1	10	1	0.03	30	1
	C_P=0.15, 0.25	1	C_Q=0.03, 0.3	Function of Z_Q	0.03	30	1
3. AS to soil moisture dynamical model error	10	1	10	1	0, 0.025, 0.075, 0.1	30	1
AS to ensemble size	10	1	10	1	0.025	5, 9, 30, 50	1
AS to no. of streamflow data used per cycle	10	1	10	1	0.025	30	1, 2, 4, 8

[a] AS: Analysis of sensitivity

All experiments were performed for MTPT2, a headwater basin located in the NWS West Gulf River Forecast Center's (WGRFC) service area (see Figure 2-3). The basin drains into the Tres Palacios River near Midfield in southern Texas and has a catchment area of 435 km^2 and a time-to-peak of 17 hours. It is one of the 22 basins in the WGRFC's service area that have been used in various DA and other hydrologic modeling studies in recent years (Seo et al. 2009; Lee et al. 2013). This basin was chosen for this study because its streamflow simulation has relative small timing errors and hence allows relatively clean assessment of the performance of DA without being compromised by phase errors (Liu et al. 2011). To the best of the authors' knowledge, no DA techniques currently exist for streamflow prediction that can handle timing errors explicitly.

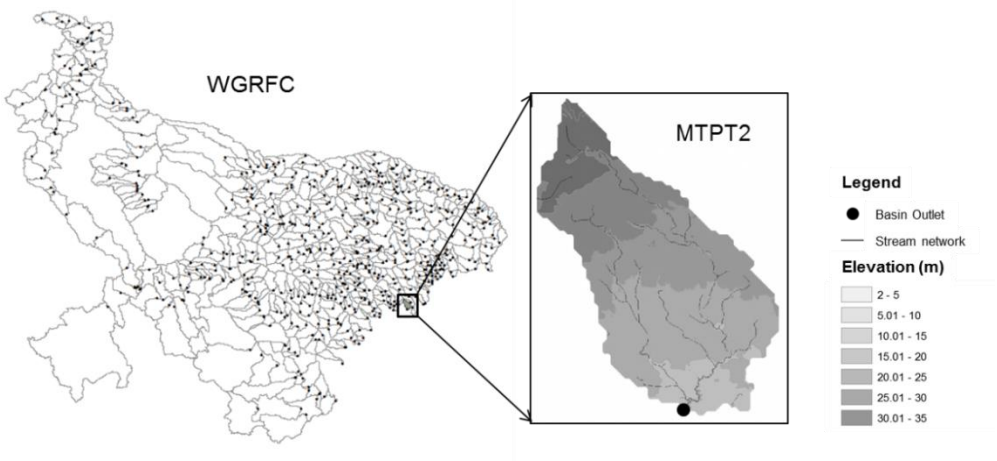

Figure 2-3 The study basin of MTPT2 in Texas in the service area of the West Gulf River Forecast Center (WGRFC).

The streamflow data used are the hourly observations from the United States Geological Survey (USGS). The precipitation data used are the MAP estimates derived from the hourly Multisensor Precipitation Estimator (MPE, Seo et al. 2010) products operationally produced by WGRFC. The MAPE data used are the monthly climatological estimates based on pan evaporation

data as adjusted through the manual calibration process, which is explained below. In application of the SAC-SMA model, it is common to multiply PE by a potential evaporation adjustment factor to account for seasonal variations in vegetation activity. Manual calibration refers to the iterative adjustment of the climatological MAPE by human forecasters based on evaluation of the long-term streamflow simulation results. For further details, the reader is referred to Koren et al. (1998). The simulation period was 1996 to 2005. The assimilation cycle was an hour. The maximum lead time for prediction was 72 hours. For prediction, we used the observed, rather than predicted, MAP and MAPE. As such, the prediction results assume clairvoyant future MAP (FMAP) and MAPE (FMAPE). In the real-time forecasting mode, there will, in general, be large uncertainties in FMAP and FMAPE, or input certainty (Krzysztofowicz 1999, Seo et al. 2006). Using perfectly known FMAP and FMAPE allows evaluation of DA in reducing hydrologic uncertainty without being masked by input uncertainty. Recall that the DA techniques considered in this work addresses only the hydrologic IC uncertainty. As such, being able to assess its potency in reducing hydrologic uncertainty is of foremost interest in this work.

For evaluation, we used the 20 largest events with peak streamflow greater than 100 m^3/s and examined the root mean square error (RMSE) of the simulated (DA-less or DA-aided) flow in reference to the observed flow, mean error of the simulated flow, correlation coefficient between the simulated and observed flow, maximum errors of under- and over-prediction in simulated flow, mean square error skill score of the DA-aided simulated flow in reference to the DA-less simulated flow and Nash-Sutcliffe efficiency of the simulated flow. It was found that RMSE represents the overall performance very well (see also Seo et al. 2003, 2009). As such, we used RMSE as the primary performance measure. We note here that the lognormal initialization may compromise the quality of ensemble mean from EnKF whereas MLEF can cope of non-normal distributions (Fletcher and Zupanski 2007). To evaluate performance in the distributional sense, however, ensemble verification is necessary, a task left as a future endeavor.

2.6. Results

In this section, we present the sensitivity analysis and comparative evaluation results. First we present the analysis of sensitivity of MLEF to variances of streamflow observation error and additive error to TCI (Experiment 1). We then present the comparative evaluation results of homoscedastic versus heteroscedastic modeling of observation errors for MLEF (Experiment 2). Finally, we compare MLEF and EnKF using the parameter settings obtained from the above experiments under varying conditions of the magnitude of variance of the dynamic model error, the ensemble size and the number of streamflow data assimilated per cycle (Experiment 3). The default parameter settings and the range of the parameter settings used are summarized in Table 2-2.

2.6.1. Sensitivity to error variances of streamflow and runoff observations

One of the most important DA parameters is the observation error variance for streamflow (Seo et al. 2003). For its determination, sensitivity analysis was carried out for a wide range of values. Figure 2-4 shows the RMSE as a function of lead time for streamflow observation error variance of 1, 10, 50 and 100 $(m^3/s)^2$. Ideally, the error variance should be modeled heteroscedastically to account for its dependence on the magnitude of the flow. For such a heteroscedastic approach to be effective, however, all other uncertainty modeling must be sufficiently accurate, a tall order in reality. While simplistic, homoscedastic modeling generally provides good performance without elaborate uncertainty modeling, and hence is appealing in practice. Figure 2-4 indicates that, in general, the smaller the error variance is, the closer the fit through the observed streamflow is, which results in smaller RMSE at short lead times but at some expense of larger RMSE at large lead times. Based on Figure 2-4, we chose 10 $(m^3/s)^2$ for σ_Q^2 for the rest of the sensitivity analysis. That the DA-aided simulation has slightly larger RMSE than

DA-less simulation at large lead times is an indication that the uncertainty modeling may need to be improved.

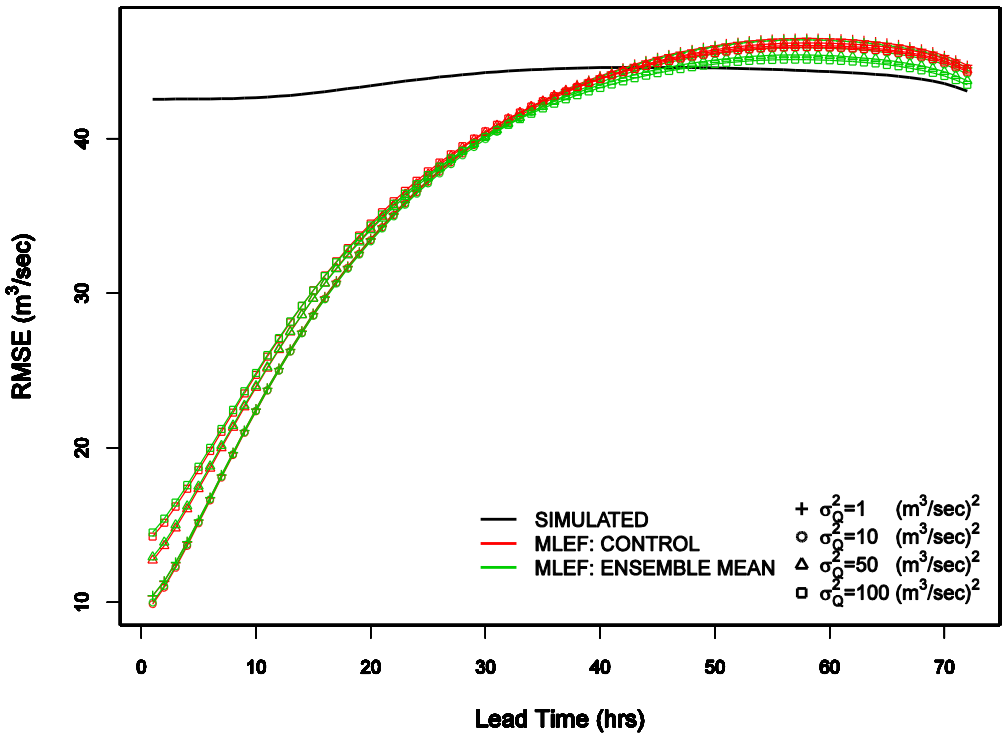

Figure 2-4 Sensitivity of the performance of MLEF on the variance of the streamflow observation error as measured by RMSE of streamflow prediction. The black, red, and green lines represent the base model simulation, the control simulation by MLEF and the ensemble mean of perturbed simulations with MLEF, respectively.

Another influential uncertainty parameter is the variance of the additive error to TCI. In reality, this error cannot be quantified as the true runoff is not observed. In this work, we assume that simulated runoff is unbiased and assign zeros as pseudo observations of this error. Conceptually, the above error is analogous to the model error for soil moisture dynamics and aims to account for the structural and/or parametric errors that may exist in hydrologic modeling outside of the soil moisture-dynamical model. Sensitivity to a range of values from 0.01 to 10 $(mm/hr)^2$

was examined for the variance of additive error to TCI. It was found that this sensitivity is similar to that to the streamflow observation error variance; increasing the additive error variance to TCI renders simulation to be less accurate at short lead times while improving performance at larger lead times. Based on the above results, we chose a value of 1 $(mm/hr)^2$ for the additive error variance to TCI for use throughout the rest of this work. To check the realism of this choice, we also calculated the sample variance of the simulated runoff, which was found to be very close to the above value.

2.6.2. Homoscedastic vs. heteroscedastic error modeling

The results presented in the previous subsection assumed homoscedastic observation errors. Here we present comparative evaluation of MLEF under homoscedastic vs. heteroscedastic modeling of observation errors. Figure 2-5 shows the RMSE of streamflow prediction vs. lead time under varying combinations of the parameter settings in heteroscedastic formulation of the observation errors in streamflow and MAP. In this formulation, the runoff error variance is also modeled as heteroscedastic as described in Section 2.4 (see also Table 2-2). For comparison, the results from homoscedastic modeling are also shown. The figure indicates that heteroscedastic modeling of observation errors does not improve DA performance over homoscedastic modeling, and that the performance of MLEF is not very sensitive to modeling of observational error variances. The first observation confirms the experience that, in practice, heteroscedastic modeling of observation errors is very difficult as the quality of the modeling must be sufficiently high not only for the observational errors but also for the model errors. The second observation suggests that, even without very accurate uncertainty modeling, reasonably good performance may be obtained from MLEF for the assimilation problem dealt with in this work.

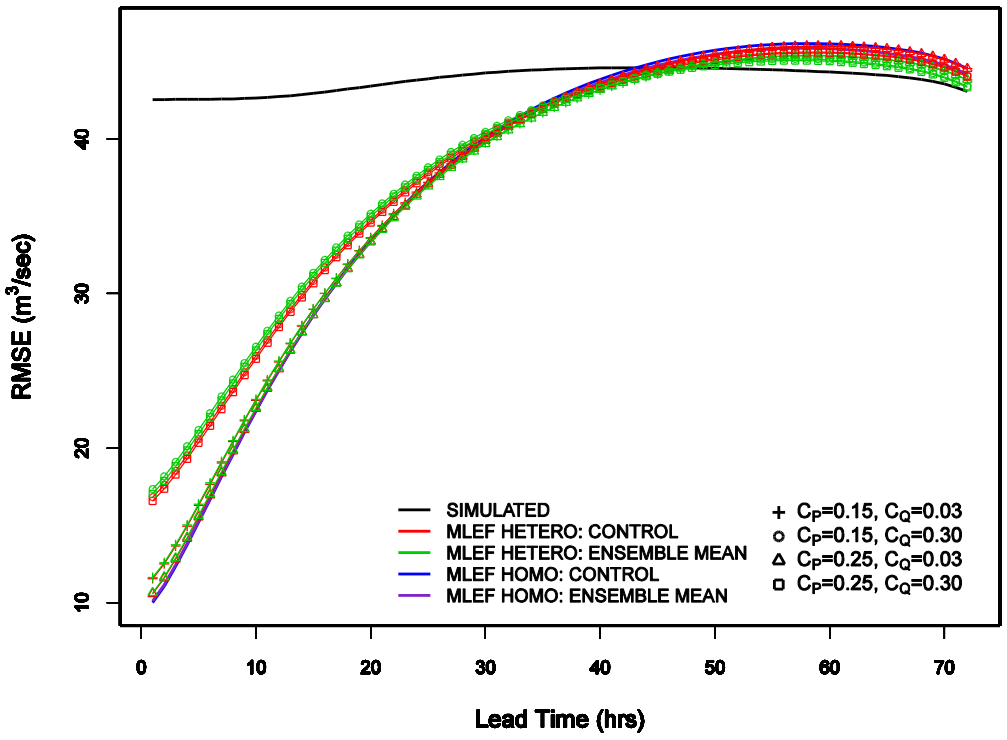

Figure 2-5 Effect of heteroscedastic modeling of observation errors in streamflow, MAP and runoff on RMSE of streamflow prediction with MLEF. The variables C_P and C_Q denote the multiplicative coefficients for MAP and streamflow observations (see Eqs. (2-18) and (2-19)). The abbreviations HETERO and HOMO denote heteroscedastic and homoscedastic modeling of observation errors, respectively.

2.6.3. Comparative results of MLEF and EnKF

In this subsection, we first evaluate sensitivity of MLEF and EnKF to uncertainty modeling of the model errors in the soil moisture dynamics. As explained in Section 2.4, in EnKF the variance of the model errors (i.e. the diagonal terms in Q_{k-1} in Eq.(2-15)) in the SAC soil moisture dynamics is prescribed as a fraction of the soil water content. In MLEF, the residual model error, i.e. the model error in an ensemble perturbation run subtracted by that in the control

run, is prescribed as a fraction of the soil water bucket size. We used values of 0, 0.025, 0.075 and 0.1 for the fraction in this work. A zero model error means a perfect model for the soil moisture dynamics whereas a large fraction means that the model soil moisture dynamics has large uncertainties.

Figure 2-6 shows that accounting for model errors in soil moisture dynamics improves the performance of DA significantly at short lead times but has slightly negative impact at larger lead times. It is seen that both MLEF and EnKF achieve their respective best with a fraction of 0.025. The MLEF result is somewhat surprising in that we expected the optimal fraction for MLEF to be smaller than that for EnKF because the former represents only the residual error (see above). With a fraction of near 0.025 and somewhat larger, MLEF generally shows significantly smaller RMSE at shorter lead times and smaller sensitivity to magnitude of the dynamical model error than EnKF. The above observation is an important consideration in operational hydrology in that accurate modeling of model errors is very difficult in practice. To better understand how the magnitude and structure of model errors may impact the performance of the DA techniques and to explain the sensitivity of MLEF to the error fraction, additional research is needed.

Figure 2-7 shows the RMSE of streamflow prediction vs. lead time for different ensemble sizes. We used 5, 9, 30 and 50 ensemble members for both EnKF and MLEF while keeping all other settings the same (see Table 2-2). Note that MLEF is not very sensitive to ensemble size and the predictions are very good even with a small ensemble size. The EnKF solution generally improves with increasing ensemble size but does not come close to the MLEF solution even when the ensemble size is larger than 50 members. The above results for MLEF are not surprising in that in MLEF the ensemble members are generated around the control solution obtained via nonlinear constrained minimization similarly to VAR. As such, for MLEF, the sensitivity to ensemble size is largely a reflection of the sampling uncertainty associated with limited ensemble size. The EnKF results, on the other hand, reflect not only the sampling uncertainty but also the

diminished quality of the solution when the distributions involved are not symmetric, as well as the suboptimal nature of the solution when the observations are nonlinearly related to the model states. Note that, even with a large ensemble size of 50, the EnKF solution is still significantly inferior to the MLEF solution. We also compared the CPU time for different ensemble sizes for both EnKF and MLEF. It was found that, whereas the increase in CPU time is sharper for MLEF with increasing ensemble size, the total CPU time for MLEF is considerably smaller than that EnKF for all ensemble sizes considered in this work.

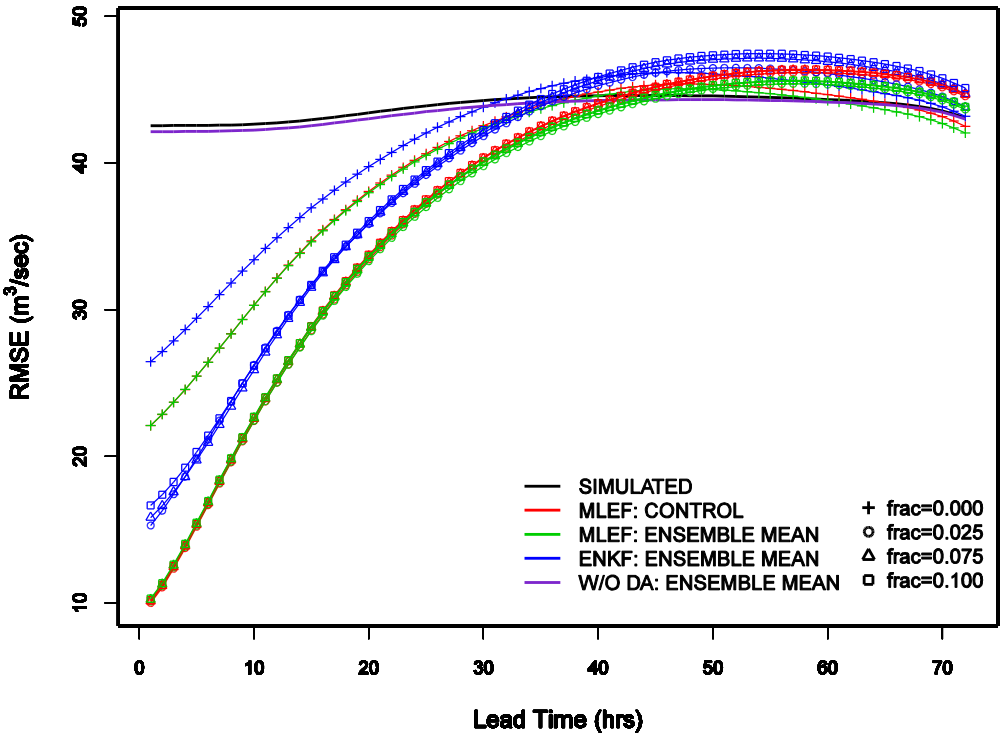

Figure 2-6 Performance of streamflow prediction with MLEF and EnKF at varying levels of the error assumed for the model dynamics.

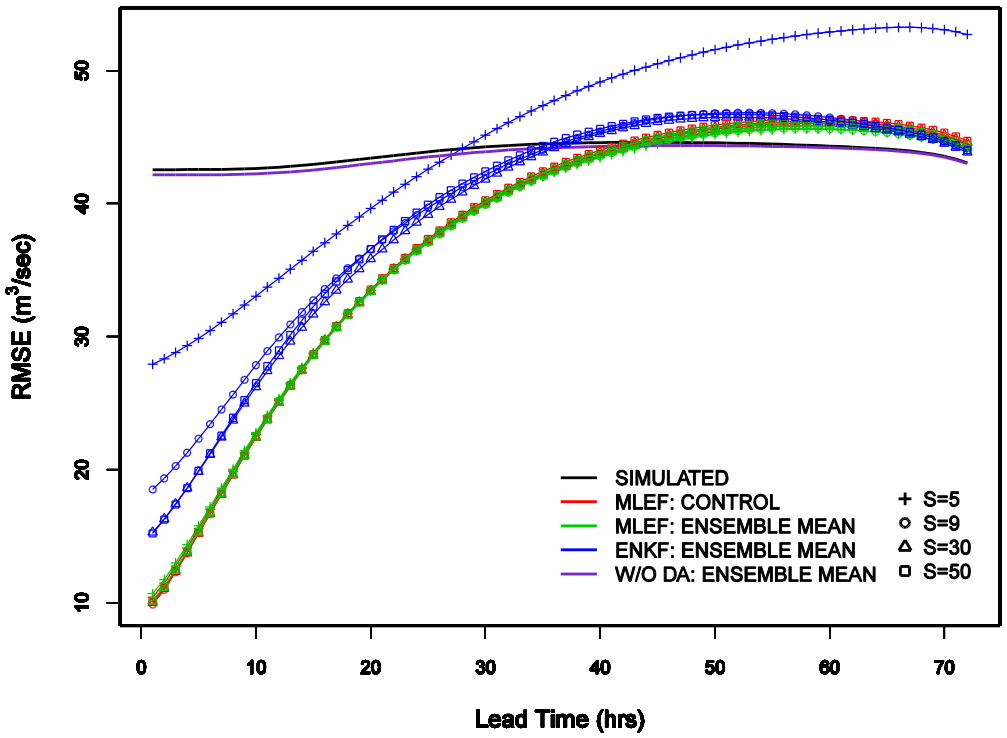

Figure 2-7 Sensitivity of DA performance on the ensemble size (S).

Figure 2-8 shows the RMSE of streamflow prediction vs. lead time for a varying number of hourly streamflow observations assimilated per cycle. Recall in the Introduction Section that the DA problem dealt with in this work is formulated as a fixed lag smoother in which the lag corresponds to the size of the assimilation window. As such, it is possible to assimilate as many streamflow observations as there are valid within the assimilation window. In this experiment, we used 1, 2, 4 and 8 streamflow observations valid at or near the end of the assimilation window. Fig 8 shows that the MLEF results deteriorate when a greater number of streamflow is assimilated. The performance of EnKF, on the other hand, improves up to 4 hourly streamflow observations assimilated per cycle and decreases when the number is increased further. The reason for the deterioration in MLEF, which was also observed with VAR (Seo et al. 2003), is that multiple observations of streamflow may translate via UH into a runoff time series that may not be

dynamically consistent. Note that, because UH is a convolution operation, assimilating a single observed flow already amounts to adjusting streamflow simulations at multiple time steps rather than only the synchronous simulated flow. In other words, UH does not offer enough degrees of freedom for assimilation of multiple streamflow observations unless they have very large observation errors. The improvement in EnKF up to 4 observations and a much slower rate of deterioration thereafter is due to the suboptimal nature of its solution which significantly reduces the sensitivity of its performance to the number of flow observations assimilated.

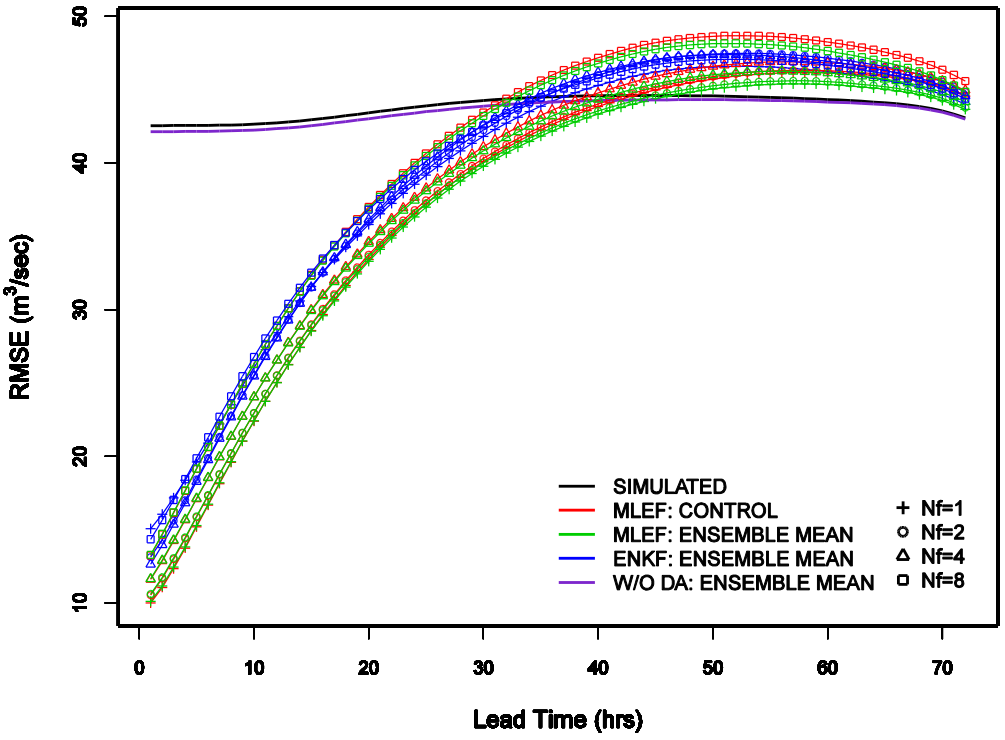

Figure 2-8 Sensitivity of DA performance on the number of streamflow observations assimilated at a given assimilation cycle (N_f).

In addition to the summary statistics presented above, we also visually examined a large number of DA-less and DA-aided predictions of individual events and the corresponding control

variables. Such an examination serves at least two very important purposes. The first is to identify the conditions under which EnKF and MLEF may perform significantly differently. The second is to assess operational viability of the techniques by critically examining different aspects of the performance of DA such as temporal consistency in DA-aided predictions for significant events. To get a better sense of the comparative performance between MLEF and EnKF, we plotted in Fig 9 the time series for the last 10 significant events (out of the 20 events whose peak flow exceeds 100 m^3/s) of the MLEF- (control) and EnKF-aided (mean of 30 ensemble members) simulations as well as the base (i.e. DA-less) simulation. The parameter values used for Figure 2-9 are based on the homoscedastic setting given in Experiment 2 of Table 2-2. To highlight the differences between MLEF and EnKF simulations, we show one of the events in an inset in semi-log scale. Note that MLEF is able to catch up with the rising and falling limb better than EnKF. Note also that for most of the cases MLEF performs better. Figure 2-10 and Figure 2-11 show selected examples of streamflow prediction with EnKF and MLEF. For the first two cases shown in Figure 2-10, both EnKF and MLEF perform well in the single-valued sense. As noted in the Introduction Section, assessment of DA performance in the ensemble sense was beyond the scope of this work. We only note here that the ensembles from DA analysis tend to be under-spread, particularly for the falling limb as may be seen in the lower panel of Figure 2-10 (see below for explanation). Figure 2-11 illustrates the limitations of EnKF when the observation process is highly nonlinear. In this and similar cases, the EnKF solution is rather poor whereas MLEF is reasonably successful in catching up with the observed flow. Such a poor-quality solution is problematic in an operational setting and questions operational viability of EnKF for solving the assimilation problem posed in this work. Figure 2-10 also shows the ensemble members of the state variables corresponding to the streamflow ensembles. Note that there is a significantly larger spread in ensemble members of the state variables of EnKF compared to those of MLEF. Note also that, between EnKF and MLEF, the updated ensemble trajectories of the model states are quite

different for some states, but that the spread of streamflow ensembles is similar between the two DA techniques. The first observation is a reflection of the fact that the analysis error covariance from MLEF is much smaller than that from EnKF. The second observation is an indication that the inverse problem posed by the assimilation problem may be significantly underdetermined. Assessment of the quality of the soil moisture ensembles was beyond the scope of this work and is left as a future endeavor. It is worth noting in Figure 2-10 that the streamflow ensembles on the falling limb are severely under-spread. This is explained in part by the fact that some of the soil moisture states hit the upper bounds prescribed by the model parameters, which collectively reduces the ensemble spread in TCI. This points out that accounting for parametric uncertainty is necessary to produce realistic uncertainty spread using ensemble DA techniques, a topic left as a future endeavor.

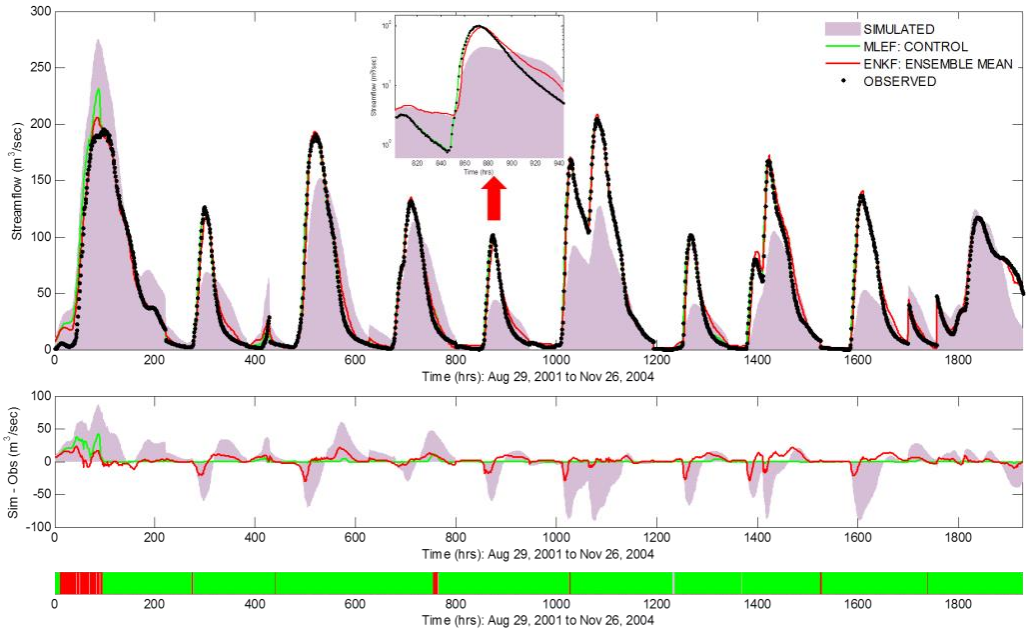

Figure 2-9 (Top) Time series of the base (purple), MLEF control (green) and EnKF ensemble mean (red) simulations for the last ten of the 20 events whose peak flow exceeds 100 (m3/sec); one of the 10 events is also blown up at log scale; (Middle) Time series of the difference between the simulated and observed flow; (Bottom) the periods of best performance among the MLEF (green), EnKF (red) and base (purple) model simulations in terms of the absolute error.

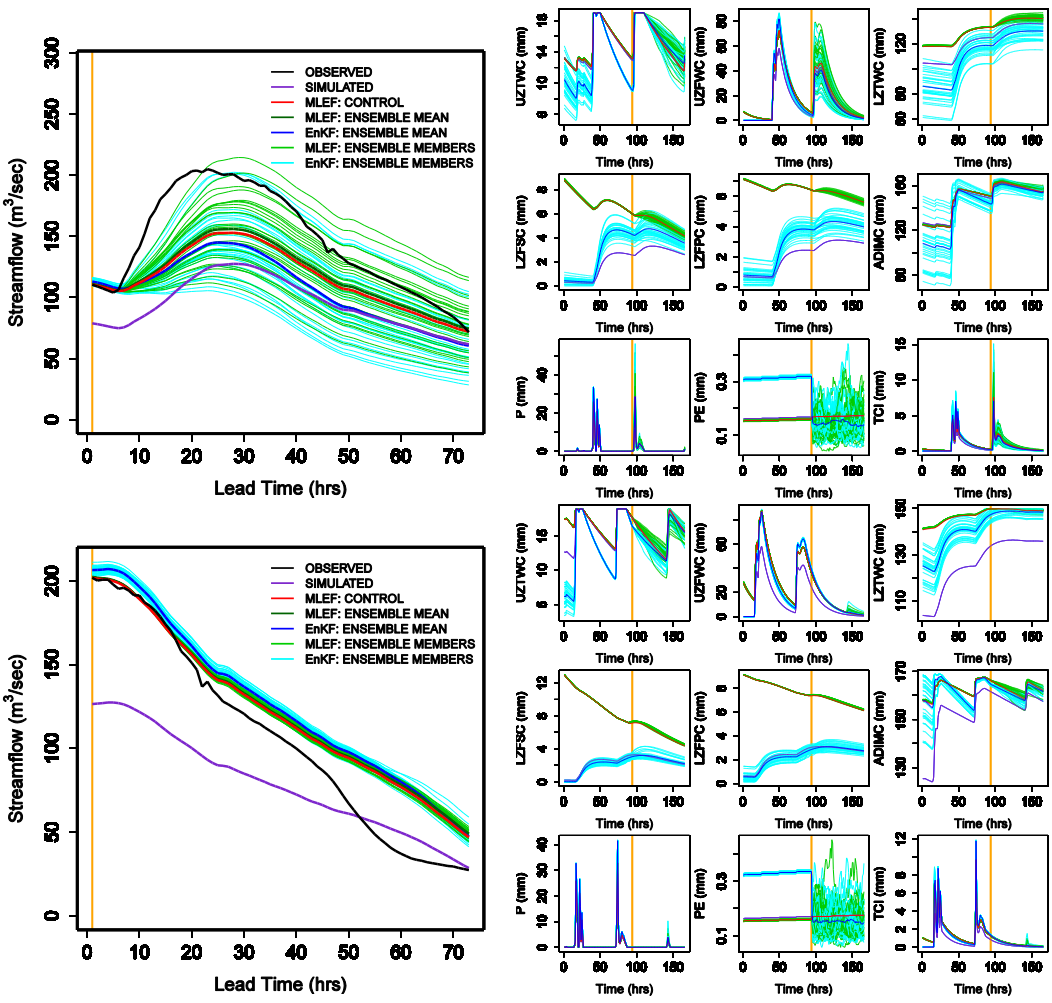

Figure 2-10 Example ensemble DA results for rising (upper panel) and falling limbs (lower panel). The left panel shows the observed and simulated hydrographs within the forecast time window of 72 hours. The right panel shows the simulated soil moisture states, observed and DA-adjusted MAP and MAPE, and unadjusted and adjusted TCI over the assimilation window (to the left of the orange vertical line) and the prediction window (to the right of the orange line). The vertical orange line denotes the prediction time of May 13, 20Z, 2004 (upper panel) and May 14, 20Z, 2004 (lower panel).

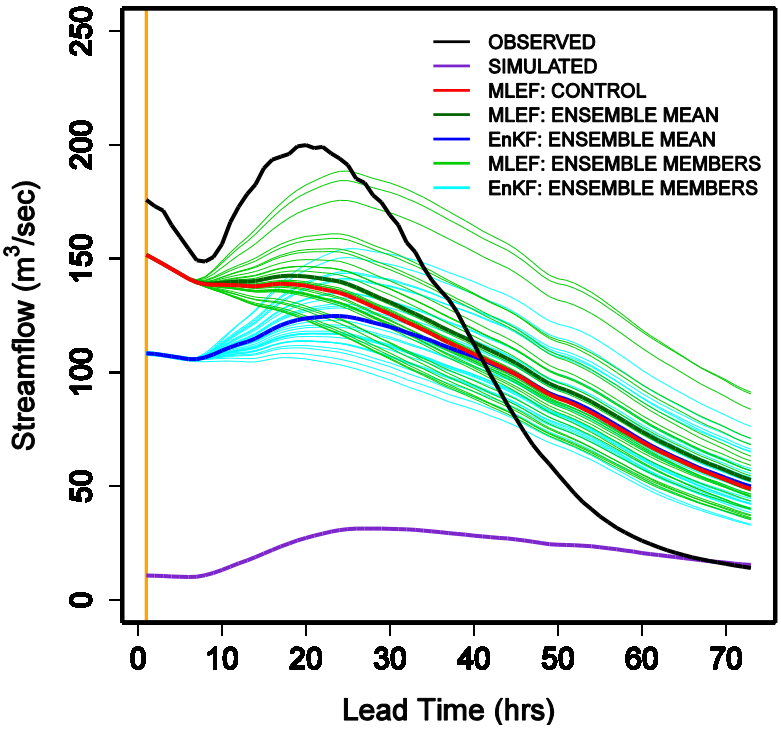

Figure 2-11 An example (prediction time Mar 18, 20Z, 1997) of significantly different performance between MLEF and EnKF.

Finally, we note here that we also evaluated both MLEF and EnKF for a second basin, GBHT2, which drains into Green Bayou in Houston, TX. It is much smaller (137km^2) and has a time-to-peak of only 6 hours. Qualitatively, the results are similar to those for MTPT2 and support the findings summarized above. While the use of only a very small number of basins for evaluation may seem insufficient, it is well known (Seo et al. 2003, 2009; Lee et al. 2012) that the performance of DA is consistently similar over different types of basins barring significant timing errors (Liu et al. 2011).

2.7. Conclusions

Performance of the two data assimilation (DA) techniques, maximum likelihood ensemble filter (MLEF) and ensemble Kalman filter (EnKF), are comparatively evaluated for the MTPT2 basin which drains into the Tres Palacios River near Midfield in southern Texas. The DA problem considered is assimilating streamflow, mean areal precipitation (MAP) and mean areal potential evaporation (MAPE) data into the Sacramento soil moisture accounting model (SAC) and unit hydrograph (UH) to update the soil moisture states for improved prediction of streamflow at the basin outlet. The primary purpose of the comparative evaluation is to assess relative performance and operational viability of the two DA techniques when the observation equation is highly nonlinear. Note that EnKF assumes linear observation equations whereas MLEF does not. The DA problem is formulated as fixed-lag smoothing following Seo et al. (2003, 2009) and Lee et al. (2011, 2012).

For comparative evaluation of MLEF and EnKF, three sets of experiments were carried out. First, sensitivity of MLEF to the variances of streamflow observation error and additive error to Total Channel Inflow (TCI) of SAC was examined. Second, using the results from the above experiment as reference, comparative evaluation of homoscedastic versus heteroscedastic modeling of observation errors was carried out for MLEF. Finally, we compared MLEF and EnKF using the parameters obtained from the above experiments under varying conditions of the magnitude of the dynamic model error, the number of ensemble members, and the number of streamflow data assimilated per cycle.

The main findings are as follows. Heteroscedastic modeling of observation errors for MAP and streamflow does not improve over homoscedastic modeling for MLEF. The most probable reason for this is that the dynamical model errors are not modeled with the accuracy necessary to benefit from the heteroscedastic modeling of the observation errors. Because the

accuracy of modeling the dynamical model errors depends on that of the model itself, however, there is a limit to improving the former. The above suggests that accurate heteroscedastic modeling of uncertainty parameters is very difficult and may not be very practical. MLEF is found to be not very sensitive to modeling of observational errors. It reflects the fact that iterative minimization in MLEF is able to converge to the solution even though the observation equation is nonlinear. The above suggests that a combination of homoscedastic modeling and sensitivity analysis may be sufficient to realize full benefits of MLEF for streamflow prediction at the outlet. Introducing model error in soil moisture dynamics (i.e. weak-constraint formulation) improves DA performance significantly at short lead times but has slightly negative impact at larger lead times. The latter observation is an indication that the dynamical model errors and their time evolution need to be modeled more accurately. The dynamical model error in EnKF is expressed as a fraction of the time-varying soil water content for all states whereas in MLEF the residual dynamical model error, defined as the difference between the model error in a perturbation run and that in the control run, is expressed as a fraction of the soil water bucket size for all states. Both MLEF and EnKF achieve best performance with a fraction of 0.025. With a fraction of near 0.025 and somewhat larger, MLEF generally shows significantly smaller RMSE in streamflow prediction at short lead times and smaller sensitivity to magnitude of the dynamical model error than EnKF. The last observation is an important consideration in operational hydrology in that, in practice, accurate modeling of model errors is very difficult. To better understand how the magnitude and structure of model errors may impact the performance of the DA techniques, however, additional research is needed. Sensitivity to ensemble size indicates that MLEF is able to produce significantly more accurate outlet streamflow predictions using fewer ensemble members than EnKF, which requires a much larger ensemble size to approach a comparable level of performance. The above results reflect the fact that in MLEF the ensemble members represent perturbations around the maximum likelihood solution whereas in EnKF they represent a set of

equally-likely suboptimal solutions. To achieve similar performance, the total CPU time required for MLEF is significantly smaller than that for EnKF. Sensitivity to the number of streamflow observations assimilated indicates that, similarly to VAR, MLEF performs best with a single streamflow observation assimilated per cycle. The above result arises because unit hydrograph, the routing model used in this work, is a convolution operation and hence has a large information overlap in simulated streamflow over successive time steps when the time step is small. Performance of EnKF, on the other hand, improves as the number of streamflow observations is increased to 4 per cycle but decreases thereafter, which reflects the suboptimal nature of the EnKF solution. It was observed that, while the streamflow ensemble results often appear similar between MLEF and EnKF, the soil moisture ensemble results are quite different between the two. It suggests that EnKF and MLEF produce rather different solutions, an indication that the inverse problem may be significantly underdetermined. To assess the quality of DA-aided solutions for the model states, however, soil moisture observations are necessary, a task left as a future research. The results summarized above are generally similar for the second test basin, GBHT2, which drains into Green Bayou in Houston, TX. In general, MLEF improves over EnKF consistently over varying conditions of observational and model errors and ensemble size. It indicates that good performance may be expected from MLEF even if the uncertainty parameters may not be of high quality, a rather desirable attribute for operational applications. It is also shown that, in certain cases, the quality of the EnKF solution is unacceptably poor whereas that of the MLEF solution remains reasonably good. There are instances in MLEF, however, when the approximate gradient evaluation may not be of high quality, which may produce temporally less than consistent results. In this work, comparative evaluation was carried out only in the single-valued sense. Additional research is necessary to produce reliable ensemble for analysis and prediction and to assess their quality via rigorous ensemble verification for both streamflow and

soil moisture. Finally, comparative evaluation of MLEF and iterative EnKF (Lorentzen and Nævdal 2011) is necessary to assess their effectiveness against computational cost.

Chapter 3

Comparative evaluation of radar-based quantitative precipitation estimates (QPE)

For effective use of radar-based QPE for high-resolution flash flood forecasting in large urban areas, it is necessary to understand and assess how the errors in radar-based QPE may differ over different spatiotemporal scales of aggregation and how they may manifest in hydrologic simulations. Toward that end, we carry out comparative evaluation of QPEs from the Multisensor Precipitation Estimator (MPE), NEXRAD Digital Hybrid Scan Reflectivity (DHR), Q2 and CASA (Collaborative Adaptive Sensing of the Atmosphere) for the Dallas-Fort Worth Metroplex (DFW). We perform scale-compatible intercomparison of the QPE products, compare them with rain gauge observations and assess the relative information content among the QPEs. Results indicate that DHR is the least skillful QPE as expected. Q2 is least biased in mean but it has the largest variability. MPE is the most skillful QPE for small amounts of precipitation while CASA is the most accurate estimation for large rainfall amount which is a desired attribute for flash flood forecasting purposes.

3.1. Introduction to hydrologic application of weather radar

More than three-quarters of the population of United States lives in urban areas that comprise only about 3% of the total land area. Given the high population density in urban areas, high-resolution observations and modeling capabilities are necessary for predicting flash floods in urban areas. Increasing occurrences of extreme precipitation expected from climate change has put such areas in an increasingly vulnerable position as even a small-scale but intense rainfall event can cause deadly flash floods and extensive damages. If there is an adequate warning and forecasting system for metropolitan cities, which occupy a small percentage of land in US, it could

potentially save a lot of lives and reduce the economic impact. The motivation of this study to develop a prototype high resolution flash flood warning system for Dallas-Fort Worth metroplex which is a large urban area.

For high-resolution observation and modeling of large urban areas, the use of weather radar and distributed hydrologic modeling is a natural progression. The main forcing data for a distributed hydrologic model is precipitation data with high spatial and temporal variability. Therefore, performance of the hydrologic model heavily relies on the accuracy of the precipitation estimation.

Traditionally, rain gauges were the main tool for direct measurement of rainfall rates and rainfall accumulation which generally provides good quality data for a small area because of small sampling volume. Rain gauges are subject to different sources of errors (Habib et al. 2010), but their main drawback is that they are point measurements and not capable of detecting and measuring rainfall at the desired resolution required by most advanced hydrological applications (Wang et al. 2008) which urge a need for another source for providing spatially distributed rainfall. It should be noted that despite the advances in remote sensing, rain gauges still provide a better estimation of what actually happened on the surface and is used as the main source of data for bias correction of rainfall maps produced from radar (Fulton et al. 1998, Seo et al. 1999, Zhang et al. 2011) and as the reference in comparison studies (Wang et al. 2008, Larson et al. 2008 to name a few).

Radar-based rainfall is a promising substitute for gauge-based rainfall because of their high temporal and spatial resolution and variability throughout US. Quantitative precipitation estimates (QPE) from radars are, however, subject to various sources of error. High-resolution distributed modeling is subject to nonlinear growth of error due to errors in QPE and in model parameters and structures. Thus, it is necessary to understand and assess how the error properties in radar-based QPE may differ over different spatiotemporal scales of aggregation and how they

may manifest in hydrologic simulations which will be useful in improving the accuracy of radar-based QPE by removing the biases or optimally combining different QPEs. Therefore, our main objective in this chapter is to comparatively evaluate QPEs from the Multisensor Precipitation Estimator (MPE), NEXRAD Digital Hybrid Scan Reflectivity (DHR), Q2 and CASA (Collaborative Adaptive Sensing of the Atmosphere). This objective will be achieved by comparing the concurrent and collocated radar and rain gauge observations retrieved from a dense rain gauge network. The topic of improving the accuracy of QPEs through optimally combining different products will be discussed in the next chapter.

There have been many studies dedicated to evaluating different radar-based precipitation estimations in the last two decades some of which will be discussed in the Section 3.2; however, there are not many studies to address the comparative evaluation of different QPEs. This was the main motivation for the comparisons carried out in this chapter.

The radar-based rainfall is an areal rainfall over the nominal resolution of QPE; in contrast, raingauge rainfall is a point measurement. Therefore, the large radar-gauge discrepancies cannot be treated as radar-rain estimation error. Ideally, one should compare the radar rainfall with the true areal rainfall over the same spatial domain of radar rainfall as rainfall is a highly intermittent phenomenon and is extremely variable in space and time (Moreau et al. 2009). However, there are not many point measurements available to derive the true areal rainfall which makes the comparison problematic. Ciach and Krajewski 1999 proposed the error variance separation (EVS) method to partition the error variance into the error of the radar averaged rainfall estimate and the error originating from the resolution difference. This method was applied in different studies thereafter (Anagnostou et al., 1999; Chumchean et al., 2003; Habib and Krajewski 2002; Young et al., 2000). However, they assumed that the covariance of radar and rain gauge rainfall errors are negligible. Ciach et al. 2003 showed that this assumption is not fulfilled.

Habib et al. 2004 proposed a conditional distribution transformation (CDT) method. They used the raingauge rainfall distributions conditioned on the radar estimates as well as additional information on spatial variability of rainfall to retrieve the conditional distribution of the corresponding true rainfall. However, the selected domains are considerably bigger than the radar resolutions which magnify the single-radar gauge representativeness errors. Zhang et al. 2007 introduced an extended error variance separation method (EEVS) which combines a kriging scheme for estimating areal rainfall from gauges with a sampling method for determining the correlation between the gauge and radar related errors. Moreau et al. 2009 also proposed a new method to derive the instrumental and the representativeness error.

All the aforementioned methods rely on the geostatistical framework which may underestimate the rainfall in the case of extreme events. To overcome this problem Gires et al. 2014 proposed a novel method to account for representativeness error by downscaling the radar rainfall using Universal Multifractals. As the main objective of this study is comparative evaluation of the QPEs and the representativeness error exists in all the products the representativeness error will not be accounted for here. Also available rain gauge network for this study is not dense enough to infer reliable conclusions about the representativeness error. The rest of the chapter is organized as follows. Description of each QPE and related studies are described in Section 3.2. Study area and data preparation are explained in Section 3.3. Section 3.4 describes the methodology used and results are presented in Section 3.5. Conclusion is given in Section 3.6.

3.2. Quantitative precipitation estimation (QPE)

Quantitative precipitation estimation is a method to estimate the amount of rainfall occurring over an area or region. This estimation can be done based on radar or satellite observations. There are many quantitative precipitation estimations available since there are different types of radar in operation and different agencies have their own product. We have

chosen four of them for this intercomparison study which are of importance and introduced in the following subsections.

3.2.1. NEXRAD Digital Hybrid Scan Reflectivity (DHR)

Next Generation Weather Radar (NEXRAD) system across the United States is the main source of sensor data for severe weather warnings and forecasts of tornadoes and flash flooding from mid 1990s (Fulton, 2002) and many of the frequently used QPE products are based on these radars such as Multisesnor Precipitation Estimator (MPE). NEXRAD currently comprises 159 sites throughout United States and select overseas locations. NEXRAD radar rainfall products have four stages (I-IV) based on the amount of processing and quality control for different uses. Stage I is the hourly rainfall estimate using radar alone with the nominal spatial resolution of 4 km x 4 km (HRAP coordinate system, Reed and Maidment 1999). Stage II provides the combination of radar and hourly rain gauge observation using optimal estimation which has mean bias correction and local adjustment embedded. To enable modeling in watershed scale, stage III product mosaics multiple radar QPEs into one product at the River Forecast Center (RFC) scale which also has interactive quality control of both gauge and radar data (Briendenbach et al. 1998).

Digital Hybrid Scan Reflectivity is one of the available products of level III products of NEXRAD radars. Once the precipitation detection function detects rainfall within the range of the radar, the preprocessing algorithm assembles reflectivity measurements from each volume scan into a fixed polar grid with resolution of 1º in azimuth by 1 km. As the name "hybrid scan" suggests, the reflectivity values of each bin are selected from the lowest four elevation angles, or tilts. The objective of introducing DHR was to use the reflectivity values as close to 1-km altitude as possible while minimizing the effect of ground clutter and terrain blockage (Fulton et al. 1998). Each WSR-88D site has a unique, hybrid scan look-up table in a polar grid at 1 km by one azimuthal degree indicating which one of the four lowest elevation angles to be used in producing

the DHR field. DHR is mainly used in flash flood forecasting application since time is of the essence. We have also used it here to assess the amount of improvement seen in different QPEs after the application of the specific processing techniques.

3.2.2. Multisensor Precipitation Estimator (MPE)

The Multisensor Precipitation Estimator (MPE, Seo et al. 2010, Kitzmiller et al. 2011) is an application for real-time multisensor precipitation estimation at 1-hr 4-km scale based on rain gauge observations, precipitation estimates from NEXRAD and, in some places, Geostationary Operational Environmental Satellite (GOES) QPE products. MPE replaced Stage III (Hudlow 1988, Shedd and Fulton 1993) in early 2000s. The MPE products generated by the RFCs are mosaicked at the National Centers for Atmospheric Prediction (NCEP) to generate the Stage IV products (Seo et al. 2010, Lin and Mitchell 2005). The MPE product is one of the most popular NWS products (http://water.weather.gov/precip/) and is used for a wide range of applications. A number of studies have been carried out to evaluate the quality of the MPE and Stage IV products.

Wang et al. (2008) compared the MPE products with Stage III using a high-density rain gauge network in the Upper Guadalupe River Basin of Texas. Uniform rainfall events were used to minimize the effects of point-to-area representativeness error. They concluded that MPE has a better agreement with the rain gauge data as reflected by higher correlation, higher probability of detection (POD) and smaller bias compared to Stage III. Wescott et al. (2008) evaluated MPE with quality controlled NWS cooperative gauges at daily and monthly scales, and at grid cell (i.e. HRAP) and county scales. They reported that MPE underestimated monthly precipitation, but that the degree of underestimation decreased over the study period of 41 months. The also reported underestimation of large precipitation amounts at daily scale.

Habib et al. (2009) investigated the accuracy of MPE for a 3-year period of 2004 to 2006. They used a dense rain gauge network in the Isaac-Verot Watershed in Lafayette, LA, to reduce

representativeness errors. There were two HRAP boxes each with 4 rain gauges in the watershed. They observed overestimation of light precipitation and underestimation of heavy precipitation. They concluded that MPE performs best for medium to large precipitation amounts. On an annual basis, the overall bias in the MPE estimates was rather small. For event-based comparisons, however, biases reached 25% for a half of the events and exceeded 50% for 10% of the events considered. Depending on the choices for bias correction and radar-gauge merging, MPE produces as many as seven products (Seo et al. 2010). The RFC forecasters choose one of the products and modify as necessary in real time based on their experience and expertise. Habib et al. (2013) performed a comparative analysis of the seven MPE products for the Isaac-Verot Watershed. The results showed that mean-field bias adjustment to radar-only product provides the largest improvement. Radar-gauge merging, on the other hand, did not necessarily result in improved accuracy and, in some cases, deteriorated the estimates.

3.2.3. Q2 QPE

The National Mosaic and Multi-Sensor Quantitative Precipitation Estimation (QPE) (NMQ) system is a multi-radar multi-sensor (MRMS) precipitation estimation and short-range forecast system (Vasiloff et al. 2007). One of the objectives of NMQ is to assimilate data from different observing networks to create high-resolution national multisensor QPEs for flash flood and flood warnings and water resources management. The NMQ system has been in operation in real time since June 2006 (Zhang et al. 2011). The next-generation QPE, or Q2 (Vasiloff et al. 2007), is a key component of the NMQ system. Q2 includes automated precipitation type classification and produces various products such as radar-only QPE, local bias-corrected radar QPE, gauge-only QPE, and QPE that combines gauge observations, orography and precipitation climatology (Zhang et al. 2011). In this work, we used the radar-only QPE product for which the primary source of radar data is NEXRAD. Wu et al. (2011) evaluated the NMQ products for the

twelve River Forecast Centers (RFC) service areas in the continental US using rain gauge observations from the Automated Surface Observing System (ASOS). They showed that the NMQ radar-only QPE has higher correlation and lower bias compared to the radar-only QPE from the WSR-88D Precipitation Processing System (PPS, Fulton et al. 1998).

3.2.4. Collaborative Adaptive Sensing of Atmosphere (CASA)

One of the limitations with NEXRAD is that they do not observe the lower atmosphere away from the radar location which causes degradation of spatial resolution at far ranges. Also, the temporal resolution is constrained by a fixed set of volume coverage patterns. This lack of resolution arises because the radar operation is independent of the weather conditions. To maximize its utility, the radar may adapt to the time-varying needs of the users (Junyent et al. 2010). To address these gaps in the current weather observation system, the NSF Engineering Research Center (ERC) for Collaborative Adaptive Sensing of the Atmosphere (CASA) developed a new weather warning systems based on dense networks of small radars (McLaughlin et al. 2005) with adaptive scanning strategy (Junyent et al. 2010).

The CASA Integrated Project was the first test bed of a networked CASA radar system composed of four X-band radars in Oklahoma. Each radar node was approximately 30 km away from the next unit. The details of the radar network, hardware and software architectures are described in Junyent et al. (2010). Attenuation is a known issue for precipitation estimation using X-band radars (Seo et al. 2010, Berne and Krajewski 2013). The CASA system uses the network reflectivity retrieval technique (Chandrasekar and Lim 2008) and the network-based attenuation correction technique (Lim et al. 2011) to mitigate the effects of attenuation. Lim et al. (2011) showed that the technique works robustly in real time in retrieving attenuation-corrected reflectivity. CASA QPE is based on specific differential propagation phase which makes it immune to absolute calibration errors (Bringi and Chandrasekar 2001). The network was

evaluated using rain gauge observations for a five-year period which showed a good agreement between radar QPE and rain gauge observations with a standard deviation of 25% and a bias of 3.7% (Chandrasekar et al. 2012). After the successful test bed demonstration of CASA in Oklahoma, the CASA system was moved to DFW in late 2012.The issues to be addressed include urban flooding, low-level wind sensing, weather forecasting, weather and water hazard decision making and network of networks demonstration. This partnership and the test bed are expected to be a prototype of a national-scale "network-of-networks" in which different users and data providers can exchange observational data across a common infrastructure. Figure 3-1 shows the layout of the first 8 radars in the network.

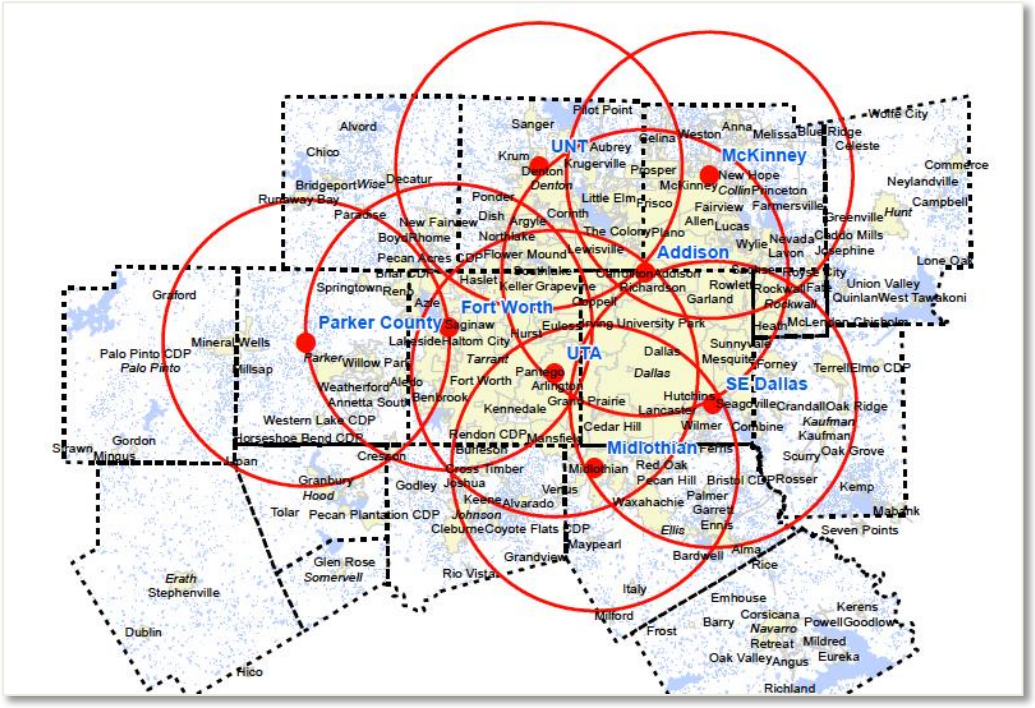

Figure 3-1 location and coverage of 8-radar (CASA) in the DFW Urban Testbed

3.3. Study area, data acquisition and preparation

The Dallas–Fort Worth metroplex in North Texas is, by population, the largest metropolitan area in Texas, the largest in the South, the fourth-largest in the United States, and the tenth-largest in the Americas. The study area is a rectangle enclosing cities of Fort Worth, Arlington and Grand Prairie (Figure 3-2). The QPEs used in this study are MPE, Q2, DHR and CASA QPE. The spatiotemporal resolution and period of record for each data set are summarized in Table 3-1. For comparative evaluation of QPEs, we use the rain gauge network deployed and operated by the City of Grand Prairie. Detailed information of all available observations are given in the following subsections.

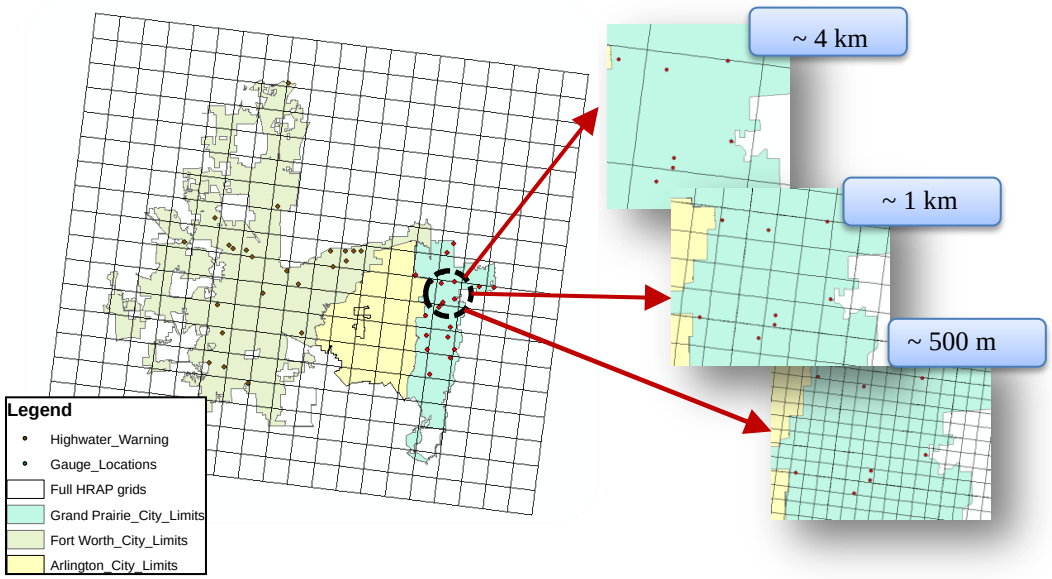

Figure 3-2 Study domain encompassing Cities of Fort Worth, Arlington and Grand Prairie and rain gauge locations

Table 3-1 Availability of radar-based QPEs and rain gauge data for the study and their spatiotemporal resolution.

Rainfall product	Temporal resolution	Spatial resolution	Start date of data availability	End date of data availability
MPE	~ 60 min	~ 4km × 4km	01/01/1996	31/06/2014
DHR	~5 to 6 min	~ 1º × 1 km	02/07/2008	11/05/2013
Q2	~5 min	~ 1km × 1 km	10/06/2011	07/31/2013
CASA	~1 min	~ 500 m × 500m	01/08/2013	31/06/2014
Grand Prairie Gauges	~15 min	-	03/12/2009	31/06/2014

3.3.1. Rain gauge observation

There are about 19 gauges deployed and operated by the City of Fort Worth as well as 20 gauges deployed by the City of Grand Prairie as a part of High Water Warning System (HWWS). These are Tipping-Bucket rain gauges with the resolution of 0.04 inch. Only rain gauges owned by the City of Grand Prairie are used in the comparative evaluation study since they were well maintained. Rain gauges were deployed at 2009 and were operational since then. Figure 3-2 depicts the location of gauges within the City of Grand Prairie. As shown Grand Prairie network is fairly dense and there are incidences of multiple gauges in one HRAP pixel.

3.3.2. DHR

As explained before, DHR is one of the available products of the level III product of NEXRAD radars. National Climatic Data Center (NCDC) is responsible to archiving and distributing the level III products for all the 159 NEXRAD radar sites. All the study area (DFW) is covered by a single NEXRAD radar called KFWS radar, one sample of the reflectivity field is shown in Figure 3-3. Distance of the rain gauges form the KFWS ranges from 25 km to 40 km.

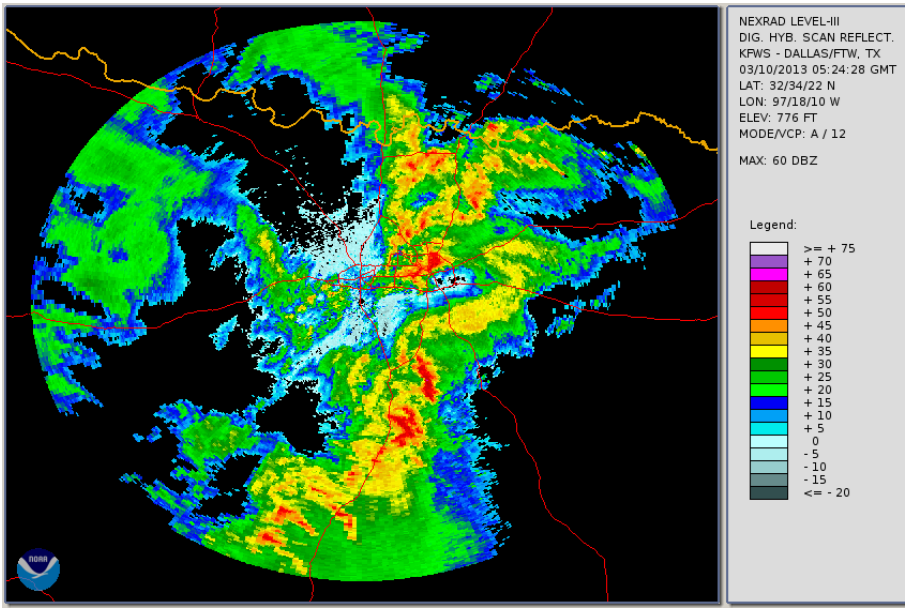

Figure 3-3 DHR reflectivity field of KFWS radar (Mar 10, 05:24Z, 2013)

Mapping from polar coordinate system to Cartesian coordinate system is done through NOAA's Weather and Climate Toolkit (WCT). A simple nearest-neighbor resampling technique is used to populate the output grid (NCDC). The Convective Z-R relationship (3-1) was applied to convert DHR reflectivity field to rainrate since convective system is the dominant rainfall system in the area and no tropical rainfall was reported in the data period.

$$Z = 300\,R^{1.4} \tag{3-1}$$

Where Z is reflectivity in mm^6m^{-3} and R is rainrate in mm/hr. To match spatially with other QPE products, the rainfall field is mapped into $1/4^{th}$ HRAP pixels (~ 1 km). A simple and naive time interpolation is applied to fix the time interval to 5 minute to ease the comparison with other QPEs. A sample of processed DHR QPE over DFW domain is given in Figure 3-4.

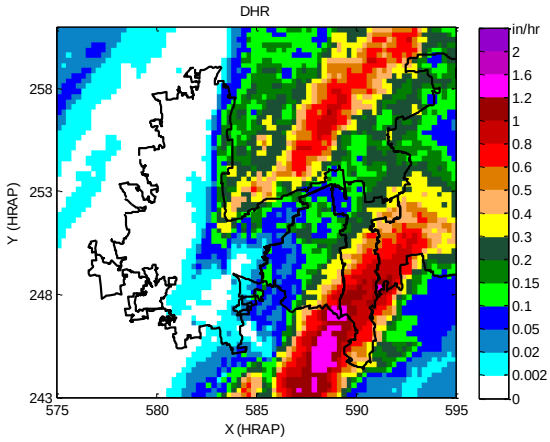

Figure 3-4 Derived DHR QPE, mapped into HRAP coordinate system, aggregated into hourly rainfall (Mar 10, 05Z, 2013)

3.3.3. MPE

MPE is retrieved from West Gulf River Forecast Center (WGRFC). It is routinely used in operational hydrologic modeling and flood forecasting. The temporal resolution is one hour and spatial resolution is full HRAP (~ 4 km). There is no preprocessing required. An example of hourly MPE over WGRFC and DFW domain are given in Figure 3-5.

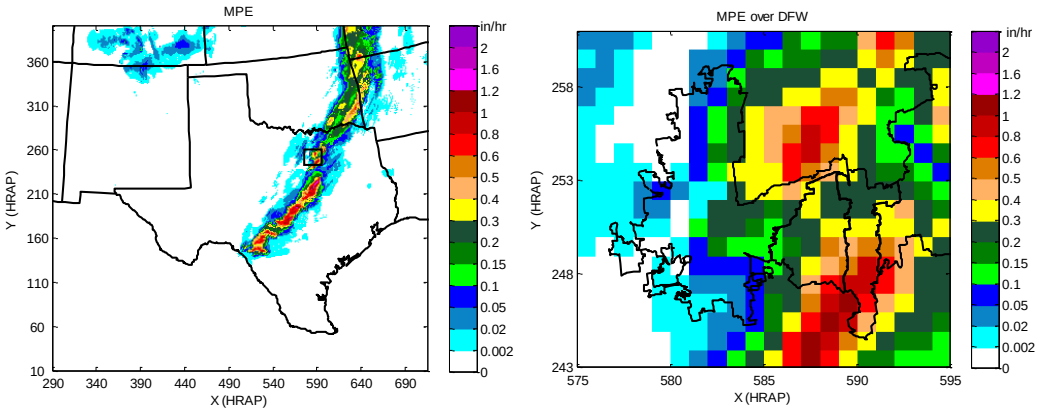

Figure 3-5 Left: Hourly MPE over WGRFC domain, the rectangle whithin the texas boundary represents the study area, Right: Hourly MPE over DFW domain (Mar 10, 05Z, 2013)

3.3.4. Q2 QPE

Q2 was retrieved from National Climate Data Center (NCDC) with geographic coordinate system (lat/lon). Therefore, an interpolation method was required to map the Q2 data to HRAP (and subHRAP) projection system. There are various interpolation methods which can be used for remapping, here the budget interpolation is used which maintains total precipitation to a desired degree of accuracy and is relative ease. This method has been used widely (Mesinger 1990; Accadia et al. 2003 and Hou et al. 2012 to name a few). In budget interpolation, remapping is performed by subdividing each output (the one we want to remap to it) grid box into a chosen number of subboxes and assigning precipitation of each subbox to the input (the input file which is going to be remapped) box on which it is centered. Details of the algorithm can be found in Accadia et al. (2003). Figure 3-6 shows an example of the Q2 mapped into HRAP coordinate system and aggregated into hourly rainfall estimation over DFW domain. The Q2 data has been archived by NCDC after December 2011 in netcdf format and 5 minute time interval. After August 2013, they have updated/upgraded the Q2 product to called Q3 product. It is distributed in binary format with the time interval of 2 minute; however, the Q3 data was not available for this study.

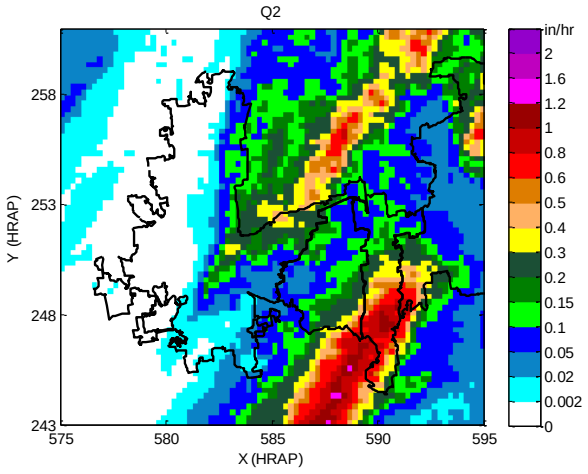

Figure 3-6 Mapped and aggregated 5 min Q2 into hourly Q2 QPE (Mar 10, 05Z, 2013)

3.3.5. CASA QPE

Unlike the other QPE products discussed so far which are derived based on Z-R relationship, the radar QPE from the CASA network is KDP-based. Rainrate can be calculated as the following:

$R=18.15\ KDP^{0.791}$ (applicable for southern Oklahoma and North Texas) (3-2)

where R and KDP denote the rainrate in mm/hr and specific differential phase in deg/km, respectively (Chandrasekar and Lim 2008). Currently, the spatiotemporal resolution of the CASA QPE is ~500 m and ~1 min. The QPE products include instantaneous rainrate, hourly rainfall accumulation and evaluation scores (under development) of rainfall accumulations over various periods. An example of CASA QPE is shown in Figure 3-7. To have a fair comparison between all QPEs, we used the common period between all QPEs which is around 7 months. The small sample size is the main but inevitable constraint of this study.

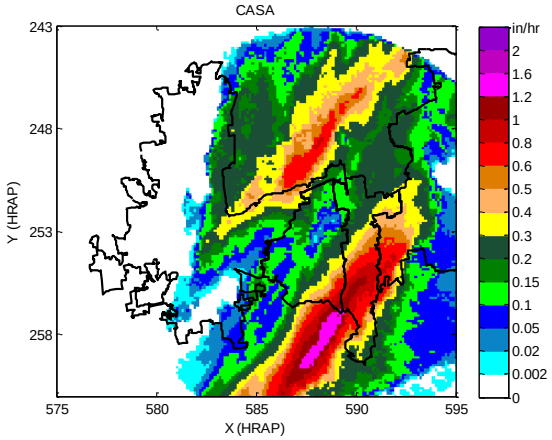

Figure 3-7 Aggregated 1 min CASA into hourly CASA QPE (Mar 10, 05Z, 2013)

3.4. Methodology

We compare all the QPEs within their common time period from Jan 2013 through August 2013. First we compare all radar-based estimations at hourly temporal resolution and their native spatial resolution with hourly raingauge observations. Then, in order to have a fair comparison, we also matched the spatial resolutions between different QPEs, i.e. compare hourly MPE, Q2, DHR and CASA QPE at full HRAP spatial resolutions. Finally, we compare Q2, DHR and CASA QPE versus rain gauge at 15 minute temporal resolution since the rain gauge data are reported every 15 minutes.

3.4.1. Error statistics

To assess the quality of the QPEs, we used visual inspection of the time series and scatter plots and a set of performance measures, including multiplicative bias, root mean square error (RMSE), Pearson's correlation coefficient (R), and mean square error (MSE) and its decomposition. The equations are given below:

$$\text{Multiplicative Bias} = \frac{m_Q}{m_G} \tag{3-3}$$

where m_Q and m_G denote the mean of QPE and gauge rainfall, respectively.

$$\text{RMSE} = \sqrt{\frac{\sum_{i=1}^{n}(Q_i - G_i)^2}{n-1}} \tag{3-4}$$

Where, Q and G denote QPE and the corresponding gauge rainfall, n denotes the number of pairs of QPE and gauge rainfall.

$$R = \frac{\text{Cov}\,(Q\,,\,G)}{\sigma_Q \sigma_G} \tag{3-5}$$

σ_Q and σ_G denote the standard deviation of QPE and gauge rainfall, respectively. MSE can also be divided into three terms (Murphy and Winkler 1987; Nelson et al. 2010):

$$\mathrm{MSE} = \left(m_Q - m_G\right)^2 + \left(\sigma_Q - \sigma_G\right)^2 + 2\sigma_Q\sigma_G(1-\rho) \quad (3\text{-}6)$$

where ρ is correlation coefficient between QPE and gauge rainfall. In the right-hand side of Eq.(3-4), the first and second terms measure the bias in the mean and standard deviation, respectively, and the third term measures the strength of covariation (the smaller, the stronger) between the estimated rainfall (radar QPE) and verifying observation (gauge rainfall) (Nelson et.al. 2010). We calculate both unconditional and conditional statistics to assess how QPEs perform at the upper tail of rainfall distribution which is more important from flood forecasting viewpoint.

3.4.2. QPE merging

We also merge all the QPEs to get a better quality product. Based on the optimal estimation theory, the final product of optimal combining should have the highest information content compared to the individual products. The information content of each QPE can also be assessed through the weights given to them in the merging process. QPE with higher information content will obtain the highest weight. Merging can be performed by giving weights to individual QPEs through minimizing the unconditional error variance which will be unbiased in unconditional means. This will lead to overestimation of light rainfall and underestimation of heavy rainfall. However, estimating large precipitation amounts as accurately as possible is more important than light rainfall in flash flood warning application. Therefore, one needs to account for conditional biases. The merging method used here is based on the conditional bias-penalized (CBP) formulation (Seo 2013, Seo et al. 2014) of Fisher estimation (Schweppe 1973) which minimizes the unconditional error variance and type II conditional bias simultaneously. Type-II bias refers to where it rains heavily but the estimator does not show any rain. The objective function to be minimized would be as follow:

$$J = E_{X,X^*}[(X - X^*)(X - X^*)^T] + E_X[(X - E_{X^*}[X^* \mid X])(X - E_{X^*}[X^* \mid X])^T \quad (3\text{-}7)$$

where, X* is the estimated rainfall and X is the observed gauge rainfall. CBP-formulation reduces Type-II bias for improved estimation of large precipitation amounts, but at the expense of somewhat increased unconditional MSE. As mentioned the QPE with higher information content will get a higher weight. It should be noted here that weights by design must sum to one and negative weight is also possible showing a smaller amount of relative contribution.

One can formulate the problem as the following Fisher optimal linear estimation (Schweppe 1973).

$$Z = HX + V \quad (3\text{-}8)$$

where the observation and observation error vectors, Z and V, are given by $Z = [z_{MPE}, z_{Q_2}, z_{CASA}, z_{DHR}]^T$ and $V = [v_{MPE}, v_{Q_2}, v_{CASA}, v_{DHR}]^T$, respectively, X is the unknown true precipitation and the structure matrix H is $H = [1\ 1\ 1\ 1]^T$. By minimization the linearly weighted sum of error variance and Type-II conditional bias, Seo (2013) arrives at the following Fisher-like solution for conditional bias-penalized optimal linear estimation:

$$\Sigma_{CBP} = \mathrm{B}[\hat{H}^T \Lambda^{-1} H]^{-1} \quad (3\text{-}9)$$

$$X^*_{CBP} = [\hat{H}^T \Lambda^{-1} H]^{-1} \hat{H}^T \Lambda^{-1} Z \quad (3\text{-}10)$$

where, Σ_{CBP} denotes the estimation error covariance matrix and X^*_{CBP} denotes the vector of estimation. In the above, the variables, $\hat{H}$, Λ and B, are given by:

$$\hat{H}^T = H^T + \alpha \Psi_{XX}^{-1} \Psi_{XZ} \quad (3\text{-}11)$$

$$\Lambda = R + \alpha(1-\alpha)\Psi_{ZX}\Psi_{XX}^{-1}\Psi_{XZ} - \alpha H \Psi_{XZ} - \alpha \Psi_{ZX} H^T \quad (3\text{-}12)$$

$$\mathrm{B} = \alpha \Psi_{XX} \Sigma_A^{-1} + I = \alpha \Psi_{XX} \hat{H}^T \Lambda^{-1} \hat{H} + (1+\alpha) I \quad (3\text{-}13)$$

In the above, α denotes the scalar weight given to the conditional bias penalty term of the objective function, Ψ_{XX} and Ψ_{ZX} denote $\mathrm{Cov}[X,X^T]$ and $\mathrm{Cov}[Z,X^T]$, respectively, and R denotes

the (nxn) observation error covariance matrix. If $\alpha=0$ (i.e. no penalty for conditional bias), the above reduces to the Fisher solution (Schweppe 1973).

3.5. Results

Comparisons are performed between the concurrent and collocated radar and rain gauge observations retrieved from the Grand Prairie rain gauge network. First we compared all the hourly QPEs at their native spatial resolution. Next we compared all the hourly QPEs at full HRAP resolution (~ 4 km) in order to have a fair compariosn. Finally, comparative evaluation was performed at the 15 minute temporal resolution. Sample results and discussion are given in the following subsections.

3.5.1. Native spatial resolution and 1 hour temporal resolution

First radar-based rainfall estimations are compared at their native resolution using the concurrent and collocated raingauges in the City of Grand Prairie. By native resolution we mean to use the MPE value from the Full HRAP bin, Q2 and DHR value from the 1/4 HRAP pixel and CASA from 1/8 HRAP pixel. Figure 3-8 shows the scatter plot of each QPE at their native resolution as well as the merged QPE versus raingauge observations for all the gauges in study area. As depicted, overall Q2 has the least bias overall followed by MPE. CASA is on the third rank and DHR has the largest bias among all the products. Q2 has the most wide spread scatter plot while CASA QPE is the tightest among all QPEs. The widespread variability of Q2 will result in higher RMSE values.

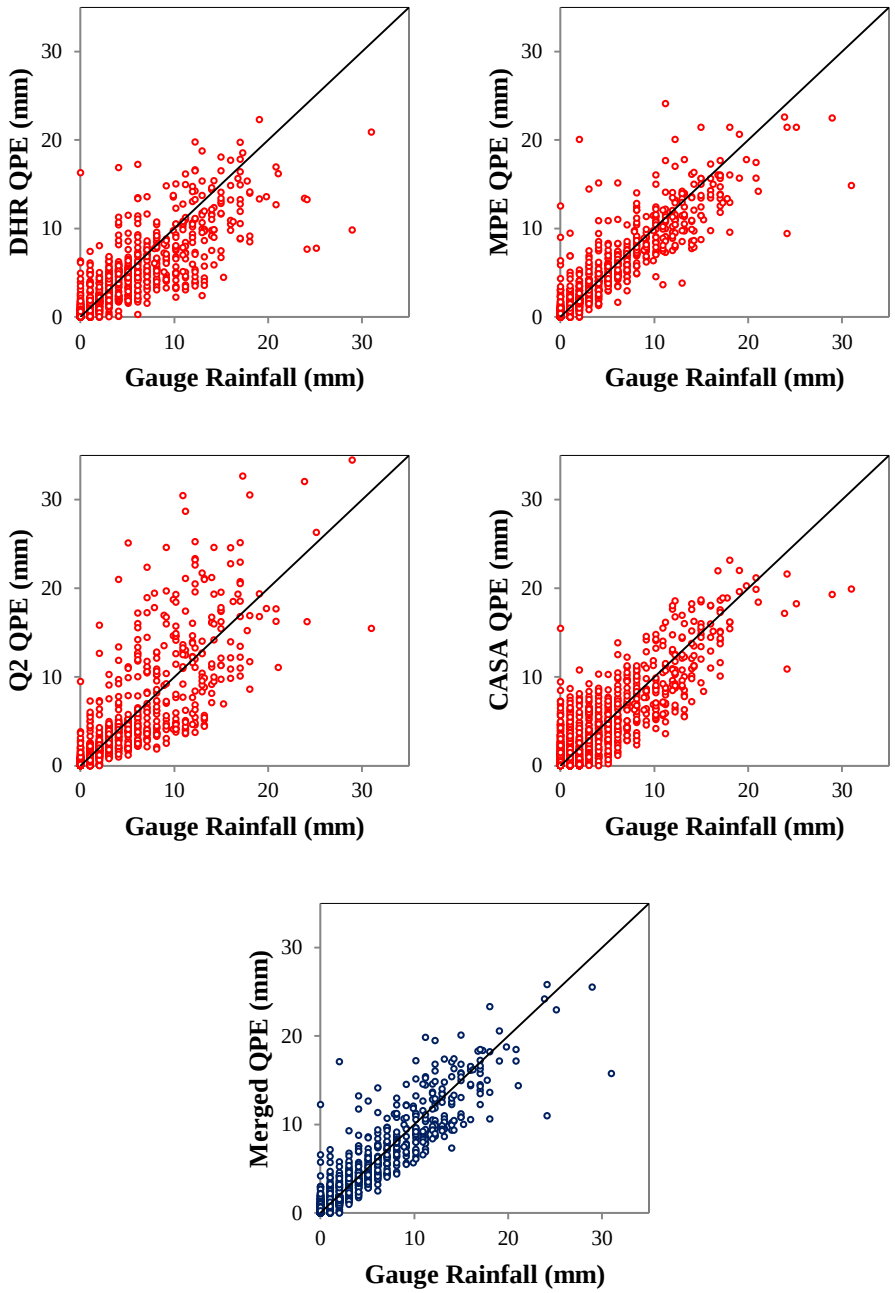

Figure 3-8 Scatter Plot of DHR, MPE, Q2 and CASA QPE versus gauge rainfall for all the rain gauges in the Grand Prairie at their native spatial resolution and 1 hour temporal resolution.

Weights given to each QPE product in the merging process for both unconditional and conditional merging is plotted in Figure 3-9. Unconditional merging means all the data points are used in the merging process. For conditional merging, only the data points with rainfall greater than a threshold value is used in the merging process and also calculation of the statistics. Using higher threshold is desired in extreme event forecasting when the end tail of the distribution is of importance. However, using higher threshold yields in smaller ample size which makes the statistics less reliable, particularly in this study which the common period between all QPEs is fairly short. Higher weight is an indication of more information content in the QPE relative to other QPEs. As depicted in Figure 3-9 MPE has the highest weight and consequently highest information content for lower rainfall amount which decreases by increasing the conditioning threshold. On the other hand, CASA has the second rank in low rainfall amounts and tend to increase as the threshold increases. This confirms that CASA is able to detect and estimate the upper tail of the rainfall distribution better than the other QPEs. However, it should be mentioned that these results are based on a fairly small amount of data and limited raingauge sites and also the rain gauge locations are fairly close to the radar location. More data points and a better scattered rain gauge network under the CASA radar umbrella is required to conclude that CASA estimate is actually better than MPE. Also notice that the DHR weights are negative. This happens since the summation of the weights should equal to one, which forces some of the weights to be negative. This indicates that DHR has less information content compared to other QPEs.

Figure 3-10, Figure 3-11, and Figure 3-12 indicate the unconditional and conditional multiplicative bias, RMSE and correlation coefficient for all QPEs as well as the merged product. All the QPEs except from DHR have a multiplicative bias factor of less than for the unconditional mode and greater than one for conditional mode. In other words, all the QPEs overestimate the rainfall when we consider all the rainfall spectrum and underestimate when only high rainfall amounts are considered. Q2 has the least multiplicative bias compared to other products for all

conditioning thresholds. MPE has the lowest bias factor after Q2 for the low rainfall values; however, it increases as the conditioning threshold increases. CASA has a high bias factor at low rainfall amount and stays almost the same for all conditioning thresholds, in high rainfall amounts CASA has a lower bias compared to MPE which is a very important point to make.

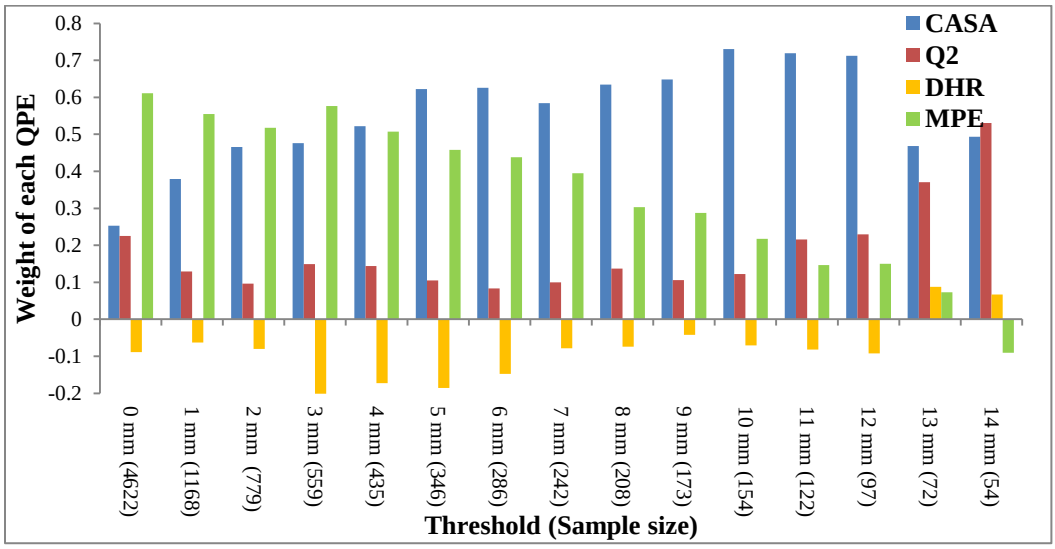

Figure 3-9 Weights assigned to CASA, Q2, DHR and MPE in the merging process. Threshold is the conditioning value. Sample size for each case is given in parenthesis.

As indicated in Figure 3-11 RMSE increases by increase of the conditioning threshold. MPE has the lowest RMSE values for low and mid rainfall amounts and CASA has the lowest RMSE values for the end tail of the rainfall distribution. Q2 and DHR have higher RMSE values than MPE and CASA at all the threshold values. Correlation coefficient has a similar pattern to RMSE, MPE has the highest correlation coefficient at low and mid rainfall amount while CASA has higher correlation coefficient for large rainfall amounts. Also DHR and Q2 does not have a good correlation coefficient compared to MPE and CASA.

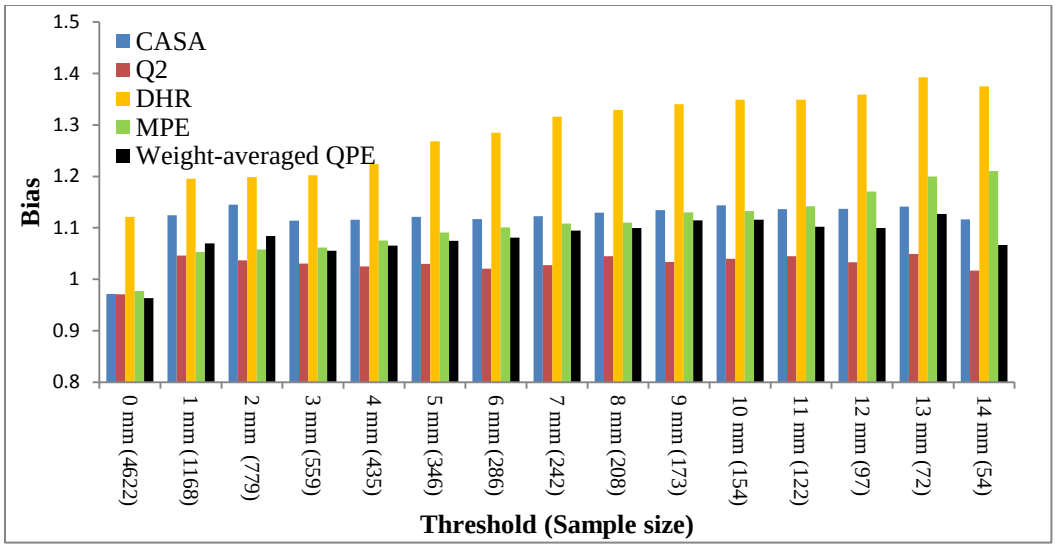

Figure 3-10 Multiplicative bias for CASA, Q2, DHR, MPE and the merged product at their native spatial resolution and hourly temporal resolution. Threshold is the conditioning value. Sample size for each case is given in parenthesis.

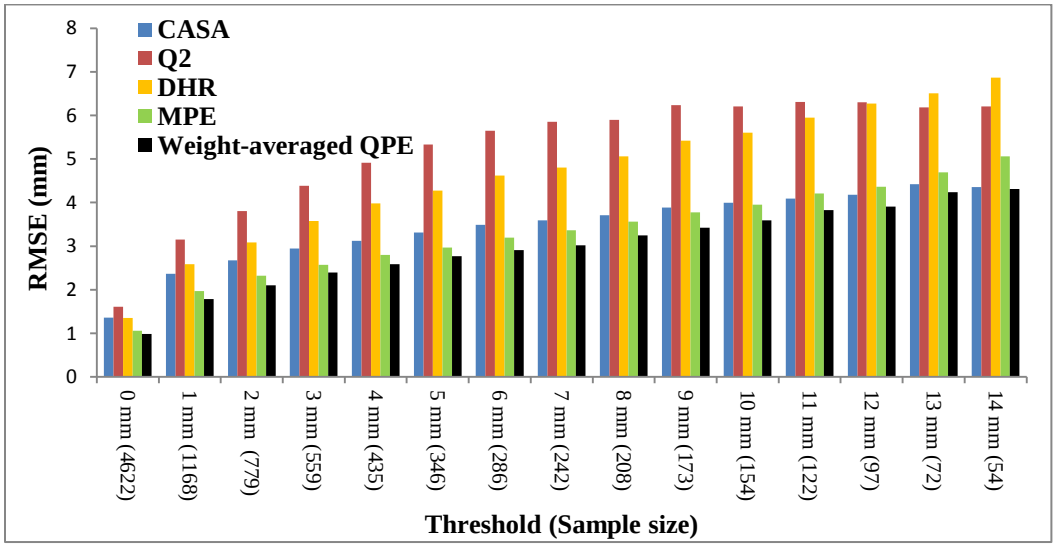

Figure 3-11 RMSE values for CASA, Q2, DHR, MPE and the merged product at their native spatial resolution and hourly temporal resolution. Threshold is the conditioning value. Sample size for each case is given in parenthesis.

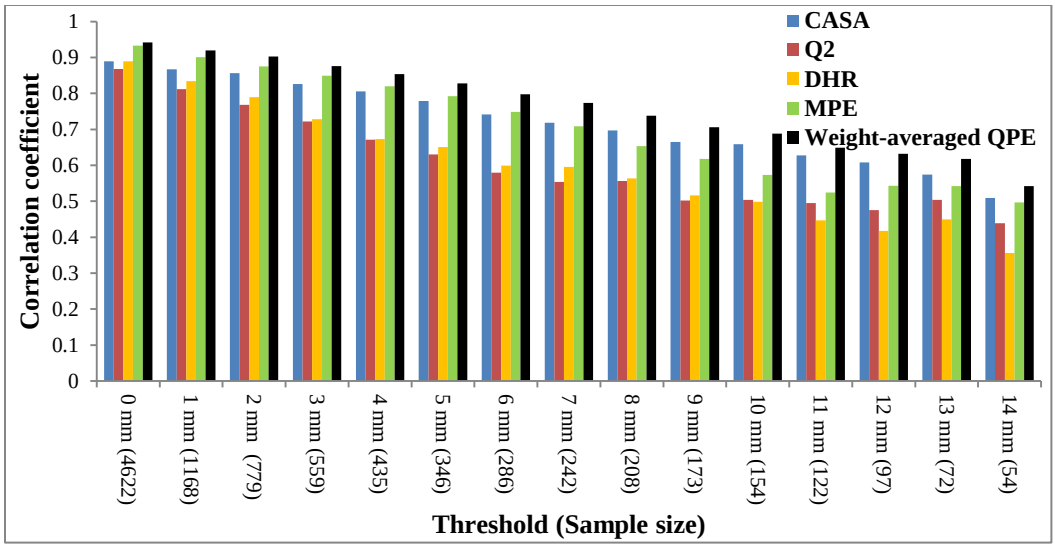

Figure 3-12 Correlation coefiicient for CASA, Q2, DHR, MPE and the merged product at their native spatial resolution and hourly temporal resolution. Threshold is the conditioning value. Sample size for each case is given in parenthesis.

The MSE decomposition is also given in Figure 3-13. As demonstrated Q2 has the least bias in mean and highest bias in standard deviation. MPE is least biased in mean for low rainfall amounts and CASA is least biased in large rainfall depths. CASA has the least bias in standard deviation among all QPEs.

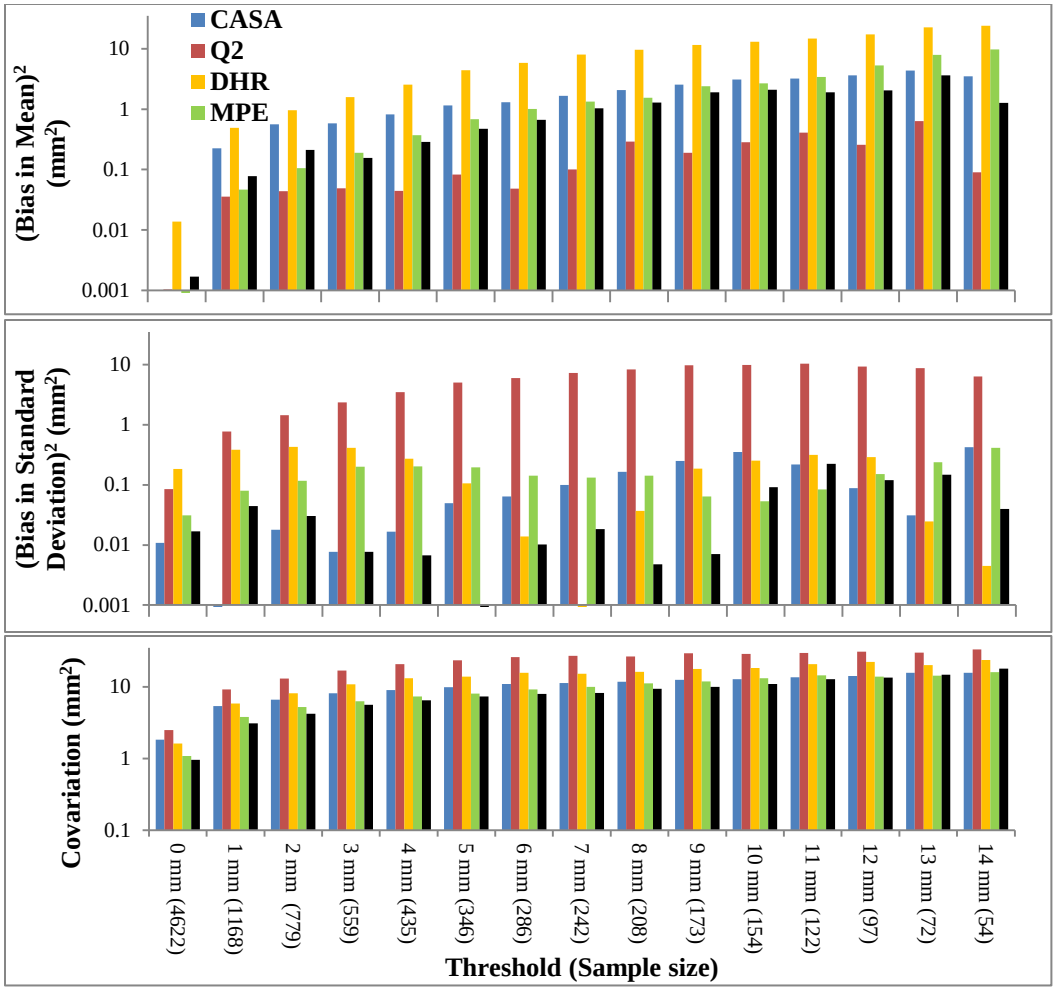

Figure 3-13 MSE decomposition for CASA, Q2, DHR, MPE and the merged product at their native spatial resolution and hourly temporal resolution. The upper panel shows the bias in mean, the middle panel shows the bias in standard deviation and the bottom panel illustrates the strength of covariation.

3.5.2. Full HRAP spatial resolution and 1 hour temporal resolution

Since the spatial resolution of CASA is the finest, the representativeness error is less pronounced in the CASA compared to other QPEs. The same is true about Q2 and DHR compared to MPE with the coarse resolution of ~ 4k. To minimize the difference originated from

representativeness error, we upscale Q2, DHR and CASA into full HRAP spatial resolution. Figure 3-14 shows the scatter plot of all QPEs and merged QPE at ~ 4 km and 1 hour. As demonstrated in the Figure 3-14 CASA accuracy deteriorates when it is upscaled to ~ 4 km which was expected, since averaging over a bigger area increases the representativeness error in the estimation. The scatter becomes wider even though it is not very significant and the bias increases. Q2 behavior is analogous to CASA, the spread of the data points increases in the scatter plot as well as the multiplicative bias amount. The deteriorated individual QPE has impacted the quality of the merged product as well. The merged product is poor compared to the case one (native spatial resolution). Therefore, coarser the resolution of the available QPE, lesser the accuracy of the rainfall estimation. Statistical indices were calculated for this case also which is not shown here. They also confirmed the conclusion derived above. Also it should be noted that the difference between two cases is not very significant and all the conclusions in Section 3.5.1 is true for this case as well.

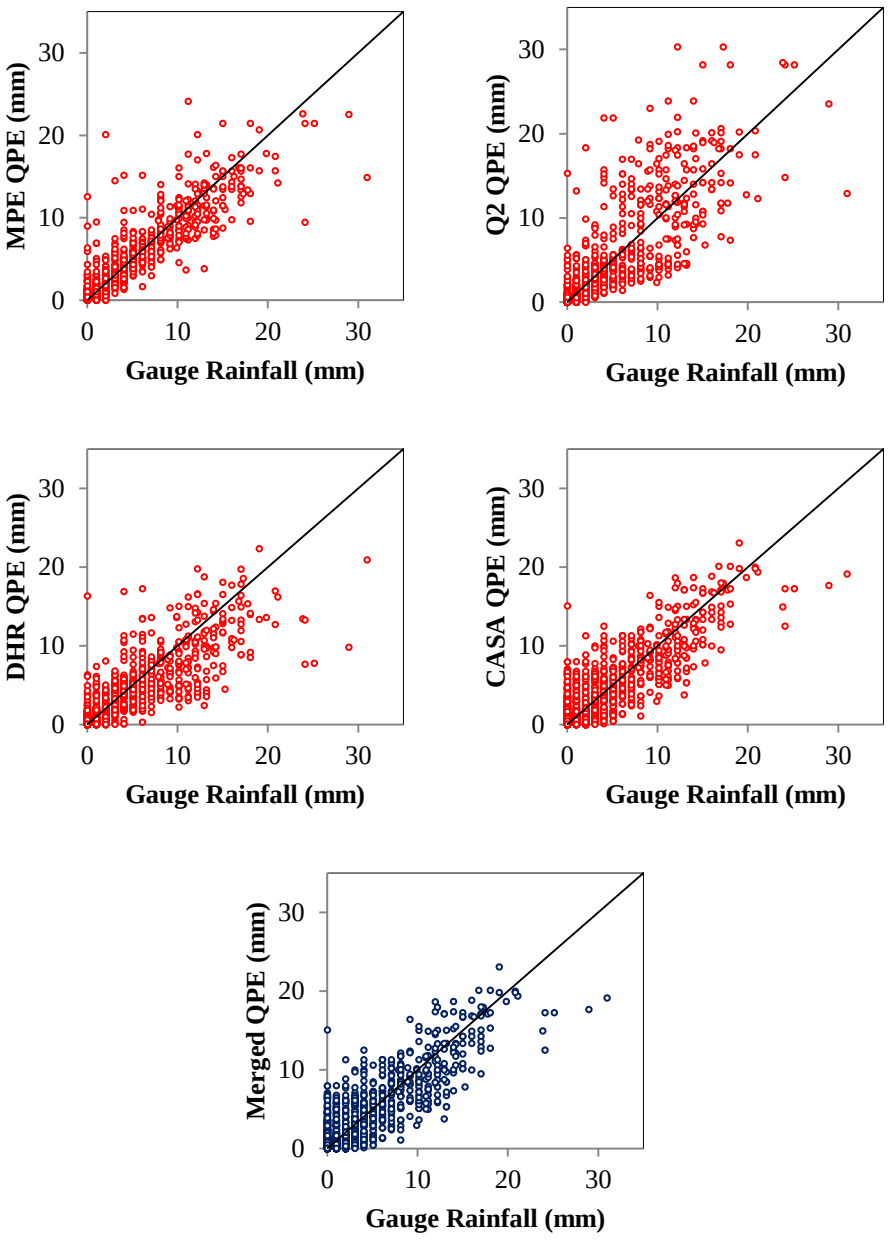

Figure 3-14 Scatter plot of DHR, MPE, Q2 and CASA QPE versus gauge rainfall at ~4 km and 1 hour.

3.5.3. Native spatial resolution and 15 minute temporal resolution

We also compared CASA, Q2 and DHR at their native resolution and 15 minute temporal resolution. The reason for choosing 15 minute is that the rain gauge data is reported every 15 minutes which limits the temporal resolution of our comparison. Scatter plots are shown in Figure 3-15.

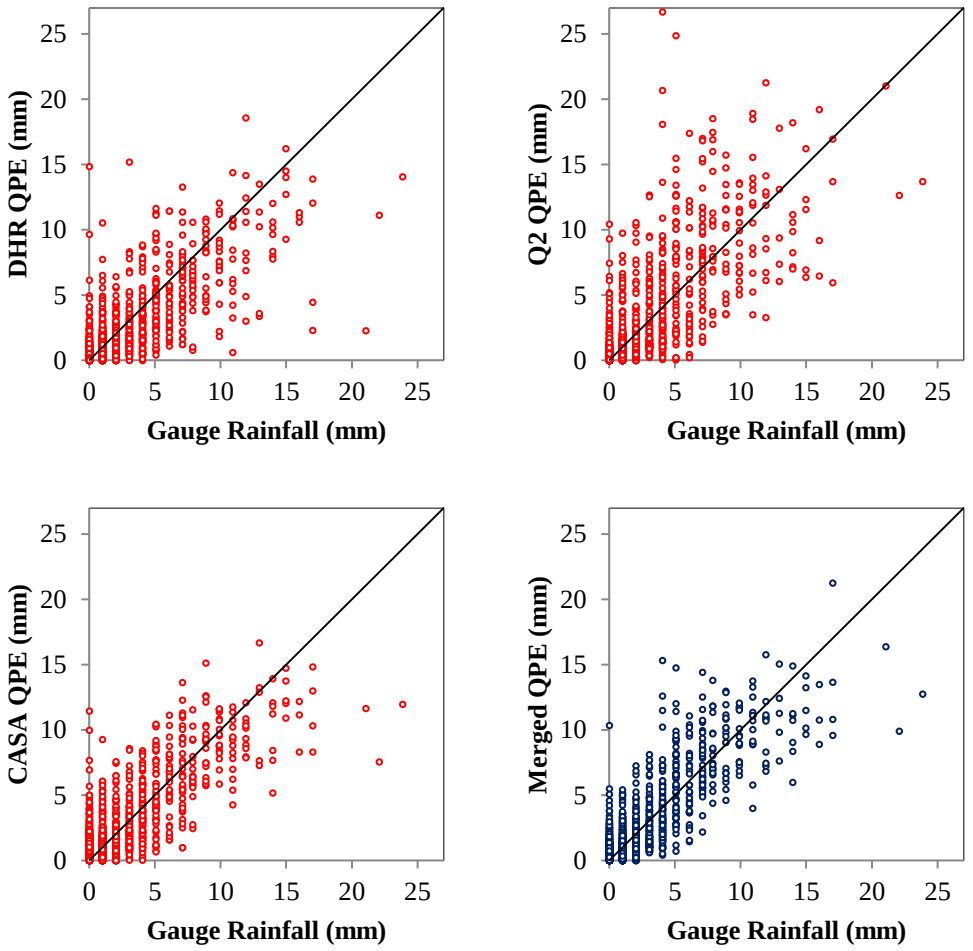

Figure 3-15 Scatter plot of DHR, Q2 and CASA QPE versus gauge rainfall at their native spatial resolution and 15 minute temporal resolution.

The scatter is wider for 15 minutes temporal resolution for all the products. Q2 has the least bias in mean and widest spread, the same as hourly temporal resolution. Weights given to individual QPE is shown in Figure 3-16. In the merging process higher weights are assigned to CASA up to the threshold of 7 mm, an indication of higher information content compared to Q2 and DHR. Above 7 mm, the sample size is too small and the statistics may not be reliable for deriving any conclusion. Multiplicative bias factor (Figure 3-17) is lowest for Q2 consistently over different thresholds. Bias for CASA increase sharply at the threshold of 1 mm which is a sever underestimation of rainfall greater than 1 mm. The underestimation problem alleviate by increasing the threshold up to 6 mm and then increases again. As discussed above the sample size for rainfall depth greater than 6 mm is small and no conclusion can be made based on the statistic measures. In terms of RMSE (Figure 3-18), CASA has the lowest values. CASA also has the highest correlation coefficient as depicted in Figure 3-19.

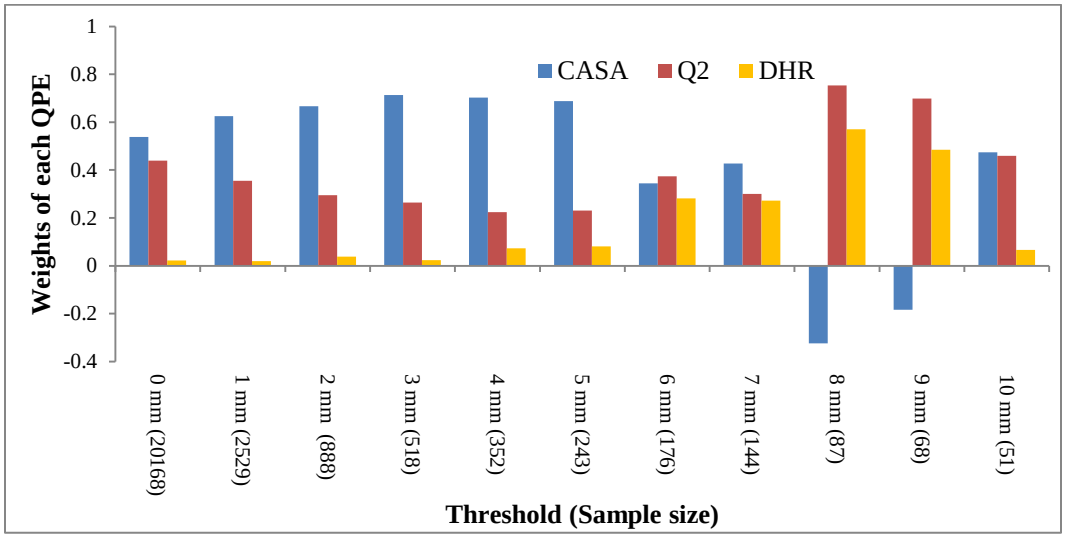

Figure 3-16 Weights assigned to CASA, Q2, and DHR in the merging process. Threshold is the conditioning value. Sample size for each case is given in parenthesis.

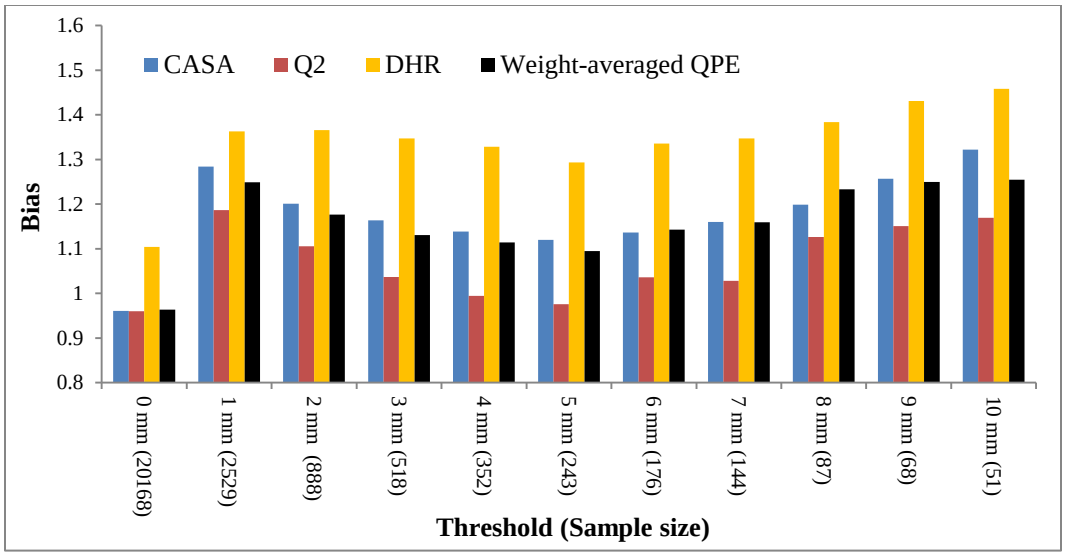

Figure 3-17 Multiplicative bias for CASA, Q2, DHR, and the merged product at their native spatial resolution and 15 min temporal resolution. Threshold is the conditioning value. Sample size for each case is given in parenthesis.

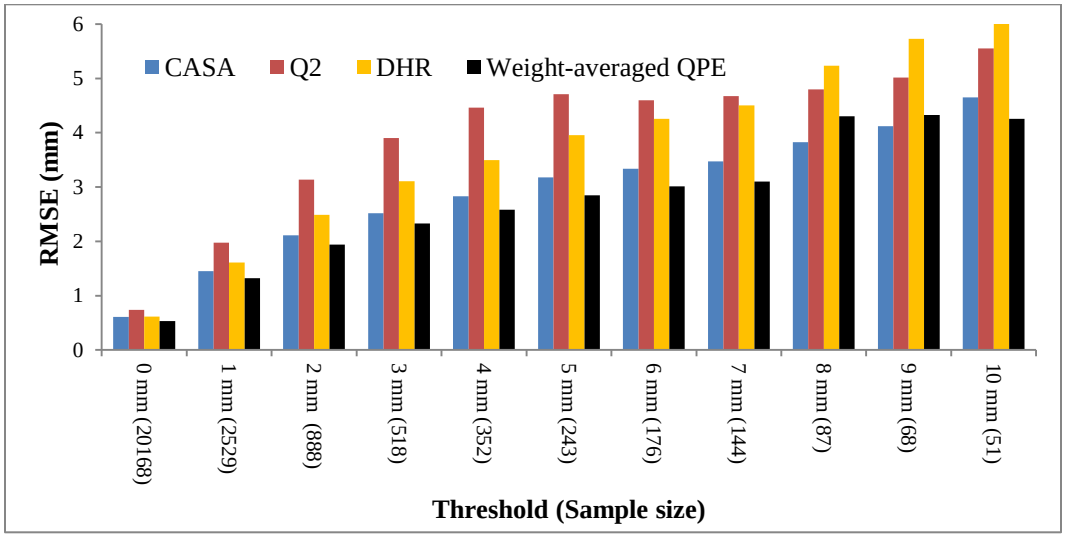

Figure 3-18 RMSE for CASA, Q2, DHR, and the merged product at their native spatial resolution and 15 min temporal resolution. Threshold is the conditioning value. Sample size for each case is given in parenthesis.

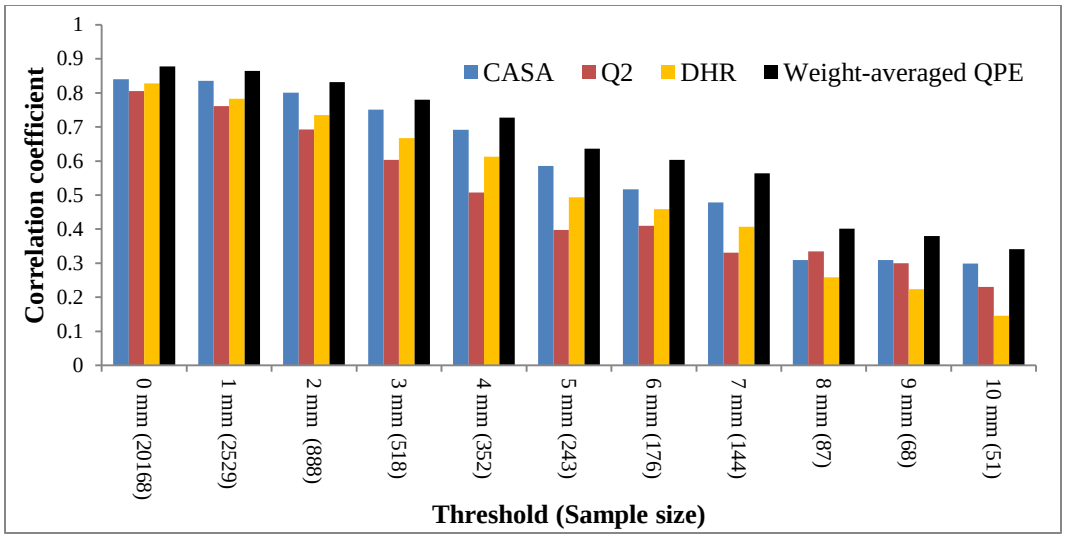

Figure 3-19 Correlation coefficient bias for CASA, Q2, DHR, and the merged product at their native spatial resolution and 15 min temporal resolution. Threshold is the conditioning value. Sample size for each case is given in parenthesis.

3.6. Conclusion

To understand and assess how the error properties in radar-based QPE may differ over different spatiotemporal scales of aggregation and how they may manifest in hydrologic simulations, we comparatively evaluate QPEs from the Multisensor Precipitation Estimator, NEXRAD Digital Hybrid Scan Reflectivity, Q2 and CASA. The rain gauge network deployed and operated by the City of Grand Prairie from the High Water Warning System is used as the true rainfall for the comparison study.

First comparison was carried out between radar-based rainfall estimations at their native resolution and 1 hour temporal resolution. Results indicated that Q2 is the least bias in mean; however, it has the largest bias in standard deviation. MPE has the highest information content relative to others at low rainfall depth and obtain the highest weights in the merging process while

CASA gets the higher weights at higher rainfall thresholds. DHR has the least amount of information relative to other QPE products.

Q2 has the least multiplicative bias factor for all conditioning thresholds. The lowest bias factor after Q2 for the low and high rainfall amount belongs to MPE and CASA respectively. In general, RMSE increases with the conditioning threshold increase. MPE has the lowest RMSE values for low and mid rainfall amounts and CASA has the lowest RMSE values for the end tail of the rainfall distribution. The same results are observed for the correlation coefficient; MPE has the highest correlation coefficient at low and mid rainfall amount while CASA has higher correlation coefficient for large rainfall amounts. DHR and Q2 has larger RMSE values and lower correlation coefficients compared to MPE and CASA. Also, as expected the merged QPE has the best performance compared to the individual QPEs.

Since the spatial resolution of CASA is the finest, the representativeness error is less pronounced in the finer resolution products such as CASA. To minimize the difference originated from representativeness error, we upscale Q2, DHR and CASA into full HRAP spatial resolution. As expected the performance of CASA and Q2 were deteriorate when upscale. They all have a wider spread in the scatter plots compared to their native resolutions. The deteriorated individual QPE has impacted the quality of the merged product as well. The merged product is poor compared to the native spatial resolution. However the trend of the statistical measures such as RMSE, multiplicative bias factor and correlation coefficient remains the same for all QPEs.

We also compared CASA, Q2 and DHR at their native resolution and 15 minute temporal resolution. The scatter is wider for 15 minutes temporal resolution for all the products compare to hourly QPE. CASA has the highest amount of information relative to Q2 and DHR up to the conditioning threshold of 7 mm. Above 7 mm, sample size is too small and the statistics are not reliable for deriving any conclusion. Multiplicative bias factor is lowest for Q2 consistently over different thresholds. CASA has a sever underestimation for rainfall greater than 1 mm which

disappears by increasing the threshold up to 6 mm. CASA has the lowest RMSE values and highest correlation coefficient.

Finally, we concluded that the quality of MPE, CASA and Q2 is good enough to be useful for flash flood forecasting purposes. DHR does not have a good performance, and using it is not recommended unless an extensive preprocessing routine has been performed. MPE is the most accurate product for low to mid rainfall depths and CASA outperform the MPE at high rainfall amounts. Combining these QPEs will provide a more accurate product; however, the amount of improvement should be evaluated.

Chapter 4

Improving high-resolution precipitation analysis via fusion of multiple radar-based precipitation products

For monitoring and prediction of water-related hazards such as flash flooding, high-resolution hydrologic and hydraulic modeling is necessary. Due to large sensitivity to errors in quantitative precipitation estimates (QPE), it is very important in high-resolution hydrologic modeling that the accuracy of high-resolution QPE be improved to the greatest possible extent. With the availability of multiple radar-based precipitation products in many areas, one may now consider fusing multiple radar-based QPEs to produce more accurate high-resolution QPE for various applications. In this work, we comparatively evaluate four procedures for such fusion based on Fisher estimation and its conditional bias-penalized variant: Direction Estimation (DE), Bias Correction (BC), Reduced-Dimension Bias Correction (RBC) and Simple Estimation (SE). They are applied to fuse the MPE and radar-only Q2 products at the 15-min 1-km resolution (Experiment 1), and the MPE and CASA product at the 15-min 500-m resolution (Experiment 2). The resulting fused estimates are evaluated using the 15-min rain gauge observations in the City of Grand Prairie in the Dallas-Fort Worth Metroplex (DFW) area. The main evaluation criterion was that the fused QPE improves over the ingredient QPEs at their native spatial resolutions, and that, at the high resolution, the fused QPE improves not only the high-resolution ingredient QPE but also the high-resolution QPE obtained by trivially disaggregating the low-resolution QPE with the high-resolution QPE. All four procedures assumed that the ingredient QPEs are unbiased which, in reality, is not very likely even if real-time bias correction was already applied. To test robustness, the evaluation procedures were evaluated with and without post-hoc bias correction of the ingredient QPEs.

The results show that only SE passes the above evaluation criterion consistently. The performance of DE and BC are generally comparable. Between the two, while DE is more attractive for computational economy, BC is more attractive for guaranteed nonnegativity of the fused estimates. The performance of RBC is very poor as it does not account for the fact that biases in the QPE products depend on the magnitude of precipitation. SE assumes that the high-resolution QPE product is skillful in capturing spatiotemporal variability of precipitation at its native scale, and that the low-resolution QPE product provides skill at its native resolution. While the above assumptions may not always be met, its simplicity and the robustness observed in this work make a strong case for operational implementation of SE as a post-processor to the QPE product generation process. Also, unless other procedures considered in this work, it is possible to update the statistical parameters necessary for SE on line similarly to the real-time bias correction currently used in MPE.

4.1. Introduction

In the U.S., more than three-quarters of the population live in urban areas which collectively comprise only about 3% of the land area. According to the U.S. Census Bureau, the urban population increased by 12.1% from 2000 to 2010 compared to the overall increase of 9.7% for the same period. For the 486 large urbanized areas, the rate was even higher at 14.3%. Given the high population density, high-resolution observing and modeling capabilities are necessary in urban areas for prediction of flash floods. Increasing occurrences of extreme precipitation expected from climate change put such areas in a particularly vulnerable position where even a small-scale but intense rainfall event can cause deadly flash floods and extensive damages.

For high-resolution observing and modeling of large urban areas, the use of weather radar and distributed hydrologic modeling is a natural progression. Quantitative precipitation estimates (QPE) from radars, however, are subject to various sources of error (Seo et al. 2010). High-

resolution distributed modeling is subject to nonlinear growth of error due to errors in QPE and in model parameters and structures (Smith et al. 2004b). For hydrologic, hydraulic and water quality modeling and prediction in urban areas, it is therefore highly desirable that the QPE is as accurate as possible at the highest resolution possible. The purpose of this work is to fuse multiple radar-based precipitation products to produce a higher-quality QPE product that improves over the ingredient QPEs at their native resolutions. Necessarily, fusion can take place only after all ingredient QPE products are generated and made available. As such, an inherent limitation with fusion is that the fused QPE may not be available for certain applications for which timeliness is of the essence.

In the Dallas-Fort Worth Metroplex (DFW), there are currently three sources of radar-based QPE, the Multisensor Precipitation Estimator (MPE, Seo et al. 2010), Q2 (Next Generation QPE, Zhang et al. 2011) and CASA (Collaborative Adaptive Sensing of Atmosphere, Chandrasekar et al. 2012). Because the radar systems, the sources of additional information and/or processing algorithms are different, the above QPE products have different error characteristics and nominal spatiotemporal resolutions. While multisensor merging of satellite, radar and/or rain gauge data for improved QPE is widely investigated (Seo et al. 2010, Li and Shao, 2010, Woldemeskel et al. 2013, Berndt et al. 2014, Chang et al, 2014, Delrieu et al, 2014), fusion of multiple gridded QPEs of different spatiotemporal resolutions for high-resolution QPE is relatively new (Ebtehaj and Foufoula-Georgiou 2011, Chandrasekar and Cifelli 2012). High-resolution QPE fusion is particularly challenging because of high dimensionality and likely under-determinedness of the estimation problem. In this work, we formulate and comparatively evaluate four relatively simple procedures for improving the accuracy of high-resolution QPE by fusing it with a lower-resolution QPE. The general methodology used is Fisher estimation (Schweppe 1973) and its conditional bias-penalized variant (Seo 2013, Seo et al. 2014). If the penalty for Type II conditional bias is not assessed, conditional bias-penalized estimation reduces to Fisher

estimation. For evaluation, we compared the fused precipitation estimates with rain gauge observations in the DFW area.

The main contributions of this work are: development and comparative evaluation of different procedures for fusing multiple radar-based precipitation products for high-resolution QPE, advancing understanding of precipitation fusion and the relationships among different procedures, and evaluation of multiple radar QPEs in the DFW area. This manuscript is organized as follows. The rest of the chapter is organized as follow. Section 4.2 describes the approach. Methodology is described in Section 4.3. The study area and the data used are described in Section 4.4. Section 4.5 describes how the statistical parameters are estimated. Section 4.6 describes the evaluation experiments. Section 4.7 presents the results. Finally, conclusion and future research recommendations are provided in Section 4.8.

4.2. Approach

Below, we describe the four different procedures used in this work in the context of fusing the MPE estimates, which have a nominal spatiotemporal resolution of 1 hr and approximately 4x4 km^2, and the Q2 estimates, which have nominal resolution of 5 min and 1x1 km^2. The rain gauge data for parameter estimation and validation are available only at a 15-min resolution. As such, we chose the target resolution for fusion to be 15 min and 1x1 km^2, rather than 5 min and 1x1 km^2. Figure 4-1 illustrates the data flow for MPE, Q2, and fusion of the two QPEs. Once the techniques are comparatively evaluated, we apply the best performing procedure for fusion of the MPE and CASA QPE as well. The nominal resolution of the CASA QPE is 1 min and 500x500 m^2. The target resolution for fusing the CASA and MPE products is 15-min and 500x500 m^2. Before we describe the procedures in the some detail, it is useful to explain first the rationale for their formulation.

In the first approach, the observation vector, Z, is made of a single MPE estimate at 1-hr 4-km resolution and all 64 (=4^3) Q2 estimates at 15-min 1-km resolution within the sampling volume of the MPE estimate. The state vector, X, denotes the true unknown precipitation at the 15-min 1-km resolution, which is then solved via Fisher estimation (Schweppe 1973) under the linear observation equation, Z=HX+V, where H denotes the structure matrix and V denotes the observation error vector. This approach is referred to as Direct Estimation (DE). Because the Fisher solution does not impose any non-negativity constraints on the estimates, DE may produce negative estimates particularly over areas of light or no precipitation. We note here that it is possible to impose non-negativity constraints and solve constrained minimization via, e.g., the Lagrange method (Szidarovszky et al. 1987). Such an approach, however, is only suboptimal and may compromise the effectiveness of the procedure, particularly for large precipitation amounts, and hence is not considered in this work. Here, all negative DE estimates are set to zero.

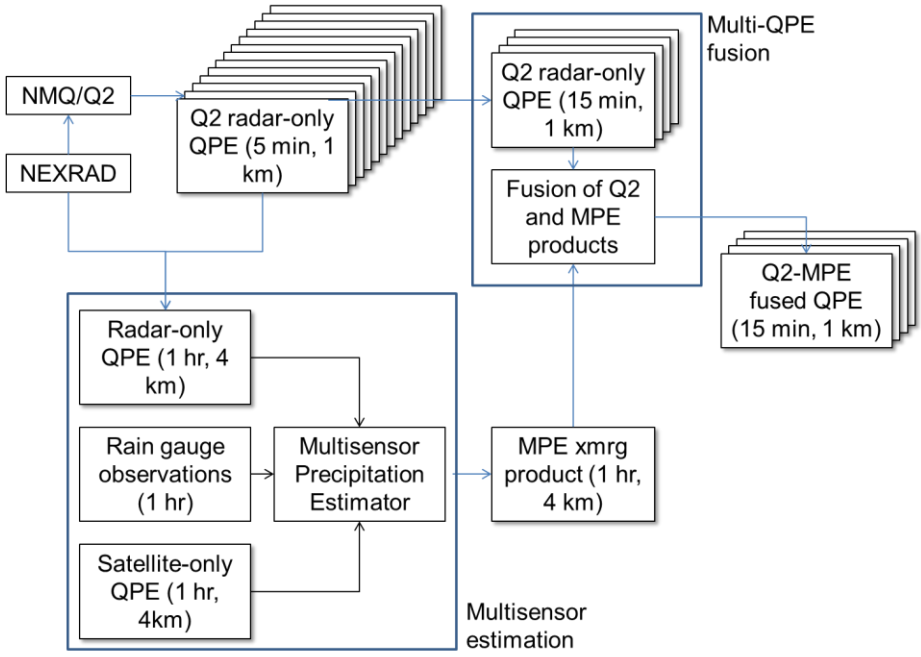

Figure 4-1 The data flow for MPE, Q2, and fusion of the two QPEs.

In the second approach, the observation vector remains the same, but the state vector is made of multiplicative adjustment factors for the Q2 estimates at 15-min 1-km resolution and the structure matrix is made of the Q2 estimates themselves. The main motivation for this formulation is to avoid producing negative estimates as DE does. This approach is referred to as Bias Correction (BC). Because the Q2 estimates form the structure matrix, H, the linear system for the optimal solution must be solved every time an MPE estimate and the corresponding Q2 estimates are fused. As such, the computational burden of applying BC over a large area can be significant. In the third approach, referred to as Reduced-Dimension Bias Correction (RBC), we reduce the dimensionality of the state vector to a minimum. In RBC, the observation equation remains the same, but a single spatiotemporally constant multiplicative adjustment factor is assumed for all 64 Q2 estimates associated with the sampling volume of the MPE estimate. The above reduces the dimensionality of the state vector in RBC to unity. It is of course possible to reduce the dimensionality only to some intermediate level (see, e.g., Lee et al. 2012). In this work, however, we are primarily interested in assessing performance of the different fusion procedures under the limiting conditions, in terms of the dimensionality of the estimation problem and parsimony for parameter estimation. As such, we did not consider employing intermediate scales (i.e. between 1 km and 15 min, and 4 km and 1 hour) of correction. While the dimensionality of the state vector is minimized, RBC still requires modeling the space-time covariance of observation errors as in DE or BC, which in practice is very difficult due to lack of ground truth. In the fourth approach, referred to as Simple Estimation (SE), the Q2 estimates are aggregated to 1-hr 4-km resolution which is merged with the MPE estimate. The merged estimate is then multiplicatively disaggregated under the assumption that the spatiotemporal pattern in the Q2 estimates is representative of the truth. In all approaches, we use the conditional bias-penalized formulation of Fisher estimation to improve estimation of heavy-to-extreme precipitation (Seo 2013, Seo et al. 2014).

4.3. Methodology

In this section, we describe Direct Estimation, Bias Correction, Simple Bias Correction and Simple Estimation; they are abbreviated herein as DE, BC, SBC and SE, respectively. The first three approaches are formulated as the following Fisher optimal linear estimation (Schweppe 1973):

$$Z = HX + V \tag{4-1}$$

where the observation and observation error vectors, Z and V, are given by $Z = [z_{Q_{1,1,1}}, z_{Q_{1,1,2}}, ..., z_{Q_{4,4,4}}, z_M]^T$ and $V = [v_{Q_{1,1,1}}, v_{Q_{1,1,2}}, ..., v_{Q_{4,4,4}}, v_M]^T$, respectively, and the structure matrix H and the state vector X vary according to the approach. In the above, $z_{Q_{i,j,k}}$ denote the Q2 estimate aggregated to 15-min accumulation at the ij-th 1x1 km^2 pixel, i=1,2,3,4, j=1,2,3,4, k=1,2,3,4, z_M denote the MPE estimate at the 1-hr 4x4 km^2 sampling volume that encompasses the 64 Q2 estimates at 15-min 1x1 km^2 scale, and $v_{Q_{i,j,k}}$ and v_M denote the observation errors associated with $z_{Q_{i,j,k}}$ and z_M, respectively.

4.3.1. Direct Estimation (DE)

The structure matrix, H, and the state vector, X, are given as follows:

$$H = \begin{bmatrix} 1 & 0 & \cdots & 0 \\ 0 & 1 & \cdots & 0 \\ \vdots & & & \\ 0 & \cdots & & 1 \\ \frac{1}{16} & \frac{1}{16} & \cdots & \frac{1}{16} \end{bmatrix} \tag{4-2}$$

$$X = [x_{1,1,1}, x_{1,1,2,}, ..., x_{4,4,4}]^T \tag{4-3}$$

where $x_{i,j,k}$ in Eq. (4-3) denotes the unknown true precipitation at the ij-th 1x1 km^2 Q2 pixel for the k-th 15-min subinterval. From the above, the observation equations for the ijk-the Q2 estimate and the MPE estimate are given by:

$$z_{Q_{i,j,k}} = x_{i,j,k} + v_{Q_{i,j,k}} \quad \text{i=1,2,3,4; j=1,2,3,4; k=1,2,3,4} \tag{4-4}$$

$$z_M = \frac{1}{16}\sum_{i=1}^{4}\sum_{j=1}^{4}\sum_{k=1}^{4} x_{i,j,k} + v_M \tag{4-5}$$

The Fisher solution to the above estimation problem is given by (Schweppe 1973):

$$\Sigma = [H^T R^{-1} H]^{-1} \tag{4-6}$$

$$X^* = [H^T R^{-1} H]^{-1} H^T R^{-1} Z \tag{4-7}$$

where R denotes the observation error covariance matrix, $\sum$ denotes the estimation error covariance matrix and X^* denotes the vector of the estimates, $X^* = [x^*_{1,1,1}, x^*_{1,1,2}, \ldots, x^*_{4,4,4}]^T$. The diagonal and off-diagonal entries of R are given by:

$$Var[v_{Q_{i,j,k}}] = E[(z_{Q_{i,j,k}} - x_{i,j,k})^2] \tag{4-8}$$

$$Var[v_M] = E[(z_M - \frac{1}{16}\sum_{i=1}^{4}\sum_{j=1}^{4}\sum_{k=1}^{4} x_{i,j,k})^2] \tag{4-9}$$

$$Cov[v_{Q_{i,j,k}}, v_{Q_{I,J,K}}] = E[(z_{Q_{i,j,k}} - x_{i,j,k})(z_{Q_{I,J,K}} - x_{I,J,K})] \tag{4-10}$$

$$Cov[v_{Q_{i,j,k}}, v_M] = E[(z_{Q_{i,j,k}} - x_{i,j,k})(z_M - \frac{1}{16}\sum_{i=1}^{4}\sum_{j=1}^{4}\sum_{k=1}^{4} x_{i,j,k})] \tag{4-11}$$

By minimization the linearly weighted sum of error variance and Type-II conditional bias (CB), $J = E_{X,X^*}[(X - X^*)(X - X^*)^T] + \alpha \bullet E_X[(X - E_{X^*}[X^* \mid X])(X - E_{X^*}[X^* \mid X])^T$ where α denotes the weight given to the penalty for Type-II CB, Seo (2013) arrives at the following Fisher-like solution for conditional bias-penalized optimal linear estimation:

$$\Sigma_{CBP} = \mathrm{B}[\hat{H}^T \Lambda^{-1} H]^{-1} \tag{4-12}$$

$$X^*_{CBP} = [\hat{H}^T \Lambda^{-1} H]^{-1} \hat{H}^T \Lambda^{-1} Z \tag{4-13}$$

where the modified structure matrix, $\hat{H}$, the modified observation error covariance matrix, Λ , and the scaling matrix, B, are given by:

$$\hat{H}^T = H^T + \alpha \Psi_{XX}^{-1} \Psi_{XZ} \tag{4-14}$$

$$\Lambda = R + \alpha(1-\alpha)\Psi_{ZX} \Psi_{XX}^{-1} \Psi_{XZ} - \alpha H \Psi_{XZ} - \alpha \Psi_{ZX} H^T \tag{4-15}$$

$$\mathrm{B} = \alpha \Psi_{XX} \Sigma_A^{-1} + I = \alpha \Psi_{XX} \hat{H}^T \Lambda^{-1} \hat{H} + (1+\alpha) I \tag{4-16}$$

In the above, Ψ_{XX} and Ψ_{ZX} denote Cov[X,X^T] and Cov[Z,X^T], respectively. Note that, if α=0 (i.e. no penalty for Type II conditional bias), Eqs.(4-12) and (4-13) reduce to the Fisher solution of Eqs.(4-1) and (4-2). Because Eqs.(4-14) through (4-16) require the a priori knowledge of Ψ_{XX} and Ψ_{ZX}, Eqs.(4-12) and (4-13) do not solve a Fisher problem but a Bayesian problem. One may also consider the conditional bias-penalized formulation to be a form of regularization in which the a priori information of Ψ_{XX} and Ψ_{ZX} is added the objective function.

4.3.2. Bias Correction (BC)

In this approach, the (nxm) structure matrix, H, and the (nx1) state vector, V, are given by:

$$H = \begin{bmatrix} z_{Q_{1,1,1}} & 0 & \cdots & 0 \\ 0 & z_{Q_{1,1,2}} & \cdots & 0 \\ \vdots & & & \\ 0 & \cdots & & z_{Q_{4,4,4}} \\ \frac{z_{Q_{1,1,1}}}{16} & \frac{z_{Q_{1,1,2}}}{16} & \cdots & \frac{z_{Q_{4,4,4}}}{16} \end{bmatrix} \tag{4-17}$$

$$X = [\beta_{Q_{1,1,1}}, \beta_{Q_{1,1,2,}}..., \beta_{Q_{4,4,4}}]^T \quad (4\text{-}18)$$

where $\beta_{Q_{1,1,1}}$ denotes the (nx1) adjustment factor for $z_{Q_{i,j,k}}$, $i, j, k = 1,..,4$. If some of the Q2 estimates are zeros, the corresponding rows in the linear system, Z=HX+V, are taken out to avoid singularity, which reduces the dimensionality of the problem. The above practice assumes that the Q2 estimates are near-perfect in delineating the precipitation area in that this particular fusion procedure cannot enlarge the precipitating area. The observation equations for the ijk-th Q2 estimate and the MPE estimate are the same as Eqs.(4-4) and (4-5), respectively, except that $x_{i,j,k}$ therein is replaced by $Z_{Qi,j,k}\beta_{Q_{i,j,k}}$. Similarly, the diagonal and off-diagonal entries of R are the same as Eqs.(4-8) through (4-11) except that $x_{i,j,k}$ is replaced by $Z_{Qi,j,k}\beta_{Q_{i,j,k}}$. In this procedure, the structure matrix, H, changes every time the Q2 estimates change. As such, BC is computationally far more expensive that DC.

4.3.3. Reduced-Dimension Bias Correction (RBC)

Whereas BC employs multiplicative adjustment factors that vary in space and time RBC assumes that they are uniform within the sampling volume of the MPE estimate. The above reduces H and X to:

$$H = [Z_{Q_{1,1,1}}, Z_{Q_{1,1,2}},..., Z_{Q_{4,4,4}}, \frac{1}{16}\sum_{i=1}^{4}\sum_{j-1}^{4}\sum_{k=1}^{4} Z_{Q_{i,j,k}}] \quad (4\text{-}19)$$

$$X = \beta_Q \quad (4\text{-}20)$$

Then, the Fisher solution for the uniform multiplicative adjustment factor, β_Q^*, is given by:

$$\beta_Q^* = \frac{WZ}{WH} = \frac{\sum_{i=1}^{4}\sum_{j=1}^{4}\sum_{k=1}^{4} w_{Q_{i,j,k}} z_{Q_{i,j,k}} + w_M z_M}{\sum_{i=1}^{4}\sum_{j=1}^{4}\sum_{k=1}^{4} w_{Q_{i,j,k}} z_{Q_{i,j,k}} + w_M z_Q^U} = w_1 + (1-w_1)\frac{Z_M}{Z_Q^U} \tag{4-21}$$

where $W = H^T R^{-1}$, $w_1 = \dfrac{\sum_{i=1}^{4}\sum_{j=1}^{4}\sum_{k=1}^{4} w_{Q_{i,j,k}} \dfrac{Z_{Q_{i,j,k}}}{Z_Q^U}}{\sum_{i=1}^{4}\sum_{j=1}^{4}\sum_{k=1}^{4} w_{Q_{i,j,k}} \dfrac{Z_{Q_{i,j,k}}}{Z_Q^U} + w_M}$, $Z_Q^U = \dfrac{1}{16}\sum_{i=1}^{4}\sum_{j-1}^{4}\sum_{k=1}^{4} Z_{Q_{i,j,k}}$.

In the above, Z_Q^U denotes the aggregated Q2 estimate to match the sampling volume of the MPE estimate. While the above simplification greatly reduces the dimensionality of the estimation problem, it is still necessary to model the observation error covariance matrix, R, and the cross covariance vector, Ψ_{XZ}, if the conditional bias-penalized solution is desired. Specifying R is a difficult task in practice as it requires statistical modeling of the space-time structure of observation errors.

4.3.4. Simple Estimation (SE)

In this approach, the 15-min 1-km Q2 estimates are aggregated to the spatiotemporal scale of the MPE estimates. The two estimates are then merged via Fisher estimation or the conditional bias-penalized variant described above:

$$X^{U*} = w_2 Z_Q^U + (1-w_2) Z_M \tag{4-22}$$

In the above, Z_Q^U denotes the aggregated Q2 estimate, w2 denotes the optimal weight, and X^{U*} denotes the optimal multi-QPE estimate at the 1-hr 4-km scale. To obtain the fused estimate at the 15-min 1-km scale, Z_Q^U is bias-corrected under the assumption that the 15-min 1-km Q2 estimates perfectly capture the spatiotemporal variability of precipitation with the sampling volume of the MPE estimate:

$$X^*_{i,j,k} = \frac{X^{U^*}}{Z^U_Q} Z_{Q_{i,j,k}},\ Z^U_Q > 0,\ \text{i=1,2,3,4; j=1,2,3,4; k=1,2,3,4} \tag{4-23}$$

In the above, $Z_{Q_{i,j,k}}$ and $X^*_{i,j,k}$ denote the Q2 and fused estimates, respectively, at the ij-th pixel and k-th 15 min subperiod. By replacing X^{U*} in Eq.(4-23) with $X^{U*} = w_2 Z^U_Q + (1-w_2) Z_M$ in Eq.(4-22), we have:

$$X^*_{i,j,k} = \left(w_2 + (1-w_2)\frac{Z_M}{Z^U_Q} \right) Z_{Q_{i,j,k}},\ Z^U_Q > 0,\ \text{i=1,2,3,4; j=1,2,3,4; k=1,2,3,4} \tag{4-24}$$

It is interesting to note that the above estimator is completely analogous to RBC, except that the weight is estimated differently. The main advantage of SE is that, unlike RBC, SE only requires modeling of the error covariance of the aggregated observations. As such, not only the space-time covariance modeling required for DE, BC and RBC is avoided, but also the estimates of the statistical parameters in the error covariance are likely to be more consistent due to the fact that the aggregated Q2 estimate and the MPE estimate share the same spatiotemporal scale of aggregation.

4.4. Study area and data acquisition

The study area is DFW in North Texas. Radar-based QPEs used in this study are the MPE, Q2 and CASA products. The spatiotemporal resolution and period of record for each data set are given in Table 3-1. The common period among all 3 QPEs is only about 7 month as the CASA radar was installed near the end of 2012. Q2 was upgraded to Q3 in Aug, 2013. The Q3 data, however, are currently not available (Jian Zhang, personal communications). The MPE products were obtained from the West Gulf River Forecast Center (WGRFC). The MPE products are on the Hydrologic Rainfall Analysis Project (HRAP) grid (Greene and Hudlow 1982) which is

about 4 km at mid-latitudes. The 5-min radar-only Q2 products were obtained from the National Climate Data Center (NCDC) in a NetCDF format and were remapped onto the 1/4th HRAP grid (i.e. ~1 km) using the budget interpolation procedure (Mesinger 1990, Accadia et al. 2003, Hou et al. 2012). The procedure performs remapping by subdividing a destination grid box into a user-selected number of sub-boxes and assigning precipitation in the source grid box to the sub-boxes whose centroids fall within the source grid box. The procedure conserves total precipitation to the desired degree of accuracy and is easy to implement. For details, the reader is referred to Accadia et al. (2003). The 1-min CASA products were obtained from Colorado State University (V. Chandrasekar, personal communications) on a 1/8th HRAP grid.

The rain gauge data used in this work are the 15-min observations from the High Water Warning System (HWWS) network operated by the City of Grand Prairie since 2009 (see Figure 4-2). As shown in the inset, in which the HRAP grid is overlaid, the rain gauge network is relatively dense and multiple HRAP bins contain multiple gauges. Similar systems are used by the adjacent cities such as Fort Worth and Arlington. The HWWS network uses tipping-bucket gauges. The data made available by the City are 15-min accumulations at 20 locations in a 1-mm resolution, which meant that the minimum detectable 15-min precipitation was 1 mm. To check the quality of the rain gauge data, we examined the scatter, quantile-quantile and double-mass plots of the rain gauge observations between each gauge and its closest neighbor. The results indicate that the rain gauge data from the City of Grand Prairie are of good quality and were accepted for use in this work. Figure 4-3 shows the departure of the 15-min precipitation at the five rain gauges of 6000, 6080, 6090, 6100 and 6306 from their spatial mean for the period of record. The minimum and maximum distances between any two gauges within the 5-gauge cluster are 1 and 5.3 km, respectively. Note that, even though the gauges are closely located to one another, there is significant variability in the observed 15-min precipitation. For example, the departure of 15-min gauge point precipitation from the spatial average of about 10 mm can be as

large as the spatial average itself and that for 18 inches is about a quarter of the spatial average. Given the large spatial variability, it is considered that the data set used in this work offers a good test for high-resolution fusion.

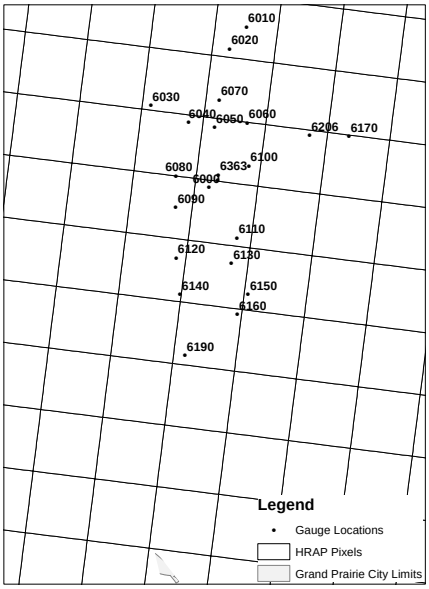

Figure 4-2 High Water Warning System (HWWS) network operated by the City of Grand Prairie with the HRAP pixels overlaid.

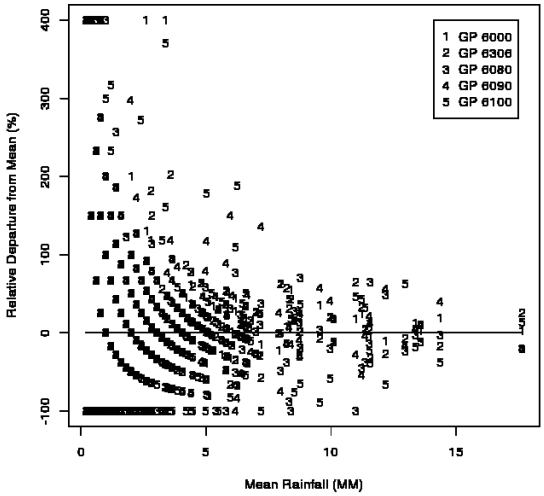

Figure 4-3 Relative departure of the 15-min precipitation at the five rain gauges of 6000, 6080, 6090, 6100 and 6300 from their spatial mean for the period of record.

Due to the relatively short common period of record, it was not possible to perform fusion of all three radar-based QPEs using the four procedures described above. Instead, we carried out fusion of two pairs of QPEs as follows: 1) fuse MPE and Q2 using DE, BC, RBC and SE for comparatively evaluation of the four procedures (Experiment 1), and 2) fuse MPE and CASA using SE for additional evaluation of SE (Experiment 2). The common periods of record for Experiments 1 and 2 are 23 and 18 months, respectively. While this study is limited to fusing two QPEs only, the procedures can be extended to a larger number of QPEs without loss of generality. For SE, the extension is particularly simple as it requires statistical parameters only at the aggregate scale. Figure 4-1 illustrates the data flow and processing for Experiment 1. Note that the source of 1-hr 4-km radar QPE can be the NEXRAD Precipitation Processing Subsystem (PPS, Fulton et al.1998) or the NMQ/Q2. According to WGRFC (Greg Story, personnel communication), Q2 was used for 1-hr 4-km radar-only QPE in their application of MPE, rather than the Digital Precipitation Array (DPA, Klazura and Imy 1993) from PPS. It means that the radar-only QPE from Q2 is already very well represented in the MPE product; both PPS and Q2 use the NEXRAD Level II data as the basis for their radar-only QPE algorithms to begin with. The impact of the duplicate use of the information in the radar-only QPE from Q2 in fusing the Q2 and MPE products as carried out in this work, however, is difficult to assess without the availability of the MPE products based on the PPS-generated radar-only QPE.

4.5. Estimation of statistical parameters

As shown above, DE, BC and RBC require the (nxn) observation error covariance matrix, $Cov[V,V^T]$, and, if the conditional bias-penalized formulation is used, the (mxm) covariance matrix of true precipitation at the target space-time scale, $Cov[X,X^T]$, and the cross-covariance matrix of true precipitation and the (mxn) observations, $Cov[X,Z^T]$. For DE, we have n=65 and

m=64. For BC and RBC, m denotes the number of positive Q2 estimates in the sampling volume of the MPE estimate and n is given by m+1. For SE, the dimensionality of the above statistics is drastically reduced to n=2 and m=1. In addition, in SE, owing to the fact that the higher-resolution observations are aggregated to the lower resolution, estimation of $\mathrm{Cov}[V,V^T]$ is not subject to scale-dependent biases due to possible representativeness errors. Note that, in practice, representativeness error is difficult to model without an extremely dense rain gauge network. In this section, we describe how the above statistics are estimated for DE in Experiment 1. Estimation of the statistics necessary for the other procedures and experiment is analogous and hence is not described.

DE requires estimation of $Var[v_M]$, $Cov[v_{Q_{i,j,k}}, v_{Q_{I,J,K}}]$, $i,j,k,I,J,K = 1,..,4$, and $Cov[v_{Q_{i,j,k}}, v_M]$, $i,j,k = 1,..,4$ (see Eqs.(4-9) through (4-11)). To estimate the statistics, we assumed that hourly point precipitation is statistically representative of the mean areal precipitation over a 4x4 km^2 area, and that 15-min point precipitation is representative of 15-min mean areal precipitation over a 1x1 km^2 area. This approximation is likely to overestimate the observation error variances in Q2 and MPE estimates by not discounting the representativeness errors, and hence may bias the error covariance estimates somewhat (see Eqs.(4-6) and (4-12), and Appendix E of Seo and Breidenbach 2002). Its impact on fusion, however, is likely to be minimal because the error variance terms cancel out (see Eqs.(4-7) and (4-13)).

To estimate the observation error covariance and to specify $\mathrm{Cov}[X,X^T]$ and $\mathrm{Cov}[X,Z^T]$, it is necessary to estimate the space-time covariance of 15-min precipitation. In this work, rather than modeling the space-time covariance explicitly (see, e.g., Cressie and Huang 1999, Gneiting 2002), they are specified by estimating the spatial correlograms of 15-min rain gauge precipitation over the study area at time lags of 0, 15, 30 and 45 min. Once the lagged correlograms were estimated, they were fitted with the exponential, Gaussian, spherical and linear models (Journel

and Huijbregts 1978), from which the best-fitting model is selected for use. Figure 4-4a shows the lagged (0, 15, 30 and 45 min) spatial correlograms of the observation errors in Q2 QPE. Figure 4-4b shows the lagged spatial correlograms of the gauge precipitation used for modeling $\mathrm{Cov}[X,X^T]$. Figure 4-4c shows the lagged cross correlograms between the gauge precipitation and the Q2 estimates used for modeling $\mathrm{Cov}[X,Z_Q]$. Also shown in the figures are the fitted correlation functions. Note that Figure 4-4b and Figure 4-4c are necessary only if the conditional bias-penalized formulation is used. It is apparent that, due to the sparsity of the rain gauges, the correlation functions can only be modeled with significant uncertainty. Note in Figure 4-4a that the correlations at lags 1 through 4 are higher than that at lag 0 at separation distances exceeding about 2.3 km, which probably reflects the effect of advection in spatiotemporal correlation structure (Seo et al. 2000). In Figure 4-4b, the high lag-0 correlation at the origin and rather large nugget effects for lag-1 (i.e. 15 min) through -3 (i.e. 45 min) correlations suggest that, not surprisingly, the Q2 estimate at the support (i.e. the space-time scale of estimation) of the estimate will have a large influence on the estimate.

Figure 4-5 shows the eigenvalue spectra (expressed as cumulative eigenvalues) of the inverse of the modified error covariance matrix, Λ^{-1}, in DE for hypothetical choices of α=0, 1 and 10. If α=0, Λ is reduced to the error covariance matrix, R (see Eq.(4-15)). Note in Eq.(4-13) that Λ^{-1} scales and rotates the observation vector, Z. The resulting matrix, $\Lambda^{-1}Z$, is then scaled by the error covariance matrix via $[\hat{H}^T\Lambda^{-1}H]^{-1}\hat{H}^T\Lambda^{-1}Z$ to yield the estimates. Hence, the eigenvalue spectrum of Λ^{-1} may be seen as a measure of the degrees of freedom in the observation vector (Rodgers 2000, Zupanski et al. 2007a). If the cumulative spectrum rises slowly, it is an indication that each observation contributes significantly independent information. If the spectrum rises fast, it is an indication that many observations may be redundant, and that the only a small subset of the observations contributes to the information content of Z. Note in Figure 4-5 that, when α=0, most observations uniquely contribute information to the estimation process, but that, as α increases, an

increasingly smaller subset of the observations does. Figure 4-5 indicates that the conditional bias penalty term (i.e. when $\alpha > 0$) has a similar effect as regularization (Tarantola 2005) in that it reduces the effective dimensionality of the estimation problem.

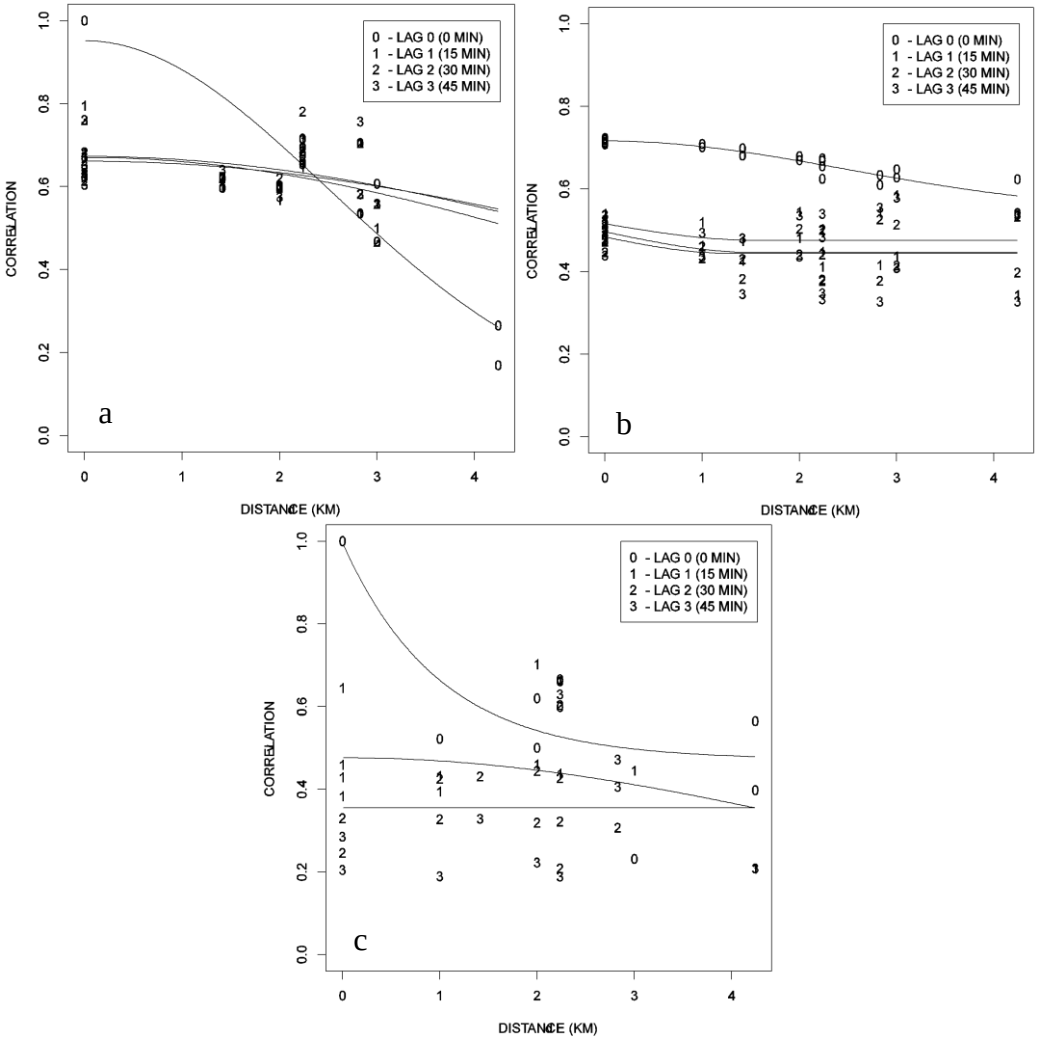

Figure 4-4 a) Lagged (0, 15, 30 and 45 min) spatial correlograms of the observation errors in Q2 QPE. B) Lagged spatial correlograms of the gauge precipitation. c) Lagged cross correlograms between the gauge precipitation and the Q2 estimates.

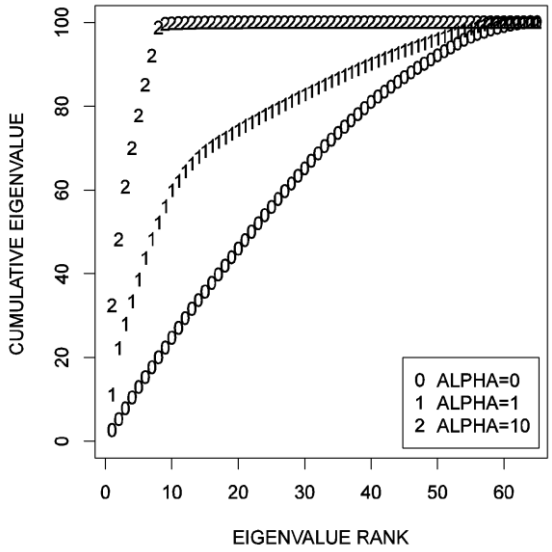

Figure 4-5 the eigenvalue spectra (expressed as cumulative eigenvalues) of the inverse of the modified error covariance matrix, Λ^{-1}, in DE for hypothetical choices of α=0, 1 and 10.

Figure 4-6 shows the weights given to the 64 15-min 1-km Q2 estimates and the 1-hr 4-km MPE estimate for estimation of the 32nd of the 64 state variables as calculated by Eq.(4-13) in DE. Note that by far the largest weight is given to the Q2 estimate associated with the state variable at that 15-min 1-km sampling volume. The second largest weight is to the MPE estimate (i.e. the 65th observation), which decreases somewhat for $\alpha > 0$. For all other Q2 estimates at non-collocating sample volumes, on the other hand, a slight negative and almost uniform weight is given. The above weight pattern applies to all other state variables at other 15-min 1-km sampling volumes and is not shown. To determine the weighting factor, α, in the conditional bias-penalized formulation of the procedures, we carried out a series of sensitivity analysis. It was seen that small values of α improves estimation of large precipitation amounts but only marginally. This is because the Q2 estimates are biased significantly high both unconditionally and conditionally over the study area. As such, we set α to zero for all results presented below. If the ingredient QPE is

conditionally biased low for large precipitation amounts, however, it will be necessary to choose a positive α that reduces CB without deteriorating performance for light to moderate precipitation excessively (Seo et al. 2014).

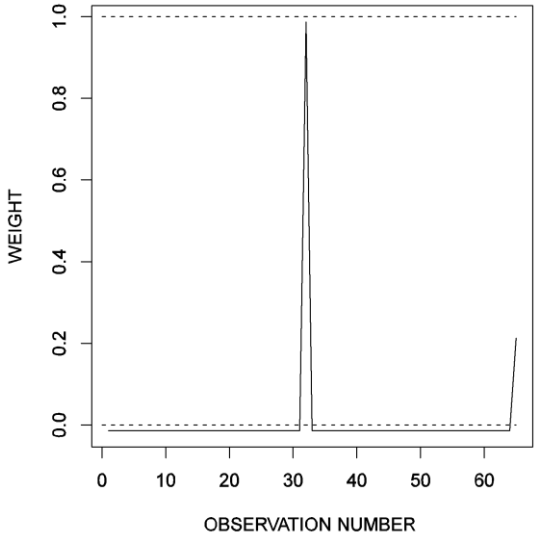

Figure 4-6 Weights given to the 64 15-min 1-km Q2 estimates and the 1-hr 4-km MPE estimate for estimation of the 32nd of the 64 state variables

4.6. Evaluation

To evaluate the fusion procedures, two experiments were carried out. In Experiment 1, we fused the 1-hr 4x4 km^2 MPE and 15-min 1x1 km^2 Q2 estimates at 15-min 1x1 km^2 scale using the four procedures described above. In Experiment 2, we fused the 1-hr 4x4 km^2 MPE and 15-min 500x500 m^2 CASA estimates at the 15-min 500x500 m^2 scale using SE only. For both experiments, the results were verified using the 15-min rain gauge observations from the High Water Warning Systems in the City of Grand Prairie (see Figure 4-1). The choices for the pairwise fusion of QPE products were made based on the data availability; the period of record common to all three products is too short to evaluate three-way fusion. For evaluation of pairwise fusion, there

exist two basic criteria that the fused QPE must pass for the procedure to be considered viable. The first is that the fused QPE at 15-min 1-km scale must be more accurate than the better of the 15-min 1-km Q2 estimates and the MPE estimates trivially downscaled based on the spatiotemporal distribution of Q2 QPE. The second is that the fused QPE at 1-hr 4-km scale must be more accurate than the MPE estimate at 1-hr 4-km scale or the Q2 estimates aggregated to 1-hr 4-km scale. If the fused QPE meet both criteria, it may be considered an improved over the ingredient QPEs regardless of the spatiotemporal scale of aggregation. Initially, the evaluation was carried out via leave-one-day-out cross validation. Comparison with dependent validation showed, however, that there is little difference between the two and dependent validation was used in the evaluation described below.

The four procedures considered in this work assume that the ingredient QPEs are bias-free. In reality, however, such an assumption may not be met even for the MPE product, which undergoes rain gauge data-based bias correction (Seo et al. 1999, Seo and Breidenbach 2002), radar-gauge merging (Seo 1999) and quality control by human forecasters. To test robustness of the procedures under realistic conditions, we carried out evaluation using the ingredient QPE products without any correction and with post hoc bias correction by applying a single multiplicative adjustment factor to each QPE product that removes the mean bias. The adjustment factor was calculated as the ratio of the verifying total rain gauge precipitation to the total precipitation estimated by the QPE. For Experiment 1, the adjustment factors for Q2 and MPE products were 0.779 (i.e. 22.1% overestimation) and 0.977 (i.e. 0.3% overestimation), respectively. For Experiment 2, the adjustment factors were 1.063(i.e. 6% underestimation) and 1.044 (4% underestimation) for the CASA and MPE products, respectively. Below, the fusion results with bias-corrected ingredient QPEs are referred to as the bias-corrected cases.

4.7. Results

Figs 4-7a through 4-7d show the percent reduction in root mean square error (RMSE) in estimation of 15-min point precipitation by the four procedures, DE, BC, RBC and SE, over the Q2 estimates (in white) and over the MPE estimates disaggregated to the 15-min 1-km scale using the Q2 estimates (in gray). The disaggregation is based on the following trivial multiplicative correction to the MPE estimate:

$$Z^{*}_{MPE_{i,j,k}} = \frac{Z_{Q_{i,j,k}}}{Z^{U}_{Q}} Z_{MPE},\ Z^{U}_{Q} > 0,\quad i,j,k = 1,..,4 \tag{4-25}$$

In the above, Z_{MPE} denotes the 1-hr 4-km MPE estimate and $Z^{*}_{MPE_{i,j,k}}$ denotes the trivially disaggregated MPE estimate to 15-min 1-km scale at the ij-th pixel and k-th subperiod. For 15-min precipitation exceeding 8.5 mm, all 4 procedures show positive reduction in RMSE over Q2 and trivially disaggregated MPE; the largest reduction is by SE at about 7% over both Q2 and trivially disaggregated MPE without bias correction. For all amounts of precipitation, however, only SE reduces RMSE over trivially disaggregated MPE even though all four procedures improve over Q2 with or without bias correction of the Q2 and MPE products. Fig 4-7e through 4-7h show the percent reduction in RMSE of hourly precipitation estimates by the four procedures over the Q2 estimates aggregated to 1-hr and 4-km scale (in white) and the MPE estimate (in gray). If fusion improves over Q2 and MPE at the 1-hr 4-km scale, we should see positive reduction in RMSE over both aggregated Q2 and MPE. The figures show that all procedures improve over aggregated Q2, but not over MPE. For hourly precipitation exceeding 16.9 mm, all four procedures improve over both aggregated Q2 and MPE, except for RBC which does not improve over MPE. The largest improvement over MPE is by BC which reduced RMSE by over 12%. For all amounts of hourly precipitation, RBC does not improve over MPE whether bias correction is made to Q2 and MPE or not, and BC does not improve over MPE without bias

correction. Both DE and SE improve over aggregated Q2 and MPE for all cases considered. The margin of improvement is slightly larger for SE. The above results indicate that only SE improves over Q2, MPE, trivially disaggregated MPE and aggregated Q2. RBC is clearly the worst performing procedure among the four considered. The significantly better performance by BC over RBC is a reflection of the fact that biases in the Q2 estimates depend on the magnitude of precipitation (not shown). The performance of DE is generally comparable to that of BC. Computationally, however, DE is much more economical than BC as the former requires calculation of the weights only once whereas BC requires calculation of weights for every MPE estimate. On the other hand, DE can produce negative estimates over areas of light to moderate precipitation, which must be corrected with potentially little control over the unbiasedness of the resulting estimates (see Seo et al.2014 for strategy for unbiasedness).

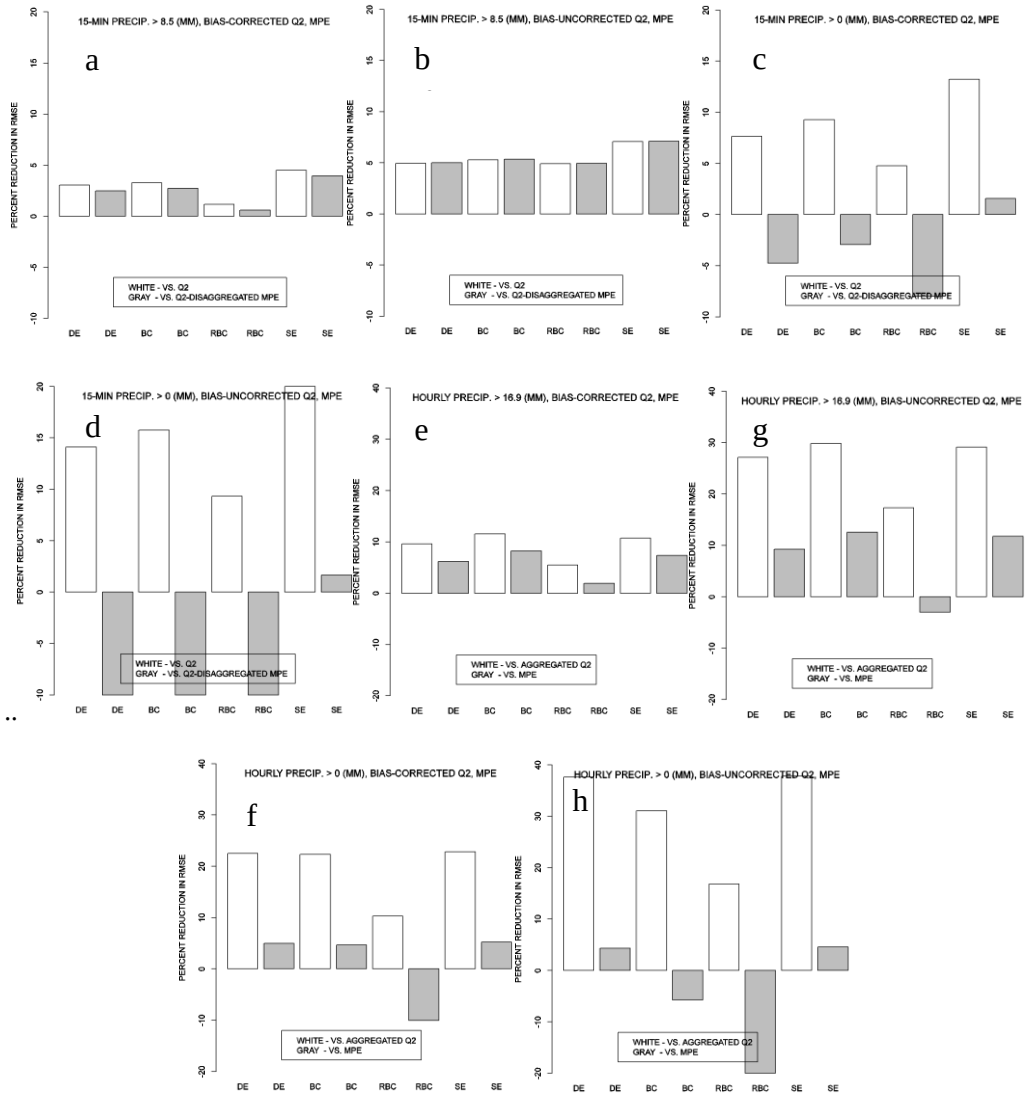

Figure 4-7 a) through d) show the percent reduction in root mean square error (RMSE) in estimation of 15-min point precipitation by the four procedures, DE, BC, RBC and SE, over the Q2 estimates (in white) and over the MPE estimates disaggregated to the 15-min 1-km scale using the Q2 estimates (in gray). E) through h) show the percent reduction in RMSE of hourly precipitation estimates by the four procedures over the Q2 estimates aggregated to 1-hr and 4-km scale (in white) and the MPE estimate (in gray).

Figure 4-8 shows example scatter and quantile-quantile plots of the SE-fused 15-min 1-km precipitation vs. the verifying observation. For comparison, those of the 15-min 1-km Q2 precipitation are also shown side by side. Figure 4-9 shows example scatter and quantile-quantile plots of 1-hr 4-km precipitation estimates by aggregated Q2 (top), MPE (middle) and fusion (bottom) vs. the verifying 1-hr point precipitation. Both the Q2 and MPE estimates used for Figure 4-8 and Figure 4-9 are without the post hoc bias correction described above. The figures hence represent a tough test for the fusion procedure in that the assumption of no bias in the ingredient QPEs is already violated. The high bias in the Q2 estimates is readily apparent in both figures. The reduced bias and scatter in the fused estimates may also be seen readily. For hourly precipitation, the MPE estimates are already of high quality. One may nevertheless see a tightened scatter of the fused estimates vs. the verifying observations. Figs 4-10a through 4-10d show the precipitation accumulation maps by Q2, MPE, DE and SE, respectively, for a 8-hr event in May 08, 2014, over DFW. The map background in the figures shows, from left to right, the Cities of Fort Worth, Arlington, Grand Prairie and Dallas (partial). The overestimation by Q2 is readily seen in Figure 4-10a. While the precipitation maps by DE and SE are generally similar, they do show certain contrasts; whereas SE shows more realistic structure around the large heavy precipitation core than DE, in the lower-left part of the domain, SE shows noisier precipitation patterns than DE.

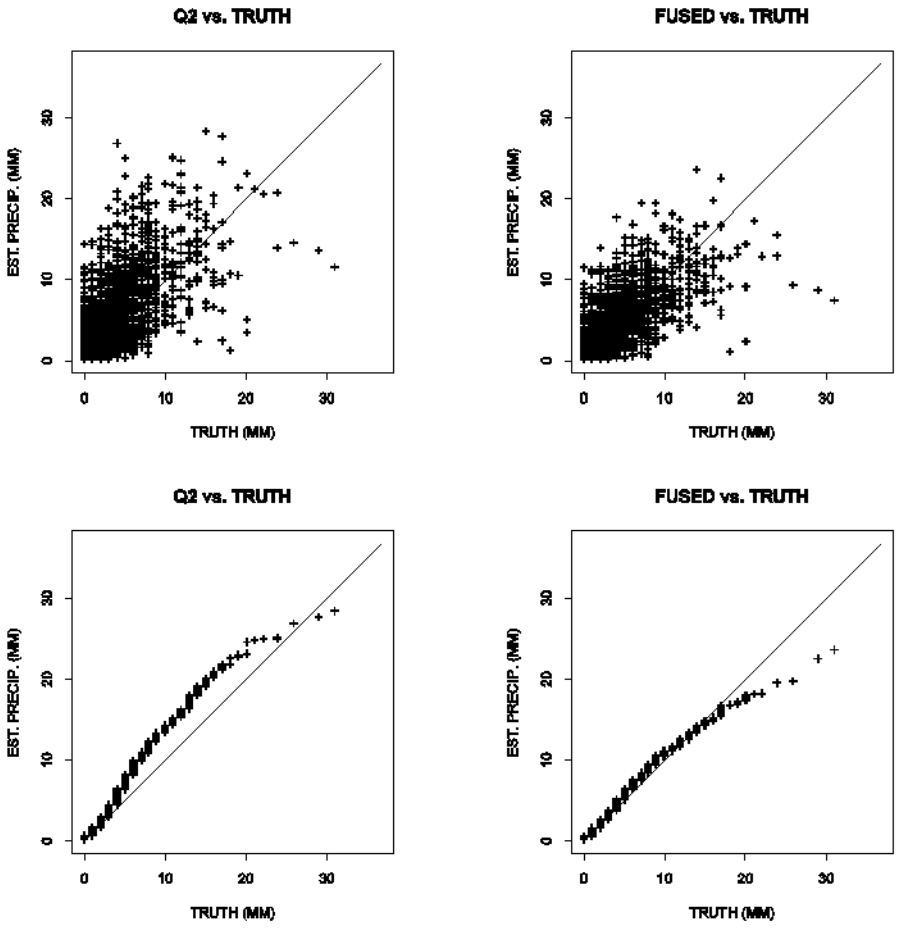

Figure 4-8 Scatter and quantile-quantile plots of the SE-fused 15-min 1-km precipitation vs. the verifying observation.

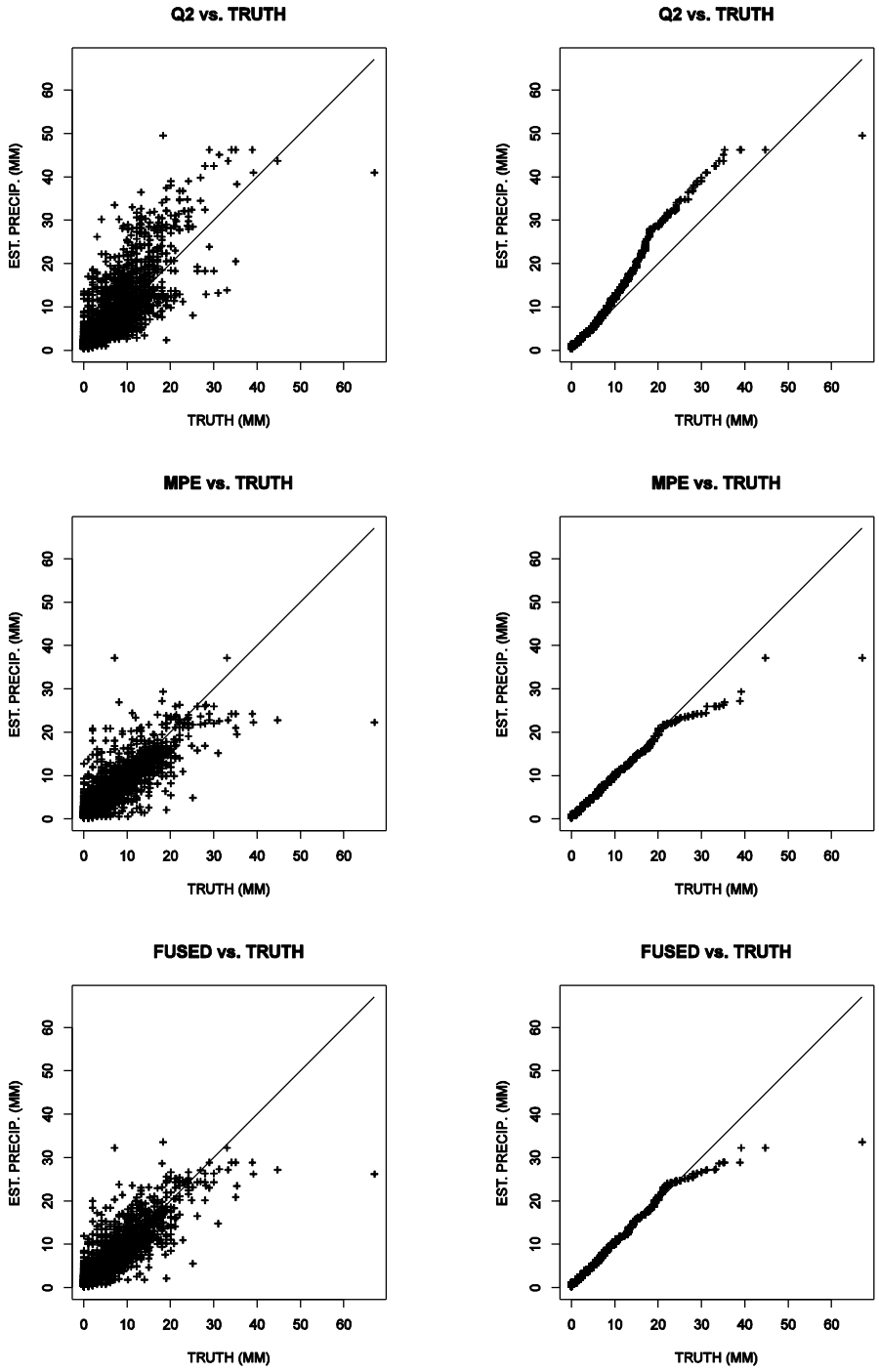

Figure 4-9 Scatter and quantile-quantile plots of 1-hr 4-km precipitation estimates by aggregated Q2 (top), MPE (middle) and fusion (bottom) vs. the verifying 1-hr point precipitation.

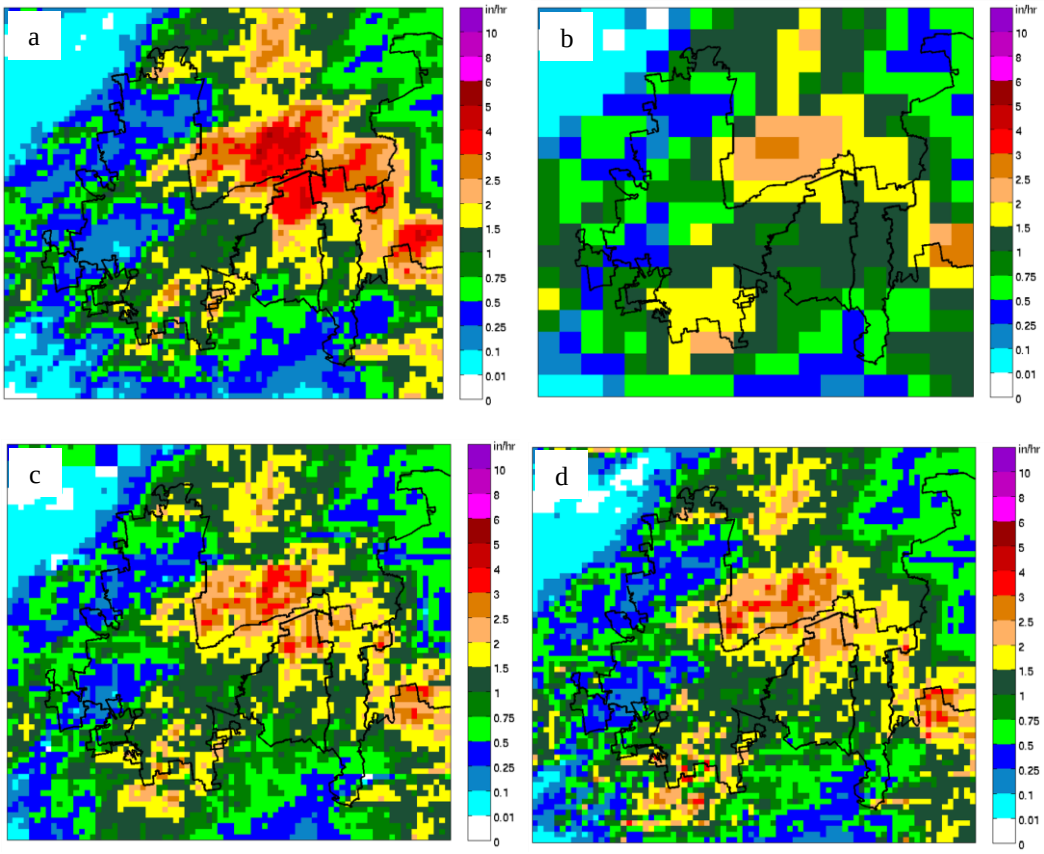

Figure 4-10 The precipitation accumulation maps by Q2, MPE, DE and SE, respectively, for a 8-hr event in May 08, 2014, over DFW.

Lastly, Figure 4-11 shows the scatter and quantile-quantile plots of the 15-min CASA (left) and SE-fused (right) precipitation vs. the verifying 15-min point precipitation. SE was used to fuse the 15-min 500-m CASA QPE (temporally aggregated from 1-min QPE) and the 60-min 4-km MPE estimates without bias correction. The trivially disaggregated result is very close to the SE result and hence is not shown. It may be observed that, while SE reduced conditional bias, it also increased the scatter somewhat for larger precipitation amounts. For Figure 4-11, SE reduced RMSE by about 9% over the CASA QPE for estimation of precipitation at 15-min 500-m scale. At the hourly scale, however, SE provided little reduction in RMSE over the MPE estimates. While it

is difficult to draw firm conclusions from Experiment 2 due to relatively small sample size, the results from the two experiments indicate that SE improves QPE under varying conditions of biasedness in the ingredient QPEs, under varying ranges of precipitation amount being estimated, and under different combinations of ingredient QPEs.

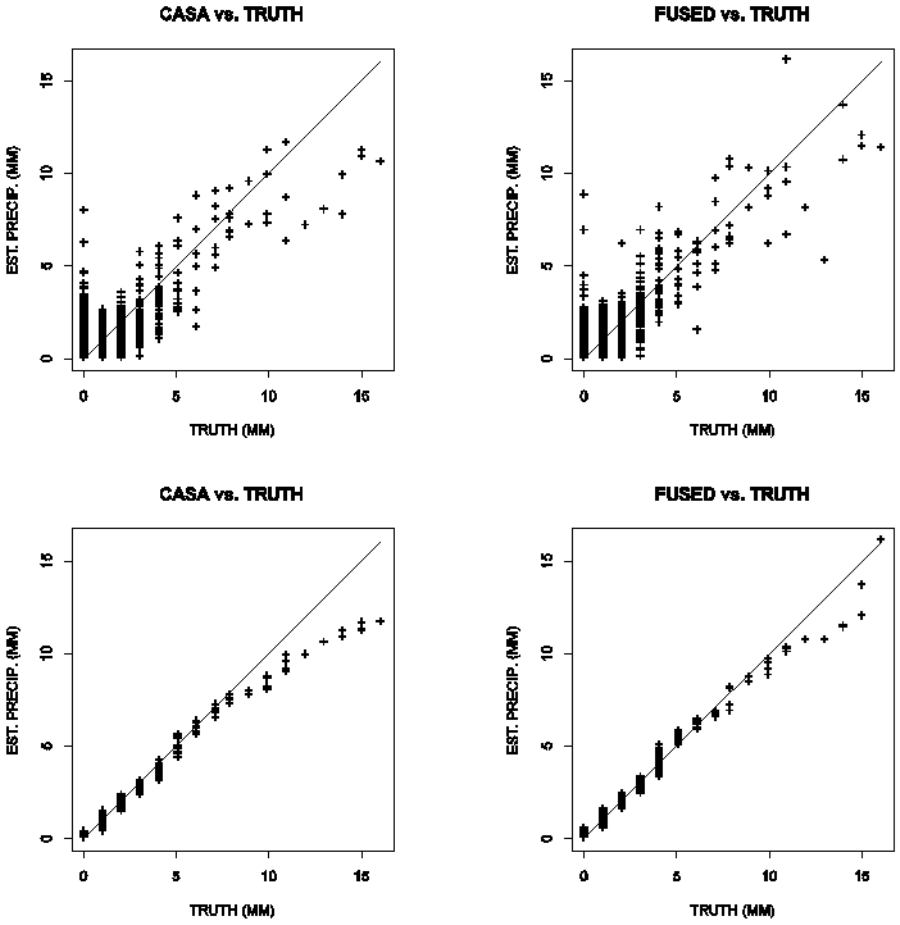

Figure 4-11 Scatter and quantile-quantile plots of the 15-min CASA (left) and SE-fused (right) precipitation vs. the verifying 15-min point precipitation.

4.8. Conclusion

For monitoring and prediction of water-related hazards such as flash flooding, high-resolution hydrologic and hydraulic modeling is necessary. Due to large sensitivity to errors in quantitative precipitation estimates (QPE), it is very important in high-resolution hydrologic modeling that the accuracy of high-resolution QPE be improved to the greatest possible extent. With the availability of multiple radar-based precipitation products in many areas, one may now consider fusing multiple radar-based QPEs to produce more accurate high-resolution QPE for various applications. In this work, we comparatively evaluate four procedures for such fusion based on Fisher estimation and its conditional bias-penalized variant: Direction Estimation (DE), Bias Correction (BC), Reduced-Dimension Bias Correction (RBC) and Simple Estimation (SE). They are applied to fuse the MPE and radar-only Q2 products at the 15-min 1-km resolution (Experiment 1), and the MPE and CASA product at the 15-min 500-m resolution (Experiment 2). The resulting fused estimates are evaluated using the 15-min rain gauge observations in the City of Grand Prairie in the Dallas-Fort Worth Metroplex (DFW) area. The main evaluation criterion was that the fused QPE improves over the ingredient QPEs at their native spatial resolutions, and that, at the high resolution, the fused QPE improves not only the high-resolution ingredient QPE but also the high-resolution QPE obtained by trivially disaggregating the low-resolution QPE with the high-resolution QPE. All four procedures assumed that the ingredient QPEs are unbiased which, in reality, is not very likely even if real-time bias correction was already applied. To test robustness, the evaluation procedures were evaluated with and without post-hoc bias correction of the ingredient QPEs.

The results show that only SE passes the above evaluation criterion consistently. The performance of DE and BC are generally comparable. Between the two, while DE is more attractive for computational economy, BC is more attractive for guaranteed nonnegativity of the

fused estimates. The performance of RBC is very poor as it does not account for the fact that biases in the QPE products depend on the magnitude of precipitation. SE assumes that the high-resolution QPE product is skillful in capturing spatiotemporal variability of precipitation at its native scale, and that the low-resolution QPE product provides skill at its native resolution. While the above assumptions may not always be met, its simplicity and the robustness observed in this work make a strong case for operational implementation of SE as a post-processor to the QPE product generation process. Also, unless other procedures considered in this work, it is possible to update the statistical parameters necessary for SE on line similarly to the real-time bias correction currently used in MPE.

As demonstrated in this work, the potency of a fusion procedure depends on the spatiotemporal variability of precipitation and the scale-dependent skill of the ingredient QPEs in capturing it. As such, it is unlikely that a single procedure would work well both in terms of effectiveness and computational economy under a wide range of conditions. We welcome any suggestions the readers may have on an experiment in which other techniques may be objectively inter-compared to advance understanding as well as practical solutions.

Chapter 5

Evaluation of the NWS distributed hydrologic model over the Trinity River Basin in Texas

Distributed hydrologic models are a promising tool for producing streamflow and other hydrologic information at high spatial resolution. Research Distributed Hydrologic Model (RDHM) developed by the National Weather Service (NWS) Hydrology Laboratory (HL) is being used to model sub-basins within the Trinity River Basin that extends from North Texas to the upper Texas Gulf Coast for a 16 year period from 1996 to 2011. The purpose is to evaluate simulation of streamflow at hourly time steps on a 4x4 km^2 grid scale to explore possible hydrologic and water resources applications. HL-RDHM uses the heat transfer version of the Sacramento soil moisture accounting model (SAC-HT) to simulate rainfall-runoff and the kinematic-wave hillslope and channel routing models for routing streamflow. For this project, the SAC-HT model was forced using hourly Multi-sensor Precipitation Estimator (MPE) produced by the NWS West Gulf River Forecast Center (WGRFC). Modeling results were evaluated using observed hourly streamflow data from 10 unregulated locations within the basin. Here, we examine how uncalibrated operational distributed models may compare with finely-tuned lumped models. The results show that uncalibrated HL-RDHM produces reasonably skillful simulations of outlet flow for the majority of the 10 headwater basins. For a half of the basins, however, bias in HL-RDHM simulation exceeds 20 percent. The findings in this work point to limited calibration to reduce systematic biases in runoff and optimization of selective routing parameters to reduce timing errors.

5.1. Introduction

Distributed hydrologic models have much to offer for producing high-resolution hydrologic information. Such information can be used for a spectrum of applications ranging from flash flood forecasting to water resources management. For that, it is necessary to take full advantage of high-resolution precipitation data. In the early 2000's, the Distributed Model Intercomparison Project (DMIP) was initiated by the National Weather Service (NWS) to evaluate the capabilities of distributed hydrologic models. One of the main findings from DMIP1 was that calibrated distributed hydrologic models can simulate streamflow at the basin outlet as well as calibrated lumped models (Reed et al., 2004). The recently-completed DMIP2 concluded that distributed models calibrated using basin outlet hydrographs do a reasonable job at partitioning precipitation into runoff and infiltration (Smith et al., 2012). DMIP2 also indicated that the distributed models are able to produce good streamflow simulations at interior points and simulate soil moisture reasonably well (Smith et al., 2012). These findings reinforce the generally-accepted view that distributed models can account for the spatial variability of basin physiography and precipitation. For distributed modeling, the ability to produce reasonable simulations at interior points and to provide gridded maps, e.g., of soil moisture, rather than necessarily to outperform lumped models, is of primary interest. As such, Smith et al. (2012) suggest that, while transitioning to distributed models, operational agencies maintain their current lumped models to allows decision making based on both results.

Since calibration of distributed models can be very labor-intensive and time consuming, we are interested in this work in assessing how uncalibrated operational distributed models may compare with finely-tuned operational lumped models for streamflow simulation. The distributed hydrologic model used in this work is the Hydrology Laboratory-Research Distributed Hydrologic Model (HL-RDHM) developed by the NWS Hydrology Laboratory (HL) which was first called

the Hydrology Laboratory-Research Modeling System (HL-RMS) (Koren et al., 2004). Koren et al. (2004) showed that HL-RDHM results are comparable to well-calibrated lumped model simulations in several headwater basins, and that they outperform lumped model simulations where spatial rainfall variability is significant.

HL-RDHM has been used in a wide range of applications. Reed et al. (2007) applied the threshold frequency (TF) component of HL-RDHM for flash flood forecasting. Yilmaz et al. (2008) evaluated HL-RDHM using multiple hydrologically relevant ‘‘signature measures’’ to quantify the performance of the model at the watershed outlet. Mejia and Reed (2010) used HL-RDHM to evaluate parameterization of channel cross sections. Lee et al. (2011) used data assimilation (DA) to improve the accuracy of streamflow prediction by assimilating in-situ soil moisture data into HL-RDHM. Fares et al. (2014) also applied HL-RDHM in a flashy tropical watershed in Hanalei Bay. The operational version of HL-RDHM, or the Distributed Hydrologic Model (DHM), is used at various River Forecast Centers (RFC) for flash flood and river flood forecasting.

The objective of this work is to evaluate HL-RDHM simulation of streamflow and soil moisture toward producing accurate and dynamically consistent water and energy balance components in the hydrologic cycle on a fine grid. Specifically, we assess how uncalibrated HL-RDHM may compare with the finely-tuned lumped models consisting of the Sacramento soil moisture accounting (SAC-SMA, Burnash et al., 1973) and unit hydrograph (Chow et al., 1988) models for the headwater basins of the Trinity River within the service area of the WGRFC. The chapter is organized as follows: Section 5.2 describes the models used. Section 5.3 describes the study basins, data used and design of experiments. We discuss the results in Section 5.4. Section 5.5 provides conclusion and discussion.

5.2. Model description

5.2.1. Distributed model

The distributed model used is HL-RDHM. The rainfall runoff component used here is the Sacramento soil moisture accounting (SAC-SMA) with the heat transfer component (SAC-HT) and the routing technique is kinematic-wave routing. SAC-SMA was first introduced by Burnash et al. (1973) (see Figure 5-1) and is been used widely in hydrologic applications.

SAC-SMA is a conceptual model of the land phase and hydrologic cycle. It accounts for percolation, soil moisture storage, drainage and evaporation processes in order to build a rational model. The model inputs are rainfall, evaporation and snow cover (optional) and the output is the inflow to channel system. Model assumes two conceptual soil layer called upper and lower zone. Upper zone has two kind of soil moisture storage, upper zone tension water which represents the amount of water stored in the soil which is closely bound to the soil particles and upper zone free water which can be percolate to the deeper layer or move laterally. Lower zone also has tension and free water content. The lower zone free water content is divided into supplemental and primary groundwater flows which control the fast and slow flows respectively. The relationship between these water contents and the surface/subsurface water is shown in Figure 5-1.

Recently, the SAC-SMA was improved by incorporating a heat transfer component (SAC-HT). A physically-based algorithm has been added to model the impacts of frozen soil on the precipitation-runoff process. The heat transfer component allows translation of water depths in SAC-SMA conceptual storages to water content in physical soil layers which are important estimates in agriculture and water resources management (Koren et al., 2007).

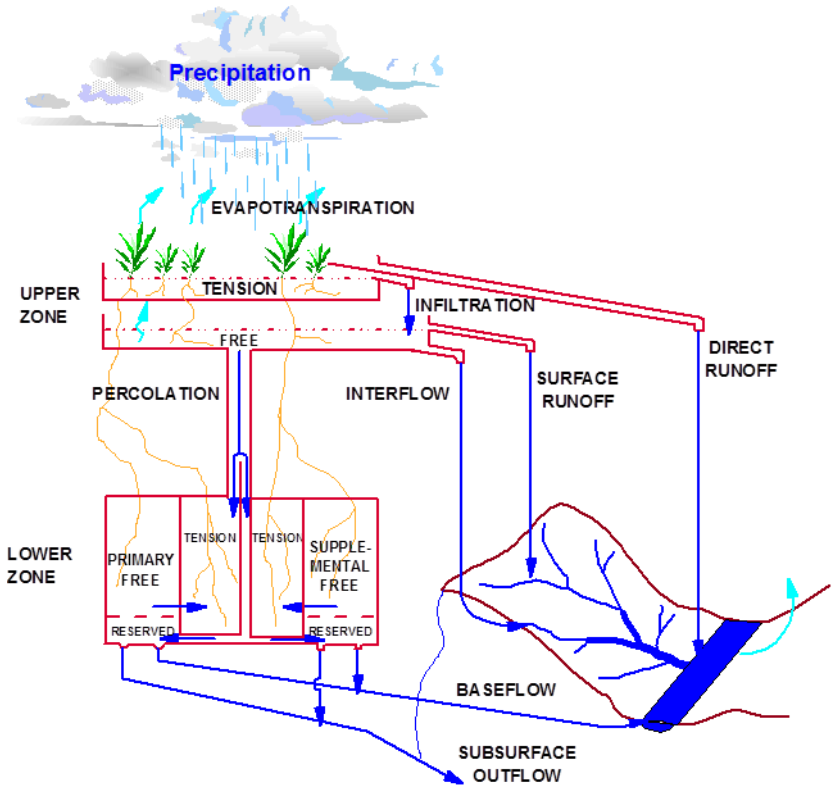

Figure 5-1 Schematic of SAC-SMA model

The basic SAC-SMA has 16 parameters which play an important role in modeling and the most important ones are given in Table 5-1. Having priori information about these parameters would improve the quality of the simulation and reduce the amount of required calibration particularly in distributed modeling which is very expensive.

Koren et al. (2000, 2003) related the SAC-SMA parameters with the soil properties such as porosity, field capacity and wilting point and derived a priori for some of the SAC-SMA parameters. The State Soil Geographic Database (STATSGO) soil texture data in 11 soil layers was used for SAC-SMA parameter estimation. Anderson et al. (2006) and Zhang et al. (2006) improved the quality of the a priori parameters and substitute the STATSGO data with the finer-scale database of soil data, the Soil Survey Geographic Database (SSURGO). A priori upper zone

tension water maximum storage (UZTWM), the upper zone free water maximum storage (UZFWM), the lower zone supplemental free water maximum storage (LZFSM), and the lower zone primary free water maximum storage (LZFPM) are illustrated in Figure 5-2 as a few samples.

Table 5-1 SAC-SMA parameters, the units, description and the allowable range

NO	Parameters	Units	Description	Allowable range	A-priori Grid Provided
1	UZTWM	mm	Upper Zone Tension Water Maximum storage	25-125	Y
2	UZFWM	mm	Upper Zone Free Water Maximum storage	10-75	Y
3	LZTWM	mm	Lower Zone Tension Water Maximum storage	75-300	Y
4	LZFSM	mm	Lower Zone Free water Supplementary Maximum storage	15-300	Y
5	LZFPM	mm	Lower Zone Free water Primary Maximum storage	40-600	Y
6	UZK	day^{-1}	Upper zone free water withdrawal rate		Y
7	LZSK	day^{-1}	Lower Zone Supplementary withdrawal rate	0.03-0.2	Y
8	LZPK	day^{-1}	Lower Zone Primary withdrawal rate	0.001-0.015	Y
9	PCTIM	%/100	% permanent impervious area	0.0-0.05	Y
10	ADIMP	%/100	% area contributing as impervious when saturated	0.0-0.2	N
11	RIVA	%/100	% area affected by riparian vegetarian, streams and lakes	0.0-0.2	N
12	ZPERC	none	Maximum percolation rate under dry condition	20-300	Y
13	REXP	none	Percolation equation exponent	1.4-3.5	Y
14	PFREE	%/100	%of percent going directly to lower zone free water	0-0.5	Y

Hillslope and channel routing in HL-RDHM is performed using kinematic-wave routing. Within each cell, fast (surface) runoff is first routed over conceptual hillslope, and then the combination of channel inflow from hillslope routing, slow runoff (subsurface/ground) and inflow from upstream cells is routed via channel routing (Koren et al., 2004) for each pixel. The a priori

parameters for routing are derived from DEM, channel top width, channel cross section and flow data (Reed et al., 2002). The a priori specific discharge is shown in Figure 5-3.

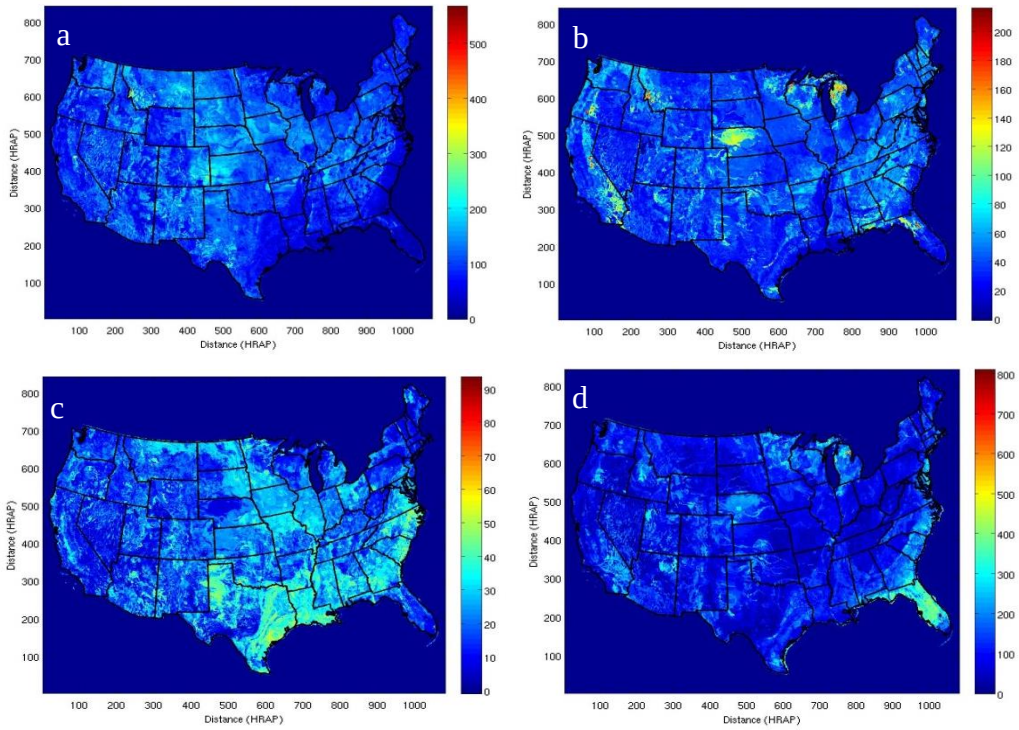

Figure 5-2 A priori parameter example obtained from NWS for a) UZTWM, b) UZFWM, c) LZFSM, and d) LZFPM.

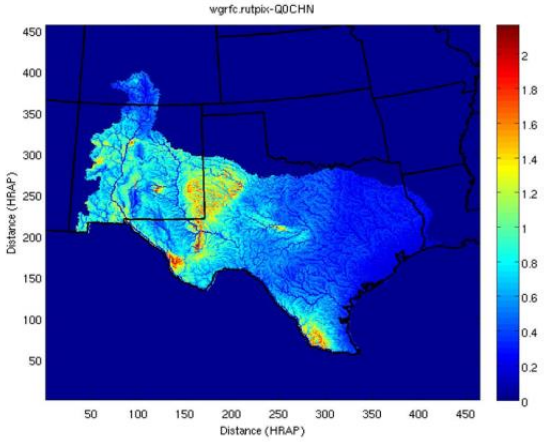

Figure 5-3 A priori specific discharge

5.2.2. Lumped model

The lumped model used is SAC-UHG, consisting of SAC-SMA as its rainfall-runoff component and unit hydrograph for routing. Operational SAC-UHG parameters, which are valid for a 6-hr time step, are obtained from WGRFC. To obtain 1-hr parameters, we used AB_OPT (Seo et al., 2009) to 1) estimate the adjustment factors to precipitation and potential evaporation (PE), PXADJ and PEADJ, respectively, 2) derive 1-hr empirical UHG and 3) obtain 1-hr SAC parameters by adjusting the 6-hr SAC parameters. In the above, the first two steps are based on adjoint-based optimization whereas the third is based on stepwise line search (SLS, Kuzmin et al., 2008).

A very important difference between SAC-UHG and HL-RDHM simulations used in this work is that the former represents dependent validation as they result from calibration whereas the latter represents independent validation. As such, the SAC-UHG results set a very high bar for the HL-RDHM results. One may not expect HL-RDHM to outperform lumped SAC-UH model as it is finely tuned and calibrated.

5.2.3. Model performance measures

To assess the performance of the simulated streamflow, we used the four common statistical measures widely used in hydrologic applications, including multiplicative percent bias (% Bias), root mean square error (RMSE), Pearson's correlation coefficient (R), and Nash-Sutcliff efficiency measure. Multiplicative percent bias measures the average tendency of the simulated streamflow to be larger or smaller than the observed streamflow. The optimal value of % Bias is 1.0. Values greater than 1 indicates an overall oversimulation of streamflow and values less than 1 indicates an overall undersimulation of streamflow. % Bias could be used to infer the mass balance problem for the simulation, i.e. for basins with high % Bias mostly mass balance does not hold.

$$\% \text{ Bias} = \frac{\sum_{i=1}^{n} Q_{Sim,i}}{\sum_{i=1}^{n} Q_{Obs,i}} \times 100 \quad (5\text{-}1)$$

where $Q_{Sim,i}$ and $Q_{Obs,i}$ denote the hourly simulated and observed streamflow, respectively. n denotes the number of pairs of simulated and observed streamflow. Root mean square error represents the standard deviation of the model prediction error, on other words, the sample standard deviation of the differences between predicted and observed streamflow. A smaller RMSE values indicated a better model performance.

$$\text{RMSE} = \sqrt{\frac{\sum_{i=1}^{n}(Q_{Sim,i} - Q_{Obs,i})^2}{n-1}} \quad (5\text{-}2)$$

Correlation coefficient is a measure of linear correlation (dependence) between two variables. Correlation coefficient values of close to one indicate a positive linear correlation between simulated and observed streamflow which is desired.

$$R = \frac{\text{Cov}\,(Q_{Sim}, Q_{Obs})}{\sigma_{Q_{Sim}} \sigma_{Q_{Obs}}} \quad (5\text{-}3)$$

$\sigma_{Q_{Sim}}$ and $\sigma_{Q_{Obs}}$ denote the standard deviation of simulated and observed streamflow, respectively. Nash-Sutcliffe model efficiency coefficient is one of most widely used measures in hydrology to assess the predictive skill of a hydrological model using the following equation.

$$NSE = 1 - \frac{\sum_{i=1}^{n}(Q_{Sim,i} - Q_{Obs,i})^2}{\sum_{i=1}^{n}(Q_{Obs,i} - \overline{Q_{Obs,i}})^2} \quad (5\text{-}4)$$

where $\overline{Q_{Obs,i}}$ is the mean of the observed streamflow. Nash-Sutcliffe can range between negative infinity and 1. NSE equal to 1 represents a perfect simulation which requires a perfect hydrological model. NSE of zero indicates the simulated streamflow is as accurate as the mean of observed streamflow. Negative values indicate that the mean observed streamflow is better than model simulation, in other words, the residual variance is larger than the observed data variance. NSE values closer to 1 indicate a better model performance and are preferred.

5.3. Study area and data used

United States has 13 river forecast center. West Gulf River Forecast Center (WGRFC) is the one which encompass most of Texas. WGRFC has several forecast groups as shown in Figure 5-4. The Trinity River forecast group has an area of 40,380 km^2. Within the group, 10 headwater basins are selected based on the availability of streamflow data. Figure 5-4 shows the locations and names of the basins selected.

The forcing data used are the operationally-produced multisensor precipitation estimates (MPE) from 1996 to 2011 and monthly climatology of potential evaporation (PE). In SAC-UHG, the simulation period varies from basin to basin and generally covers 1996 to 2012. The a priori parameters for SAC-SMA are available for 11 of the 16 parameters (Koren, 2003). The a priori parameters for routing, i.e., hillslope slope and specific discharge, are obtained following Reed et al. (2002).

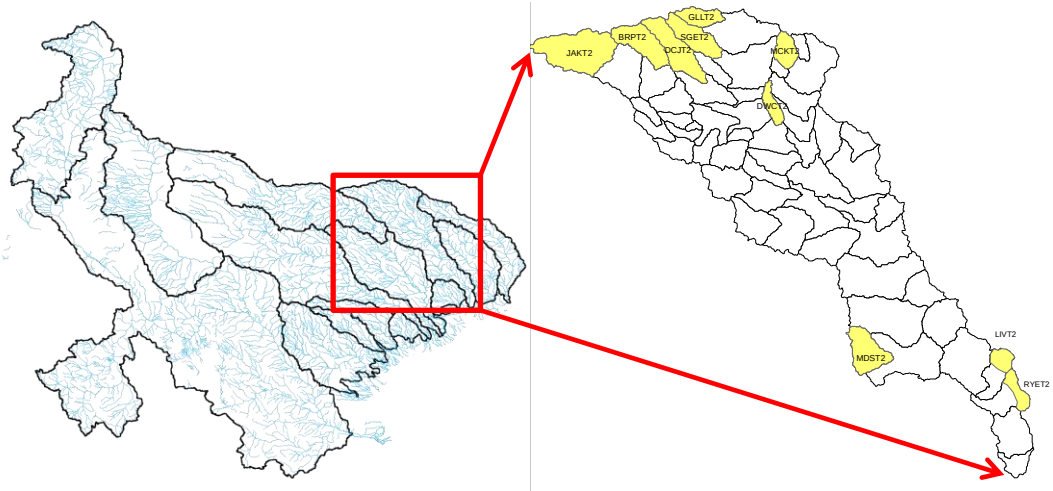

Figure 5-4 Left: WGRFC domain, Right: Trinity River Forecast Group

5.4. Results

As noted, HL-RDHM is uncalibrated while SAC-UHG is calibrated using the same streamflow data used in evaluation. As such, the SAC-UHG and HL-RDHM results represent dependent and independent validation, respectively. For comparison, the common periods between the SAC-UHG and HL-RDHM simulations are used.

Table 5-2 shows the area, time to peak and adjustment factors for precipitation (PXADJ) and potential evaporation (PEADJ) as obtained from AB_OPT. Adjustment factors deviating from unity indicates lack of mass balance such that AB_OPT had to multiplicatively increase (>1) or decrease (<1) the forcing data. Hence, for those basins for which PXADJ and/or PEADJ deviates significantly from unity (e.g. BRPT2), one may not expect HL-RDHM to simulate streamflow as well as SAC-UHG. In other words, in the lumped model, the adjustment factors for precipitation and potential evaporation are taken into account to minimize the effect of the input uncertainty; however, such measures are not considered for HL-RDHM.

Table 5-2 Area, time to peak, adjustment factors for precipitation and PE

Basin Name	**Area (km^2)**	**T_p (hrs)**	**PXADJ**	**PEADJ**
JAKT2	1768	32	1.10	1.19
BRPT2	862	19	0.69	1.14
DCJT2	1036	17	0.82	1.07
SGET2	764	7	0.63	1.16
GLLT2	443	5	0.64	1.13
DWCT2	316	4	1.07	0.95
MCKT2	425	14	1.02	0.95
MDST2	831	26	0.99	0.99
LIVT2	365	8	1.01	1.10
RYET2	381	48	1.05	1.13

To summarize the evaluation results, we calculated percent bias, root mean square error, correlation coefficient and Nash-Sutcliffe efficiency (see Figure 5-5). Note that the HL-RDHM

simulations compare reasonably well with the SAC-UHG for the majority of the basins. However, in some of the basins such as BRPT2, JAKT2 and MDST2, very large errors are observed in the HL-RDHM simulations as elaborated below. These three basins have Nash-Sutcliffe value of less than zero meaning that the model simulation is less accurate than using the mean of observed data, in other word; the model performance is less informative than the climatological information.

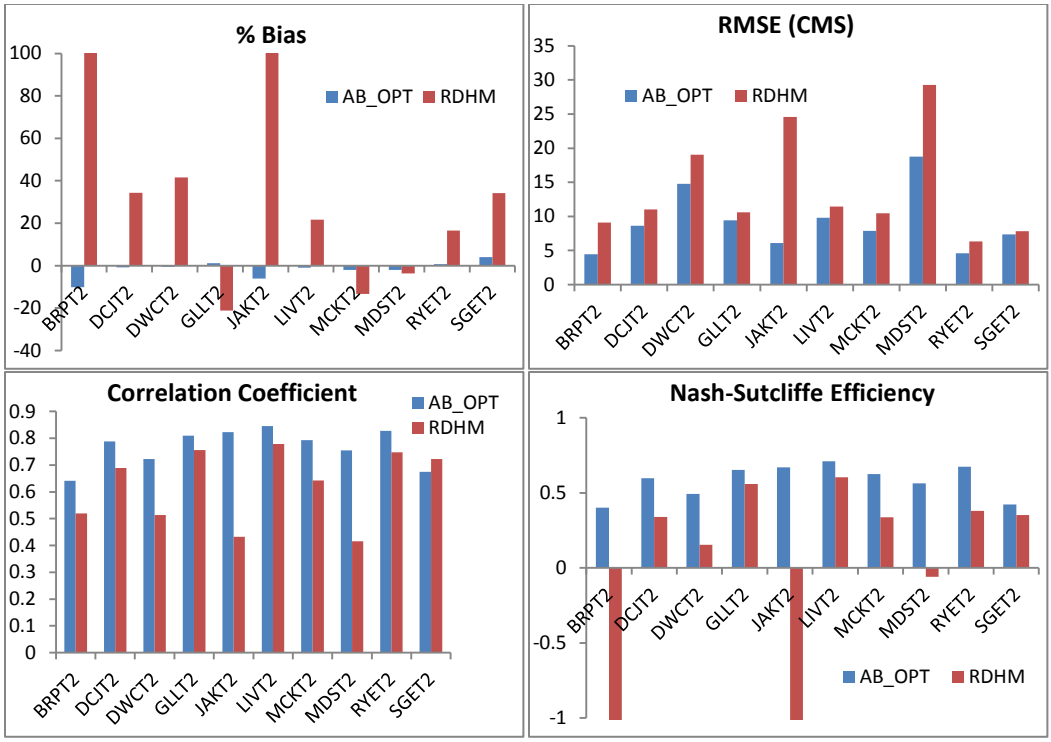

Figure 5-5 % Bias, RMSE, Correlation Coefficient and Nash-Sutcliffe efficiency indices of HL-RDHM and SAC-UHG (AB_OPT) for 10 headwater basins in Trinity River basin

BRPT2 has percent bias of greater than 100 with relatively low RMSE values. This basin suffers from extensive missing data, and hence the results may not be considered reliable due to small sample size. Also the bias adjustment factor obtained from calibration of the lumped model is 0.69 for precipitation, so there is an overestimation of a rainfall involved which was alleviated

through adjustment of precipitation in SAC-UHG. However, there is not such consideration takien into account with HL-RDHM in order to minimize the effect of input uncertainty and consequently the model suffers from mass balance problem. As shown in Figure 5-6 the unit hydrograph is pretty smooth for BRPT2 and there is not much of routing error like timing error involved which is the reason of having low RMSE values even with existence of very high % Bias.

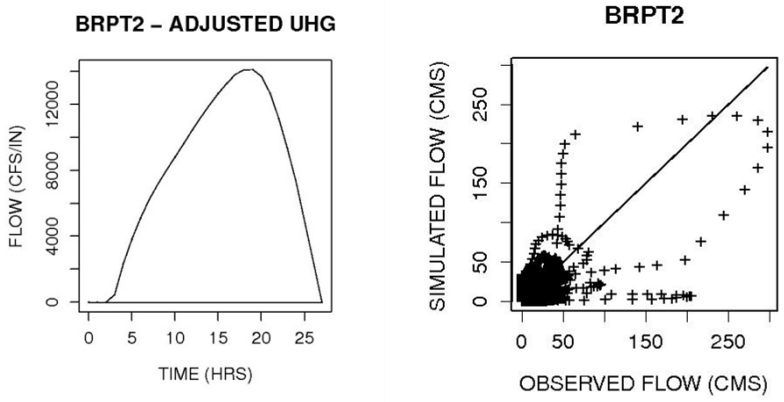

Figure 5-6 Left: BRPT2 unit hydrograph derived via AB_OPT, Right: Simulated streamflow from SAC-UHG versus observed streamflow

Percent bias for JAKT also exceeds 100% (see Figure 5-8). This very high bias also is observed in operational streamflow forecasting (personal communication with WGRFC), the cause of which is not clear and warrants careful investigation. It also has high RMSE values and low correlation coefficient which can be attributed to both mass balance problem and the significant timing error (Figure 5-7). The time series of several significant events with their peak exceeding the 98 percentile is plotted in Figure 5-8.

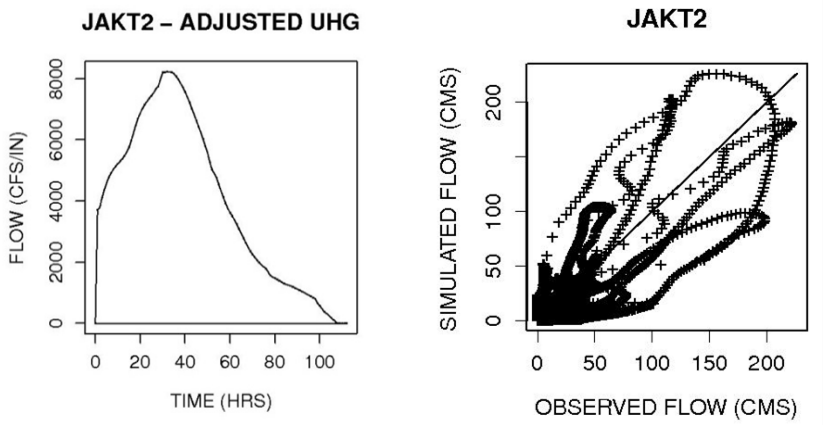

Figure 5-7 Left: JAKT2 unit hydrograph derived via AB_OPT, Right: Simulated streamflow from SAC-UHG versus observed streamflow

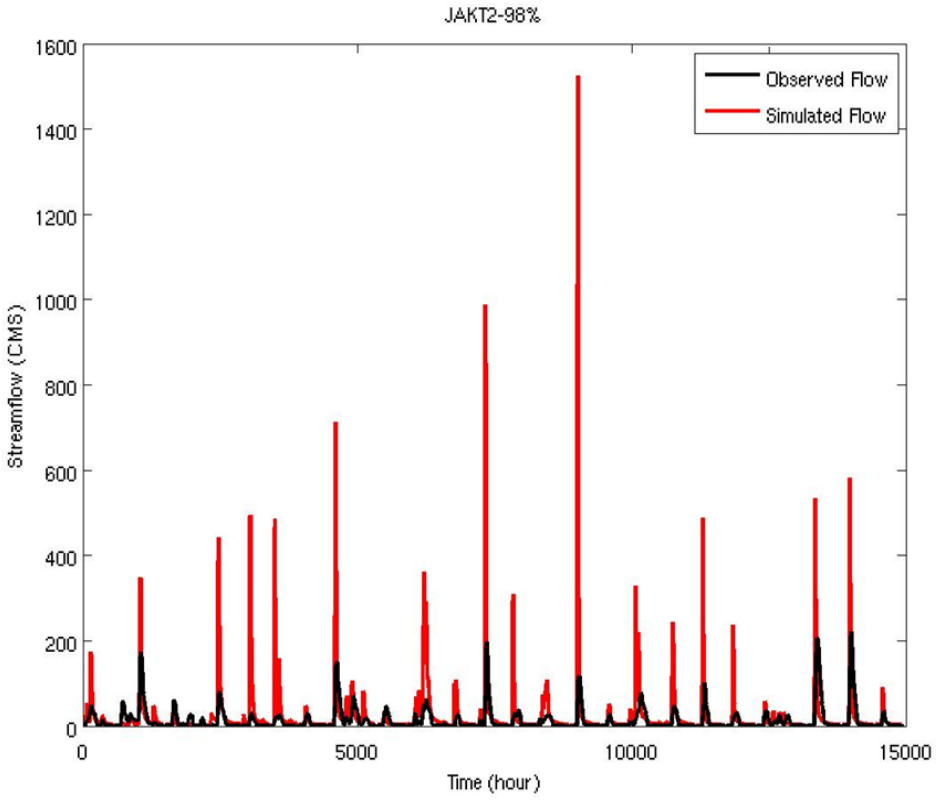

Figure 5-8 Streamflow simulation from HL-RDHM and streamflow observation time series for some significant events (peak flow above 98 percentile)

MDST2 has low percent bias which is not surprising, since the PXADJ and PEADJ factors for MDST2 are close to 1 indicating that mass balance holds for this basin. However, MDST2 has high RMSE and low correlation coefficient. As shown in Figure 5-9, this basin has a rather complex unit hydrograph (left) and shows timing errors. The timing errors manifest as loops in the scatter plot of simulated vs. observed streamflow (right) and account for high RMSE and low correlation for this basin. The timing error can be alleviated through calibration of the routing parameter.

For basins with large spatial variability in physiography and/or forcing data, we may expect distributed models to do better than lump models. RYET2 provides such an example, which is elongated in shape and slow responding with a very complex unit hydrograph (Figure 5-11) with multiple peaks. Note in Figure 5-12 that HL-RDHM does a very good job for this basin and simulates some of the significant events better than SAC-UHG (upper panel in Figure 5-12).

Finally, we emphasize that the SAC-UH was finely tuned and calibrated and the same set of data was used in both calibration and validation. Therefore, outperforming SAC-UHG was a high bar for HL-RDHM. Also, producing reasonable simulation in the form of gridded maps of streamflow, soil moisture and other hydrologic components (having reasonably accurate simulations for interior points) at the expense of somewhat increased RMSE of streamflow at the outlet locations is more important than outperforming the lumped models.

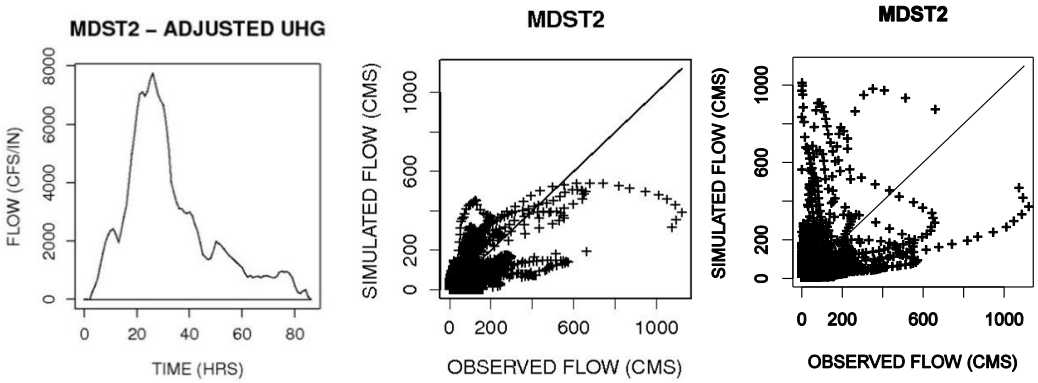

Figure 5-9 Left: MDST2 unit hydrograph derived via AB_OPT, Middle: Simulated streamflow from SAC-UHG versus observed streamflow, Right: Simulated streamflow from HL-RDHM versus observed flow.

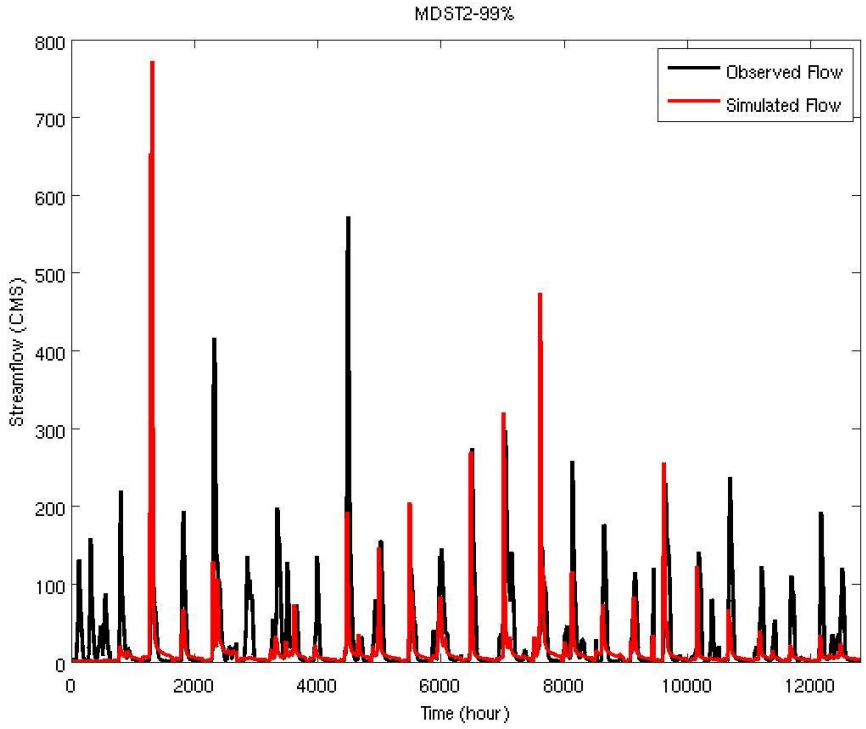

Figure 5-10 Time series of simulated streamflow (HL-RDHM) versus observed streamflow of some significant events (with peak flow above 99 percentile)

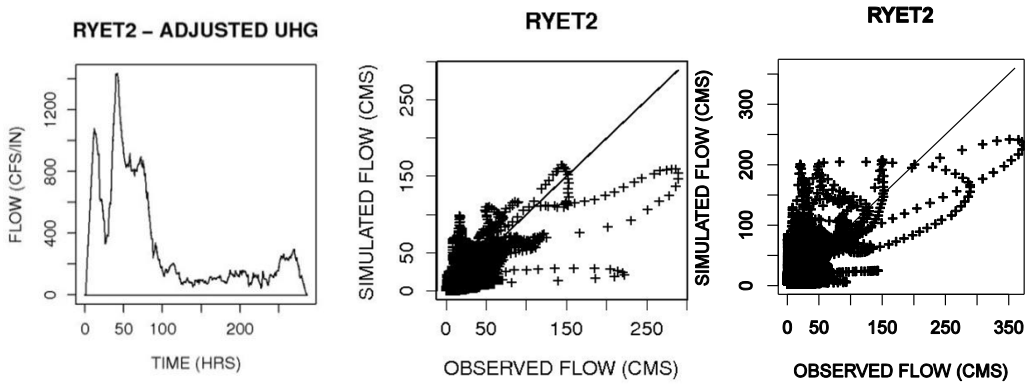

Figure 5-11 Left: RYET2 unit hydrograph derived from AB_OPT, Middle: Simulated flow resulted from SAC-UHG versus observed flow, Right: Simulated flow resulted from HL-RDHM versus observed flow

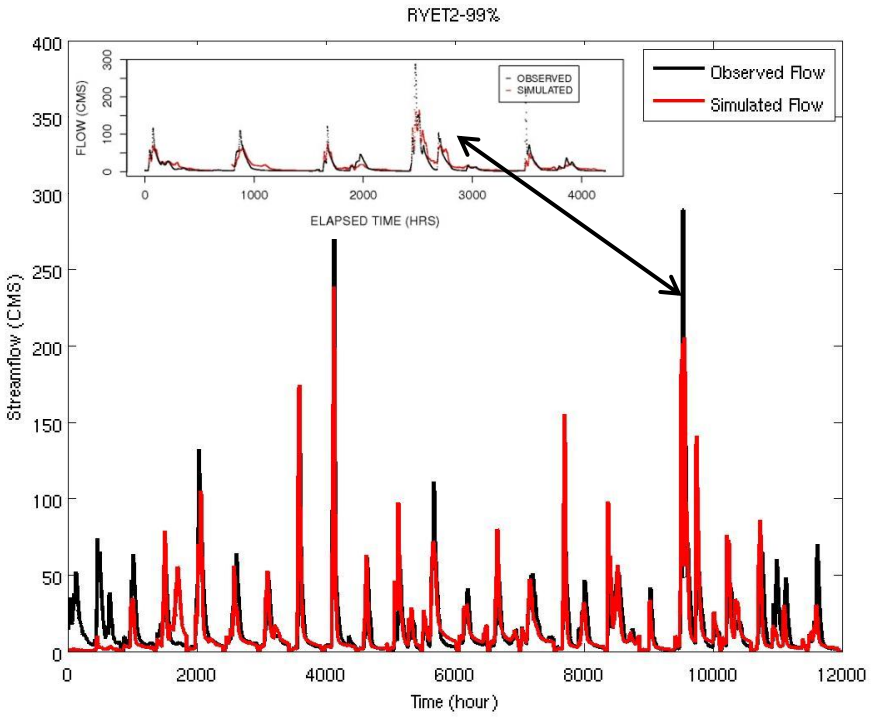

Figure 5-12 Time series of simulated versus observed streamflow of some significant events (peak flow above 99 percentile) for SAC-UHG (upper panel) and HL-RDHM (lower panel). Arrow shows the one significant event simulation in both SAC-UHG and HL-RDHM

5.5. Conclusion

Distributed models are a promising tool for producing high-resolution streamflow and soil moisture information. In this chapter, we examine how uncalibrated operational distributed models may compare with finely-tuned lumped models. This comparison poses an extremely stringent test for the distributed models in that the simulations from the calibrated lumped model represent dependent validation whereas those from the uncalibrated distributed models represent independent validation. The comparative simulation experiment is carried out for 10 headwater basins in the Trinity River Basin in TX covering periods of 1996 to 2012. The motivation for the above comparison stems from the fact that calibration of distributed models is generally very expensive and as such is to be minimized or avoided if possible.

The results show that uncalibrated HL-RDHM produces reasonably skillful simulations of outlet flow for the majority of the 10 headwater basins. For a half of the basins, however, bias in HL-RDHM simulation exceeds 20 percent. Gross oversimulation by HL-RDHM is observed for JAKT2 and BRPT2 while HL-RDHM did very well for RYET2, a slowly responding basin with complex UHG. There are two issues required to be addressed the mass balance issues which can be addressed by introducing multiplicative adjustment factors or using higher quality input forcing to minimize the effect of input uncertainty on the modeling results. Routing problem, i.e. timing error, can be alleviated by improving the routing parameter. The findings in this work point to limited calibration to reduce systematic biases in runoff and optimization of selective routing parameters to reduce timing error.

In general, this study showed capability of HL-RDHM at the scale which River Forecast Centers operate. Next chapter will discuss the HL-RDHM application in a very fine scale and urbanized area

Chapter 6

High resolution distributed model and scale sensitivity

Urban flash flooding is a serious problem in large, highly populated areas such as the Dallas-Fort Worth Metroplex (DFW). Being able to monitor and predict flash flooding at a high spatiotemporal resolution is important to mitigating its threat and to cost-effective emergency management. Under ideal conditions, the higher the resolution of the model and the precipitation input is, the better the spatiotemporal specificity of the model output will be. In reality, due to errors in the precipitation input, the model parameters and the model itself, there are practical limits to the model resolution. In this work, we assess the sensitivity of streamflow simulation to the spatiotemporal resolution of precipitation input and hydrologic modeling to identify the scale at which the relative error may be at minimum given the quality of the precipitation input and limitations of the model. The hydrologic model used in this work is the National Weather Service (NWS) Hydrology Laboratory's Distributed Hydrologic Model (HL-RDHM) applied at different spatiotemporal resolutions ranging from 250 m to 4 km and from 1min to 1 hour for three urban catchments in the Dallas-Fort Worth Metroplex (DFW) area. The high-resolution precipitation input is from the DFW Demonstration Network of Collaborative Adaptive Sensing of the Atmosphere (CASA) radars. The model simulation results are evaluated using the water level data obtained from the City of Grand Prairie in DFW.

6.1. Introduction

To take full advantage of high-resolution quantitative precipitation information (QPI) from weather radars, it is necessary to operate hydrologic models at a scale comparable to the scale of that information. Under ideal conditions, the higher the resolution of distributed modeling and precipitation input is, the more desirable the model output will be as it provides better

spatiotemporal specificity. Due to the errors in precipitation input, model parameters and the model itself, however, there are practical limits to the resolution of modeling. To illustrate, Figure 6-1 shows the relative error in runoff simulation as a function of the scale of sub-catchment delineation and the magnitude of error in precipitation input under the assumption of a perfect hydrologic model (Smith et al. 2004b). If the precipitation input is perfect, a finer-scale sub-catchment delineation would yield more accurate simulation of areal runoff. If there are large errors in the precipitation input, however, the accuracy of areal runoff simulation deteriorates as the resolution of modeling increases. For skillful flash flood forecasting, it is hence important to identify the scale at which the relative error may be at minimum given the quality of radar QPE and the hydrologic model being used (Berne and Krajewski 2013). While not directly tested in this research, a relevant hypothesis is that, with improved accuracy, polarimetric QPE will allow higher-resolution modeling (see Figure 6-1).

For urban flash flood forecasting, variability in runoff and streamflow can conceptually be captured by employing hydrologic and hydraulic models and precipitation input at a sufficiently high resolution. In reality, however, all models and precipitation input have errors of varying nature and magnitude. Because the errors are nonlinearly transformed by the models in a scale-dependent way, the accuracy of simulated runoff and flow are generally not proportional to the resolution of modeling (Smith et al. 2004b, Berne and Krajewski 2013). To infer this relationship, we test and ascertain the limits of the available QPEs and hydrologic modeling in the DFW area. Specifically, this research aims at identifying the optimal spatiotemporal scale for hydrologic modeling given the QPE available. Toward that end, we carry out scale sensitivity experiments in which higher-resolution precipitation and selected model parameters are upscaled to lower resolutions. The results characterize and quantify the marginal information content in higher-resolution precipitation input and hydrologic modeling. The rest of the chapter is as follows. Study area an data acquisition is described in Section 6.2. Section 6.3 briefly introduces

the hydrologic model and rating curve derivation is explained in Section 6.4. Calibration and initialization is given in Section 6.5. Results of sensitivity analysis to temporal and spatial scale of modeling are described in Section 6.6. Conclusion is given in Section 6.7.

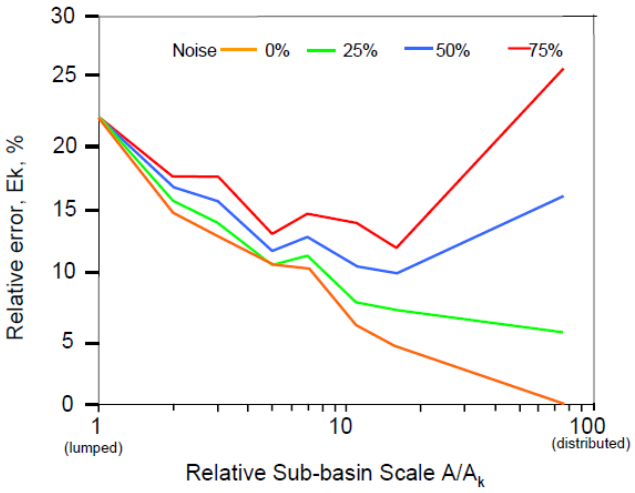

Figure 6-1 Relative error in streamflow simulation at the catchment outlet as a function of the scale of subbasin delineation and the magnitude of error in precipitation input (from Smith et al. 2004b).

6.2. Study area and data acquisition

The modeling domain is a rectangular area that encompasses the Cities of Fort Worth, Arlington and Grand Prairie in the Dallas-Fort Worth Metroplex (DFW) area in Texas (Figure 6-2). The rainfall data used is the Collaborative Adaptive Sensing of the Atmosphere (CASA) QPE. Currently, a network of CASA X-band radars, referred to as the DFW Demonstration Network, is being deployed in the area. One of the limitations with NEXRAD is that they do not observe the lower atmosphere away from the radar location, which causes degradation of spatial resolution at far ranges. Also, the temporal resolution is constrained by a fixed set of volume

coverage patterns (VCP). The lack of resolution arises because the radar operation is independent of the weather conditions. To maximize its utility, the radar may adapt to the time-varying needs of the users (Junyent et al. 2010). To address the above gaps in the current weather observation system, the NSF Engineering Research Center (ERC) for CASA developed a new weather warning systems based on dense networks of small radars (McLaughlin et al. 2005) with adaptive scanning strategy (Junyent et al. 2010). The CASA Integrated Project was the first test bed of a networked CASA radar system composed of four X-band radars in Oklahoma. Each radar node was approximately 30 km away from the next unit. The details of the radar network, hardware and software architectures are described in Junyent et al. (2010). CASA QPE is based on specific differential propagation phase which makes it immune to absolute calibration errors (Bringi and Chandrasekar 2001). Attenuation is a known issue for precipitation estimation using X-band radars (Seo et al. 2010, Berne and Krajewski 2013). The CASA system uses the network reflectivity retrieval technique (Chandrasekar and Lim 2008) and the network-based attenuation correction technique (Lim et al. 2011) to mitigate the effects of attenuation. Lim et al. (2011) showed that the technique works robustly in real time in retrieving attenuation-corrected reflectivity. The network was evaluated using rain gauge observations for a five-year period which showed a good agreement between radar QPE and rain gauge observations with a standard deviation of 25% and a bias of 3.7% (Chandrasekar et al. 2012). After the successful test bed demonstration of CASA in Oklahoma, the CASA system was moved to DFW in late 2012. In this work, the 1-min 500-m QPE product from the CASA radar installed at the University of Texas at Arlington, XUTA, was used along with the MPE products from the NWS West Gulf River Forecast Center (WGRFC). Figure 6-2a shows the coverage of XUTA with the city limits of Fort Worth, Arlington and Grand Prairie. The historical CASA QPE is available only for significant events as the radar has been operating only in times of precipitation. The period of record for the CASA QPE used in this work is from Jan 2013 to Dec 2013.

For hydrologic evaluation, we used water level observations as explained below. The Cities of Fort Worth, Arlington and Grand Prairie have been operating the so-called High Water Warning Systems (HWWS) at 23, 6 and 23 locations through their cities since 2007, 2013 and 2009, respectively. The HWWS observes in real time precipitation, water level and, if equipped, meteorological variables. The rain gauge observations have been used to validate the radar-based QPEs as described in Chapter 2 and 3. Water level observations at most locations are based on pressure transducers location at the channel bottoms. Though the real-time observations from the HWWS are archived, the historical data have not been looked at until this study. To ensure that high-quality data are used, we visually examined the historical water level time series and selected three locations in the City of Grand Prairie (see Figure 6-2b).

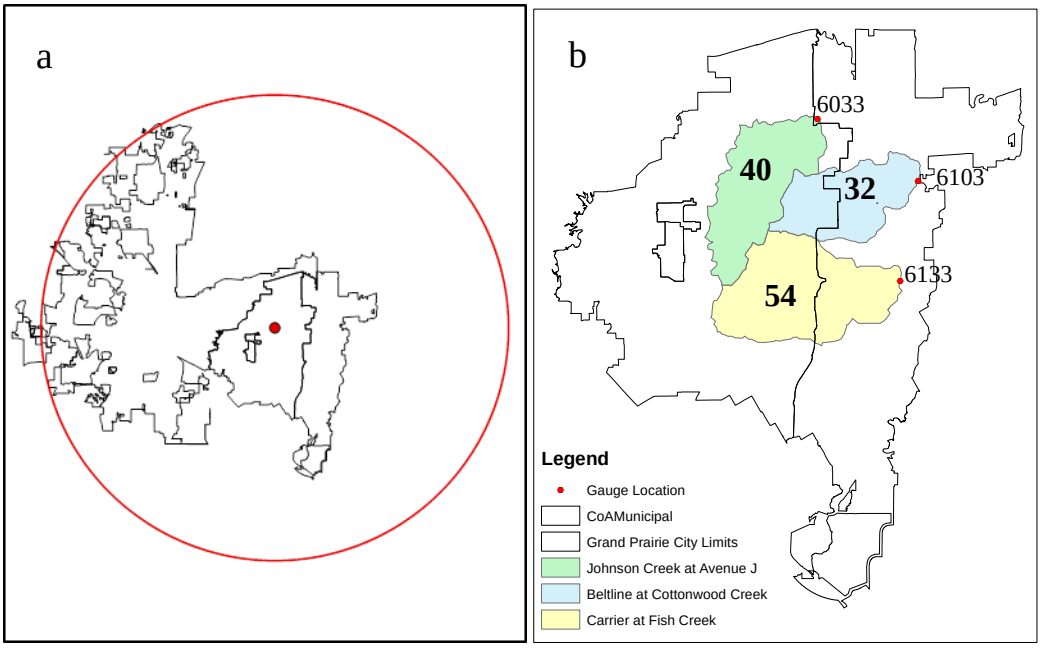

Figure 6-2 a) Radar umbrellas of XUTA b) Study domain and selected basins for the scale sensitivity (Area of each basin is given in the figure in bold (km^2))

Figure 6-3 shows the cross-correlation between 15-min precipitation and streamflow time series, indicating time-to-peaks of 1.75, 3.25 and 3.25 hours for Catchments 6033, 6013 and 6133; the catchment areas are 40, 32 and 54 km^2, respectively. Figure 6-4 shows the PCTIM map (see Appendix A for details) over the three catchment areas. Note that Catchment 6033, which shows the smallest time-to-peak, has the largest impervious area.

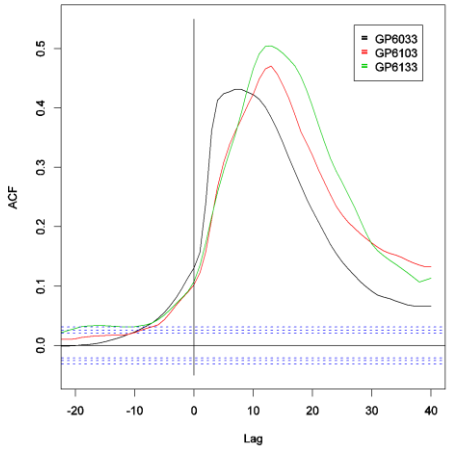

Figure 6-3 Cross-correlation between 15-min precipitation and streamflow time series indicating time-to-peaks of approximately 1.75, 3.25 and 3.25 hours for Catchments 6033, 6013 and 6133, respectively.

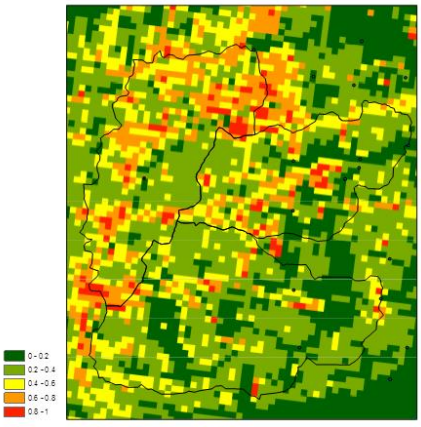

Figure 6-4 PCTIM at 1/16 HRAP resolution over the three study catchments.

6.3. Hydrologic model

For hydrologic modeling, the NWS Hydrology Laboratory's Research Distributed Hydrologic Model (HL-RDHM) was used: specifically, the Sacramento soil moisture accounting model with heat transfer, or SACHT, for rainfall-runoff and the kinematic wave model for routing (Koren et al. 2004). HL-RDHM has been used operationally in NWS on a 4 km grid forced by hourly precipitation, but not at as fine a spatiotemporal resolution as 500 m and 1 min used in this work. HL-RDHM is recognized as one of the best performing distributed models, as demonstrated in the Distributed Model Intercomparison Projects (Reed et al. 2004, Smith et al. 2012). It is used operationally in NWS at the River Forecast Centers (RFC), Weather Forecast Offices (WFO) and National Centers for Environmental Prediction (NCEP). For rainfall-runoff modeling, HL-RDHM implements the gridded version of SAC (Burnash 1995). SAC is capable of simulating both saturation- and infiltration excess runoff. For the upper layer storages, saturation excess is assumed; no surface runoff occurs before the upper-zone tension and free water capacities are filled. Once the upper layers are filled, surface runoff occurs from infiltration excess as a function of percolation (Koren et al. 2004). The gridded a priori parameters for SAC and kinematic-wave routing are available from NWS for the continental US at a 4km x 4km resolution. Not all a priori parameters for SAC (Koren et al. 2000, Anderson et al. 2006, Zhang et al. 2012) may be considered realistic in the study area due to urbanization and coarse resolution. In this work, we used the a priori parameter settings for all parameters, except Permanent Impervious Area (PCTIM) and the two channel routing parameters, hillslopeslope and specific discharge, by uniformly disaggregating them onto finer grids. The urban environment differs most significantly from others in that it has large impervious areas, and that the drainage of storm water occurs not only through land surface but also through man-made storm drainage systems. Collectively, a large fraction of an urban area is impervious. Imperviousness, however, generally has very large

spatial variability in large urban areas. Appendices A and B describe how the high-resolution PCTIM and channel routing parameters were derived for this study, respectively.

6.4. Derivation of rating curves

To stablish a rating curve, concurrent observations of stage and streamflow are necessary that cover the expected range of stage at the specific river gauge (Herschy 1993). Unfortunately, streamflow observations are not available at any of the HWWS locations. In this work, we derived rating curves based on numerical modeling following Kean and Smith (2005, 2010). Appendix C describes the procedure used. Once the rating curves for different grain sizes (i.e. D_{84}) were derived, we compared, as a reality check, with the rating curves derived based on HL-RDHM simulations as explained below.

We simulated streamflow forced with MPE precipitation at 1/8-HRAP and 15-min spatiotemporal resolution in which the 1-HRAP 1-hr MPE estimates are uniformly disaggregated onto 1/8-HRAP subgrid and 15-min subintervals. The 15-min subinterval corresponds to the sampling interval of stage observations. The choice for the 1/8 HRAP subgrid is somewhat arbitrary and is made to avoid favoring high- or low-resolution simulations. We then converted the stage observations at the three HWWS locations to pseudo streamflow observations by fitting the following stage-discharge relationship (Herschy 1993) to match the simulated streamflow:

$$Q = c\,(h + a)^n \tag{6-1}$$

where Q is the discharge, h denotes the stage data, c and n are constants and a is the stage at zero flow (datum correction). Usually, the stage-discharge relationship is established through plotting the discharge and stage data on logarithmic papers, since the logarithmic form of the rating curve can be developed into a straight line, or straight-line segments, by adding or

subtracting a constant value (a, datum correction) to the stage logarithmic scale. Possibility of extrapolation at either the top or bottom is another advantage of using logarithmic form.

The datum correction is the stage value corresponding to zero discharge, the lowest point on the low-water control. In other words, it is the stage (gauge height) at which water ceases to flow over the control. The stage of zero is determined by adding or subtracting a constant until the log-log plots looks like a straight line. We have used multiple segments for each location to obtain the best possible fit (Herschy 1993). Figure 6-5 displays the shifted stage (stage + datum correction) versus simulated discharge value from HL-RDHM forced by MPE. Equations (6-2), (6-4) and (6-3) represent the derived rating curves (stage-discharge relationship) for gauges 6033, 6103 and 6133, respectively.

$$\begin{cases} Q = 0.8\,(h - 486.17)^{2.3} & h < 489.2\ ft \\ Q = 1.95\,(h - 486.17)^{1.5} & 489.2 < h < 498.2\ ft \\ Q = 0.00213\,(h - 486.17)^{4.15} & h > 498.2\ ft \end{cases} \quad (6\text{-}2)$$

$$\begin{cases} Q = 0.4\,(h - 456.4)^{2} & h < 462.9\ ft \\ Q = 0.00118\,(h - 456.4)^{4.15} & h > 462.9\ ft \end{cases} \quad (6\text{-}3)$$

$$\begin{cases} Q = 1.75(h - 460.7)^{1.14} & h < 472.7\ ft \\ Q = 6 \times 10^{-6}\,(h - 460.7)^{6} & h > 472.7\ ft \end{cases} \quad (6\text{-}4)$$

The fitted rating curves are shown in Figure 6-5. For each location, shown in black is the rating curve selected from multiple curves obtained via the Kean and Smith method for different values of the roughness height, z_0 (mm) (see Appendix C). Note that the two rating curves match reasonably well. The results presented below are based on the empirical rating curves (in red) in Figure 6-5.

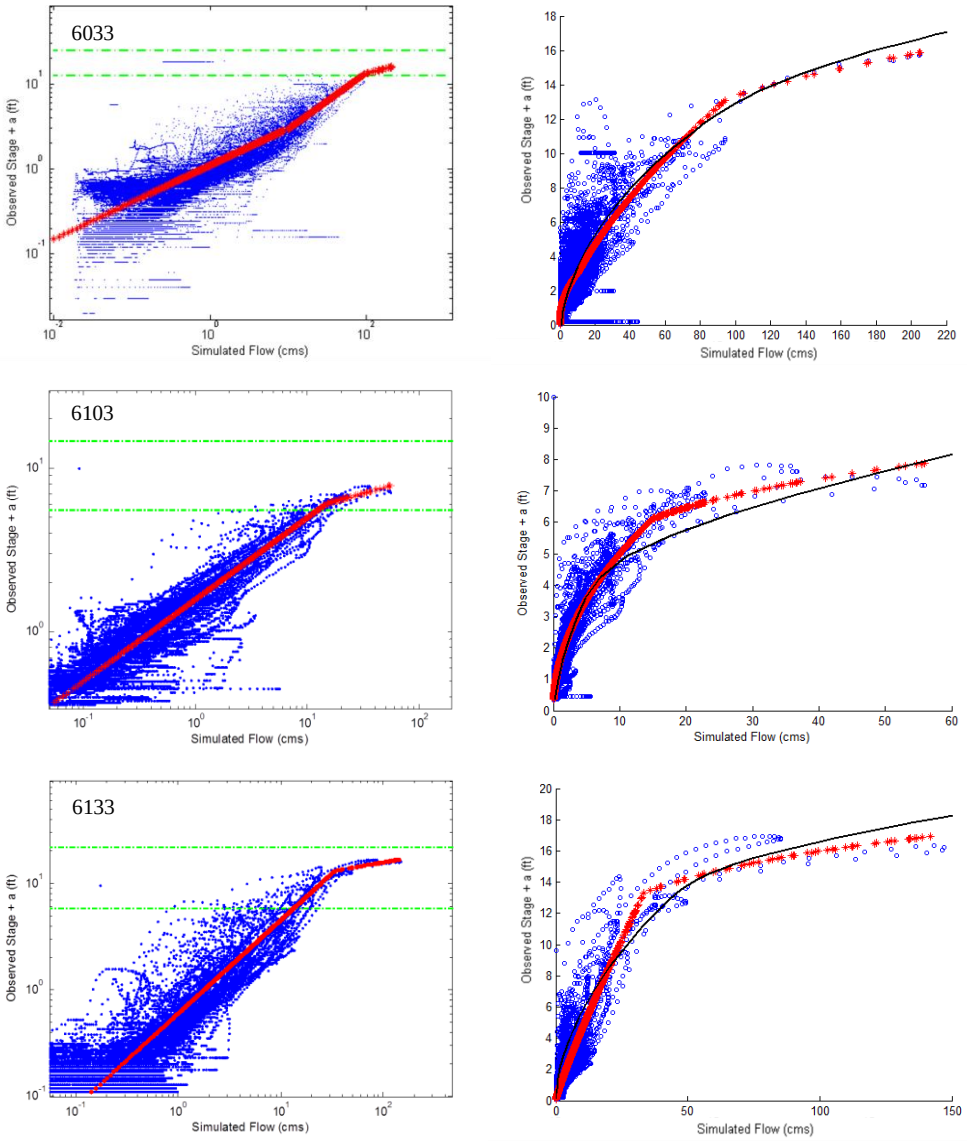

Figure 6-5 Left: Shifted observed stage versus simulated flow forced by MPE (1/8 HRAP & 15 min) at log-log scale, The lower dashed green line is corresponding to the stage that there is a change in the cross section and the upper dash green line is the road height. Right: Shifted observed stage versus simulated flow forced by MPE (1/8 HRAP & 15 min). Red dots are the empirical fitted rating curve. Black line is rating curve derived from Kean and Smith method.

6.5. Calibration and initialization

There are multiple sources of error in simulating streamflow. The precipitation data may have not only spatiotemporally-varying random errors but also systematic errors. The model initial conditions may be erroneous. The model parameters may be erroneous and/or lack spatial resolution. The models may have structural deficiencies due to lack of model physics, scale issues and/or errors in the physiographic data used. In addition, there may be human and/or natural control of the movement of water that is not modeled. Ideally, one may assess sensitivity to resolution of precipitation input and hydrologic modeling in an ensemble framework in which the uncertainties due to all significant errors are accounted for to the extent that the current understanding allows. Such an analysis, however, was beyond the scope of this work. Instead, we carried out conditional analysis in which the sensitivity of streamflow simulation at the catchment outlet is assessed to the resolution of the precipitation input, PCTIM and the channel routing parameters, given that all other initial, and observed and fixed boundary conditions are perfectly known. In reality, the conditioning variables are never perfectly known. The objective in this work was to exercise, in emulation of the real world, what one may consider to be a best practice in reducing errors in the conditioning variables. Toward that end, we carried out limited bias correction and calibration of the precipitation input and channel routing parameters, respectively, as described below. Note that calibration of distributed parameters is an emerging area of research (smith et al. 2013, Duan 2013; Gupta et al. 2013). In this work, the channel routing parameters were adjusted spatially uniformed following the NWS approach for calibrating HL-RDHM (Kuzmin et al. 2008, Smith et al. 2013).

We applied a multiplicative adjustment factor to the precipitation input, β_P, to reduce volume errors in streamflow simulation, and, to reduce time errors, uniformly apply multiplicative adjustment factors, β_{Q_o} and β_{Q_M}, to the channel routing parameters of specific discharge, Q_0,

and the exponent, Q_M, respectively (see Appendix B). In this way, the errors in streamflow simulation are reflective as much as possible of the effects of varying resolution of precipitation and hydrologic modeling. The multiplicative bias in CASA QPE over the 2013-2014 period estimated as described above was 1.3 for Catchments 6033 and 6103, and 1.1 for Catchment 6133.

Timing errors are often a large contributing factor to errors in streamflow simulation. They may originate from different sources: errors in capturing the spatiotemporal distribution of precipitation, errors in soil moisture accounting, and/or errors in routing. In this work, we carried out spatially uniform adjustment of the channel routing parameters only. To optimize the adjustment, we considered the root mean square error (RMSE) of simulated streamflow, mean (i.e., volume) error in simulated streamflow, correlation between simulated and observed flows, timing error in peak simulated flow as a function of the observed peak flow, probability of detection (POD) and false alarm rate (FAR). All statistics were calculated only for the significant events for which the CASA QPE was available. There were 16, 19 and 21significant events for the three locations of 6033, 6103 and 6133, respectively. POD and FAR, which are widely used in forecast verification (Brown et al. 2010), are particularly important for flash flood forecasting in urban areas (Barnes et al. 2007, Fares et al. 2014). In calculating POD and FAR, we used the 99^{th}, 99.5^{th}, 99.7^{th} and 99.9^{th} percentiles as the thresholds as estimated from the observed flow within the period of record.

Figure 6-6 through Figure 6-7 show the RMSE and volume error for all combinations of the multiplicative adjustment factors to the specific discharge and the exponent. In the figures, simulated-vs.-observed peaks, timing errors, POD and FAR are displayed only for the best five combinations of the adjustment factors. The final adjustment factors selected for each basin are listed in Table 6-1.

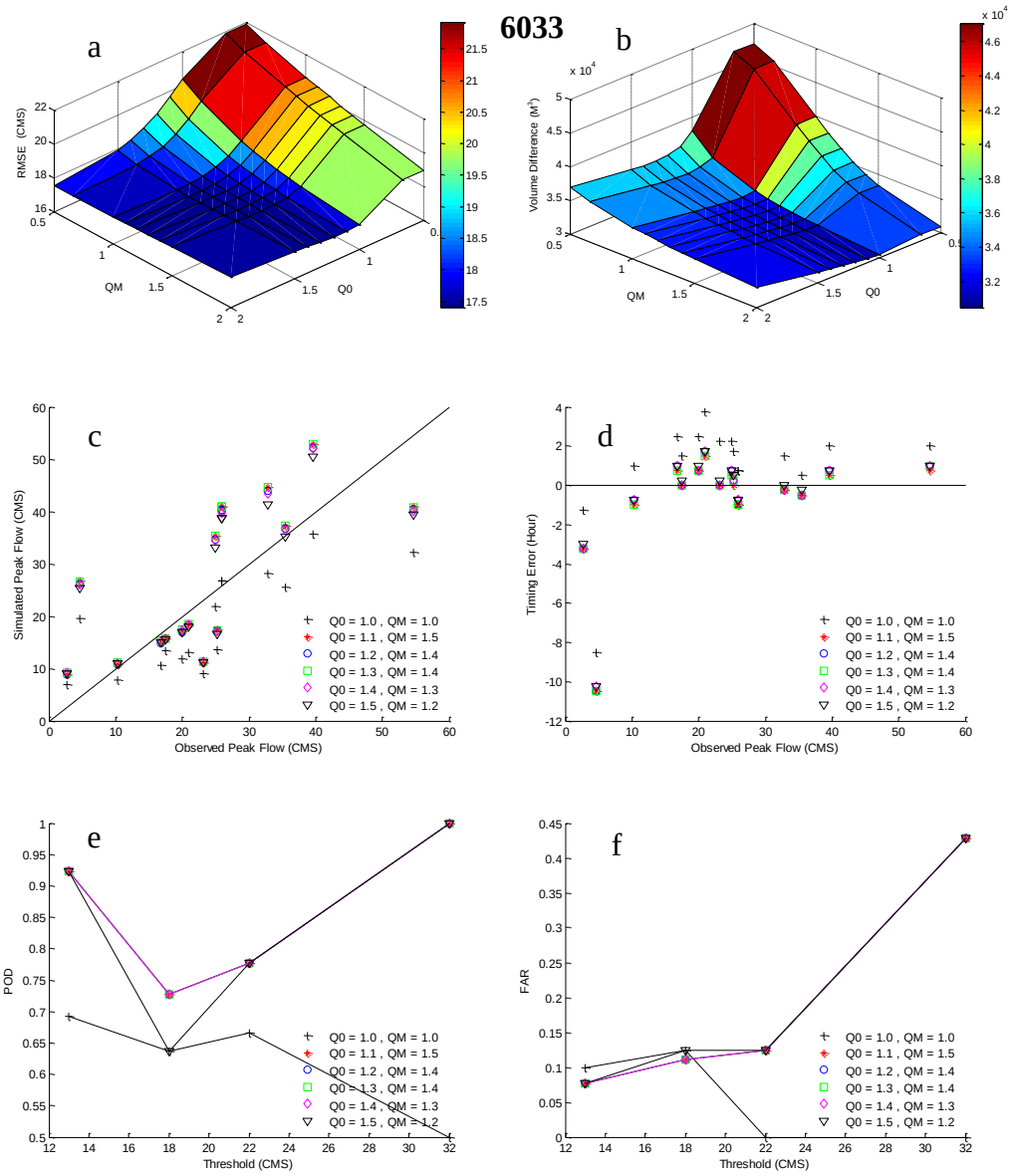

Figure 6-6 a) RMSE value b) Difference between the simulated and observed volume c) Simulated peak flow versus observed peak flow for individual events d) Timing error as a function of observed peak flow, e) Probability of detection f) False alarm rate for the best five combination of multiplicative factor for Q0 (specific discharge) and QM (exponent) for 6033 (best case, Q0=1.1, QM=1.5)

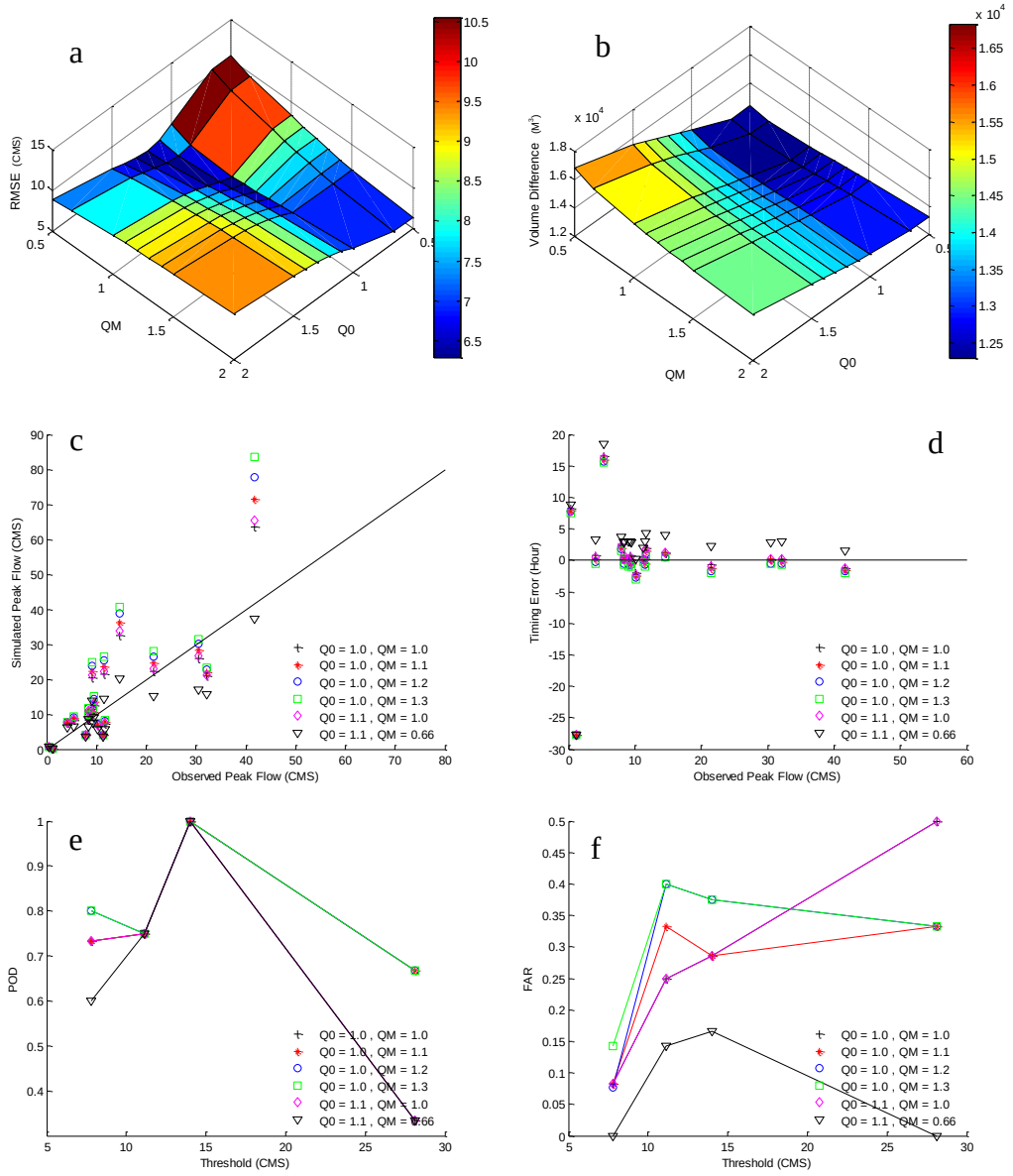

Figure 6-7 a) RMSE value b) Difference between the simulated and observed volume c) Simulated peak flow versus observed peak flow for individual events d) Timing error as a function of observed peak flow, e) Probability of detection f) False alarm rate for the best five combination of multiplicative factor for Q0 (specific discharge) and QM (exponent) for 6103 (best case, Q0=1, QM=1.1)

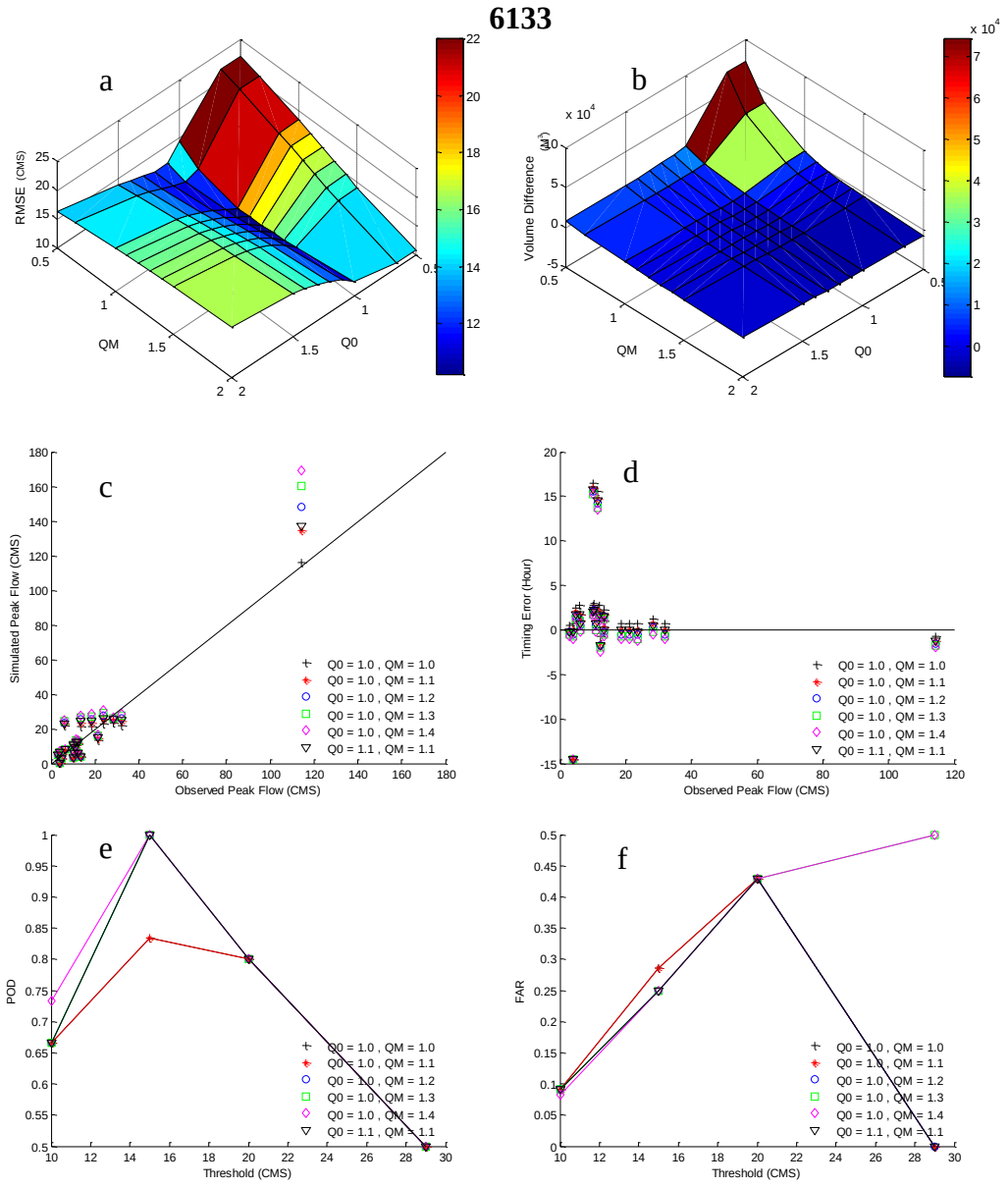

Figure 6-8 a) RMSE value b) Difference between the simulated and observed volume c) Simulated peak flow versus observed peak flow for individual events d) Timing error as a function of observed peak flow, e) Probability of detection f) False alarm rate for the best five combination of multiplicative factor for Q0 (specific discharge) and QM (exponent) for 6133 (best case, Q0=1.1, QM=1.1)

Table 6-1 Selected multiplicative factors for precipitation, specific discharge and exponent.

Basin	PADJ	Q0 (specific discharge)	QM (exponent)
6033	1.3	1.1	1.5
6103	1.3	1.0	1.1
6133	1.1	1.1	1.1

To warm up the model states, the SAC model was run from 1996 to 2013 using the historical Stage 3/MPE data. It is well known that the Stage 3 products have significant low biases (Seo et al. 1999, Seo and Breidenbach 2000, Seo et al. 2011). Given the long warmup period, however, one may expect the effects of the low bias to be lost for the simulations carried out in this work. In the warmup run, the SAC was run at a spatiotemporal resolution of $1/8^{th}$ HRAP and 15 min, for which the MPE estimates were uniformed disaggregated from the native 1-HRAP and 1-hour resolution.

6.6. Scale sensitivity

To assess the sensitivity of streamflow simulation to the resolution of precipitation input and hydrologic modeling given the a priori SAC parameters, initial SAC and kinematic wave routing states, we compared streamflow simulations from HL-RDHM over a range of spatiotemporal resolutions. The above represents analysis of sensitivity of streamflow simulation on the resolution of precipitation, PCTIM, Qo and QM conditional on all other input, parameters and states of the SAC and kinematic-wave routing models being perfectly prescribed.

6.5.1. Sensitivity analysis to spatial resolution

Sensitivity analysis was performed at resolutions of 1/2 (2 km), 1/4 (1 km), 1/8 (500 m) and 1/16 (250 m) HRAP. The temporal resolution was fixed at 15 minutes. Table 6-2 shows the RMSE of streamflow simulation at different spatial resolutions. Figure 6-9 through Figure 6-11 show (simulated peak flow – observed peak flow) as a function of the observed peak flow, (simulated time-to-peak – observed time-to-peak) as a function of the observed peak flow, and (simulated flow volume – observed flow volume) as a function of the observed flow volume for significant events at different spatial resolutions for Catchments 6033, 6133 and 6033. The figures do not indicate any consistent patterns. Whereas the highest resolution simulation does indicate sharper rise in hydrographs for Catchments 6033 and 6133 resulting in earlier time-to-peak, this pattern does not hold for Catchment 6013. Also, while the simulated flow peaks higher and produces larger volume at higher resolutions for Catchment 6103, this pattern is reversed for Catchment 6133.

Table 6-2 RMSE values for different spatial resolutions

Spatial resolution	6033	6103	6133
1/2 HRAP	17.3609	6.54	12.92
1/4 HRAP	17.3906	6.24	12.18
1/8 HRAP	17.4673	6.73	11.59
1/16 HRAP	17.5892	6.59	11.15

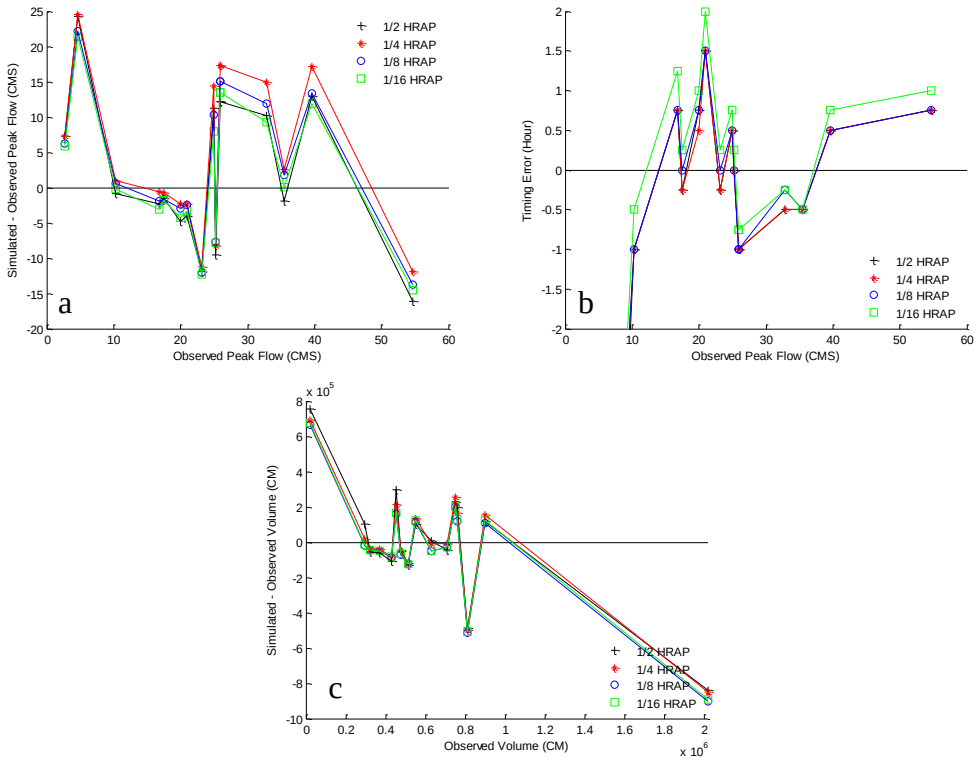

Figure 6-9 a) (simulated peak flow – observed peak flow) as a function of the observed peak flow, b) (simulated time-to-peak – observed time-to-peak) as a function of the observed peak flow, and c) (simulated flow volume – observed flow volume) as a function of the observed flow volume for significant events at different spatial resolutions for Catchment 6033

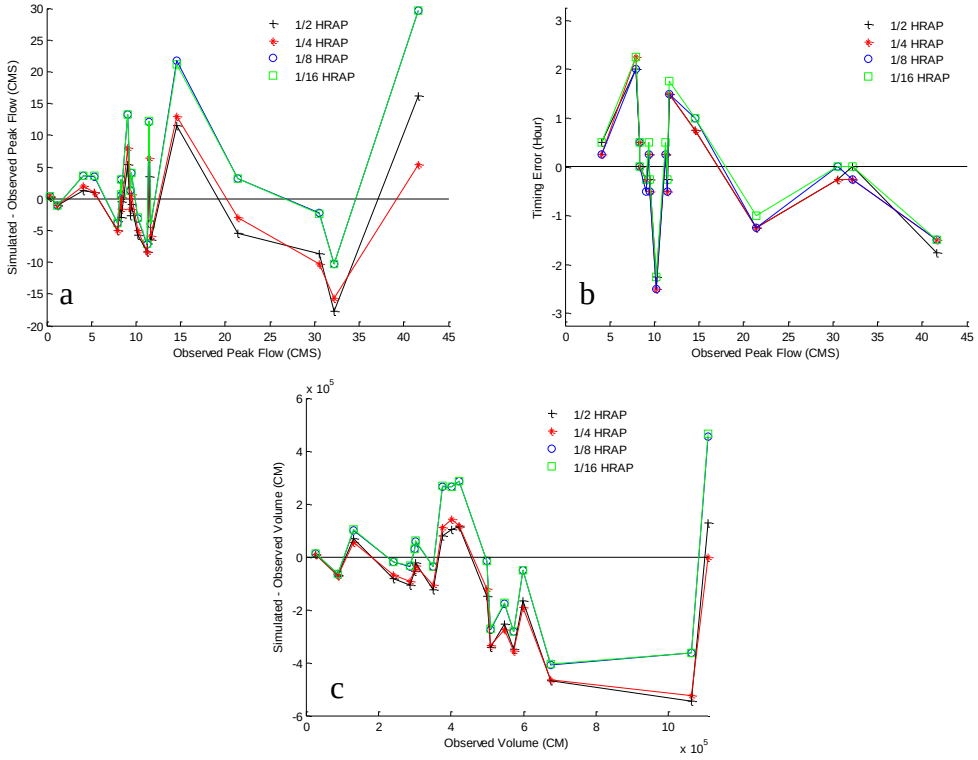

Figure 6-10 a) (simulated peak flow – observed peak flow) as a function of the observed peak flow, b) (simulated time-to-peak – observed time-to-peak) as a function of the observed peak flow, and c) (simulated flow volume – observed flow volume) as a function of the observed flow volume for significant events at different spatial resolutions for Catchment 6103

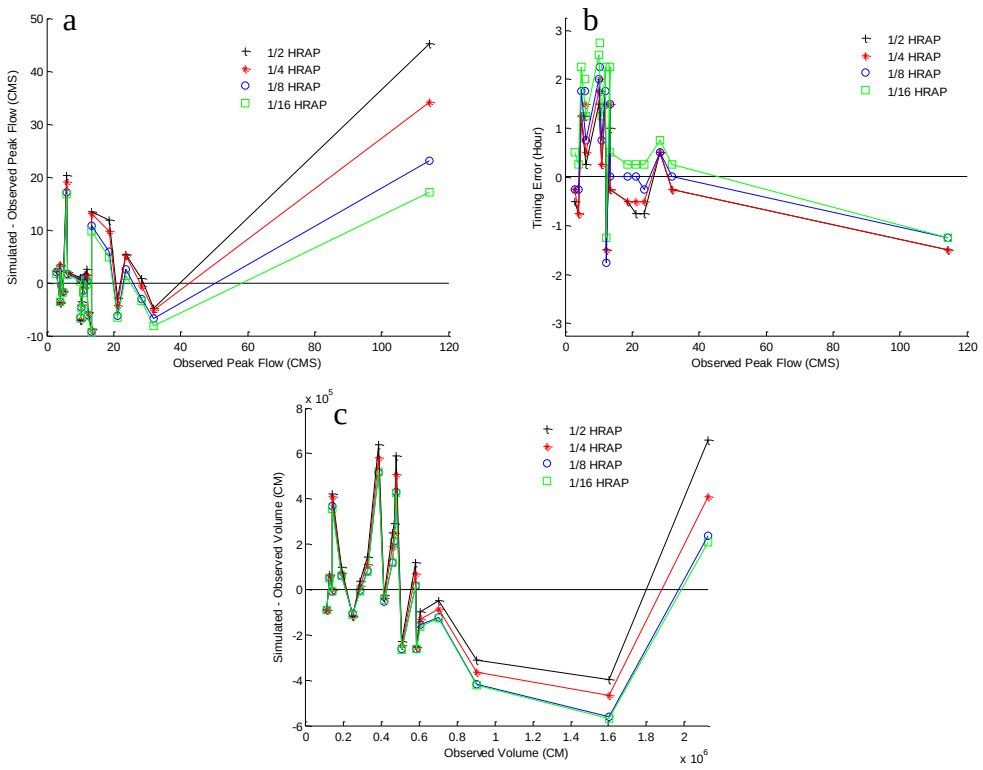

Figure 6-11 a) (simulated peak flow – observed peak flow) as a function of the observed peak flow, b) (simulated time-to-peak – observed time-to-peak) as a function of the observed peak flow, and c) (simulated flow volume – observed flow volume) as a function of the observed flow volume for significant events at different spatial resolutions for Catchment 6133

Figure 6-12 shows the cross correlation between the simulated and observed flows as a function of spatial resolution. While the differences are very small, it is seen that, the higher the resolution is, the higher the correlation is. While these differences are statistically not significant, they do indicate sensitivity to the resolution for the specific events considered in this work. Figure 6-13 shows the cross correlation between the observed and simulated flows forced by CASA QPE (in red) and by MPE (in black) as a function of spatial resolution for all 3 catchments (left) and for Catchment 6033 only (right). Note that, while the differences are, again, very small, the

correlation of MPE-forced simulation, which is representative of all 3 catchments, is higher, but that, for Catchment 6033, the correlation of CASA QPE-forced simulation is higher. Note in Figure 6-13 that Catchment 6033 has the largest impervious areas and hence is likely to be more sensitive to spatiotemporal variability of precipitation, which the CASA QPE would capture better than MPE due to higher resolution.

Figure 6-14 (Left and Right) show the smoothed power spectra of observed (in black) and simulated (in color) streamflow at all spatial resolutions forced by the CASA QPE and the MPE, respectively. The temporal resolution used in these simulations is 15 min. In both figures, the simulations at 1 HRAP were not successful due to too coarse a resolution and may be ignored. The figures confirm the findings above that there is little sensitivity to spatial resolution in these simulations, that the MPE-forced simulations capture the lower-frequency variability (up to a wavelength of about 5 hours) better than the CASA QPE-forced, but that the CASA QPE-forced simulations are marginally better than the MPE-forced for capturing higher-frequency variability. Note, however, that, given the time-to-peak is on the order of a few hours for these catchments (see Figure 6-3), higher frequency variability contributes little to the overall quality of streamflow simulation. A number of different inferences are possible from the findings above. One may hypothesize that, given the relatively large size of these catchments, the spatiotemporal variability of precipitation may be filtered out through the hydrologic processes. Testing of this hypothesis is left as a future endeavor for which spectral analysis of precipitation input at different spatial resolutions may be carried out. Analysis of spatial statistical structure of 15-min point precipitation in the study area indicates that the spatial correlation scale is larger than the range of spatial resolutions considered in this work (Rafieeinsab et al. 2014), in which case the impact of higher-resolution QPE would not be felt in streamflow simulation. Additional research is necessary to test this hypothesis as well.

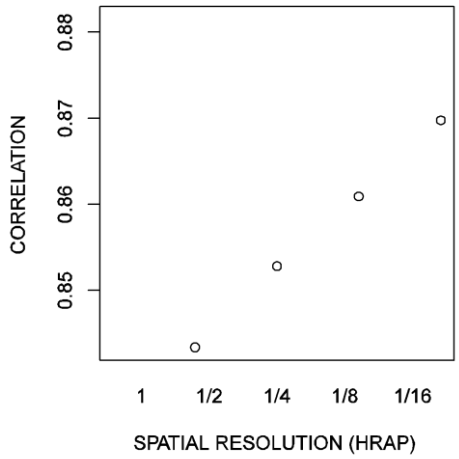

Figure 6-12 Cross correlation between simulated and observed flow as function of spatial resolutions. They are based on the combined time series of all three catchments.

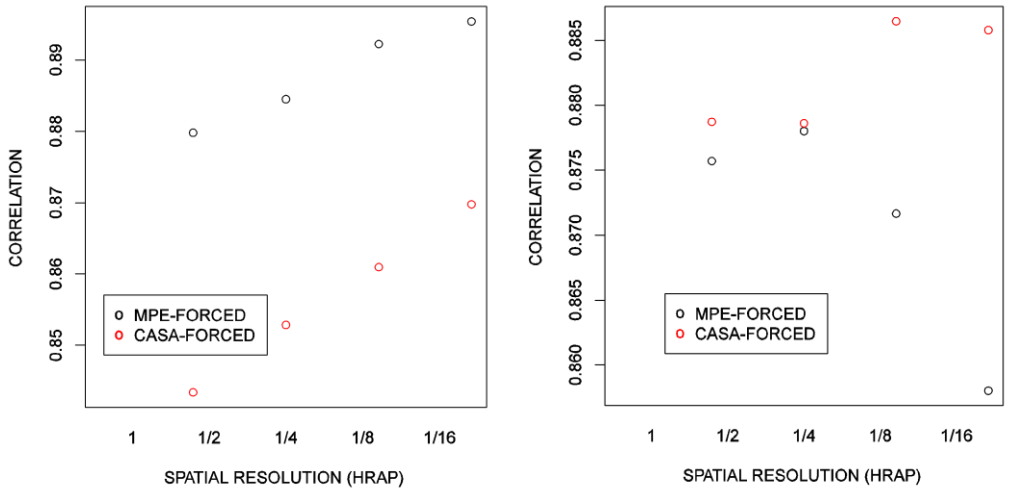

Figure 6-13 Cross correlation between observed and simulated flows forced by CASA QPE (in red) and by MPE precipitation (in black) as a function of spatial resolution for all 3 catchments (left) and for Catchment 6033 only (right).

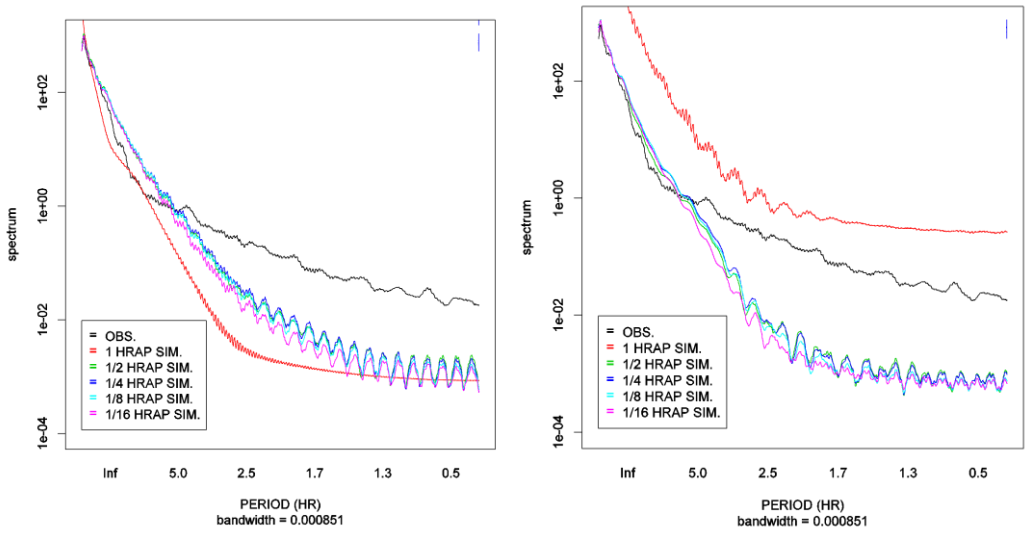

Figure 6-14 Smoothed power spectra of observed (in black) and simulated (in color) streamflow at all spatial resolutions forced by the CASA QPE (Left) and the MPE (Right)

6.5.2. Sensitivity to temporal resolution

Sensitivity analysis was performed at temporal resolutions of 1, 5, 15, 30 and 60 minutes. To render the sample size the same for all simulations, only the streamflow results at the top of the hour were considered for all cases. The RMSE of simulated flow for different temporal resolutions is given in Table 6-3. Figure 6-15 shows the percent difference in RMSE relative to the smallest RMSE for each catchment. It is clearly seen that the errors are reduced at lower resolutions of 30 to 60 min. Figure 6-16 through Figure 6-18 show (simulated peak flow – observed peak flow) as a function of the observed peak flow, (simulated time-to-peak – observed time-to-peak) as a function of the observed peak flow, and (simulated flow volume – observed flow volume) as a function of the observed flow volume for significant events at different temporal resolutions for Catchments 6033, 6103 and 6133. The figures indicate that, the higher the temporal resolution is, the larger the simulated peak flow is, but that there is little or no dependence of time-to-peak or flow volume on temporal resolution.

Table 6-3 RMSE values for different temporal resolutions

Temporal resolution (min)	6033	6133	6103
1	6.39	12.24	7.364
4	6.24	12.07	7.1818
15	6.05	11.52	6.766
30	5.94	10.84	6.3904
60	6.1	10.48	6.0258

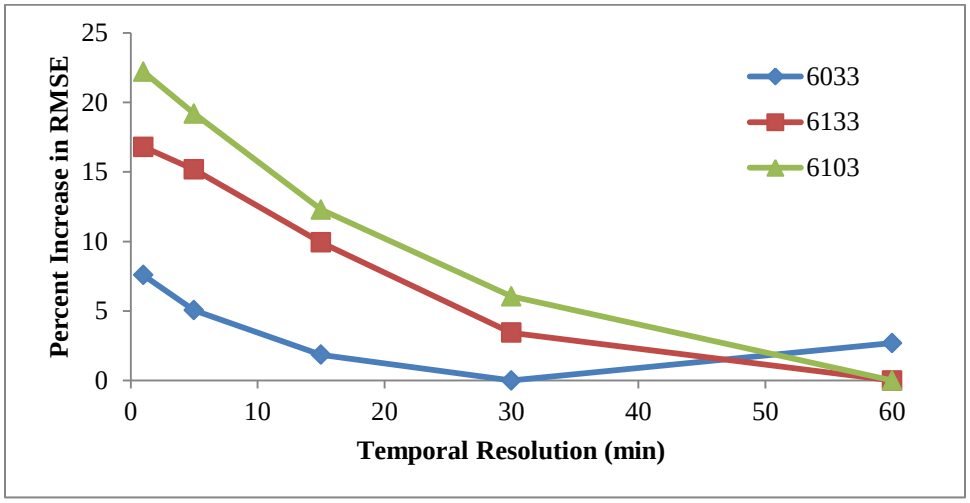

Figure 6-15 Percentage increase in RMSE at 1, 5, 15, 30 and 60 minute temporal resolutions.

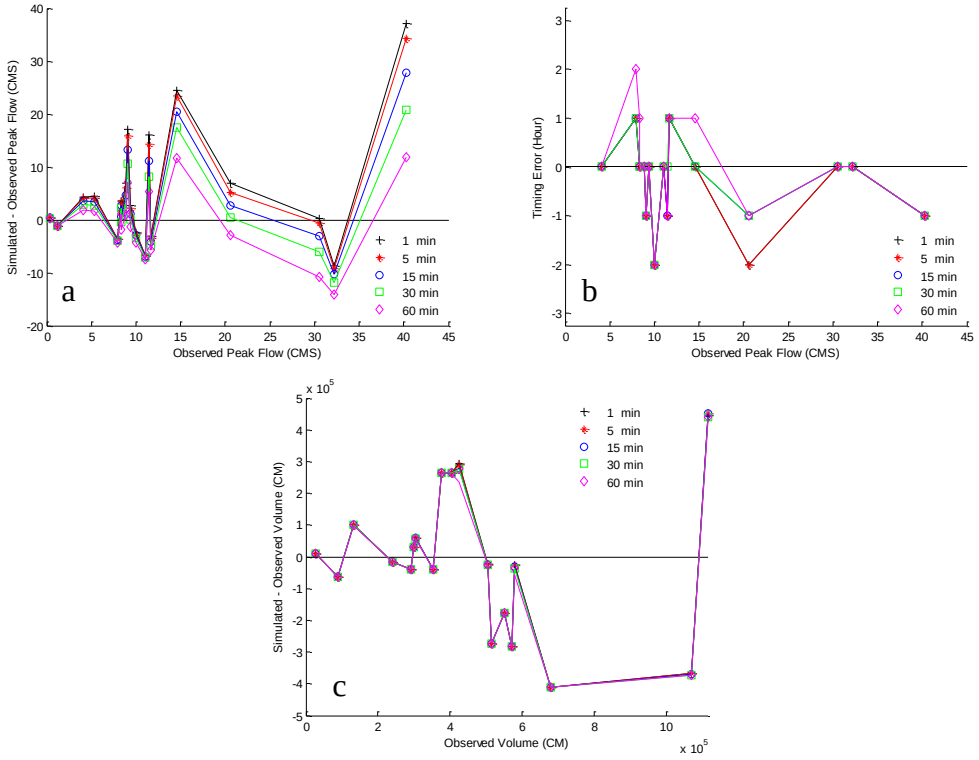

Figure 6-16 a) (simulated peak flow – observed peak flow) as a function of the observed peak flow, b) (simulated time-to-peak – observed time-to-peak) as a function of the observed peak flow, and c) (simulated flow volume – observed flow volume) as a function of the observed flow volume for significant events at different temporal resolutions for Catchment 6033

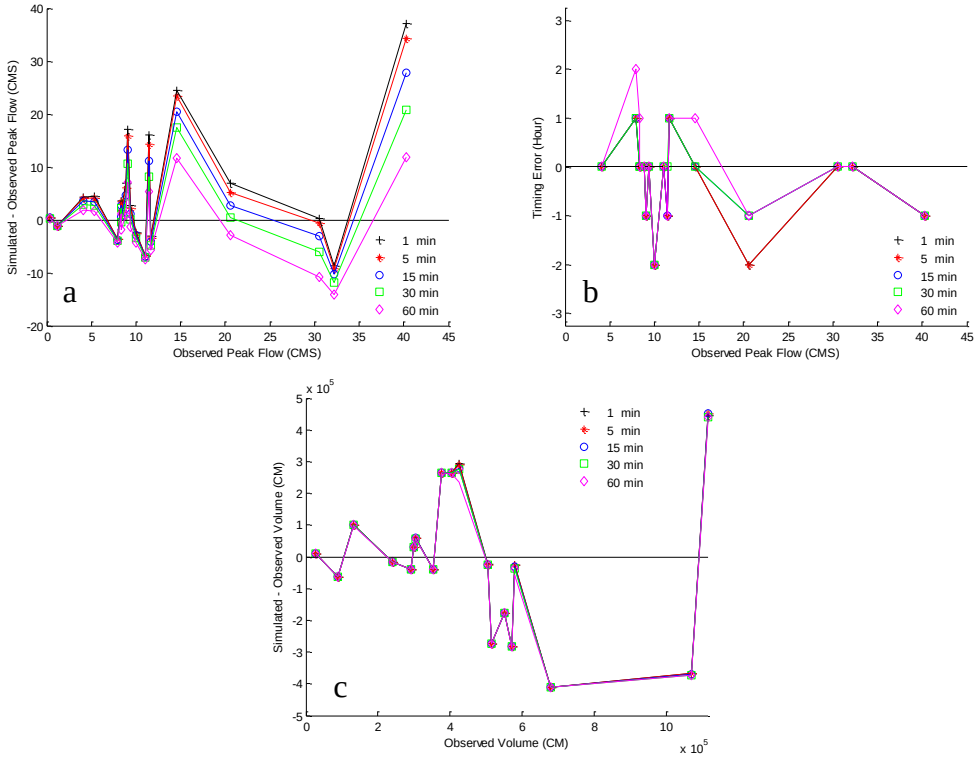

Figure 6-17 a) (simulated peak flow – observed peak flow) as a function of the observed peak flow, b) (simulated time-to-peak – observed time-to-peak) as a function of the observed peak flow, and c) (simulated flow volume – observed flow volume) as a function of the observed flow volume for significant events at different temporal resolutions for Catchment 6103

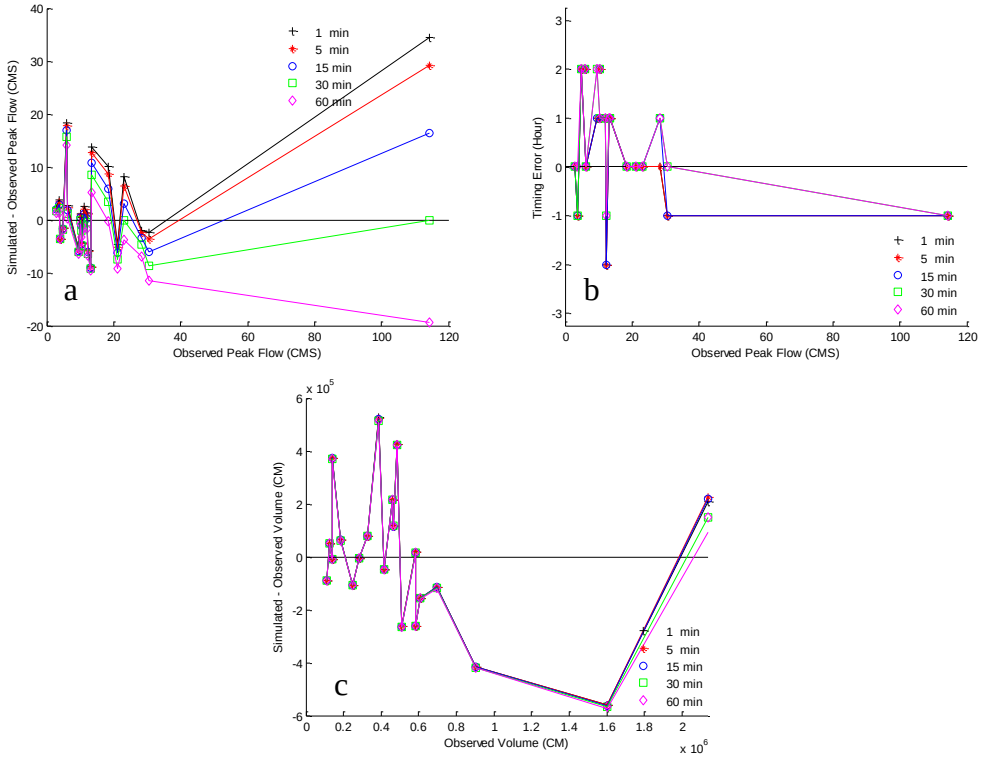

Figure 6-18 a) (simulated peak flow – observed peak flow) as a function of the observed peak flow, b) (simulated time-to-peak – observed time-to-peak) as a function of the observed peak flow, and c) (simulated flow volume – observed flow volume) as a function of the observed flow volume for significant events at different temporal resolutions for Catchment 6133

Figure 6-19 shows the auto-correlation function (ACF) of the observed (in black) and simulated (in color) streamflow at different temporal resolutions. Note that the ACF of the simulated matches that of the observed most closely at a 30-min resolution. Figure 6-20 shows the smoothed power spectra of the observed (in black) and simulated (in color) streamflow at different temporal resolutions. Note that the spectrum of the simulated matches that of the observed most closely at 30 to 60-min resolutions. The observed spectrum indicates that most of the power is associated with wavelengths larger than a few hours (i.e., the time-to-peak scale for the study

catchments) and that, at higher frequency, the spectrum takes on a white-noise character. Most of the power, however, is associated with time scales at or larger than the time-to-peak; it suggests that, for the catchments studied in this work, streamflow simulation does not significantly benefit from higher temporal resolution. These results support the findings from Figure 6-16 through Figure 6-18 described above. The above picture, however, may change for smaller catchments, investigation of which is left as a future endeavor.

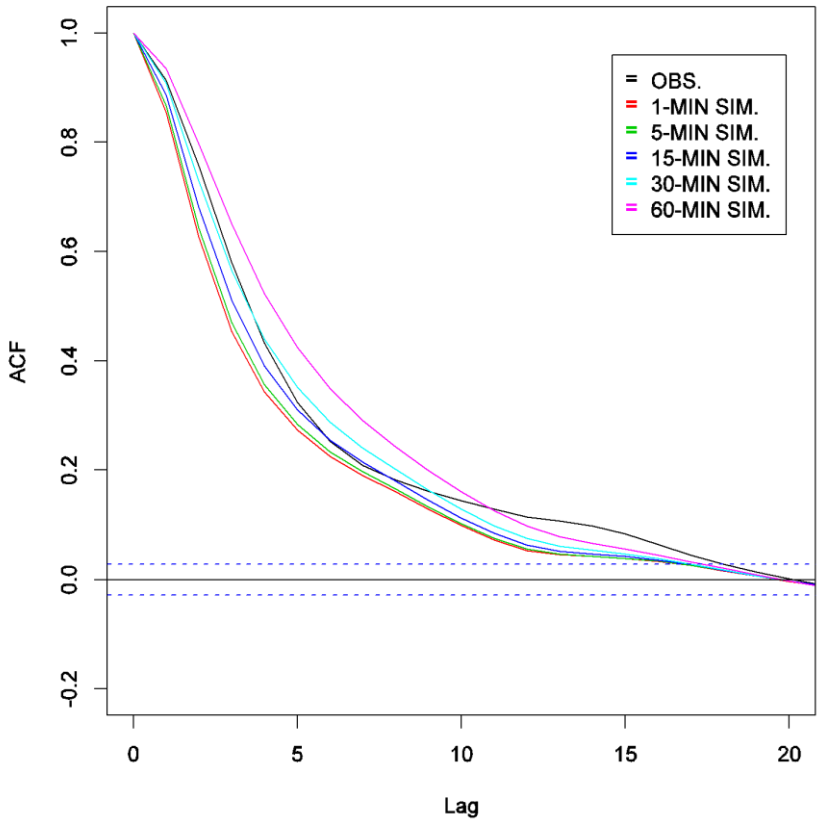

Figure 6-19 Autocorrelations of observed (in black) and simulated (in color) streamflow at different temporal resolutions.

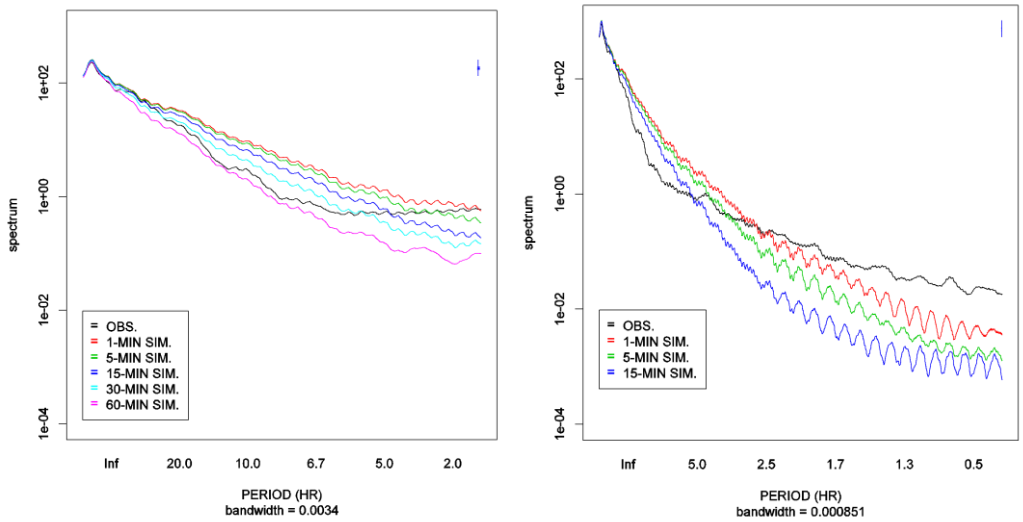

Figure 6-20 Smoothed power spectra of observed (in black) and simulated (in color) streamflow at all temporal resolutions (left) and at resolutions of 1-, 5- and 15-min only (right).

6.7. Conclusion and future research recommendations

To assess the sensitivity of streamflow simulation to the resolution of precipitation input and hydrologic modeling, conditional sensitivity analysis was carried out. Streamflow was simulated for three catchments in DFW using HL-RDHM with the resolution of precipitation varying from 1/16 to 1 HRAP and 1 to 60 min, and the spatial resolution of PCTIM and the two channel routing parameters varying form 1/16 to 1 HRAP while all other input and model parameters and states were assumed to be perfectly prescribed. The precipitation input used was the CASA QPE available at 500-m 1-min resolution. The size of the catchments ranged from 32 to 54 km^2.

The results indicate little consistent pattern in dependence on spatial resolution. Whereas the highest resolution simulation does indicate sharper rise in hydrographs for Catchments 6033 and 6133 resulting in earlier time-to-peak, this pattern does not hold for Catchment 6013. Also,

while the simulated flow peaks higher and produces larger volume at higher resolutions for Catchment 6103, this pattern is reversed for Catchment 6133. While the differences are very small, the cross correlation between the simulated and observed flows as a function of spatial resolution shows that, the higher the resolution is, the higher the correlation is. While the differences are very small, the correlation of the MPE-forced simulation representative of all 3 catchments is higher than that of the CASA QPE-forced simulation. For Catchment 6033, which has the largest impervious area and hence is likely to be more sensitive to spatiotemporal variability of precipitation, the correlation of CASA QPE-forced simulation is higher. The smoothed power spectra of observed and simulated streamflow at all spatial resolutions forced by the CASA QPE and the MPE confirm the above findings. The spectra also show that the MPE-forced simulations capture the lower-frequency variability (up to a wavelength of about 5 hours) better than the CASA QPE-forced, but that the CASA QPE-forced simulations are marginally better than the MPE-forced for capturing higher-frequency variability. Given that the time-to-peak is on the order of a few hours for these catchments, higher frequency variability contributes little to the overall quality of streamflow simulation. One may hypothesize that, given the relatively large size of the catchments, the spatiotemporal variability of precipitation may be filtered out through the hydrologic processes. Analysis of spatial statistical structure of 15-min point precipitation in the study area indicates that the spatial correlation scale is larger than the range of spatial resolutions considered in this work (Rafieeinsab et al. 2014). In such a case, the impact of higher-resolution QPE would not be felt in streamflow simulations. Additional research is necessary to test the above hypotheses.

For sensitivity to temporal resolution, it is clearly seen that the errors are reduced at lower resolutions of 30 to 60 min. The sensitivity analysis results indicate that, the higher the temporal resolution is, the larger the simulated peak flow is, but that there is little or no dependence of time-to-peak or flow volume on temporal resolution. While the differences are very small, the cross

correlation between the observed and simulated flows at all temporal resolutions supports the above finding. The autocorrelation function of the simulated streamflow matches that of the observed most closely at a 30-min resolution. Similarly, the spectrum of the simulated streamflow matches that of the observed most closely at 30 to 60-min resolutions. The observed spectrum indicates that most of the power is associated with wavelengths larger than a few hours (i.e., the time-to-peak scale for the study catchments) and that, at higher frequency, the spectrum takes on a white-noise character. Most of the power, however, is associated with time scales at or larger than the time-to-peak; it suggests that, for the catchments studied in this work, streamflow simulation does not significantly benefit from higher temporal resolution. The above picture, however, may change for smaller catchments, investigation of which is left as a future endeavor.

Chapter 7

Conclusion and future research recommendations

There exist different sources of error in hydrologic predictions which may be categorized into three main groups, input uncertainty, parametric and structural uncertainty, and uncertainty in initial conditions. The first of the two main objectives of this study is to advance the understanding of these uncertainties and reduce them to the greatest possible extent. In this study, uncertainty in initial conditions is reduced via two data assimilation techniques with the aim of improving streamflow predictions. The accuracy of high-resolution QPE is improved via fusion of different available radar-based QPEs which reduces the input uncertainty for more accurate hydrologic prediction. The second main objective of this study is test the practical limits of high resolution hydrologic modeling given the quality of the radar-based QPE to produce timely and accurate spatial streamflow information. Toward that end, we carried out scale sensitivity analysis using HL-RDHM over different spatiotemporal scales to identify the scale at which the relative error in simulated streamflow may be at minimum. The following summarize the main findings and future research recommendations.

7.1. Comparative evaluation of maximum likelihood ensemble filter and ensemble Kalman filter

Performance of the two data assimilation (DA) techniques, maximum likelihood ensemble filter (MLEF) and ensemble Kalman filter (EnKF), are comparatively evaluated. The primary purpose of the comparative evaluation is to assess relative performance and operational viability of the two DA techniques when the observation equation is highly nonlinear. Note that EnKF assumes linear observation equations whereas MLEF does not. We performed comparative evaluation of homoscedastic versus heteroscedastic modeling of observation errors for MLEF as

well as comparative evaluation of MLEF and EnKF under varying conditions of the magnitude of the dynamical model error, the number of ensemble members, and the number of streamflow data assimilated per cycle. The main findings and recommendation are as follows:

- In general, MLEF improves over EnKF consistently over varying conditions of observational and model errors and ensemble size.
- Heteroscedastic modeling of observation errors for MAP and streamflow does not improve over homoscedastic modeling for MLEF.
- MLEF is found to be not very sensitive to modeling of observational errors.
- Introducing model error in soil moisture dynamics improves DA performance significantly at short lead times. MLEF generally shows smaller sensitivity to the magnitude of the dynamical model error than EnKF.
- Sensitivity to ensemble size indicates that MLEF is able to produce significantly more accurate streamflow predictions at the catchment outlet using fewer ensemble members than EnKF. To achieve similar performance, the total CPU time required for MLEF is significantly smaller than that for EnKF.
- Additional research is necessary to produce reliable ensembles for analysis and prediction and to assess their quality via rigorous ensemble verification for both streamflow and soil moisture.
- Additional research is also necessary to assess the quality of DA-aided solutions for the model states using soil moisture observations.

7.2. Comparative evaluation of radar-based quantitative precipitation estimates (QPE)

This dissertation also investigates how different radar-based QPEs available in the Dallas-Fort Worth Metropolex area may differ in accuracy over different spatiotemporal scales of

aggregations. To that end, comparative evaluation was carried out for the Multisensor Precipitation Estimator, NEXRAD Digital Hybrid Scan Reflectivity, Q2 and CASA. The main findings are as follows:

- DHR has the least amount of information relative to other QPE products.
- Q2 is found to be least biased in the mean, most biased in variability, and more skillful for larger amounts.
- MPE has the highest information content relative to others and obtain the highest weights in the merging process at low rainfall depth while CASA has the higher weights at higher rainfall thresholds.
- CASA is found to be the most skillful overall, particularly for larger amounts, add skill due to increased location specificity from higher resolution.
- Parsimonious threshold-dependent multi-QPE merging may provide the most skillful estimate.
- Additional research is necessary to consider time series representation of multiple QPE vs. the verifying observations to provide event-specific view of the quality of the QPEs.
- Additional researched is needed to account for representativeness errors in rain gauge observations.
- Hydrologic evaluation is necessary to assess the significance of the differences and improvemments in terms of runoff and flow.

7.3. Improving high-resolution precipitation analysis via fusion of multiple radar-based precipitation products

Due to large sensitivity of hydrologic modeling and prediction to errors in quantitative precipitation estimates (QPE), it is very important in high-resolution hydrologic modeling that the

accuracy of high-resolution QPE be improved to the greatest possible extent. In this work, we comparatively evaluate four procedures for such fusion: Direction Estimation (DE), Bias Correction (BC), Reduced-Dimension Bias Correction (RBC) and Simple Estimation (SE). They are applied to fuse the MPE and radar-only Q2 products at the 15-min 1-km resolution (Experiment 1), and the MPE and CASA product at the 15-min 500-m resolution (Experiment 2). Main finding are as follows:

- The performance of DE and BC are generally comparable. Between the two, while DE is more attractive for computational economy, BC is more attractive for nonnegativity of the fused estimates.
- The performance of RBC is very poor as it does not account for the fact that biases in the QPE products depend on the magnitude of precipitation.
- Only SE passes the evaluation criterion consistently of being superior to the ingredient QPEs and trivially downscaled lower-resolution QPE.
- The simplicity and robustness of SE observed in this work make a strong case for its operational implementation as a post-processor to the QPE product generation process.

7.4. Evaluation of the NWS distributed hydrologic model over the Trinity River Basin in Texas

Distributed models are a promising tool for producing high-resolution streamflow and soil moisture information. We examine how uncalibrated operational distributed models may compare with finely-tuned lumped models. The comparative simulation experiment is carried out for 10 headwater basins in the Trinity River Basin in TX. The motivation for the above comparison stems from the fact that calibration of distributed models is generally very expensive and as such is to be minimized or avoided if possible. The main findings follow below:

- Uncalibrated HL-RDHM produces reasonably skillful simulations of outlet flow for the majority of the 10 headwater basins.
- For a half of the basins, however, bias in HL-RDHM simulation exceeds 20 percent. Gross oversimulation by HL-RDHM is observed for JAKT2 and BRPT2 while HL-RDHM did very well for RYET2, a slowly responding basin with complex UHG.
- The findings in this work point to limited calibration to reduce systematic biases in runoff and optimization of selective routing parameters to reduce timing error.
- HL-RDHM is suitable for high resolution hydrologic modeling in the DFW area.

7.5. High resolution distributed model and scale sensitivity

To assess the sensitivity of streamflow simulation to the resolution of precipitation input and hydrologic modeling, conditional sensitivity analysis was carried out. Streamflow was simulated for three catchments in DFW ranging from 40 to 52 km^2 using HLRDHM with the resolution of precipitation varying from 1/16 to 1 HRAP and 1 to 60 min, and the spatial resolution of PCTIM and the two channel routing parameters varying form 1/16 to 1 HRAP. The precipitation input used was the CASA QPE available at 500-m 1-min resolution. The main finding are as follows:

- Little consistent pattern is observed in dependence of streamflow simulation on spatial resolution.
- While the differences are very small, the cross correlation between the simulated and observed flows as a function of spatial resolution shows that, the higher the resolution is, the higher the correlation is.
- The power spectra of simulated and observed streamflow show that the MPE-forced simulations capture the lower-frequency variability (up to a wavelength of about 5

hours) better than the CASA QPE-forced, but that the CASA QPE-forced simulations are marginally better than the MPE-forced for capturing higher-frequency variability.

- Given that the time-to-peak is on the order of a few hours for these catchments, higher frequency variability contributes little to the overall quality of streamflow simulation. One may hypothesize that, given the relatively large size of the catchments, the spatiotemporal variability of precipitation may be filtered out through the hydrologic processes. In such a case, the impact of higher-resolution QPE would not be felt in streamflow simulations. Additional research is necessary to test the above hypotheses.
- For sensitivity to temporal resolution, it is seen that the errors are reduced at lower resolutions of 30 to 60 min for the urban catchments studied in this work.
- The sensitivity analysis results indicate that, the higher the temporal resolution is, the larger the simulated peak flow is, but that there is little or no dependence of time-to-peak or flow volume on temporal resolution.
- The autocorrelation function of the simulated streamflow matches that of the observed most closely at a 30-min resolution. Similarly, the spectrum of the simulated streamflow matches that of the observed most closely at 30 to 60-min resolutions.
- For the catchments studied in this work, streamflow simulation does not significantly benefit from higher temporal resolution. The above picture, however, may change for smaller catchments, investigation of which is left as a future endeavor.
- Additional research is necessary to identify and attribute the sources of errors in streamflow simulation.

Admittedly, the research carried out in this dissertation addresses only a few challenges in hydrologic prediction. Undoubtedly, much additional work is needed to fully address them. It is hoped that the additional knowledge gained and the tools developed will serve as building blocks and lead to an evolving system for monitoring and prediction of water resources and water-related hazards, particularly in large urban areas, that integrates advanced sensing, data fusion, data assimilation and high-resolution modeling to provide accurate, and time- and location-specific information that improves the quality of life and sustainability.

Appendix A

Derivation of high-resolution permanent impervious area (PCTIM)

Permanent impervious area is one of the SAC-SMA parameter which impacts directly on the production of direct runoff. Urbanization has increased the percentage of the impervious areas which result in less infiltration and higher runoff values. Therefore, urban areas are more prone to flooding, particularly flash flooding.

Since impervious areas play an important role in rainfall-runoff processes in urban areas, fractional impervious area maps are produced based on the information obtained from the Cities of Fort Worth, Arlington and Grand Prairie at different spatial resolutions. Each city provided some partial information about the impervious areas within the cities as listed in Table A-1. All the impervious maps were merged together (Figure A-1) and the percentage of the imperviousness was calculated for each pixel (ranging from 250 m to 4 km). As depicted in Figure A-2 finer resolution has more specific information.

Table A-1 Available GIS layers from cities of Fort Worth, Arlington, and Grand Prairie.

Map Layer	Fort Worth	Arlington	Grand Prairie
Building footprint	✓	✓	✓
Impervious cover of commercial	This has parking lots for commercial buildings	-	This has parking lots for commercial buildings
Pavements	It has only streets	It has all streets and parking lots	-
Centerline of sidewalk	Made a buffer (3.25 ft) So each sidewalk is 6.5 ft wide.	-	-
Centerline of streets	-	-	Made a buffer 6 ft for each lane (Standard width for lane is 12 ft)

Figure A-1 Merged impervious covers obtained from the Cities of Fort Worth, Arlington and Grand Prairie

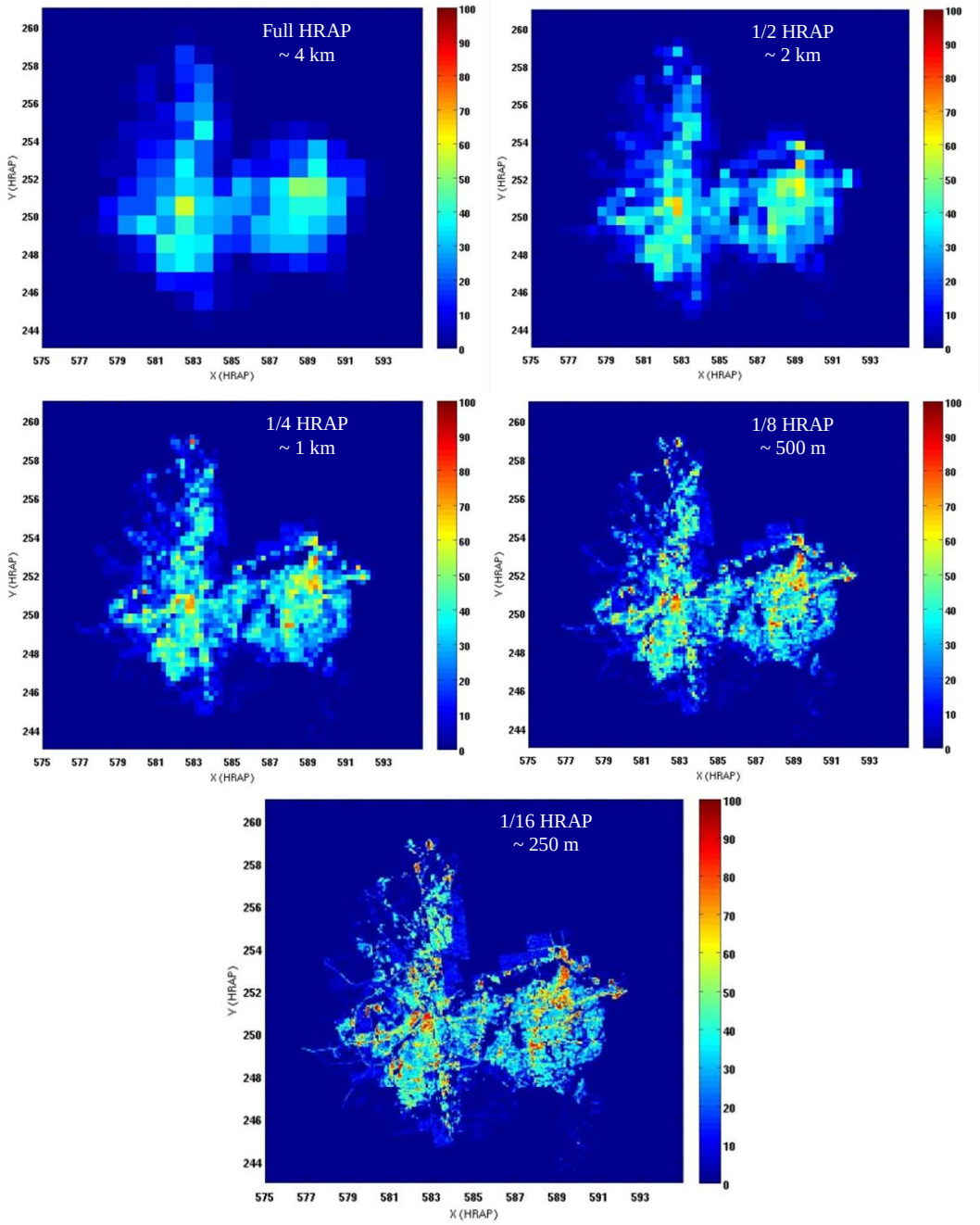

Figure A-2 Impervious fraction at different spatial resolutions within the Cities of Fort Worth, Arlington and Grand Prairie.

Appendix B

Derivation of high-resolution kinematic-wave channel routing parameters

A distributed model requires cell-to-cell connectivity information to perform routing. This cell-to-cell connectivity can be derived based on the flow direction. DEM data are available at various fine resolutions such as ~10 m, however, the distributed hydrologic models like HL-RDHM operates at coarser resolutions (e.g., ~4 km). Hence, there is a need to derive the flow direction and consequently the cell-to-cell connectivity at the coarse resolution at which the model operates. Reed (2003) proposed a new algorithm, called cell outlet tracing with an area threshold (COTAT) to assign flow direction to any cell at the coarse resolution from the available information at higher resolutions. An area threshold is used to control the tendency toward diagonal flows in the output. The basic steps in COTAT algorithm is explained below and is described in detail in Reed 2003.

1. Identify an outlet pixel in each coarse-resolution cell
2. For each cell, trace downstream, from its outlet pixel, along the flow path defined by high-resolution flow direction
3. For each subsequent outlet pixel reached, determine its total drainage area and subtract the drainage area of the starting outlet pixel
4. Assign the flow direction of the starting cell toward the neighboring cell with the farthest outlet along the trace

The National Elevation Dataset (NED) with 30 meter resolution from NHDPlus Version 2 dataset is used here. The derived flow directions at different resolutions are illustrated in Figure B-1. As depicted 4 km resolution is not capturing the river system very well, however, having higher resolutions such as 500 meter or 250 meter can represent the river system detail well.

Hillslope and channel routing in HL-RDHM is performed using kinematic-wave routing. Within each cell, fast (surface) runoff is first routed over conceptual hillslope, and then the combination of channel inflow from hillslope routing, slow runoff (subsurface/ground) and inflow from upstream cells is routed via channel routing (Koren et al., 2004). A conceptual hillslope consists of a number of uniform hillslopes (the number of uniform hillslopes depends on the stream channel density specified for the cell and the cell area). The conceptual channel that passes water from cell-to-cell usually represents the

highest order stream in a selected cell. The cell-to-cell connectivity sequence which is used to transfer water from upstream to downstream cells and to the basin outlets.

Koren et al. (2004) described the mathematical formulas for hillslope and channel routing and also the algorithms that can be used to derive the distributed hillslope and channel routing parameters. For the hillslope routing, the following equation is used to calculate the discharge per unit area of hillslope.

$$q_h = 2k_q D \frac{\sqrt{S_h}}{n_h} h^{5/3} \tag{B-1}$$

where k_q is a unit transformation coefficient, and D is stream channel density in km^{-1}. S_h is hillslope slope, n_h is hillslope roughness coefficient and h is the average hillslope water. Default and spatially constant values for drainage density (D) and the hillslope roughness (n_h) is used for most of studies. We also use the default value here. The hillslope slope can be derived by simple averaging the slope calculated based on DEM data for 30m×30m pixels to get the coarse resolution slope with user-defined resolutions (ranging from 250m to 4km). The derived hillslope slopes are plotted in Figure B-2.

For the channel routing method, we have used the rating curve option (rutpix9) available in HL-RDHM. The channel discharge for each cell is a power function of the cross sectional area (A) as follows:

$$Q_c = q_0 A^{q_m} \tag{B-2}$$

where q_0 is the specific channel discharge per unit channel cross section area, and q_m is the power value. To derive the q_0, rearrange Eq. (B-2) as following:

$$q_0 = \frac{Q_c}{A^{q_m}} \tag{B-3}$$

Therefore, specific discharge can be calculated if the A and Q_c are known. Mean annual flow can be derived using the USGS CONUS-side dataset of mean average annual runoff (Figure B-3). A also can be derived from the following equation.

$$A = \frac{Q}{V} \tag{B-4}$$

where V is velocity and can be calculated using the empirical equation developed by Jobson (1996) which is simplified to the following equation:

$$V = 0.094 + 0.0143\left(\frac{D_a^{1.25}\sqrt{g}}{Q}\right)^{0.919} S^{0.159}\frac{Q}{D_a} \quad \text{(B-5)}$$

where D_a is the upstream drainage area and can be calculated using the flow direction and cell size grids, g is a known constant. With A and Q known, q_m is the only unknown for q_0 calculation. The exponent value is simply assigned 1.3. Figure B-4 shows the derived specific discharge over DFW domain.

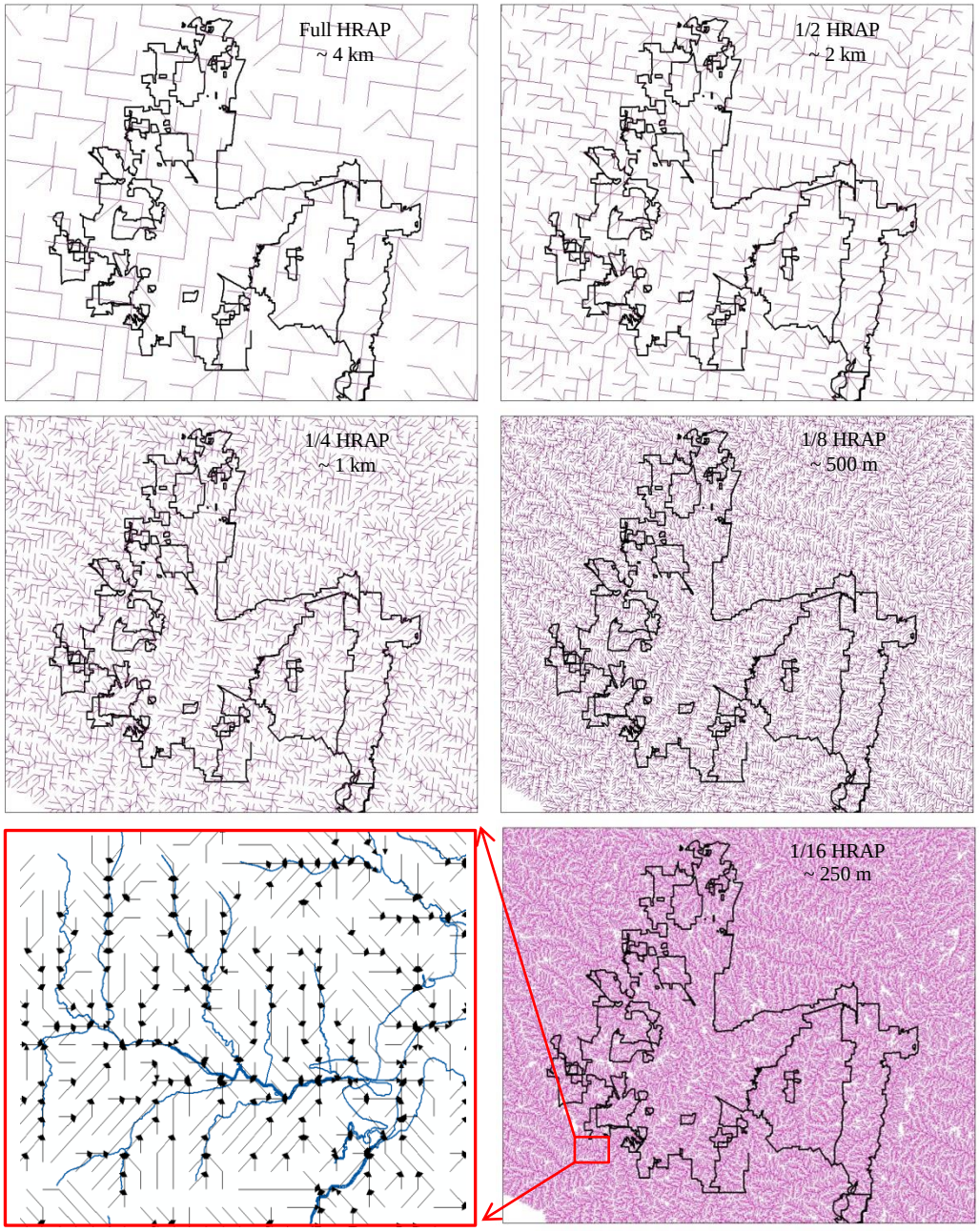

Figure B-1 Derived flow line at different spatial resolutions within the Cities of Fort Worth, Arlington and Grand Prairie. Lower left plot is a close up from flowlines overlaid on FEMA water feature line for 1/16 HRAP resolution (~ 250 meter).

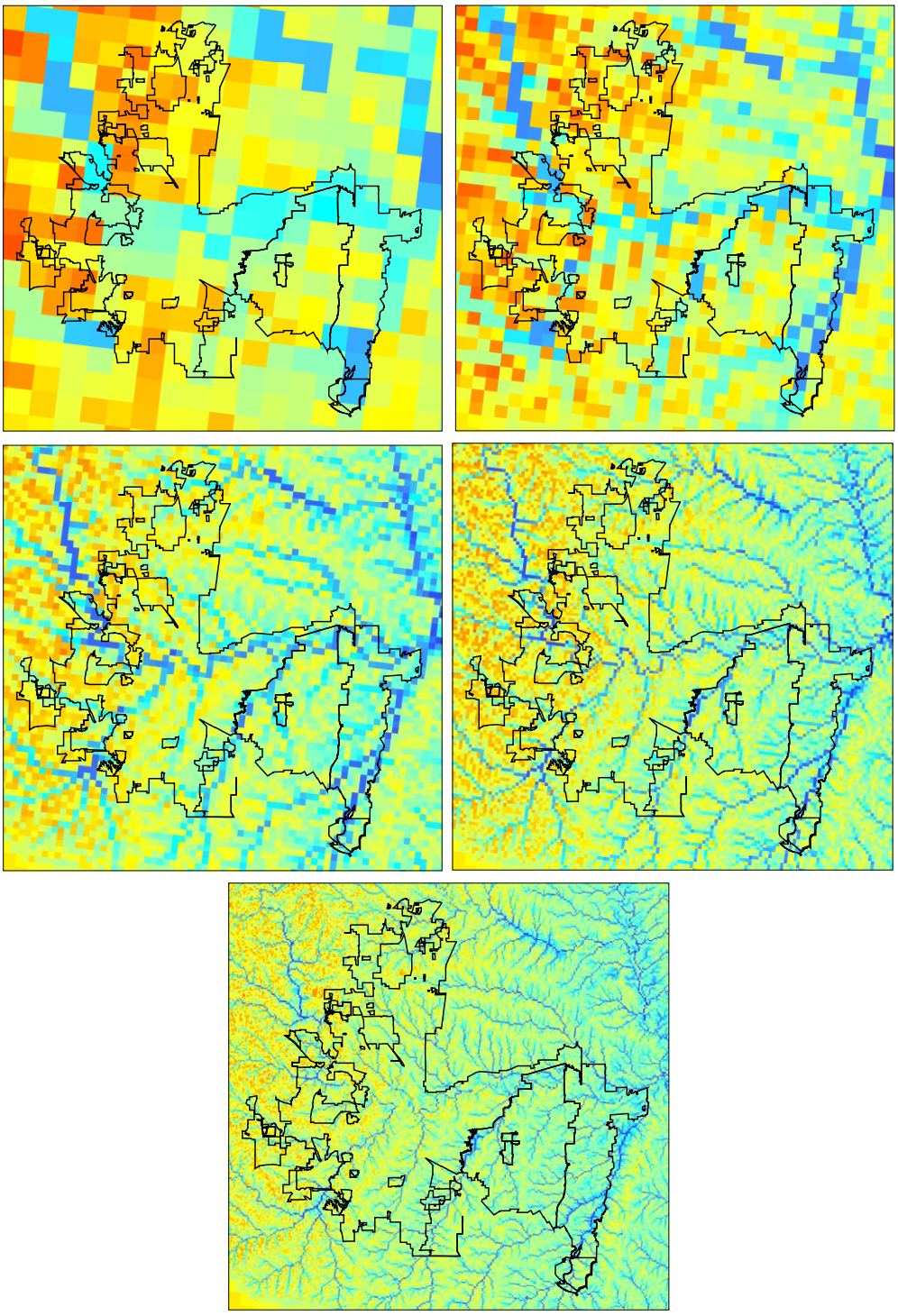

Figure B-2 Derived hillslope slope at different resolutions within DFW domain

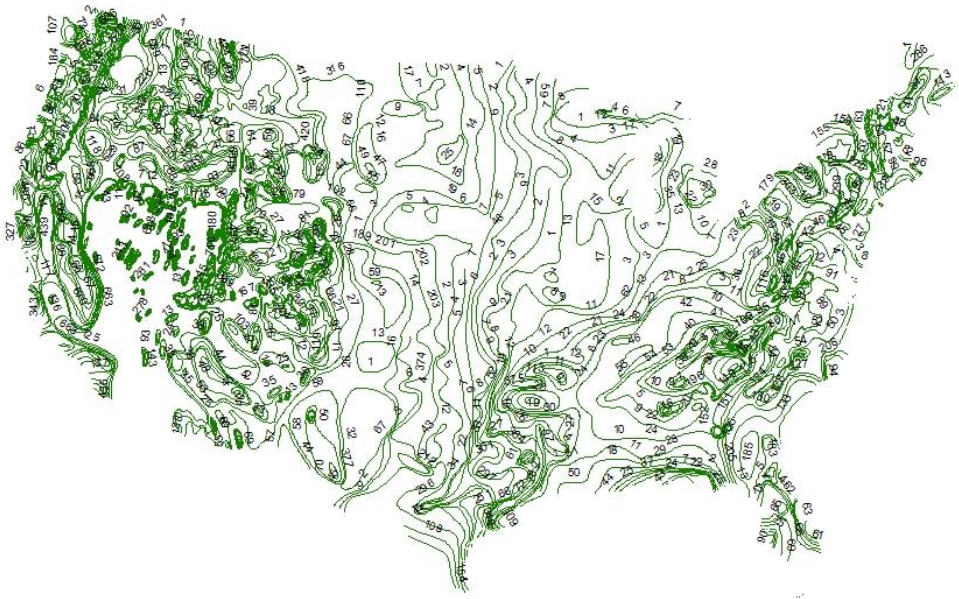

Figure B-3 Mean annual runoff for US (Gebert et al. 1987)

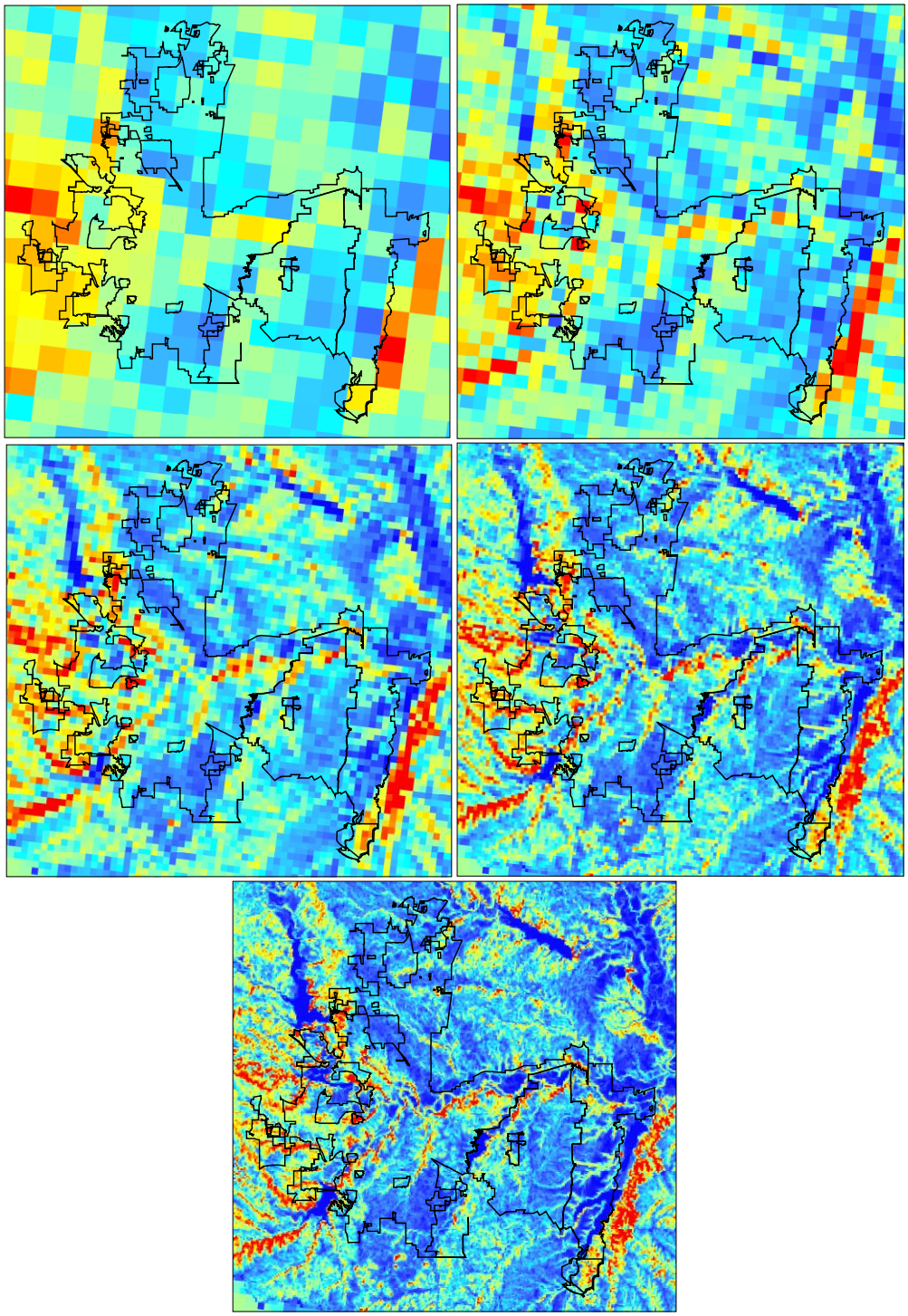

Figure B-4 Derived specific discharge at different resolutions within DFW domain.

Appendix C

Derivation of rating curves

Kean and Smith (2005, 2010) developed a fluid mechanically based method to generate stage-discharge relation (rating curve) for geomorphically stable channels. The model consists of two categories: 1) a set of procedure for quantifying the various contributions to the total flow resistance in the channel and 2) a flow model into which the results of these procedures are embedded.

The channel roughness is estimated from the field measurement of the following parameters: 1) channel geometry, 2) the physical roughness of the bed, banks, and floodplain, and 3) the vegetation density on the banks and floodplain. Kean and Smith method models streamflow in a channel reach by solving Saint-Venant equations for steady, non-uniform flow in one dimension. The equations conserve mass ($\partial Q/\partial x=0$) and momentum,

$$\frac{1}{2}\frac{\partial(u^2)_{av}}{\partial x} + g\frac{\partial E}{\partial x} + \frac{1}{\rho}\frac{(\tau_b)_{av}}{R} = 0 \qquad \text{(C-1)}$$

in which $(u^2)_{av}$ is the square of the downstream velocity component averaged over the cross section, $(\tau_b)_{av}$ is the perimeter-averaged shear stress, E is the elevation of the water surface, and R is the hydraulic radius.

To apply the Kean and Smith model, we used LiDAR data to create the channel shape and derive the river cross sections. LiDAR is an optical remote-sensing technique that uses laser light to densely sample the surface of the earth, producing highly accurate x, y, z measurements. The derived river cross sections were then transferred to FastMECH software to build mesh. FaSTMECH (Flow and Sediment Transport with Morphological Evolution of Channels) is a river flow/riverbed variation analysis solver developed by Dr. Jonathan Nelson of the U.S. Geological Survey (USGS). The created mesh will then be used in the model to calculate the bed slope, water slope, wetted area and perimeter at different stages.

The physical roughness of the bed can be related to the particle size of the bed material by $z_o = 0.1D_{84}$, where D_{84} is the diameter of sediment at the 84th percentile of the grain size distribution. To determine D_{84} value and then relative bed roughness (z_o), we used the grain size distribution of the seven channels in Fort Worth (Table C-1). By using D_{84} of these seven channels in Fort Worth, an ensemble of

stage-discharge relations were calculated at the location of the water level sensors. It should be noted the effect of the vegetation density was disregarded to calculate the rating curve.

Table C-1 D_{84} and corresponding relative bed roughness values of seven channels in Fort Worth

Channel	D_{84} (mm)	z_0 (mm)
Misty Meadow	21.5	2.15
SC-2	23.1	2.31
Edgecliff Branch	37	3.7
SC-1	42	4.2
Royal Creek (2)	53	5.3
Royal Creek (1)	60	6
Marys Creek	114.4	11.44

References

Accadia, C., S. Mariani, M. Casaioli, A. Lavagnini and A. Speranza, 2003: Sensitivity of precipitation forecast skill scores to bilinear interpolation and a simple nearest-neighbor average on high-resolution verification grids. Weather and Forecasting, 18, 918-932.

Anagnostou, E.N., Krajewski, W.F., Smith, J.A., 1999. Uncertainty quantification of mean-areal radar-rainfall estimates. J. Atmos. Oceanic Technol. 16, 206–15.

Anderson, J.L., 2001. An ensemble adjustment Kalman filter for data assimilation. Mon. Wea. Rev. 129, 2884-2903.

Anderson, R.M., Koren, V., Reed, S.M., 2006. Using SSURGO Data to Improve Sacramento Model a-priori Parameter Estimates. J. of Hydrol., 320(1): 103-116.

Barnes, L.R., Gruntfest, E.C., Hayden, M.H., Schultz, D.M., and Benight, C., 2007: False Alarms and Close Calls: A Conceptual Model of Warning Accuracy. Wea. Forecasting, 22, 1140–1147.

Berndt, C., Rabiei, E., Haberland, U., 2014. Geostatistical merging of rain gauge and radar data for high temporal resolutions and various station density scenarios. J. of Hydrol., 508, 88-101.

Berne, A., and W. F. Krajewski, 2013. Radar for hydrology: Unfulfilled promise or unrecognized potential?, Advances in Water Resources, 51, 357–366.

Bocquet, M., 2011. Ensemble Kalman filtering without the intrinsic need for inflation. Nonlin. Processes Geophys., 18, 735–750.

Breidenbach, J.P., Seo, D.J., Fulton, R. A., 1998. Stage II and III post processing of the NEXRAD precipitation estimates in the modernized National Weather Service, 14th Conf on IIPS, AMS, Phoenix, Jan.

Bringi, V. N. Chandrasekar, V., 2001. Polarimetric Doppler Weather Radar: Principles and applications, Cambridge University Press, 648 pp., 2001.

Brocca, L., Melone, F., Moramarco, T., Wagner, W., Naeimi, V., Bartalis, Z., Hasenauer, S., 2010. Improving runoff prediction through the assimilation of the ASCAT soil moisture product. Hydrol. Earth. Syst. Sci. 14, 1881–1893.

Brown, J.D., Demargne, J., Seo, D.J., Liu, Y., 2010. The Ensemble Verification System (EVS): A software tool for verifying ensemble forecasts of hydrometeorological and hydrologic variables at discrete locations. Environmental Modelling & Software, 25 (7), 854–872.

Burnash, R.J.C., Ferral, R.L., McGuire, R.A., McGuire, R.A., 1973. A generalized streamflow simulation system: conceptual modeling for digital computers. US Department of Commerce National Weather Service and State of California Department of Water Resources.

Carpenter, T.M., Georgakakos, K.P., 2004. Impacts of parametric and radar rainfall uncertainty on the ensemble streamflow simulations of a distributed hydrologic model. J. Hydrol. 298, 202-221.

Carrio, G.G., Cotton, W.R., Zupanski, D., Zupanski, M., 2008. Development of an Aerosol Retrieval Method: Description and Preliminary Tests. J. Appl. Meteor. Climatol. 47, 2760-2766.

Chandasekar, V., Lim, S., 2008. Retrieval of reflectivity in a networked radar environment. Journal of Atmospheric and Oceanic Technology, 25, 1755-1767.

Chandrasekar, V., Wang, Y., Chen, H.: The CASA quantitative precipitation estimation system: a five year validation study, Nat. Hazards Earth Syst. Sci., 12, 2811-2820, doi:10.5194/nhess-12-2811-2012, 2012.

Chandrasekar, V., Cifelli, R., 2012. Concept and principles of rainfall estimation from radar: Multi sensor environment and data fusion. Indian Journal of Radio & Space Physics, Vol 41, August, 389-402.

Chang, F.J.,Chiang, Y.M., Tsai, M.J., Shieh, M.C., Hsu, K.L., Sorooshian, S., 2014. Watershed rainfall forecasting using neuro-fuzzy networks with the assimilation of multisensor information. J. of Hydrol., 222(1-4), 93-108.

Chen, F., Crow, W.T., Starks, P.J., Moriasi, D.N., 2011. Improving hydrologic predictions of a catchment model via assimilation of surface soil moisture. Adv. Water Resour. 34, 526-536.

Chow, V.T., Maidment, D.R., Mays, L.W., 1988. Applied Hydrology, McGraw-Hill, New York, pp. 530-537.

Chumchean, S., Sharma, A., Seed, A., 2003. Radar rainfall error variance and its impact on radar rainfall calibration. J. Phys. Chem. Earth 28, 27–39.

Ciach, G.J., Krajewski, W.F., 1999. On the estimation of radar rainfall error variance. Adv. Water Resour. 22, 585-595.

Ciach, G.J., 2003. Local random errors in tipping-bucket rain gauge measurements. J. Atmos. Oceanic Technol. 20, 752-759.

Ciach, G.J., Habib, E., Krajewski, W.F., 2003. Zero-covariance hypothesis in the error variance separation method of radar rainfall verification. Adv. Water Resour. 26, 573–80.

Clark, M.P., Rupp, D.E., Woods, R.A., Zheng, X., Ibbitt, R.P., Slater, A.G., Schmidt, J., Uddstorm, M.J., 2008. Hydrologic data assimilation with the ensemble kalman filter: use of streamflow observations to update states in a distributed hydrological model. Adv. Water Resour. 31, 1309-1324.

Cloke, H.L., Pappenberger, F., 2009: Ensemble flood forecasting: a review. J. Hydrol. 375, 613-626.

Cohn, S.E., Sivakumaran, N.S., Todling, R., 1994: A fixed-lag Kalman smoother for retrospective data assimilation. Mon. Wea. Rev., 122, 2838-2867.

Cohn, S.E., 1997: Estimation theory for data assimilation problems: Basic conceptual framework and some open questions. J. Meteor. Soc. Japan 75, 257–288.

Cressie, N., and Huang, H.C. 1999. Classes of Nonseparable, Spatiotemporal Stationary Covariance Functions. Journal of the American Statistical Association, 94, 1330-1340.

Delrieu, G., Wijbrans, A., Boudevillain, B., Faure, D., Bonnifait, L., Kirstetter, P.E., 2014. Geostatistical radar–raingauge merging: A novel method for the quantification of rain estimation accuracy. Advances in Water Resources 71, 110–124.

De Lannoy, G.J.M., Houser, P.R., Pauwels, V.R.N., Verhoest, N.E.C., 2007. State and bias estimation for soil moisture profiles by an ensemble Kalman filter: effect of assimilation depth and frequency. Water Resour. Res. 43, W06401. doi:10.1029/2006WR005100.

Demargne, J., Wu, L., Regonda, S., Brown, J., Lee, H., He, M., Seo, D.J., Hartman, R., Fresch, M., Zhu, Y., 2014. The science of NOAA's operational hydrologic ensemble forecast service. Bull. Amer. Meteor. Soc. 95(1), 79-98. doi:http://dx.doi.org/10.1175/BAMS-D-12-00081.

Duan, Q., 2013. Global Optimization for Watershed Model Calibration. In: Q. Duan, S. Sorooshian, H. Gupta, H. Rosseau and R. Turcotte (Editors), Calibration of Watershed Models. Water Science and Applications. AGU, 89-104..1

Ebtehaj, A.M., Foufoula-Georgiou, 2013. On variational downscaling, fusion, and assimilation of hydrometeorological states. A unified framework via regularization. Water Resources Research, 94, 5944-5963.

Evensen, G., 1994. Sequential data assimilation with a nonlinear quasi-geostrophic model using Monte Carlo methods to forecast error statistics. J. Geophys. Res. 99 (C5), 10143–10162.

Evensen, G., van Leeuwen, P.J., 2000. An ensemble Kalman smoother for nonlinear dynamics. Mon. Wea. Rev. 128, 1852-1867.

Evensen, G., 2003. The ensemble Kalman filter: theoretical formulation and practical implementation. Ocean Dynamics, 53, 343-367.

Fares, A., Awal, R., Michaud, J., Chu, P.S., Fares, S., Kodama, K., Rosener, M., 2014. Rainfall-runoff modeling in a flashy tropical watershed using the distributed HL-RDHM model. J. of Hydrol., http://dx.doi.org/10.1016/j.jhydrol.2014.09.042

Fletcher, S.J., Zupanski, M., 2007. An Alternative to bias correction in retrievals and direct radiance assimilation. Proceedings of the 11th symposium on Integrated Observing and Assimilation Systems for Atmosphere, Oceans and land Surface, January 14–18, San Antonio, TX, Amer. Meteor. Soc.

Fulton, R.A., Breidenbach, J.P. Seo, D.J., Miller, A.D., 1998. The WSR-88D Rainfall Algorithm. Journal of Weather and Forecasting, 13, 377-395.

Fulton, R.A., 2002. Activities to improve WSR-88D radar rainfall estimation in the National Weather Service. In: Proceedings of the Second Federal Interagency Hydrologic Modeling Conference, Las Vegas, Nevada, July 28–August 1.

Gebert ,W.A., Graczyk, D.J., Krug, W.R. 1987. Average annual runoff in the United States, 1951–80. Hydrol Invest Atlas HA-710, US Geological Survey, Reston, VA.

Gires, A., Tchiguirinskaia, I., Schertzer, D., Schellart, A., 2014. Influence of small scale rainfall variability on standard comparison tools between radar and rain gauge data. J. Atmos. Sci. 138, 125-138.

Gneiting, T., 2002. Nonseparable, Stationary Covariance Functions for Space-Time Data, Journal of the American Statistical Association, Vol. 97, No. 458 (Jun., 2002), pp. 590-600.

Greene, D.R., Huldow, M.D., 1982. Hydrolometeorologic grid mapping procedure. American Water Resours. Assn. Int. Symp. On Hydrolometeorol. AURA, Herndon, Va.

Gupta, H.V., Sorooshian, S., Hogue, T.S., Boyle, D.P., 2013. Advances in Automatic Calibration of Watershed Models. In: Q. Duan, S. Sorooshian, H. Gupta, H. Rosseau and R. Turcotte (Editors), Calibration of Watershed Models. Water Science and Applications. AGU, 9-28.

Habib, E., Krajewski, W.K., 2002. Uncertainty analysis of the TRMM ground-validation radar-rainfall products: Application to the TEFLUN-B field campaign. J. Appl. Meteor., 41 (5), 558-572.

Habib, E., Ciach, G.J., Krajewski, W.F., 2004. A method for filtering out raingauge representativeness errors from the verification distributions of radar and raingauge rainfall. Adv. Water Resour. 27, 967-980.

Habib, E. Larsona, B.F., Graschelb, J., 2009. Validation of NEXRAD multisensor precipitation estimates using an experimental dense rain gauge network in south Louisiana. J. of Hydrol., 373 (3-4), 463-478.

Habib, E., Lee, G., Kim, D., Ciach, G.J., 2010. Ground-based direct measurements. chapter in AGU Book Volume on Rainfall: State of the Science, F. Testik and M. Gebremichael, Editors. Geophys. Monogr. Ser. 191. doi:10.1029/GM191.

Habib, E., Qin, L., Seo, D.J., Ciach, G.J., Nelson, B., 2013. Independent Assessment of Incremental Complexity in NWS Multisensor Precipitation Estimator Algorithms. J. Hydrol. Eng. 18, 143-155.

Herschy, R.W., 1993. The stage-discharge relation. Streamflow Measurement and Instrumentation, 4(1), 11-16.

Hou, D., Charles, M., Luo, Y., Toth, Z., Zhu, Y., Krzysztofowicz, R., Lin, Y., Xie, P., Seo, D.J., Pena, M., and Cui, B., 2012. Climatology-Calibrated Precipitation Analysis at Fine Scales: Statistical Adjustment of Stage IV towards CPC Gauge Based Analysis. Journal of Hydrometeorology. doi: http://dx.doi.org/10.1175/JHM-D-11-0140.1

Hudlow, M. D., 1988: Technological developments in real-time operational hydrologic forecasting in the United States, J. Hydrol., 102(1-4), 69-92.

Ibbitt, R.P., Clark, M.P., Woods, R.A., Zheng, X., Slater, A.G., Rupp, D.E., Schmidt, J., Uddstrom, M., 2007. Hydrological data assimilation with the ensemble Kalman filter: use of streamflow observations to update states in a distributed hydrological model. In: AGU fall meeting, San Francisco.

Jazwinski, A.H., 1970. Stochastic Processes and Filtering Theory. Academic Press, 376 pp.

Jobson, H.E., 1996, Prediction of traveltime and longitudinal dispersion in rivers and streams: U.S. Geological Survey Water-Resources Investigations Report 96-4013, 69 p.

Junyent, F., Chandrasekar, v., McLaughlin, D., Insanic, D., Bharadwaj, N., 2010: The CASA Integrated Project 1 Networked Radar System. J. Atmos. Oceanic Technol., 27, 61–78. doi: http://dx.doi.org/10.1175/2009JTECHA1296.1

Kalman, R.E., 1960. A new approach to linear filtering and prediction problems. J. Basic Eng. 82 (1), 35-45. doi:10.1115/1.3662552

Kean , J.W., Smith, J.D., 2005. Generation and verification of theoretical rating curves in the Whitewater River Basin, Kanssa. J. Geopgys. Res., 110.

Kean , J.W., Smith, J.D., 2010. Calculation of stage-discharge relations for gravel belled channels. Journal of Geophysical Research-Earth Surface, 115.

Kim, H.H., Park, S.K., Zupanski, D., Zupanski, M., 2010. Uncertainty analysis using the WRF maximum likelihood ensemble filter system and comparison with dropwindsonde observations in Typhoon Sinlaku (2008). Asia-Pac. J. Atmos. Sci. 46 (3), 317-325. doi: 10.1007/s13143-010-1004-1.

Klazura, G.E., Imy, D.A, 1993. A description of the initial set of analysis products available from the NEXRAD WSR-88D System. Bull. Amer. Meteorol. Soc., 74, 1293-1312.

Koren, V., Schaake, J., Duan, Q., Smith, M., Cong, S., 1998. Unpublished Report: "PET Upgrades to NWSRFS, Project Plan," unpublished report, August 13, 1998.

Koren, V.I., Smith, M., Wang, D., and Zhang, Z., 2000. Use of soil property data in the derivation of conceptual rainfall-runoff model parameters, American Meteorological Society 15th Conference on Hydrology, Long Beach, CA, pp. 103-106.

Koren, V.I., Smith, M.B., and Duan, Q., 2003. Use of a priori parameter estimates in the derivation of spatially consistent parameter sets of rainfall-runoff models. In: Q. Duan, S. Sorooshian, H. Gupta, H. Rosseau and R. Turcotte (Editors), Calibration of Watershed Models. Water Science and Applications. AGU, 239-254.

Koren, V., Reed, S., Smith, M., Zhang, Z., Seo, D.J., 2004. Hydrologic Laboratory Modeling System (HL-RMS) of the US National Weather Service. J. of Hydrol., 291, 297-318.

Koren, V., Smith, M., Cui, Z., Cosgrove, B., 2007. Physically-based modifications to the Sacramento soil moisture accounting model: modeling the effects of frozen ground on the rainfall-runoff process. NOAA Technical Report NWS 52, US.

Kuzmin, V., Seo D.J., and Koren, V., 2008. Fast and efficient optimization of hydrologic model parameters using a priori estimates and stepwise line search. J. of Hydrol., 353, 109-128.

Krzysztofowicz, R., 1999. Bayesian Theory of Probabilistic Forecasting via Deterministic Hydrologic Model. Water Res. Res. 35(9), 2739–2750.

Larson, B.F., Tokay, A., Habib, E., Nelson, B.R., 2008 .Validation of NWS Stage IV MultiSensor Precipitation Estimates (MPE) in the Mid-Atlantic Region. 88th Annual AMS meeting.

Lee, H., Seo, D.J., Koren, V., 2011. Assimilation of streamflow and in situ soil moisture data into operational distributed hydrologic models: Effects of uncertainties in the data and initial model soil moisture states. Adv. Water Resour. 34, 1597-1615.

Lee, H., Seo, D.J., Liu, Y., Koren, V., McKee, P., Corby, R., 2012.Variational assimilation of streamflow into operational distributed hydrologic models: effect of spatiotemporal adjustment scale. Hydrol. Earth Syst. Sci. 16, 2233-2251.

Lee, H., Zhang, Y., Seo, D.J., Kuligowski, R.J., Kitzmiller, D., Corby, R., 2013. Utility of SCaMPR satellite versus ground-based quantitative precipitation estimates in operational flood forecasting - the effects of TRMM data ingest. Submitted to the J. Hydrometeorol.

Li, M., Shao, Q., 2010. An improved statistical approach to merge satellite rainfall estimates and raingauge data. J. of Hydrol., 385, 51-64.

Li, Z., Navon, I.M., 2001. Optimality of variational data assimilation and its relationship with the Kalman filter and smoother. Q. J. Roy. Meteor. Soc. 127 (572), 661–683. doi: 10.1002/qj.49712757220.

Lim, S., Chandrasekar, V., Lee, P., Jayasumana, A.P., 2011: Real-Time Implementation of a Network-Based Attenuation Correction in the CASA IP1 Testbed. J. Atmos. Oceanic Technol., 28, 197–209. doi: http://dx.doi.org/10.1175/2010JTECHA1441.1

Linder G.A., Miller, A.J., 2012. Numerical modeling of stage-discharge relationship in urban streams. J. Hydrol. Eng., 17, 590-596.

Liu, Y., Gupta, H.V., 2007. Uncertainty in hydrologic modeling: toward an integrated data assimilation framework. Water Resour. Res. 43:W07401. doi:10.1029/2006WR005756.

Liu, Y., Brown, J., Demargne, J., Seo, D.J., 2011. A wavelet-based approach to assessing timing errors in hydrologic predictions. J. Hydrol. 397, 210-224.

Liu, H., Tian, F., Hu, H.C., Hu, H.P., Siavapalan, M., 2013. Soil moisture control on patterns of grass green-up in Inner Mongolia: an index based approach. Hydrol. Earth Syst. Sci., 17, 805-815.

Lokupitiya, R.S., Zupanski, D., Denning, A.S., Kawa, S.R., Gurney, K.R., Zupanski, M., 2008. Estimation of global CO_2 fluxes at regional scale using the maximum likelihood ensemble filter. J. Geophys. Res-Atmos. 113 (D20):19. doi:10.1029/2007JD009679.

Lorentzen, R.J., Nævdal, G., 2011. An Iterative Ensemble Kalman Filter. IEEE T. Automat. Contr. 56 (8).

McLaughlin, D.J., Chandrasekar, V., Droegemeier, K., Frasier, S., Kurose, K., Junyent, F., Philips, B., Cruz-Pol, S., Colom, J., 2005. Distributed Collaborative Adaptive Sensing (DCAS) for Improved Detection, Understanding, and Prediction of Atmospheric Hazards. Ninth Symposium on Integrated Observing and Assimilation Systems for the Atmosphere, Oceans, and Land Surface (IOAS-AOLS), American Meteor. Society.

Maybeck, P.S., 1979. Stochastic models, estimation, and control. Vol. I. Academic Press, New York.

Mejia, A.I. and Reed, S.M., 2011. Evaluating the effects of parameterized cross section shapes and simplified routing with a coupled distributed hydrologic and hydraulic model. J. of Hydrol., 409, 512-524.

Murphy, A.H., and Winkler, R.L. 1987. A general framework for forecast verification. Monthly Weather Review 115, 1330-1338.

Mesinger, F., 1996: Improvements in quantitative precipitation forecasting with the Eta regional model at the National Center for Environmental Prediction. Bull. Amer. Meteor. Soc., 77, 2637-2649.

Moradkhani, H., Hsu, K., Gupta, H., Sorooshian, S., 2005. Uncertainty assessment of hydrologic model states and parameters: sequential data assimilation using the particle filter. Water Resour. Res. 41. W05012. doi:10.1029/2004WR003604.

Moreau, E., Testud, J., Le Bouar, E., 2009. Rainfall spatial variability observed by X-band weather radar and its implication for the accuracy of rainfall estimates. Adv. Water Resour. 32, 1011-1019.

NCDC, http://www.ncdc.noaa.gov/wct/tutorials/?file=advanced-format_types.

Nelson B.R., Seo D.-J., Kim, D., 2010. Multisensor Precipitation Reanalysis, J. Hydrometeor., 11, 666–682.

NOAA Technical Report NWS 52.

Rodgers, C. D., 2000: Inverse Methods for Atmospheric Sounding: Theory and Practice. World Scientific, 238 pp.

Rakovec, O., Weerts, A.H., Hazenberg, P., Torfs, P.J.J.F., Uijlenhoet, R., 2012. State updating of a distributed hydrological model with Ensemble Kalman Filtering: effects of updating frequency and observation network density on forecast accuracy. Hydrol. Earth Syst. Sci. 16, 3435-3449.

Regonda, S., Seo, D.J., Lawrence, B., Brown, J.D., Demargne, J., 2013: Short-term ensemble streamflow forecasting using operationally-produced single-valued streamflow forecasts-A Hydrologic Model Output Statistics (HMOS) approach. J. Hydrol., 497, 80–96, doi:10.1016/j.jhydrol.2013.05.028.

Reichle, R.H., McLaughlin, D.B., Entekhabi, D., 2002. Hydrologic data assimilation with the ensemble Kalman filter. Mon. Wea. Rev. 130 (1), 103-114.

Reed, S.M., Maidment, D.R., 1999. Coordinate Transformations for Using NEXRAD Data in GIS-Based Hydrologic Modeling. Journal of Hydrologic Engineering, Vol. 4, No. 2, pp. 174-182, (doi: http://dx.doi.org/10.1061/(ASCE)1084-0699(1999)4:2(174))

Reed, S., Koren, V., Zhang, Z., Smith, M. and Seo, D.J., 2002. Distributed modeling for improved NWS river forecasts. Proceedings of the Second Federal Interagency Hydrologic Modeling Conference, Las Vegas, NV (2002).

Reed, S.M., 2003. Deriving flow directions for coarse-resolution (1-4 km) gridded hydrologic modeling. Water Resources Research, 39 (9), 1238, doi:10.1029/2003WR001989,2003

Reed, S., Koren, V., Smith, M., Zhang, Z., Modera, F., and Seo, D.J., 2004. Overall distributed model intercomparison project results. J. of Hydrol., 298, 27-60.

Reed, S., Schaake, J. and Zhang. Z., 2007. A distributed hydrologic model and threshold frequency-based method for flash flood forecasting at unguaged locations. J. of Hydrol., 337, 402-420.

Sakov, P., Oke, P.R., 2008. A deterministic formulation of the ensemble Kalman filter: an alternative to ensemble square root filters. Tellus, 60A(2), 361-371.

Schaake, J., Demargne, J., Hartman, R., Mullusky, M., Welles, E., Wu, L., Herr, H., Fan, X., Seo, D.J., 2007a: Precipitation and temperature ensemble forecasts from single-value forecasts. Hydrol. Earth Syst. Sci., Discuss. 4, 655-717.

Schaake, J., Hamill, T.M., Buizza, R., Clark, M., 2007b: HEPEX, the Hydrological Ensemble Prediction Experiment. Bull. Amer. Meteor. Soc. 88, 1541-1547.

Schellekens, J., Weerts, A.H., Moore, R.J., Pierce, C.E., Hildon, S., 2011. The use of MOGREPS ensemble rainfall forecasts in operational flood forecasting systems across England and Wales. Adv. Geosci. 29, 77-84.

Schweppe, F.C., 1973. Uncertain Dynamic Systems. Prentice-Hall, Englewood Cliffs, NJ, 563 pp.

Seo, D.J., 1998. Real-time estimation of rainfall fields using radar rainfall and rain gage data. J. Hydrol., 208, 37-52.

Seo, D.-J., Breidenbach, J.P., and Johnson, E.R., 1999. Real-time estimation of mean field bias in radar rainfall data, J. Hydrol., 233 (3-4), 131-171.

Seo, D. J., Perica, S., Welles, E., and Schaake, J., 2000. Simulation precipitation fields from Probabilistic Quantitative Precipitation Forecast, J. Hydrol., 239, 203-229.

Seo, D. J. Breidenbach, J. P., 2002. Real-time correction of spatially nonuniform bias in radar rainfall data using rain gauge measurements, J. Hydrometeorol., 3, 93-111.

Seo, D.J., Koren, V., Cajina, N., 2003. Real time variational assimilation of hydrologic and hydrometeorological data into operational hydrologic forecasting. J. Hydrometeorol. 4, 627-641.

Seo, D.J., Herr, H., Schaake, J., 2006. A statistical post-processor for accounting of hydrologic uncertainty in short-range ensemble streamflow prediction. Hydrol. Earth Syst. Sci., Discuss., 3, 1987-2035.

Seo, D.J., Cajina, L., Corby, R., Howieson, T., 2009. Automatic state updating for operational streamflow forecasting via variational data assimilation. J. Hydrol. 367, 255-275.

Seo, D.J., Seed, A., Delrieu, G., 2010. Radar-based rainfall estimation, chapter in AGU Book Volume on Rainfall: State of the Science, F. Testik and M. Gebremichael, Editors. Geophys. Monogr. Ser. 191. doi:10.1029/GM191.

Seo, D-J. 2013. Conditional bias-penalized kriging. Stochastic Environmental Research and Risk Assessment, 27, 43-58. DOI 10.1007/s00477-012-0567-z.

Seo, D.J., Siddique, R., Zhang, Y., Kim, D., 2014. Improving real-time estimation of heavy-to-extreme precipitation using rain gauge data via conditional bias-penalized optimal estimation. J. of Hydrol., Volume 519, Part B, 27 November 2014, Pages 1824-1835.

Sorooshian, S., Dracup, J.A., 1980. Stochastic parameter estimation procedures for hydrologie rainfall–runoff models: Correlated and heteroscedastic error cases. Water Resour. Res. 16 (2), 430–42.

Smith, M.B., Seo, D.-J., Koren, V.I., Reed, S., Zhang, Z., Duan, Q.-Y., Moreda, F., and Cong, S., 2004a. The distributed model intercomparison project (DMIP): motivation and experiment design. Journal of Hydrology, Vol. 298, Nos. 1-4, 4-26.

Smith, M., Koren, V., Zhang, Z., Reed, S., Seo, D.J., Moreda, F., Kuzmin, V., Cui, Z., Anderson, R., 2004b. NOAA NWS distributed hydrologic and modeling research and development. NOAA Technical Report NWS 51, US.

Smith, M., Koren, V., Zhang, Z., Zhang, Y., Reed, S.M., Ciu, Z., Modera, F., Cosgrove, B.N. Mizukami, N., Anderson, N., and DMIP2 Participants., 2012. Results of the DMIP 2 Oklahoma Experiments. J. of Hydrol. 418-419, 17-48.

Smith, M., Laurine, D.P., Korev, V., Reed, S.M., Zhang, Z., 2013. Hydrologic Model Calibration in the National Weather Service. In: Q. Duan, S. Sorooshian, H. Gupta, H. Rosseau and R. Turcotte (Editors), Calibration of Watershed Models. Water Science and Applications. AGU, 133-152.

Szidarovszky, F., E. Y. Baafi, and Y. C. Kim, 1987. Kriging without negative weights, Mathematical Geology, 19(6), 549-559.

Tarantola, A., 2005, Inverse Problem Theory (free PDF version), Society for Industrial and Applied Mathematics, ISBN 0-89871-572-5.

Thielen, J., Schaake, J., Hartman, R., Buizza, R., 2008. Aims, challenges and progress of the Hydrological Ensemble Prediction Experiment (HEPEX) following the third HEPEX workshop held in Stresa 27 to 29 June 2007. Atmos. Sci. Lett. 9 (2), 29-35. doi: 10.1002/asl.168.

van Leeuwen, P.J., Evensen, G., 1996. Data assimilation and inverse methods in terms of a probabilistic formulation. Mon. Wea. Rev., 124, 2898–2913.

Vasiloff, S.V., Seo, D.J., Howard, K.W., Zhang, J., Kitzmiller, D.H., Mullusky, M.G., Krajewski, W.F., Brandes, E.A., Rabin, R.M., Berkowitz, D.S., Brooks, H.E, McGinley, J.A., Kuligowski, R.J., Brown, B.G., 2007: Improving QPE and Very Short-Term QPF: An Initiative for a Community-wide Integrated Approach, Bulletin of the American Meteorological Society, December, 1899-1911.

Wang, X., Xie, H., Sharif, H., Zeitler, J., 2008. Validating NEXRAD MPE and stage III precipitation products for uniform rainfall on the Upper Guadalupe River Basin for the Texas Hill Country. J. Hydrol., 348, 73-86.

Weerts, A.H., Serafy, G.Y.H.El., 2006. Particle filtering and ensemble Kalman filtering for state updating with hydrological conceptual rainfall-runoff models. Water Resour. Res. 42 (9), W09403, doi:10.1029/2005WR004093.

Westcott, N.E., Knapp, H.V., Hillberg, S.D., 2008. Comparison of gage and multi-sensor precipitation estimates over a range of spatial and temporal scales in the Midwestern United States. J. of Hydrol., 351, 1-12.

Werner, K., Brandon, D., Clark, M., Gangopadhyay, S., 2005. Incorporating Medium-Range Numerical Weather Model Output into the Ensemble Streamflow Prediction System of the National Weather Service. J. Hydrometeor. 6, 101-114.

Werner, M., Cranston, M., Harrison, T., Whitfield, D., Schellekens, J., 2009. Recent developments in operational flood forecasting in England, Wales and Scotland. Meteorol. Appl.16 (1), 13-22. doi: 10.1002/met.124

Whitaker, J.S., Hamill, T.M., 2002. Ensemble data assimilation without perturbed observations. Mon. Wea. Rev. 130, 1913-1923.

Woldemeskel, F.M., Sivakumar, B., Sharma, A., 2013. Merging gauge and satellite rainfall with specification of associated uncertainty across Australia. J. of Hydrol. 499, 167-176.

Wu, L., Seo, D.J., Demargne, J., Brown, J., Cong, S., Schaake, J., 2011: Generation of ensemble precipitation forecast from single-valued quantitative precipitation forecast via meta-Gaussian distribution models. J. Hydrol., 399(3–4), 281–298.

Wu, W., Kitzmiller, D.,Wu, S., 2012: Evaluation of Radar Precipitation Estimates from the National Mosaic and Multisensor Quantitative Precipitation Estimation System and the WSR-88D Precipitation Processing System over the Conterminous United States. J. Hydrometeor, 13, 1080–1093. doi: http://dx.doi.org/10.1175/JHM-D-11-064.1

Xie, X., Zheng, D., 2010. Data assimilation for distributed hydrological catchment modeling via ensemble kalman filter. Adv. Water Resour. 33 (6), 678-690.

Yalmiz, K.K., Gupta, H.V., Wagener, T., 2008. A process-based diagnostic approach to model evaluation: Application to the NWS distributed hydrological model. Water Resources Research, 44, 1-18.

Young, C.B., Bradley, A.A., Krajewski, W.F., Kruger, A., Morrissey, M.L., 2000. Evaluating NEXRAD multisensory precipitation estimates for operational hydrologic forecasting. J. Hydrometeorol. 1, 241–54.

Zhang, Z., Koren, V., Reed, S., Smith, M.B. and Moreda, F., 2006. Comparison of simulation results using SSURGO-based and STATSGO-based parameters in a distributed hydrologic model. 3rd Federal Interagency Hydrologic Modeling Conference, Reno, NV.

Zhang Y, Adams T, Bonta JV, 2007. Subpixel-scale rainfall variability and the effects on separation of radar and gauge rainfall errors. J. Hydrometeorol. 8, 1348–63.

Zhang, J., Howard, K., Langston, C., Vassiloff, S., Kaney, B., Arthur, A., Cooten, S.V., Kelleher, K., Kitzmiller, D., Ding, F., Seo, D.J., Wells, E., Dempsey, C., 2011. National mosaic and multi-sensor QPE (NMQ) system description, results and future plans. Bull. Amer. Meteor. Soc., 92, 1321–1338. doi: http://dx.doi.org/10.1175/2011BAMS-D-11-00047.1

Zupanski, M., 2005. Maximum likelihood ensemble filter: Theoretical aspects. Mon. Wea. Rev. 133, 1710-1726.

Zupanski, D., Hou, A.Y., Zhang, S.Q., Zupanski, M., Kummerowa, C.D., and Cheung, S.H., 2007a. Applications of information theory in ensemble data Assimilation, QUARTERLY JOURNAL OF THE ROYAL METEOROLOGICAL SOCIETY Q. J. R. Meteorol. Soc. 133: 1533–1545.

Zupanski , D., Denning, A.S., Uliasz, M., Zupanski, M., Schuh, A.E., Rayner, P.J., Peters, W., Corbin, K.D., 2007b. Carbon flux bias estimation employing Maximum Likelihood Ensemble Filter (MLEF). J. Geophys. Res. 112 (D17). doi:10.1029/2006JD008371.

Zupanski, D., Paquin, K., Kelly, R., Nelson, S., Zupanski, M., Jankov, I., Mallapragada, P., 2010. Applications of data assimilation methodologies in wind power forecasting. Geophysical Research Abstracts, Vol. 12, EGU2010-7652-1, 2010. EGU General

Biographical Information

Arezoo Rafieei Nasab, obtained an B.Sc. degree in Irrigation and Drainage Engineering at University of Zabol in 2005. She pursued graduate studies in Water Resources Management at K. N. Toosi University of Technology and obtained M.Sc. degree in 2008. In addition to her academic experience, she worked for two years as a research assistant in the Department of Hydrology and Water Resources in the Soil Conservation and Watershed Management Research Institute (SCWMRI) of Iran where she was first acquainted with the operational side of hydrology. She started her Ph.D. program in fall 2011 under supervision of Dr. Dong-Jun Seo and gained significant experience in hydrologic models and forecasting. She has been awarded the Outstanding Graduate Student (Spring 2013). She graduated on December, 2014.